

From structure to application: studies on adenine-, pyrene- and lanthanide-based metal-organic frameworks

Thèse N° 7496

Présentée le 5 décembre 2019

à la Faculté des sciences de base

Laboratoire de simulation moléculaire

Programme doctoral en chimie et génie chimique

pour l'obtention du grade de Docteur ès Sciences

par

Andrzej GLADYSIAK

Acceptée sur proposition du jury

Prof. A. Züttel, président du jury

Prof. B. Smit, Dr K. Stylianou, directeurs de thèse

Prof. C. E. Housecroft, rapporteuse

Prof. R. Černý, rapporteur

Prof. M. Mazzanti, rapporteuse

2019

Acknowledgements

I would first like to thank my supervisors, Berend Smit and Kyriakos Stylianou, for their expert research guidance, for many ardent scientific discussions, and for being on my side in both good and bad times throughout the entirety of my PhD studies. I thank Tu Nguyen for his competent scientific advice, a lot of help in the laboratory, and fruitful collaboration. Many thanks go to Samantha Anderson – an ideal lab co-worker, always ready to help and to share the deepest experimental secrets, with whom I conducted some very successful experiments in Sion, Didcot and Grenoble. I acknowledge my lab friends, Bardiya Valizadeh, Arun Chidambaram, Chris Ireland, Mish Ebrahim, Pelin Kınık, Alina Kampouri, and Sergey Shyshkanov, for many interesting scientific discussions, for excitement in sharing the lab during the years of our PhD, and for friendly companionship. Special thanks to the youngest lab member, Sylvain Sudan, who did so well while preparing his MSc thesis under my humble co-supervision. To those who appeared in the lab only for a short period – Farrokh Mohammadnezhad, Aylin Kınık, and Nancy Domingues – it was nice to share the time with you! I thank Pascal Schouwink for many formal and informal discussions in the X-ray laboratory, for steady guidance in the most difficult crystallographic cases, and for sharing invaluable tips and tricks with me. I am grateful to Iurii Dovgaliuk, Dmitry Chernyshov, and other members of the Swiss-Norwegian Beamlines team for supporting me during the difficult yet exciting and rewarding experiments at the ESRF in Grenoble. I express my thanks to Mariana Spodaryk for introducing me to the fundamentals impedance spectroscopy. Many thanks to my fellows from the computational division, Katie Deeg, Pete Boyd, Matt Witman, Mohamad Moosavi, Daniele Ongari, and Kaili Ordiz, for their sheer scientific competence, patience in explaining the intricacy of molecular simulations to me, and for successful and enjoyable collaborations, and also to Efrem Braun, Johanna Huck, Michelle Liu, Rocio Mercado, Sudi Jawahery, Aliaksandr Yakutovich, Amber Mace, Andrés Guerrero, Daiane Borges, Leopold Talirz, Olga Syzgantseva, Özge Kadioğlu, Senja Barthel, Yongjin Lee, Zhi Li, and Kevin Jabłonka, with whom I did not have an opportunity to extensively collaborate, but with whom I could always talk and discuss in a friendly way. I thank Jung-Hoon Lee, Robert Palgrave, John Bacsá, and Professors: Matthew Rosseinsky, Jorge Navarro, Grigoris Itskos, Jeff Reimer, Lev Sarkisov, and Andreas Züttel, for their input to the jointly published papers. I am equally thankful to the members of my PhD committee, Professors Catherine Housecroft, Marinella Mazzanti, and Radovan Černý, for carefully reading the thesis, and providing me with valuable feedback which helped me improve it. I am deeply indebted to Professor Andrzej Katrusiak: thanks to his guidance during my MSc studies, I could enter the PhD programme at the EPFL. I am thankful to Weizhao Cai, Witold Zieliński, Szymon Sobczak, and my other peers from Poznań for their support. I thank the LSMO secretaries, Laure Dayer, Constance Witman, and Evelyn Ludi, for their steady help in various administrative and non-scientific questions. There were for sure many others who contributed to the preparation of my PhD thesis – various collaborators at the EPFL, external collaborators, local contacts at the synchrotron facilities, editors of the journals and anonymous reviewers of our papers, people met during conferences and those contacted only by email – whom I herein collectively thank.

Abstract

Metal–organic frameworks (MOFs) are coordination polymer materials in which inorganic metal ions or clusters are linked with multitopic organic ligands by means of coordination bonds. Their structural versatility allows for design of materials based on pre-formed building blocks, whereas their crystallinity enables the study of their underlying structures on the atomic level. The bottom-up approach of materials discovery involves first the study of the structure of the newly synthesised material followed by a detailed characterisation, from which a potential application is inferred.

This thesis presents the synthesis, structural determination and full characterisation of 10 novel MOFs constructed from ligands including adenine and pyrene-based H₄TBAPy as well as a lanthanide-based MOF. Based on their crystal structures, a variety of applications has been postulated for these materials, and the comparison with the materials already known in the literature has been undertaken.

In **SION-10**, the presence of active Cu^{II} centres and non-coordinated Cu^{II}–adenine complexes in the structural voids of the material was found to be key factors enabling the capture of ammonia with this material. Adenine-based **SION-31–35** served as a platform for investigation of N-protonation sites due to the different binding modes displayed by adenine in their structures. Bi-porous nature of the pyrene-based **SION-8** was used for as a proof of concept for CO₂/CH₄ separation of tuneable selectivity and for irreversible capture of iodine. In **SION-7**, the mutual orientation of the pyrene-based ligands and the pore content were shown to influence the fluorescence emission of the material, and to be finely tuneable by temperature changes. The lanthanide-based **SION-2** was found to exhibit a strong negative thermal expansion effect, which arises from the coordination flexibility of lanthanides, the geometric features of the material, and the presence of guest molecules.

The modified bottom-up approach of materials discovery is an efficient method of accessing novel materials for targeted applications.

KEYWORDS: metal–organic frameworks, materials design, X-ray structural analysis, adenine, pyrene, lanthanides

Résumé

Les structures métal–organiques (MOFs) sont des matériaux polymères de coordination dans lesquels des ions ou des agrégats de métaux inorganiques sont liés à des ligands organiques multitopiques par le biais de liaisons de coordination. Leur polyvalence structurelle permet de concevoir des matériaux à base de blocs de construction préformés, alors que leur cristallinité permet d'étudier leurs structures sous-jacentes au niveau atomique. L'approche ascendante de la découverte de matériaux implique d'abord l'étude de la structure du matériau nouvellement synthétisé, suivie d'une caractérisation détaillée, à partir de laquelle une application potentielle est déduite.

Cette thèse présente la synthèse, la détermination structurelle et la caractérisation complète de 10 nouveaux MOFs construits à partir de ligands comprenant l'adénine et le H₄TBAPy à base de pyrène, ainsi qu'un MOF à base de lanthanide. En basant sur leurs structures cristallines, de diverses applications ont été postulées pour ces matériaux, et la comparaison avec les matériaux déjà connus dans la littérature a été entreprise.

Dans la **SION-10**, la présence de centres Cu^{II} actifs et de complexes Cu^{II}–adénine non coordonnés dans les vides structuraux du matériau s'est révélée un facteur clé permettant la capture de l'ammoniac avec ce matériau. Les **SION-31–35**, basées sur l'adénine, ont servi de plate-forme pour l'étude des sites de protonation des atomes d'azote en raison des différents modes de liaison démontrés par l'adénine dans leurs structures. La nature bi-poreuse de la **SION-8** à base de pyrène a été utilisée comme preuve de concept pour la séparation CO₂/CH₄ à sélectivité ajustable et pour la capture irréversible de l'iode. Dans la **SION-7**, on a démontré que l'orientation mutuelle des ligands à base de pyrène et le contenu des pores influencent l'émission de fluorescence de ce matériau, et peuvent être réglées avec précision par les changements de température. On a constaté que la **SION-2** à base de lanthanides présente un fort effet de dilatation thermique négatif, résultant de la flexibilité de coordination des lanthanides, des caractéristiques géométriques du matériau et de la présence de molécules-invités.

L'approche ascendante modifiée de la découverte de matériaux est une méthode efficace d'accès à de nouveaux matériaux pour des applications ciblées.

MOTS-CLÉS: structures métal–organiques, conception des matériaux, analyse structurale aux rayons X, adénine, pyrène, lanthanides

Table of contents

Acknowledgements	3
Abstract	4
Résumé	5
Table of contents	6
1. Introduction	9
2. Metal–organic frameworks	13
2.1. Historical overview	13
2.2. Characteristic features of MOFs	15
2.3. Topological description of MOFs	17
3. Experimental methods	19
3.1. MOF synthesis	19
3.2. X-ray diffractometry	20
3.2.1. Interaction of X-rays with crystals	20
3.2.2. Single-crystal X-ray diffractometry	22
3.2.3. Powder X-ray diffractometry	26
3.3. Photoelectron spectroscopy	27
3.4. Thermogravimetric analysis	29
3.5. Infrared spectroscopy	29
3.6. Gas sorption	30
3.6.1. Adsorption isotherms	30
3.6.2. BET equation	31
3.6.3. Isosteric heat of adsorption	31
4. Adenine-based ship-in-a-bottle MOF with active Cu ^{II} sites for efficient detection and capture of ammonia	33
4.1. Introduction	33
4.2. Experimental section	33
4.2.1. Synthesis of SION-10	33
4.2.2. Single-crystal X-ray diffraction	34
4.2.3. Breakthrough experiments for NH ₃ capture	35
4.3. Results and discussion	36
4.4. Conclusions	40
4.5. Appendix	41
5. Protonation states and location of protonated N atoms of adenine in metal–organic frameworks	47
5.1. Introduction	47
5.2. Experimental section	48
5.2.1. Synthesis	48
5.2.2. Single-crystal X-ray diffraction	49
5.2.3. Powder X-ray diffraction	49
5.2.4. X-ray photoelectron spectroscopy	49
5.3. Results and discussion	50
5.3.1. Synthesis and characterisation	50
5.3.2. Single-crystal X-ray diffraction analysis	51
5.3.3. Investigation of the protonation states of adenine and location of the protonated N atoms	55
5.4. Conclusions	62
5.5. Appendix	63
6. Tuneable CO ₂ /CH ₄ separation performance in a bi-porous flexible Ca ^{II} -based MOF	69
6.1. Introduction	69
6.2. Experimental section	70

6.2.1.	Synthesis of SION-8	70
6.2.2.	SCXRD analysis.....	70
6.2.3.	VT and VP PXRD analysis and complementary bulk characterisation.....	71
6.2.4.	Sorption studies.....	71
6.2.5.	Breakthrough experiments.....	71
6.3.	Results and discussion.....	72
6.3.1.	Crystal structure description.....	72
6.3.2.	Bulk characterisation.....	73
6.3.3.	Stepwise activation.....	74
6.3.4.	Framework flexibility.....	76
6.3.5.	Response of the structure to N ₂ , CO ₂ , and CH ₄ adsorption and temperature changes.....	76
6.3.6.	Single-component N ₂ , CO ₂ , and CH ₄ adsorption.....	79
6.3.7.	CO ₂ /CH ₄ separation.....	81
6.4.	Conclusions.....	82
6.5.	Appendix.....	83
7.	Permanent adsorption of iodine by a pyrene-based MOF resulting in an enhancement of electrical conductivity.....	93
7.1.	Introduction.....	93
7.2.	Experimental section.....	94
7.2.1.	Synthesis of SION-8 and iodine loading.....	94
7.2.2.	Single-crystal X-ray diffraction analysis.....	94
7.2.3.	Impedance spectroscopy measurements.....	94
7.3.	Results and discussion.....	95
7.4.	Conclusions.....	99
7.5.	Appendix.....	100
8.	Temperature-dependent interchromophoric interaction in a porous pyrene-based metal–organic framework.....	105
8.1.	Introduction.....	105
8.2.	Experimental section.....	106
8.2.1.	Procedures and materials.....	106
8.2.2.	Synthesis of SION-7	106
8.2.3.	Single-crystal X-ray diffraction.....	106
8.2.4.	Other characterisation techniques.....	107
8.3.	Results and discussion.....	107
8.3.1.	Synthesis and crystal structure analysis.....	107
8.3.2.	Thermal stability and phase transitions.....	109
8.3.3.	Optical properties.....	110
8.3.4.	Temperature-dependent interchromophoric interaction.....	110
8.4.	Conclusions.....	115
8.5.	Appendix.....	116
9.	Guest-dependent negative thermal expansion in a lanthanide-based metal–organic framework.....	129
9.1.	Introduction.....	129
9.2.	Experimental section.....	130
9.3.	Results and discussion.....	131
9.4.	Conclusions.....	135
9.5.	Appendix.....	135
10.	Outlook.....	143
	References.....	145
	CV.....	153

1. Introduction

Discovery of novel materials is a necessary condition for the development of new technologies, improving living standards and in general for the economic and social advancement.

The traditional approach of materials discovery starts with a desired application, i.e. a need that is to be satisfied, and only then a material bearing desired properties is sought. Historically, many materials were discovered in such a way, in numerous cases in a complete oblivion of the physical and chemical processes underlying their characteristics. Thus, for many years the progress in the field of materials science was impeded by lack of fundamental understanding of primary processes taking place at the molecular level.

A more sophisticated approach of materials discovery involves departing from the molecular structure. Once such a structure of a material is established, then its physical and chemical properties are investigated, which in turn allows for a postulation of the material for a desired application. Synthesis of many drugs, synthetic dyes and engineering alloys, and subsequent introduction thereof in practice stands as a striking proof of utility of this bottom-up approach.

In our thesis we focus our attention on metal–organic frameworks (MOFs), which constitute an excellent platform for the design of new materials aimed at desired applications. These novel hybrid materials offer a unique opportunity to enrich the bottom-up materials discovery approach by the possibility of making adjustments during the investigation. The structure of MOFs can be assembled from their primary components – organic ligands and inorganic metal clusters – which already prompts a vast designability of these materials. The crystalline nature of MOFs enables the investigation of their underlying structure by means of X-ray diffraction. Furthermore, using a range of complementary experimental techniques, physical and chemical properties of MOFs can be investigated. A special feature of MOFs is that, depending on the ultimate goal, their structure can be adjusted, either through pre- or post-synthetic modification. The iterative nature of MOF research allows for the optimisation of a target property before the material is suggested for a practical application (Figure 1).

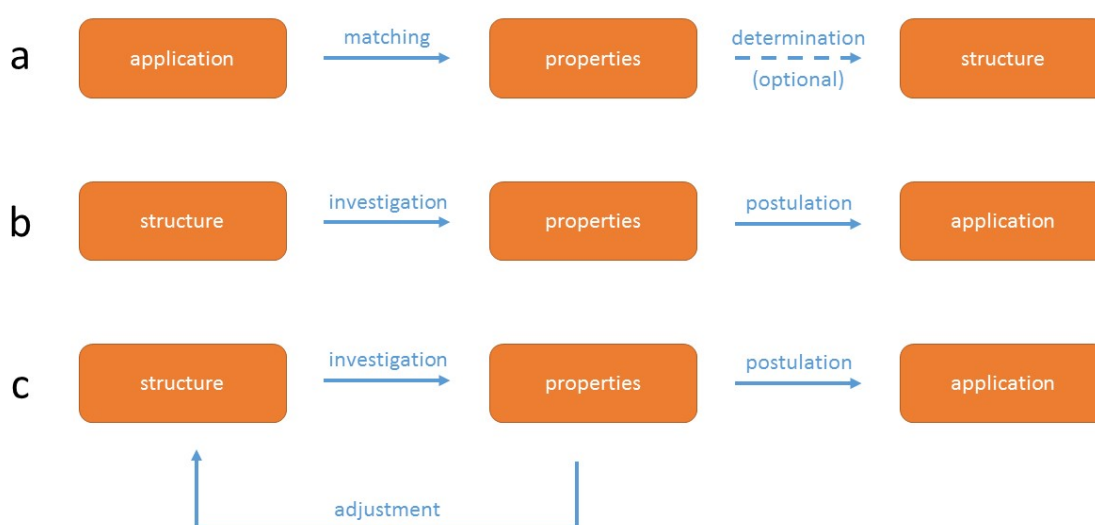


Figure 1. (a) Scheme of the traditional route of materials discovery, departing from a desired application to which a material is matched. (b) Bottom-up approach of materials discovery taking advantage of the fundamental knowledge of molecular structure and interactions. (c) A modified bottom-up approach allowing for structural adjustments during the materials discovery process.

The field of MOFs is more widely introduced in the following chapter. Chapter 3, in turn, is intended to give a short overview of the experimental procedures involved in the preparation of the current thesis. A strong emphasis has been put on explaining the role of X-ray diffraction in revealing the 3D structure of crystalline materials.

Over the course of preparation of our thesis, we synthesised 10 novel MOFs, revealed their structure with single-crystal X-ray diffractometry, and fully characterised them with a vast range of experimental techniques. Based on the structural characteristics of these materials (nature of the metal, of the ligand, or an interplay between them, geometrical or topological features), we proposed their use in a variety of applications, and compared them with the materials already known in the literature. The summary of the content of the current thesis is given in [Table 1](#).

Table 1. Short summary of the materials presented in this thesis along with their major characteristics and postulated applications.

Chapter	Material	Formula	Structural characteristics	Application
4	SION-10	$[Cu_4(btc)_2(Ade)(1HAde)(\mu_3-OH)(H_2O)_3] \cdot 0.4 [Cu(Ade)_2(H_2O)_4] \cdot 10.5 H_2O$	Active Cu sites Ship-in-a-bottle structure	Ammonia capture
5	SION-31 SION-32 SION-33 SION-34 SION-35	$[Ni_2(btc)(Ade)(H_2O)_5] \cdot 3H_2O$ $[Ni(ipa)(3HAde)]$ $[Ni_2(btec)(7HAde)_2(H_2O)_2] \cdot 4H_2O$ $[Cu_3(pzdc)_2(1HAde)(H_2O)_4]$ $[Zn_2(btc)(Ade)(H_2O)_2]$	Multimodularly coordinated adenine residues	Determination of N protonation sites
6	SION-8	$[Ca_2(TBAPy)(\mu_2-OH)_2] \cdot 2DMF$	Hydrophobic and hydrophilic pores Stepwise activation	Tuneable CO ₂ /CH ₄ selectivity
7	SION-8 ⊃I ₂	$[Ca_2(TBAPy)(H_2O)_2] \cdot DMF \cdot 0.81I_2$	Iodine molecules entrapped within the pores	Increased electrical conductivity
8	SION-7	$[Mg_{1.5}(HTBAPy)(H_2O)_2] \cdot 3DMF$	Face-to-face arrangement of chromophores Guest molecules present	Tuneable excimer emission
9	SION-2	$[Tb_2(DHBDC)_3(DMF)_4] \cdot 2DMF$	<i>pcu</i> -type topology Coexistence of rigid planes and flexible linkers	Negative thermal expansion

H₃btc = benzene-1,3,5-tricarboxylic acid; HAde = adenine; H₂ipa = isophthalic acid; H₄btec = 1,2,4,5-benzenetetracarboxylic acid; H₃pzdc = 3,5-pyrazoledicarboxylic acid; H₄TBAPy = 1,3,6,8-tetrakis(*p*-benzoic acid)pyrene; DMF = *N,N*-dimethylformamide; H₂DHBDC = 2,5-dihydroxybenzene-1,4-dicarboxylic acid

Biologically-derived ligands have attracted researchers' considerable attention with their low toxicity and biocompatibility. Nucleobases, in particular adenine, capable of coordinating to the metal centres via multiple coordination modes, has successfully been incorporated in a number of MOFs. Our approach was to use two ligands: adenine and benzene-1,3,5-tricarboxylic acid, together with Cu^{II} metal centres, to yield a rigid 3D MOF, **SION-10**. The presence of active Cu^{II} centres and non-coordinated Cu^{II}-adenine complexes entrapped in the structural voids of the material (a so-called ship-in-a-bottle structure), encouraged us to investigate the capture of ammonia with this material. Further details on this investigation are presented in Chapter 3.

Combining adenine with different carboxylate ligands along with Ni^{II} , Cu^{II} and Zn^{II} metal centres yielded five novel MOFs termed by us **SION-31–35**. The versatility of the structural characteristics of just these five MOFs, with adenine being coordinated to the metals in various ways, prompted us to put them in a broader context of all known adenine-based MOFs. Adenine protonation states and N protonation sites were of our particular interest. Based on the crystallographic and XPS data supported with the literature survey, we established simple rules allowing synthetic chemists to predicate whether the adenine residue in some newly synthesised MOFs is protonated, and if so, where the protonation takes places. Chapter 4 describes this project more extensively.

Pyrene, a fluorescent polycyclic aromatic hydrocarbon, has been used as a building block for the synthesis of many MOFs. Their main characteristics are: hydrophobicity, rigidity, and fluorescence. In the case of a newly synthesised MOF constructed from Ca^{II} and a pyrene-based ligand H_4TBAPy (**SION-8**), however, the hydrophobicity is highly anisotropic, since one set of pores is endowed with a purely hydrophobic character, whereas the pores of the second type are partially hydrophilic. This striking difference of the chemical character between the two types of pores allowed for a gradual partial activation of the material, which in turn prompted us to study the tuneable CO_2/CH_4 separation selectivity. Moreover, introduction of iodine (I_2) molecules inside the hydrophobic pores of the partially activated material led to dramatic changes of the spectroscopic properties and the electrical conductivity of the material. Chapters 5 and 6 provide more information about **SION-8** and its I_2 -loaded analogue.

In **SION-7**, a material constructed from the pyrene-based H_4TBAPy and Mg^{II} , the fluorescence properties were in the centre of our attention. The fluorescence of the material was found to depend on the mutual interaction between the pyrene-based chromophores (interchromophoric interaction). This interaction changes as a function of the geometrical position of ligands with respect to each other, and is influenced from the side of the pores by guest solvent molecules. These two factors, the geometry of the ligand and the pore content, can in turn be finely tuned by temperature. More about this temperature-depended interchromophoric interaction is provided in Chapter 7.

Last but not least, the introduction of lanthanide (Ln) atoms into the 3D framework of a MOF has been found as strategy to provoke colossal mechanical effects. A Tb^{III} -based MOF called **SION-2** was found to exhibit the strongest negative thermal expansion among all known Ln -based MOFs. Preliminary results on the thermal expansion of this material published in one of our previous papers were the inspiration for a thorough follow-up study. We found that the material owes this effect to the Ln -atoms, capable of adopting a range of coordination geometries, acting as nodes of its underlying *pcu*-type network, and to the geometry of the structure, featuring both the rigid planes and flexible links. The negative thermal expansion effect has also been found dependent on the guest content within the structural voids. Last chapter of the current thesis presents this project in a broader perspective.

2. Metal–organic frameworks

2.1. Historical overview

Although the coordination compounds have been known in the literature for more than a century, the emergence of coordination polymers, currently referred to as metal–organic frameworks (MOFs), took place relatively recently.¹ The predecessors of coordination polymers were so-called Hofmann clathrates, the first representative of which, $[\text{Ni}(\text{CN})_2(\text{NH}_3)](\text{C}_6\text{H}_6)$, was first synthesised in 1897,² and its structure was revealed in 1952.³ This compound consists of infinite 2D layers constructed upon the $\text{Ni}-\text{C}\equiv\text{N}-\text{Ni}$ coordination schemes, wherein Ni^{II} atoms adopt octahedral and square-planar coordination geometries in an alternating manner, in between of which benzene molecules are trapped (Figure 2a). Further advancements made by Iwamoto and co-workers such as employment of α,ω -diaminoalkanes instead of ammonia ligands allowed the synthesis of 3D materials such as $[\text{Cd}(\text{HMDA})\text{Ni}(\text{CN})_4](\text{C}_7\text{H}_9\text{N})$ (HMDA = hexamethylenediamine, $\text{C}_7\text{H}_9\text{N}$ = *o*-toluidine).⁴ The length of the organic spacer was found to be systematically variable to allow for size-selective inclusion of guest molecules.⁴⁻⁵ However, Structural collapse of Hofmann clathrates and related materials upon removal of the guest molecules from the structures was commonly observed.

The first coordination polymer which was not based solely on organic linkers rather on ditopic CN^- inorganic ligands, was bis(succinonitrilo)copper(I) nitrate, $[\text{Cu}(\text{SUC})_2](\text{NO}_3)$,⁶ synthesised by Saito and co-workers. The authors prepared a range of similar polymers, and found that short-chain bis(alkylnitrilo) ligands such as succinonitrile yield 1D coordination polymers, while longer-chain glutaronitrile (GLU) and adiponitrile (ADI) give rise to 3D networks, among which $[\text{Cu}(\text{ADI})_2](\text{NO}_3)$ was found to be interpenetrated (Figure 2b).⁶⁻⁷

The term ‘polymeric frameworks’ appears in the literature for the first time in 1989, when Hoskins and Robson synthesised $\text{Cu}(\text{TCTPM})\text{BF}_4 \cdot x\text{C}_6\text{H}_5\text{NO}_2$ based on Cu^{I} and TCTPM = 4,4',4'',4'''-tetracyano-tetraphenylmethane.⁸ They recognised that principles of nodes and links, conceptualised by Wells for inorganic nets,⁹ can be applied to predict structures that will result from linking of molecular building units of a given geometry and connectivity.⁸ In this way, they demonstrated that this approach opens up the possibility to design the coordination networks with predetermined structures. The same strategy was further adopted by Zaworotko, who pointed out that the use of elongated linkers such as 1,4-dicyanobenzene, 4,4'-bipyridine, and 2,5-dimethylpyrazine yields isostructural networks with different degrees of interpenetration due to the different pore sizes of the resulting networks.¹⁰ High level of synthetic control was also shown by Robson and co-workers who deliberately replaced the $\text{Pt}(\text{CN})_4^{2-}$ units within the $[\text{CuPt}(\text{CN})_4](\text{NMe}_4)$ network¹¹ by cyanophenyl-functionalised porphyrin TCP to yield $[\text{Cu}(\text{Cu-TCP})](\text{BF}_4)$ of the same platinum sulphide (*pts*) net.¹² Finally, the term ‘metal–organic framework’ was first introduced by Yaghi in 1995 while reporting a copper(I)–4,4'-bipyridyl polymer $[\text{Cu}(\text{bpy})_{1.5}]\text{NO}_3 \cdot 1.25\text{H}_2\text{O}$.¹³

The common feature of the coordination polymers presented up to this point is their charged nature: since those materials were synthesised based on neutral ligands (nitriles, pyridine derivatives), the positive charge of the metal centres needed to be counterbalanced by non-polymeric anions present in eventual structural voids rather than by ligands forming the network. The usage of anionic ligands such as carboxylates significantly changed the landscape of coordination networks. The advantages of using charged ligands, including stronger (more ionic) interaction between the metal nodes and the ligands, as well as absence of counterions filling the pores necessary to preserve the overall framework neutrality, were exemplified by the pioneering works by Yaghi and co-workers. The first MOF synthesised based on charged ligands was $\text{Co}(\text{BTC})(\text{py})_2$ (BTC^{3-} = benzene-1,3,5-tricarboxylate, Figure 2c), whose structure consists of alternating layers of loosely bound pyridine molecules and the coordinatively bonded sheets of Co-BTC.¹⁴

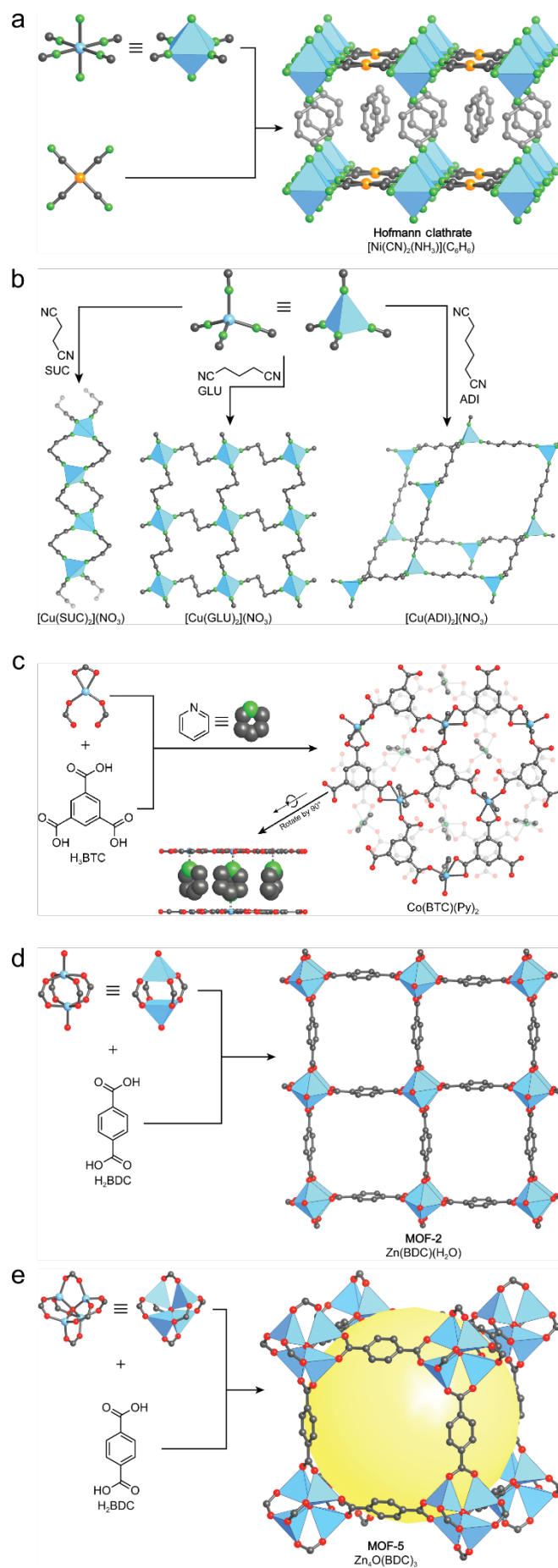


Figure 2. Milestones of progress in the synthesis of framework materials. (a) Hofmann clathrates composed of 2D layers of composition $\text{Ni}(\text{CN})_2(\text{NH}_3)$ with C_6H_6 molecules trapped in between of them. (b) Coordination polymers $[\text{Cu}(\text{SUC})_2](\text{NO}_3)$, $[\text{Cu}(\text{GLU})_2](\text{NO}_3)$, and $[\text{Cu}(\text{ADI})_2](\text{NO}_3)$ based on coordination of neutral succinonitrile, glutaronitrile and adiponitrile ligands, respectively, to the single-atom Cu^+ centres. (c) $\text{Co}(\text{BTC})(\text{py})_2$ 2D metal–organic framework composed of charged BTC^{3-} ligands coordinated to Co^{3+} metal centres. (d) $\text{Zn}(\text{BDC})(\text{H}_2\text{O})$ (MOF-2), wherein the approach of using SBUs instead of individual metal centres was first adopted. (e) $\text{Zn}_4\text{O}(\text{BDC})_3$ (MOF-5), an archetypal representative of MOF family, characterised by the presence of $\text{Zn}_4\text{O}(\text{COO})_6$ SBUs and by higher-than-expected porosity. Figure reproduced from Yaghi *et al.* (2019).¹

An important subsequent advancement in the search for more robust and rigid MOFs was the employment of secondary building units (SBUs), i.e., metal–oxygen polynuclear clusters instead of individual metal atoms as nodes forming the coordination frameworks. Such an approach was adopted for the first time in the synthesis of MOF-2, $\text{Zn}(\text{BDC})(\text{H}_2\text{O})$ (BDC^{2-} = benzene-1,4-dicarboxylate), constructed upon dimeric $\text{Zn}_2(\text{COO})_4$ paddlewheel SBUs that are linked by BDC^{2-} struts to form a square grid (**sql**, [Figure 2d](#)).¹⁵ Even more successful was the synthesis of MOF-5, $[\text{Zn}_4\text{O}(\text{BDC})_3](\text{DMF})_x$, wherein in-situ formed $\text{Zn}_4\text{O}(\text{COO})_6$ SBUs consisting of four tetrahedral (ZnO_4) units sharing a common vertex, joined by ditopic BDC^{2-} linkers gave rise to a 3D framework structure of **pcu** topology ([Figure 2e](#)).¹⁶ The framework was found to contain large cavities accounting for 61% of the unit-cell volume. Solvent exchange from DMF (in which the synthesis had been performed) to more volatile CHCl_3 facilitated the activation of the MOF-5 framework, which exhibited a permanent porosity characterised by a record-breaking surface area.¹⁶

The transition from 2D to 3D coordination polymers, the usage of charged organic ligands bonded by polynuclear metal clusters, and the discovery of MOFs' porosity were the milestones of progress in the synthesis of framework materials ([Figure 2](#)). These tools allowed to undertake the modular synthesis to target MOFs materials of desired characteristics. In the 21st century we are witnessing a surge in the effort to synthesise novel MOFs. However, the research topics shifted from the fundamental studies of synthetic protocols, structures and topologies of MOFs towards more application-oriented focusses.

2.2. Characteristic features of MOFs

MOFs are 1-, 2- or 3-dimensional coordination polymers in which inorganic metal ions or clusters are linked with multitopic organic ligands by means of coordination bonds ([Figure 3](#)).¹⁷ Although conceptually they are similar to inorganic porous materials such as zeolites and open framework inorganic materials,¹⁸ the usage of a wide variety of organic linkers instead of that of a relatively limited library of inorganic anions (SiO_4^{4-} , PO_4^{3-} , AsO_4^{3-} , SO_4^{2-}), makes MOFs an effectively distinct domain.¹⁹

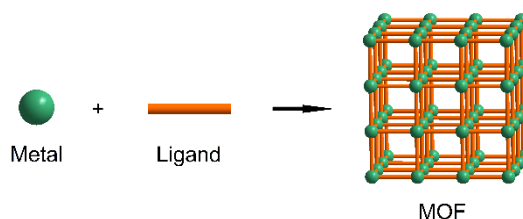


Figure 3. Schematic of formation of a metal–organic framework (MOF).

The main characteristics of MOFs include their (i) crystallinity, (ii) porosity, (iii) structural versatility, and (iv) practical applicability.

The fact that MOFs are polymers relate them to the organic polymers, which have been synthesised with success and applied in numerous branches of industry for nearly a century.²⁰ Their distinguishing characteristic, however, is that they are *crystalline*, i.e., instead of packing randomly in the 3D space, they are organised in such a way that the same motif repeats itself in the 3D space in a periodic way. On the one hand, this periodicity ensures the uniformity of properties within the entire bulk on the material. On the other hand, it enables the study of the MOFs' underlying structure by means of X-ray diffraction²¹ – the technique with allows for the facile determination of the molecular structure with the atomic resolution.

Size and shape of the ligands employed during the MOF synthesis often results in some considerable void space not occupied by any of the MOF components. This space is filled upon the synthesis with molecules of solvents which were used to dissolve the MOF components prior to synthesis. The solvent guest molecules can assume discrete positions,^{21a} but in the majority of cases they are heavily disordered, and their positions cannot be inferred from X-ray diffraction. They can be removed from the parent framework in a process called activation or desolvation. An activated MOF often exhibit high *porosity*, i.e. they adsorb small-molecule gases (such as N₂ or CO₂) at low pressures, and they show type I isotherm behaviour. Some MOF materials exhibit extremely high internal surface areas²² and void volumes,²³ and remarkable low densities.²⁴ Porous MOFs have been investigated for CO₂ capture and sequestration,²⁵ and for the storage of strategically important gases such as H₂ and CH₄,²⁶ with the former being considered as an ideal energy carrier, while the latter has been suggested as a bridge fuel to a cleaner energy future.²⁷ Porosity to different gasses can differ considerably, hence the origin of gas sorption selectivity.^{25, 28} On the top of that, the flexibility of certain MOFs can have a tremendous impact on their sorption properties.^{19b, 29}

Structural versatility of MOFs is par excellence reflected by the number of different structures reported to date. Metals used for the MOF synthesis traditionally include 3d transition metals, in particular Cu, Fe, and Zn,^{16, 30} however, with the advancement of synthesis techniques, virtually all metals, including lanthanides and actinides, were found to form extended coordination polymers.³¹ The number of organic ligands which have successfully been incorporated into a 3D framework is even higher; these ligands can be classified into 7 groups: (i) carboxylic acid containing ligands, (ii) nitrogen containing ligands (pyridyl, pyrrol, imidazolyl), (iii) cyano ligands, (iv) phosphonic acid containing ligands, (v) sulfonyl ligands, (vi) ligands based on mixed functional groups, (vii) metal-bearing ligands. Numerous strategies of ligand design yielding MOFs with targeted properties have successfully been established.³² Worthwhile mentioning is the reticular synthesis strategy, wherein a series of isostructural MOFs can be obtained by incorporation of increasingly longer ligands into the network of metal centres.^{17a, 33}

Finally, with all the characteristics taken into account, MOFs have found numerous potential *applications*. The presence of active catalytic centres or confined pockets on the pore surfaces of MOFs entails their usage in catalysis.³⁴ If the interaction of an analyte with the MOF results in a substantial change of one of its physical properties (absorbance or fluorescence spectrum, crystal packing), then such a material can be used for sensing applications.³⁵ Strong interactions between the pore surfaces and the adsorbates can find the use not only in CO₂ capture and sequestration or CH₄ and H₂ storage outlined before, but may also find an application in the removal of toxic species.³⁶ Dissimilar strength of interactions between different gasses can in turn be exploited for gas separation.^{28b} Special characteristics of some MOFs, i.e., second-order electrical susceptibility, electrical polarization, non-zero magnetic moment or sufficiently low band gap coupled with a considerable charge mobility lead to their potential usage in non-linear optics,³⁷ ferroelectricity,³⁸ magnetism,³⁹ and electrical conductivity,⁴⁰ respectively.

2.3. Topological description of MOFs

Topology refers to a simplified representation of an extended (polymeric) crystal structure considering only the connectivity and not the chemical identity or metrics of its constituents. It is invariant to bending, stretching, and collapsing, but not to the making and breaking of connections. The basic notions used in the description of a topology are a net, a link, and a node.

A *net* is a special form of graph being an infinite array of nodes connected by links. It is simple, i.e., there is at most one link joining two nodes, and there are no loops (links connecting a node to itself); it is also connected, meaning that every node is connected to every other by a continuous path of links. Nets can be uninodal (constructed upon only one type of nodes) or multinodal (with more than one type of nodes); it can equally be 1-, 2-, or 3-periodic ('dimensional'). A *link* is a 2-connecting element of a net, while *nodes* are 3-connecting or higher. If a link turns out to be 3-connecting, then an additional node must be introduced in order to adhere to the definition of a net.⁴¹

Descriptions of extended chemical structures (e.g., diamond) as infinite nets date back to the earliest crystallographic studies. Of particular importance were the works by Wells, who applied the topological description to a range of inorganic networks and recognised the importance of structures with symmetry-related vertices and edges.⁹ A net-based approach in the description of coordination polymers was notably pursued by Robson.⁴²

The deconstruction of a MOF structure to a net refers to a process when parts of a real network are identified as abstract links and nodes. Care must be taken while assigning such roles to the MOF constituents: e.g., different topological descriptions will be obtained by choosing individual metal atoms as nodes, and while choosing metal clusters (SBUs) as nodes. The node/link assignment should also be chemically meaningful, e.g., a tetradentate ligand should be described as a single 4-connecting node rather than two interconnected 3-connecting nodes.

The identification of a net is executed using the following protocol. All topologically unique nodes are first identified, and then the number and the size of shortest circuits (smallest loops in the net containing two given links from a given node plus a number of other nodes) is calculated. Identification of simplest nets can be done by hand, however, for those which are more complicated, computer programs using automatic search and calculation procedures are invaluablely helpful; one of such programs, TOPOS Pro by Blatov and co-workers,⁴³ was extensively used throughout this thesis. The two aforementioned metrics – number of topologically inequivalent nodes, and number of nodes in their shortest circuits – are summarised in so-called point (Schläfli) symbols. The last step of net identification consists of matching the point symbol of the net under investigation with those already known and labelled.

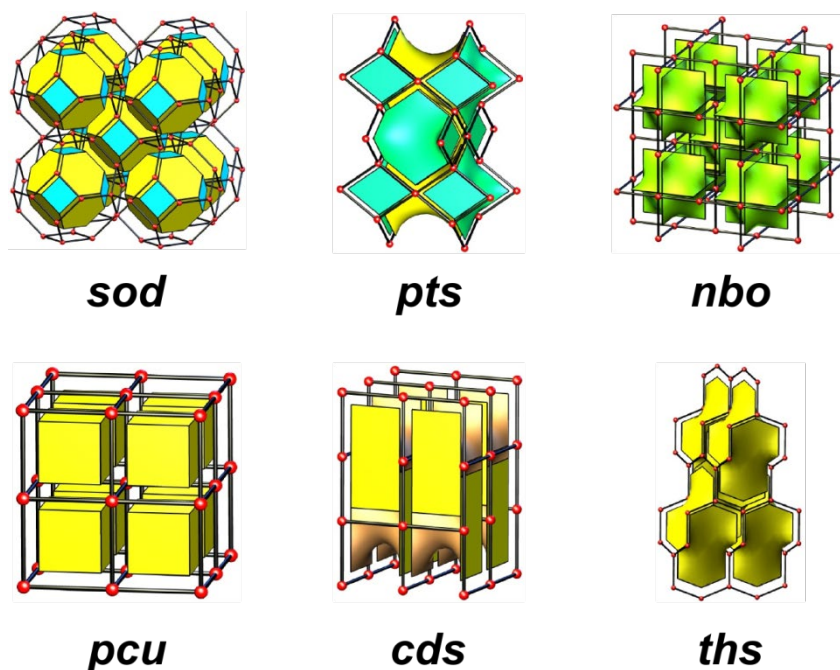


Figure 4. Examples of 3-periodic nets which derive their names from elements and inorganic compounds, and which are commonly used to describe the topology of MOFs.

For the sake of brevity, nets are referred to using the three-letter codes, which relate them to the structures of metals and simple inorganic compounds, including naturally occurring minerals, wherein those nets were originally identified.⁴⁴ Some of the most popular nets owe their names to sodalite (**sod**), PtS (cooperite, **pts**), NbO (**nbo**), α -Po (primitive cubic lattice, **pcu**), CdSO₄ (**cds**), SrAl₂ (**sra**), and ThSi₂ (**ths**, [Figure 4](#)).⁴² Sometimes two or more copies of the same net are mechanically entangled within the same crystal structure. We refer to this phenomenon as *interpenetration*.⁴⁵ Nets and in particular synthesis of networks of targeted geometry by design is the core of the discipline called *reticular chemistry*.^{17a}

Data for many of the nets most important for reticular chemistry are collected in a database known as the Reticular Chemistry Structure Resource (RCSR),⁴⁶ which contains about 2000 entries. The program TOPOS Pro recognises even more, about 70 000 types of nets.⁴³

3. Experimental methods

3.1. MOF synthesis

Synthesis of MOFs is a complex process, encompassing both a chemical reaction and a crystallisation. During the MOF synthesis, new coordination bonds need to be of intermediate strength. First the metal–ligand (instead of the metal–solvent) bonds should be preferentially formed, but at the same time, the bonds should easily dissociate so that any erroneous bonding (potentially leading to disorder or precocious structure termination) can be corrected.⁴⁷ Depending on the desired application, a synthesis yielding a MOF in form of nanoparticles or crystalline powder may be considered successful, however, for the purpose of structural analysis, the resultant material in form of well-shaped single crystals has proven to be the most useful.

Originally, MOFs were synthesised by slow evaporation of their components from saturated organic solutions. As an advancement of this method, conventional heating was started to be applied, which shortened the duration of the synthesis from weeks to days. In this method a metal salt and an organic linker are mixed in a high boiling point solvent (e.g., DMF, DEF, or DMSO) in a glass vial. A range of conditions have tremendous impact on the success of a synthesis, and in many instances only a limited number of sets of finely adjusted conditions gives rise to the desired chemistry of a new compound and to the satisfactory quality of the resultant crystals. Conditions that play a crucial role in MOF synthesis are:

- nature of the ligand and the metal, choice of metal salt,
- nature and volume of the solvent(s),
- temperature, heating and cooling rates,
- time,
- pH, presence of an acidic modulator.

In critical cases, changing only one parameter may involve a failure of the entire synthesis. In some other cases, a change of the solvent may yield a product of different stoichiometry or dimensionality.⁴⁸ Various products obtained as a result of using different metal sources (the same metal, but different counterion) have equally been reported.⁴⁹

In a typical example, the synthesis of a new MOF starts with choosing a set of conditions adopted from the literature for a similar compound. The procedure is then adjusted by systematically screening one parameter (for example, time of the reaction), while keeping all other parameters constant. After each reaction, visual inspection of the resultant material as well as standard characterisation techniques (PXRD and BET surface area) serve as assessment tools allowing for comparison between similarly successful results. Several iterations of the procedure should lead to revealing of the optimised synthetic protocol.

Obviously, the development of the field of MOFs gave rise to a range of alternative synthesis methods. Instead of conventional heating method described above, the solvothermal method has been used with great success.⁵⁰ It encompasses heating the reaction mixture to a temperature higher than the boiling point of the solvent used.⁵¹ For safety reason, pressure-resistant equipment (so-called bombs lined with Teflon reactors) need to be used. Microwave synthesis is still another technique that is gaining popularity. In this method, energy is delivered by means of microwaves instead of thermal (infrared) radiation, which turn out to be more efficient as power is applied only within the reactive mixture directly (molecules of non-zero dielectric moment are forced to oscillate at the frequency of the microwaves), while the air and the container are not heated.⁵² Microwave synthesis can provide with sufficient amounts of powdered materials in a relatively short times, but single crystals of high quality are very unlikely yet not impossible to be formed with it.⁵³ More specific ways of MOF synthesis include electrochemical,⁵⁴ mechanochemical,^{28a, 55} and sonochemical⁵⁶ methods.

3.2. X-ray diffractometry

The fact that MOFs form single crystals, i.e., solids constructed from molecular building blocks periodically arranged in 3D space, allows for the investigation of their structures with X-ray diffraction. Historically, single-crystal X-ray diffractometry (SCXRD) allowed the emergence of MOF chemistry, and continues to be the most prominent tool in the investigation of new MOF structures. It allows for the determination of the crystal structure with atomic precision (figures presenting the SCXRD-derived atomic models appear in nearly all MOF papers), and for the calculation of multiple metrics (density, pore volume, pore content) crucial for the applied studies on MOFs. Indeed, a discovery of a new MOF structure is a breakthrough in every single MOF research project: only if the atomic structure of a MOF is known, further steps of investigation (pre- or post-synthetic functionalisation, pore activation, proposal of an application) may be undertaken. Powder X-ray diffractometry (PXRD) is an experimental technique which is complementary to SCXRD. It studies the powdered/ground samples of MOFs, and benefits from many advantages compared to SCXRD, although it features some drawbacks, too.

3.2.1. Interaction of X-rays with crystals

Electromagnetic radiation can be considered as a wave of oscillating electric and magnetic fields. Electron, an elementary particle with the charge of $-e$, interacts with the electric field by absorbing its energy, oscillating about its equilibrium position, and subsequently emitting a secondary wave of the same energy. This process is called elastic scattering, wherein 'elastic' means that there are no losses in energy. The electromagnetic radiation scattered by an electron has the form of a spherical secondary wave. Each atom j contains Z electrons, and their ability to scatter electromagnetic radiation is quantified by the atomic scattering factor $f_j \propto Z$. Molecules, in turn, are built from n atoms, and the secondary waves scattered off their electrons interfere with each other, meaning that the result of scattering from a molecule is no longer a single spherical wave, but a superposition of nZ waves. As a result, the scattering in certain directions can be observed and detected (constructive interference), while in some others its intensity drops to zero (destructive interference). Both constructive and destructive interference of scattered secondary waves is called diffraction. Since the distances between atoms in molecules are of the range of $1 \text{ \AA} = 10^{-10} \text{ m}$, therefore, the constructive interference is strongest when the electromagnetic radiation in the X-ray range ($0.1\text{--}100 \text{ \AA}$) is used. Of course, the diffraction from a single molecule is by far too weak to be detected by any means. But since crystals are periodic arrangements of multiple atoms/ions/molecules in 3D space, the diffracted beams are accordingly amplified.

The geometry of the diffraction of X-rays from crystals is described by the Bragg's law (Eq. 1, Figure 5), which states that the constructive interference of X-rays scattered off a set of crystalline planes takes place only when the difference in diffracted beam paths (expressed as a function of the spacing between the planes and the beam incident angle) is an integer multiple of the wavelength. Since the geometry of X-ray diffraction from a crystalline plane is the same as the geometry of visible light reflection from a mirror (with the caveat that the diffraction takes place only under specific angles, while a mirror reflects under all angles), the diffracted beams are often called reflections.

$$n\lambda = 2d_{hkl} \sin \theta \quad (1)$$

where:

n – integer

λ – X-ray wavelength

d_{hkl} – spacing between the set of the planes (hkl)

θ – incident angle (the angle between incident ray and the scatter plane)

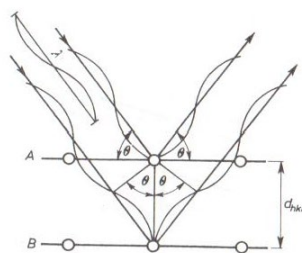


Figure 5. Geometry of X-rays of the wavelength of λ diffracted under an angle of 2θ by a set of crystalline planes A and B separated by an interplanar spacing of d_{hkl} , explaining the mathematical form of the Bragg's law.

Positions of the diffracted beams determined from an X-ray diffraction experiment (diffraction pattern) give valuable information about crystal's symmetry. A single parallelogram which makes up the entire crystal by simple translations in 3D space is called the unit cell. The size and the shape of the unit cell are described with the so-called unit-cell parameters, which include lengths of the three edges of the unit parallelogram a , b , and c , and three angles between them α , β and γ . (**Figure 6**).

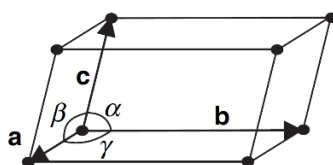


Figure 6. A crystallographic unit cell and parameters a , b , c , α , β and γ that unequivocally define it.

Crystals are characterised not only by the long-range order (periodicity of the arrangement of unit cells), but also by the short-range order (regular ordering of atoms within a unit cell). In vast majority of cases, a unit cell contains several copies of the same motif of atoms, called asymmetric unit, which are related to one another by means of symmetry operations. There are four simple symmetry operations and symmetry elements representing them: inversion (an inversion centre), rotation (a rotation axis), reflection (a mirror plane) and translation (a translation vector). The other three complex symmetry operations and symmetry elements include: roto-inversion (combination of rotation with inversion, represented by a roto-inversion axis), helicoidal rotation (combination of rotation with translation, represented by a screw axis) and glide reflection (combination of reflection with translation, represented by a glide plane). It was demonstrated that in crystals, in order to keep the arrangement of atoms periodic, there are 230 possible combinations of symmetry elements, called space groups.⁵⁷ All of them are described in detail in Vol. A of the International Tables for Crystallography.⁵⁸ Providing with the full set of unit-cell parameters as well as with the space-group symbol fully describes the crystal's symmetry.

While the positions of the diffracted beams in the diffraction pattern inform about the unit cell and the symmetry of the crystal, their intensities are related to the content of the unit cell. A set of integer indices h , k , l can be assigned for each discrete diffracted beam. Then, the structure factor F_{hkl} is given by the Fourier transform of the electron density in the unit cell, which can be expressed as a sum of the waves scattered from all atoms in the unit cell (**Eq. 2**).

$$F_{hkl} = \sum_{j=1}^N f_j e^{2\pi i(x_j h + y_j k + z_j l)} \quad (2)$$

where:

h, k, l – Miller indices (integer indices of a diffracted beam)

N – number of atoms in the unit cell

x_j, y_j, z_j – fractional coordinates describing the position of an atom in the unit cell

Accordingly, the electron density can be described as an inverse Fourier transform of the sum of all structure factors (Eq. 3).

$$\rho(x, y, z) = \frac{1}{V} \sum_h \sum_k \sum_l F_{hkl} e^{-2\pi i(x_j h + y_j k + z_j l)} \quad (3)$$

where:

$\rho(x, y, z)$ – electron density at a point in the 3D space described by the coordinates x, y, z

V – unit-cell volume

In a general case, structure factor is a complex number composed of both amplitude and phase. In fact, during a diffraction experiment, the intensities of the diffracted beams are proportional to the square of the modules of the respective structure factors (Eq. 4).

$$I_{hkl} = c \cdot |F_{hkl}|^2 \quad (4)$$

where:

I_{hkl} – intensity of the diffracted beam hkl

c – proportionality constant

Therefore, while the knowledge about a crystal structure (unit-cell parameters, symmetry and atomic positions) allows for the straightforward calculation of all the respective structure factors and the diffracted beam intensities, the opposite is more complicated. An X-ray diffraction experiment provides only with the amplitudes of structure factors, whereas their phases need to be obtained in another manner. The loss of structure factor phase information during the diffraction experiment is called phase problem, while the process of obtaining a priori unknown structure factor phases is called structure solution.

3.2.2. Single-crystal X-ray diffractometry

SCXRD is concerned with the study of diffraction from single crystals, typically of the size of approximately 0.1 mm. SCXRD experiments are customarily performed on instruments called diffractometers. Three principal components of a diffractometer include: an X-ray source, a goniometer and a detector (Figure 7).

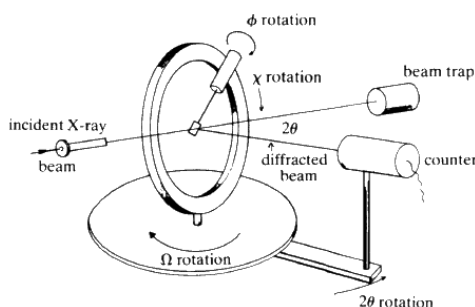


Figure 7. A four-circle diffractometer and its principal components.

X-ray source the most commonly encountered in a laboratory is the sealed X-ray tube. In an evacuated chamber, the electrons are accelerated by means of high difference of potentials between the cathode and the anode. The cathode is commonly made of a tungsten filament, while the anode is a target plate made of high-purity metal. When the electrons hit the target, their deceleration produces X-rays in a broad and continuous spectrum (white radiation). On the top of it, incident electrons of specific energy knock out electrons from the inner shells of the atoms in the metal target. Electrons from the neighbouring shells replace the ejected electrons, and the difference of the energy is emitted by the atom in form of characteristic radiation. The radiation leaves the X-ray tube through the beryllium windows, its strongest line is isolated from the spectrum by a graphite crystal, and subsequently collimated. As a result, a monochromatic (single-wavelength) X-ray beam can be shone on the crystal. The most commonly used anode materials, Cu and Mo, produce X-rays with the wavelengths of 1.54187 Å and 0.71075 Å, respectively.⁵⁹ A scheme of a typical laboratory X-ray tube as well as a spectrum thereof is shown in Figure 8.

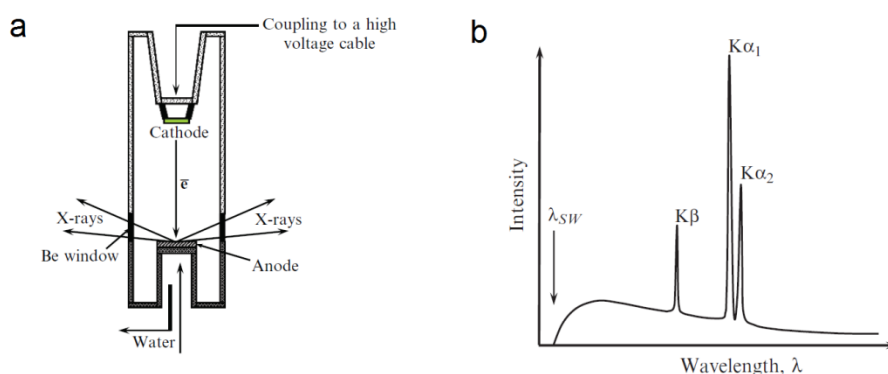


Figure 8. (a) A scheme of a sealed X-ray tube commonly used in X-ray laboratories. (b) A spectrum of a laboratory X-ray tube. Figure adapted from Pecharsky & Zavalij (2009).⁶⁷

Synchrotrons are an alternative source of X-rays. They are large scientific facilities, and produce the most powerful X-ray beams available nowadays. The main part of a synchrotron is the storage ring, wherein electrons are accelerated in high vacuum to relativistic velocities. The ring is made up of straight sections and insertion devices (magnetic arrays: undulators, wigglers), with short arcs (dipole magnets: bending magnets) that bend the particles around the curved trajectory. When the magnets bend the trajectory of electrons, a surplus of energy is emitted in form of X-rays. The spectrum is broad and continuous, so the role of the monochromator is to choose a single wavelength needed. X-ray beam delivered by a synchrotron is not only monochromatic, but also coherent and polarised.

A simple scheme of a synchrotron and the spectrum produced by a bending magnet are shown in Figure 9.

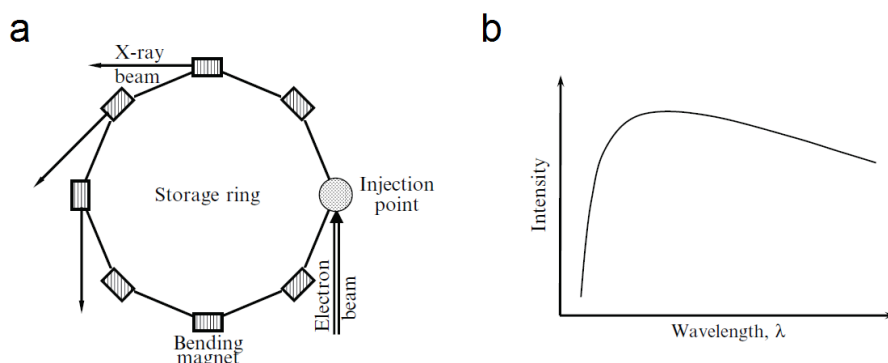


Figure 9. (a) A scheme of synchrotron showing its major components. (b) A spectrum of radiation delivered by a bending magnet. Figure adapted from Pecharsky & Zavalij (2009).⁶⁷

In a diffraction experiment, X-rays produced by either of the described sources are shone onto a crystal supported by a goniometer. Since the exposure of a crystal remaining in a singular orientation to X-rays is unlikely to produce diffraction (only some specific angles are allowed by the Bragg's law, Eq. 1), the system of motors should additionally allow for the flexible positioning of the crystal. In this way, a range of reflections originating from different crystalline planes can be recorded.

Modern X-ray detectors have the form of 2D plates. Charge-coupled device (CCD) cameras are the most widespread type of such area detectors. When a quantum of X-rays hits the detector, the phosphor finely dispersed on its surface converts it into a bunch of photons in the visible-light region, which are then counted by a photomultiplier tube, converted to an electrical signal, and digitised. In this way, the diffracted beam can be quantified in a broad dynamic range of intensities. The newest development are detectors based on complementary metal–oxide–semiconductor (CMOS) system. Here the readout is considerably faster, and no transformation of the X-ray photons into visible light is necessary. This design also has the advantage of zero dark current or readout noise.

In a typical diffraction experiment, at first a suitable single crystal needs to be chosen. In case of MOF crystals, in order to prevent the exposure to air, a crystal is taken directly from the reaction mixture, immersed in silicone oil, and picked with a polymer fibre attached to the brass base. The crystal is then mounted onto the goniometer head of the diffractometer, and centred optically with the camera. Initial exposures provide general information about the crystal's quality, while with a set of a few images taken at different orientations one can determine approximate unit-cell parameters. Then, depending on the crystal's symmetry, an appropriate measurement strategy is adopted, and the optimum exposure time is chosen depending on the crystal's scattering power. The measurement is run by rotating the crystal around a given axis of the experimental setup (usually ω and ϕ scans) and simultaneous recording of diffraction images. Both the measurement and the subsequent data treatment are controlled by the computer software.

SCXRD measurements performed over the preparation of the current thesis were conducted in-house in the X-ray laboratory at the EPFL Valais in Sion as well as at the European Synchrotron Radiation Facility in Grenoble, France. The summary of technical characteristics of these two laboratories is given in Table 2.

Table 2. Technical characteristics of two SCXRD facilities used to determine the crystal structures presented in the current thesis.

	X-ray laboratory EPFL Valais Sion Coordinator: Dr. Pascal Schouwink	BM01 Swiss-Norwegian Beamline European Synchrotron Radiation Facility, Grenoble, France Coordinator: Dr. Dmitry Chernyshov
Diffractometer	Bruker D8 Venture	PILATUS@SNBL
X-ray source	Microfocus sealed X-ray tube	Synchrotron (bending magnet)
Wavelength	Mo K α (0.71075 Å)	~0.7 Å, tuneable
Monochromator	Graphite	Si(111) double crystal
Goniometer	Four-circle (ω , κ , ϕ , 2θ)	Single-spindle (ω)
Detector	Photon 100	Pilatus2M
Detector type	CMOS	CMOS
Software	APEX3	Bubble, CrysAlisPro
Average duration of a measurement	8 hours	6 minutes

The process of converting raw images from the detector to digital software-readable data is called data reduction or integration. In this process, based on a pre-determined unit cell, the computer program searches for reflection positions in each diffraction image, and integrates the intensity recorded by the detector. As a result, instead of a set of diffraction images, which use a lot of digital memory space, a compact list of reflection in the handy ASCII format is obtained. Such a list can subsequently be used as an input for further data treatment.

The important step to take before the structure solution from SCXRD data is carried out is a correction for absorption. On its transmission through a crystal, the X-ray radiation is weakened by diverse physical processes like elastic and inelastic scattering. The higher the atomic number, the stronger the absorption effect, and since MOFs are considered medium absorbers, numerical (analytical) correction using the symmetry equivalents is sufficient. Numerical correction for absorption relies on multiple observations of the same reflection, which should in theory have the same intensity (the possible differences may originate not only from the absorption of the crystal, but also from the absorption of the crystal support or an inhomogeneous X-ray beam). On a contrary, empirical correction is sometimes needed for highly absorbing crystals. This method consists of creating a model of the shape and size of the crystal, and then calculating the path length when a particular X-ray beam travels through the crystal.

Structure solution is the decisive step of structural analysis. Here the phase problem is solved, and, by means of Fourier transform, an electron density map is built. This is only based on the electron density map that the atomic model of the crystal structure can be found. The most widely used structure solution methods are referred to as direct methods, since they find structure factor phases directly from the structure factor amplitudes based on the assumption of the positivity and atomicity (construction upon a few maxima separated by vast regions of nearly-zero intensity) of the electron density within a unit cell.

Since the atomic coordinates obtained from the structure solution may be highly inaccurate, and many details of the structure (atom types, positions of H atoms, disorder) may not be resolved, a process of making the structure more precise is required. This process is called crystal structure refinement. It relies on the least-square minimisation of the difference between the observed (derived from the experiment) and the calculated (obtained from the atomic model) structure factors. The most widely used computer program providing structure refinement is SHELXL.⁶⁰ JANA2006 is its important alternative since it offers some additional options; in particular, it can be used for the refinement of incommensurately modulated structures.⁶¹

MOF structures often pose important challenges such as large lattice constants, high number of atoms in the asymmetric unit, disorder and/or twinning. The refinement of a disorder is allowed by structure refinement programs only when there are a few (2–4) components contributing to the disordered group of atoms. However, in many instances, the molecules of solvents entrapped in the pores of MOFs are disordered over multiple positions up to a point that their refinement is not possible. In such a case the contribution of the disordered molecules to the measured structure factors should be subtracted. PLATON SQUEEZE⁶² or the equivalent masking procedure implemented in the OLEX2 program suite⁶³ can carry out this task. The procedure can allow for the improvement of the quality of the model as well as the quantification of the size and content of the pores. The subtracted electron density is integrated and output in form of an electron count.

The final crystal structure is written into a crystallographic information file (cif) which is an archive file for the transmission of crystallographic data.⁶⁴ Once validated with the CheckCIF procedure,⁶⁵ it can be attached to a scientific publication as a supplementary material, and deposited with a crystallographic database. The Cambridge Structural Database, which crystal structures of organic and organometallic compounds can be sent to, counts by now nearly 1 000 000 entries.⁶⁶

3.2.3. Powder X-ray diffractometry

Powder X-ray diffractometry (PXRD) is another experimental technique invaluable for the solid state characterisation. Although its use for the MOF crystal structure determination is quite limited (the obstacles are: large unit-cell sizes, high number of atoms in the asymmetric units as well as large amounts of solvent molecules heavily disordered within the pores), its use to prove material's identity and crystallinity is prevalent. The advantages of PXRD with respect to the SCXRD technique include: representability (the whole of a sample, instead of a unique crystal, is investigated), simplicity of sample preparation and data presentation (a finely ground powder is simply placed on the X-ray beam path, and the diffraction pattern is presented in form of a simple numerical function), and speed (data collection is much faster compared to SCXRD).

PXRD relies on the same physical principles as its single-crystal counterpart. The instrumentation used in PXRD measurements is highly comparable to the one described above, although some important technical differences in the design of diffractometers and detectors do exist. In a PXRD experiment, powder, i.e., a collection of a large number of very small crystallites, and not a single crystal, is investigated. As a result, instead of sharp dot-like reflections, the diffraction pattern of a crystalline sample recorded with an area detector features multiple diffraction rings, the so-called Debye rings. Once integrated, the Debye rings are conventionally presented in form of a diffractogram, i.e., a plot of intensity of the diffracted beams as a function of the diffraction angle 2θ . This leads to the simplicity of the form the results are presented, but also to an inevitable peak overlap (Figure 10).⁶⁷ For this reason, indexing of a PXRD pattern, an important step of the full pattern decomposition, is challenging, especially in the structures of low symmetry.

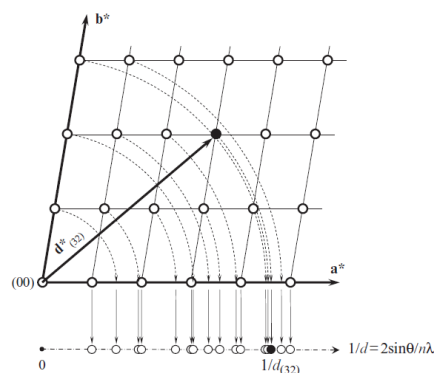


Figure 10. Individual reflections, which in SCXRD show up as discrete points in the reciprocal space, in a powder diffraction pattern are projected onto a single $1/d$ (or equivalent 2θ) axis, resulting in considerable peak overlap. In this example, the (32) reflection nearly overlaps with the reflections (41) and (30). Figure adapted from Pecharsky & Zavalij (2009).⁶⁷

Phase identity of a MOF sample can be confirmed by comparing the recorder PXRD pattern with the one calculated from the structure determined with SCXRD. The latter can always be done, since structure factors can be calculated based on the knowledge of the content of the unit cell (Eq. 2). Program MERCURY offers the feature of PXRD pattern calculation.⁶⁸ Identity between the SCXRD-derived and the experimental PXRD patterns means that the sample is chemically pure. In turn, a set of additional Bragg peaks normally comes from another phase, which constitutes an impurity of the desired material.

Another important feature of MOFs, i.e., their stability, can also be tracked upon by PXRD. Multiple PXRD patterns are recorded once the sample is subjected to critical external stimuli (activation, impact of water (hydrolytic stability) or other solvents, ageing), and then compared to the original PXRD pattern. Decrease in peak intensity together with increase of the background are indicative of steady sample degradation and/or partial loss of crystallinity. On the other hand, when the PXRD pattern stays intact, then it means that the sample is stable under the screened conditions.

3.3. Photoelectron spectroscopy

X-ray photoelectron spectroscopy (XPS, alternatively referred to as ESCA – electron spectroscopy for chemical analysis) is a surface-specific analytical technique used to study the energy of occupied atomic/molecular orbitals in atoms and molecules.⁶⁹ Its counterpart using solely the UV radiation as a source of photons is called UV Photoelectron spectroscopy (UPS). The foundations of this experimental technique were laid by Turner, Spicer, Vilesov and Siegbahn in 1960s.

The physical phenomenon constituting the fundamental of XPS is the photoelectric effect. When a molecule is irradiated with X-rays, the energy of an X-ray photon ejects an electron (hereafter called a photoelectron), and the ionisation occurs. The kinetic energy (E_k) of these photoelectrons is given by the Einstein's equation (Eq. 5)

$$E_k = h\nu - E_B - \varphi \quad (5)$$

where:

$h\nu$ – the photon energy

E_B – the binding energy of the photoelectron

φ – the work function of the sample

Electrical connection between the sample and the electron analyser simplifies this equation to Eq. 6.

$$E_k = h\nu - E_B \quad (6)$$

According to the Koopmans' theorem, $-E_B$ is identified with the energy of the atomic or molecular orbital in which the photoelectron resides before the ejection. Since the energy of the incident X-ray photons is known, and the kinetic energy of the photoelectrons can be measured experimentally, then the binding energies and consequently energy levels can straightforwardly be deduced.

In practice, photoelectron spectra are customarily recorded with a specially designed instrument called an X-ray photoelectron spectrometer (Figure 11). It consists of an X-ray source, a sample holder, an electron analyser and a detector. The entire experimental set-up operates under ultrahigh vacuum. The design of the X-ray sources used in photoelectron spectroscopy is identical to that of the sealed X-ray tubes used for diffraction purposes. In XPS, however, soft X-rays are predominantly used. Dual Al and Mg anode X-ray sources are typically used in lab-based XPS experiments, with X-ray photon energy of 1486.6 eV ($\lambda = 8.34 \text{ \AA}$) for Al K α and 1253.6 eV ($\lambda = 9.89 \text{ \AA}$) for Mg K α . As an alternative to double anode sources, monochromatic X-ray sources are used; the use of a monochromator (e.g., a quartz crystal) coupled to the spectrometer largely increases the spectral purity of the beam, thus resulting in XPS spectra of higher resolution.

The incident X-ray beam is shone upon the solid sample, and the kinetic energy of the ejected photoelectrons is analysed with a concentric hemispherical analyser (Figure 11). The latter consists of two concentric hemispheres, with radii R_1 (inner hemisphere) and R_2 (outer hemisphere). The two hemispheres are negatively polarised with potentials V_1 and V_2 ($V_2 > V_1$). Only the photoelectrons which bear the kinetic energy eV_0 ($V_0 =$ median equipotential, Eq. 7) will pass through the analyser on the median equipotential surface of the radius R_0 , i.e. without hitting the top or bottom of the analysing chamber, and will be focused on the lens.

$$V_0 = \frac{V_1 R_1 + V_2 R_2}{2R_0} \quad (7)$$

By continuously scanning the V_0 values, photoelectrons of different kinetic energies can be detected. The most commonly used device for photoelectron detection is the channel electron multiplier, wherein the use of a system of dynodes allows electron gains of up to 10^8 . Electrons are subsequently converted to an electrical signal, which is then digitised.

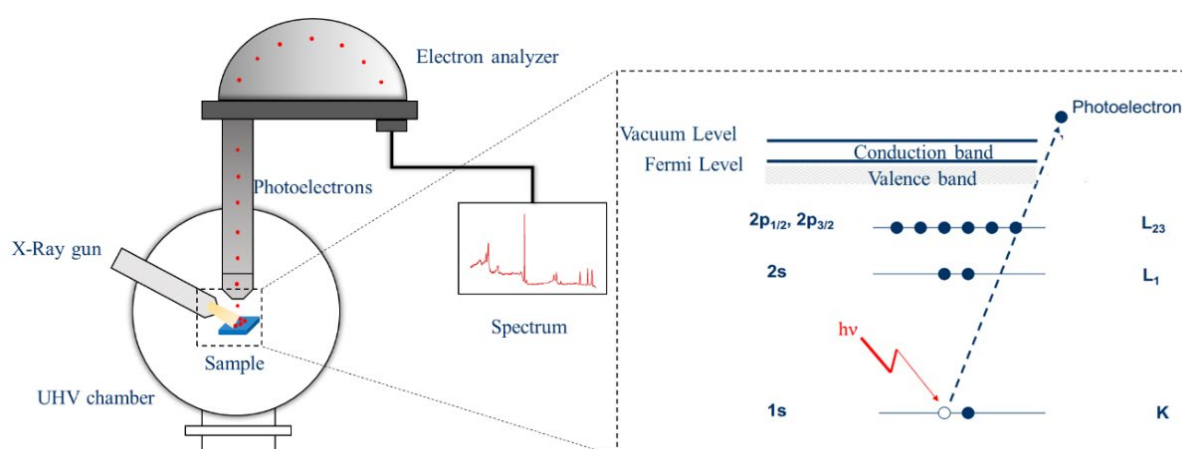


Figure 11. A scheme of a photoelectron spectrometer showing its principal components, and the principle of photoelectron emission.

By collecting the photoelectrons with the analyser, multiplying with the detector, counting and analysing the number of electrons as a function of their binding energy, the XPS spectrum is obtained. The spectra over a relatively wide E_B range (survey scans) give a signature of the elements as a function of their atomic number, thus providing quantitative elemental analysis. Moreover, the spectra recorded over a narrower E_B range (high-resolution scans) allow for the identification of subtle E_B differences of a particular element present in different local chemical environments.

The technique of XPS has made a considerable success in chemical analysis. Still at the beginning of its development, it revealed the electronic structure and the energies of the molecular orbitals within the N_2 molecule. The use of XPS in determining oxidation states of metals in their compounds is also commonly known. In the current thesis, the XPS spectra of 1s orbitals belonging to the nitrogen atoms are analysed as part of our investigation of the protonation states of adenine in novel adenine-based MOFs.

3.4. Thermogravimetric analysis

Crucial information about the thermal stability of a MOF material can be obtained from thermogravimetric analysis (TGA). This technique relies on continuous monitoring of the mass of a solid sample while its temperature is increased. As a result, a thermogram, i.e. a dependence of the mass loss as a function of temperature, is obtained. In a typical experiment, a small amount of solid sample (ca. 20 mg) is placed onto a platinum or Teflon pan and hung on a wire connected with the microbalance. This setup is then introduced into a furnace, wherein a hot stream of gas (either air or nitrogen) imposes a certain, continuously increasing temperature on the sample. Typically, a MOF loses its weight in several steps. First, at moderate temperatures, mass loss indicates that the solvent molecules from within the pores are gradually lost. Then, a plateau of the thermogram evidences the stabilisation of the activated (desolvated) MOF. Subsequent abrupt mass loss is symptomatic of the thermal decomposition of the framework material, which afterwards is composed only of the mineralised residue. Consequently, TGA can not only provide information about the thermal stability, but also serves as an auxiliary method to confirm the chemical formula of the compound, and to determine the solvent content.

3.5. Infrared spectroscopy

Electromagnetic radiation in the infrared (IR) range ($400\text{--}4000\text{ cm}^{-1}$) covers the same energy range as the bending, stretching and oscillatory motions of atoms linked by chemical bonds. Thus, once absorbed, IR rays of a particular wavenumber can serve as an analytical tool to prove the presence of specific functional groups. For instance, a carbonyl group $C=O$ normally absorbs at $1670\text{--}1780\text{ cm}^{-1}$, a hydroxy group in alcohols at $3400\text{--}3650\text{ cm}^{-1}$, while aromatic rings normally have two absorption bands at $1450\text{--}1600$ and $1660\text{--}2000\text{ cm}^{-1}$, respectively. Moreover, the absorption in the $400\text{--}1500\text{ cm}^{-1}$ region is characteristic for a given substance, i.e. serves as its chemical fingerprint. Its identity with another IR fingerprint region underpins the chemical equivalence of two corresponding samples.

Fast recording an IR spectrum from a solid sample is allowed by Fourier transform IR (FT-IR) spectrometers. In MOF chemistry, IR spectroscopy is used as a tool confirming the presence of certain functional groups within a sample, as a way to prove the chemical equivalence of samples obtained in subsequent batches, and to ascertain the complete activation (release of solvent molecules) of a sample of MOF.

3.6. Gas sorption

Adsorption is a process of attachment of molecules to the surface of the solid.⁷⁰ The substance that is attached to the surface is called adsorbate, while the solid, whose surface the adsorbate is attached to, is called adsorbent. When the adsorption process entails the formation of new chemical bonds, the process is called chemisorption. Inversely, when adsorption relies solely on weak (dispersion or van der Waals) interactions, we talk about physisorption. Although the rule of thumb prompts that physisorption processes have typical values of enthalpy of adsorption of about -20 kJ/mol, whereas the enthalpy of chemisorption is much greater (about -200 kJ/mol), the distinction between the two processes should preferentially be made by means of supplementary spectroscopic methods.

Adsorption of gases onto the surface of MOFs constitutes one of the main branches of MOF-related research. The internal surface of activated MOFs greatly enhances their adsorption capacities, which in turn can find applications in CO_2 capture and sequestration, CH_4 and H_2 storage as well as the removal of volatile organic compounds.

3.6.1. Adsorption isotherms

At a given gas pressure, the adsorbate reaches a dynamical equilibrium with the adsorbent, i.e., the rates of adsorption and desorption become equal, and a constant amount of gas is adsorbed onto the surface. If then the pressure is changed, a new dynamical equilibrium is attained leading to a different amount of the adsorbed gas. Plotting multiple values of amount of gas adsorbed at equilibrium at a fixed given temperature as a function of pressure produces an adsorption isotherm. Experimentally, adsorption isotherms are recorded using either a gravimetric or a volumetric method.

The International Union of Pure and Applied Chemistry (IUPAC) classifies physisorption isotherms into the following 6 types (Figure 12):⁷¹

- Type I isotherm is concave to the pressure axis, and the amount adsorbed approaches a saturation value at higher pressures. It is characteristic of the microporous solids as the micropore size, and not the internal surface area, is a limiting factor of adsorption.
- Type II isotherm is concave at lower pressures and convex at higher pressures. The beginning of almost linear section in the middle of the isotherm (point B in Figure 12) is often considered as a point where the monolayer adsorption is completed. This type of adsorption isotherm is characteristic for non-porous or macroporous adsorbents.
- Type III isotherm is convex in its entire range. Some non-porous adsorbents display this type of isotherm.
- Type IV isotherm is similar to the type II (concave section followed by a convex section as well as the monolayer completion point B, Figure 12), however, the capillary condensation within the mesopores results in the hysteresis loop at high pressures.
- Type V isotherm is in turn similar to the type III (isotherm convex throughout the entire pressure range), and again, the capillary condensation within the mesopores results in the hysteresis loop at high pressures.
- Type VI isotherm is composed of alternating concave and convex sections. It is similar to the situation described by the type II isotherm, but repeated several times. This type of isotherm represents multilayer adsorption on a non-porous substrate.

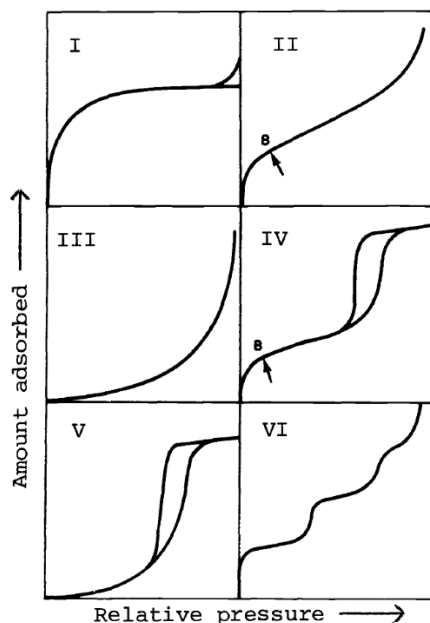


Figure 12. IUPAC classification of the physisorption isotherms. I–VI isotherm types are discussed in the text. Figure reproduced from Sing (1982).⁷¹

3.6.2. BET equation

The method of Brunnauer, Emmet and Teller (BET) is a common tool for the determination of the surface area.⁷² It is customarily given as a linear relation of $p/n^a(p^0 - p)$ on p/p^0 (Eq. 8).

$$\frac{p}{n^a \cdot (p^0 - p)} = \frac{1}{n_m^a \cdot C} + \frac{(C - 1)}{n_m^a \cdot C} \cdot \frac{p}{p^0} \quad (8)$$

where:

n^a – amount adsorbed at a relative pressure of p/p^0

n_m^a – monolayer capacity

C – constant relative to the enthalpy of adsorption

The calculation of specific surface area is then made by plugging n_m^a derived from the linear fitting to the following formula (Eq. 9).

$$a_s(\text{BET}) = \frac{n_m^a \cdot N_A \cdot a_m}{m} \quad (9)$$

where:

N_A – Avogadro constant

a_m – molecular cross-sectional area

m – mass of the adsorbent

The values of a_m are specific for given adsorbates, and can be calculated under the assumption that molecules undergo hexagonal close packing on a solid surface. For example, $a_m(\text{N}_2) = 0.162 \text{ nm}^2$, and $a_m(\text{Xe}) = 0.172 \text{ nm}^2$.⁷¹

3.6.3. Isosteric heat of adsorption

Isosteric heat of adsorption Q_{st} is defined as the standard enthalpy of adsorption at a fixed surface coverage.⁷⁰ It is a measure of the strength of interaction between the host framework and the

molecules of adsorbate. There exist numerous ways how Q_{st} can be determined experimentally. In each of them, the derivation of Q_{st} is possible from the temperature dependence of the equilibrium adsorption isotherms.

Virial-type equation provides information about the Q_{st} at zero coverage, and relies on fitting the adsorption data to the following expression (Eq. 10).

$$\ln\left(\frac{n}{p}\right) = A_0 + A_1 n + A_2 n^2 + \dots \quad (10)$$

where:

n – amount adsorbed

p – pressure

A_0, A_1, A_2, \dots – virial coefficients

Taking only the first two terms of the series into account leads to the linear expression, where A_0 serves as the intercept, and A_1 is the slope. Q_{st} is then found from the temperature dependence of A_0 (Eq. 11).

$$Q_{st} = R \frac{\partial A_0}{\partial (1/T)} \quad (11)$$

where:

R – gas constant

T – temperature

Another method giving information about Q_{st} at zero coverage relies first on the Henry's law, which states that at low pressures the amount adsorbed n is directly proportional to the pressure p , and the coefficient of proportionality takes the name of Henry's constant K_H (Eq. 12).

$$n = K_H p \quad (12)$$

The isosteric heat of adsorption can then be obtained by using the Clausius-Clapeyron equation (Eq. 13).⁷³

$$\lim_{n \rightarrow 0} (Q_{st}) = R \left(\frac{\partial (\ln K_H)}{\partial (1/T)} \right) \quad (13)$$

At a given coverage n the isosteric heat of adsorption Q_{st} can equally be calculated with the Clausius-Clapeyron equation (Eq. 14). The calculation relies on the comparison of two isotherms recorded at two different temperatures T_1 and T_2 , whereby the same partial coverage n was attained when the pressure values reached p_1 and p_2 , respectively (Eq. 15).

$$\ln\left(\frac{p_2}{p_1}\right) = -\frac{Q_{st}}{R} \left(\frac{1}{T_2} - \frac{1}{T_1} \right) \quad (14)$$

$$Q_{st} = R \left(\frac{T_2 T_1}{T_2 - T_1} \right) \ln\left(\frac{p_1}{p_2}\right) \quad (15)$$

4. Adenine-based ship-in-a-bottle MOF with active Cu^{II} sites for efficient detection and capture of ammonia

This chapter has been adapted from: A. Gładysiak, T. N. Nguyen, J. A. R. Navarro, M. J. Rosseinsky, and K. C. Stylianou, *Chem. Eur. J.*, **23**, 13602–13606, (2017).

My contribution to this work consisted in the synthesis, SCXRD analysis, ammonia loading, and characterisation of the discussed material, analysis and plotting of the experimental data (including adsorption isotherms and breakthrough curves), and participation in writing of the manuscript.

4.1. Introduction

Ammonia (NH₃) is a corrosive and toxic gas with a strong odour that is widely produced and used in industries. In industrial settings, 25 ppm of NH₃ is the exposure limit recommended by the US Occupational Safety and Health Administration,⁷⁴ and exposure to up to 300 ppm of NH₃ can cause serious health issues.⁷⁵ Meanwhile, there is still a very high demand for NH₃ at the industrial scale as reflected by its production of 145 million tons in 2014.⁷⁶ NH₃ is an important raw material for the manufacturing of large numbers of chemicals including fertilizers, dyes, plastics, and pharmaceuticals,⁷⁷ and is considered as a potential carbon-free green fuel due to its high energy density and its lower cost of production, storage, and delivery compared to hydrogen.⁷⁸ Both the danger and usefulness of NH₃ have motivated researchers to develop economical and responsive materials that can selectively detect and capture NH₃; for example, NH₃ sensors based on catalytic metals⁷⁹ and conducting polymers⁸⁰ have been reported, whilst porous materials such as activated carbons,⁸¹ organic polymers,⁸² covalent organic frameworks,⁸³ and MOFs⁸⁴ are known as efficient NH₃ sorbents.

Recently, there is an increasing interest in developing porous and robust MOFs for the selective detection, capture and destruction of harmful molecules including toxic industrial chemicals (SO₂ and NH₃), and chemical warfare agents (sarin, sulphur mustard, and dimethyl methylphosphonate).^{36b, 36c, 85} Due to the high basicity and corrosivity of NH₃, the most challenging task in the MOF research area is to develop sorbents and detectors that can efficiently capture and detect NH₃, and can be recycled while retaining their structural integrity.⁸⁶ Recently, Dincă *et al.* have reported mesoporous and robust azolate-based MOFs exhibiting open Mn^{II}, Co^{II}, and Ni^{II} sites which display high and reversible NH₃ uptake.⁸⁴ The strategy of employing azolates to increase the stability of MOFs, initially addressed by Rosi *et al.*,⁸⁷ motivated us to synthesize **SION-10** by employing adenine in the MOF structure. We chose to use Cu^{II} in which, along with other d-element cations in MOFs, has the potential to introduce strong interactions with NH₃.^{86, 88} **SION-10** is a 3-dimensional MOF based on the earth abundant Cu^{II} and readily available benzene-1,3,5-tricarboxylic acid and adenine ligands. It exhibits reversible NH₃ uptake, and displays a visible and reversible colour change upon adsorption and desorption of NH₃.

4.2. Experimental section

4.2.1. Synthesis of **SION-10**

128 mg (1.04 mmol) of copper(II) carbonate along with 84 mg (0.40 mmol) of 1,3,5-benzenetricarboxylic acid and 80 mg (0.59 mmol) of adenine were mixed with 10 mL of deionized water and placed in a high-pressure vessel. The vessel was sealed and heated under hydrothermal

conditions (100 °C) for 48 hours. The resultant plate-like bluish crystals were subsequently filtered and washed with water. From among powder matrix it was possible to isolate one single crystal suitable for X-ray diffraction analysis.

4.2.2. Single-crystal X-ray diffraction

One bluish crystal of **SION-10** with the dimensions of $0.065 \times 0.04 \times 0.02$ mm³ was chosen for the structure determination. The single-crystal X-ray diffraction measurement was performed at I19 Beamline of the Diamond Light Source, UK, using the beam of the wavelength $\lambda = 0.6889$ Å at 120 K. The total of 34911 reflection intensities were measured up to $\theta_{\max} = 27.338^\circ$ and integrated with the SAINT program.⁸⁹ The structure was solved with the ShelXT program package⁹⁰ as implemented in the OLEX2 program suite,⁹¹ and refined with the program ShelXL.⁶⁰ The asymmetric unit of **SION-10** is shown in Figure 13. Details on crystal structure refinement and experimental data for **SION-10** are listed in Table 3.

The highly disordered non-coordinated H₂O solvent contribution to the calculated structure factors was calculated with the program SQUEEZE.⁶² Using the void probe radius of 1.20 Å the program outputs 3 structural voids: two relatively small symmetrically equivalent voids containing negligible amount of electron density, and the third large one ($V_{\text{void}} = 517$ Å³, 20.3% of the unit-cell volume), which contains the excess electron density corresponding to 20 H₂O molecules per unit cell (207 e⁻, 10 H₂O molecules per asymmetric unit). The formula of **SION-10**, being the sum of atoms in the refined structure, [Cu₄(btc)₂(Ade)(1HAde)(μ_3 -OH)(H₂O)₃]·0.4[Cu(Ade)₂(H₂O)₄]·0.5(H₂O), was therefore augmented with 10 H₂O molecules to give the overall [Cu₄(btc)₂(Ade)(1HAde)(μ_3 -OH)(H₂O)₃]·0.4[Cu(Ade)₂(H₂O)₄]·10.5(H₂O).

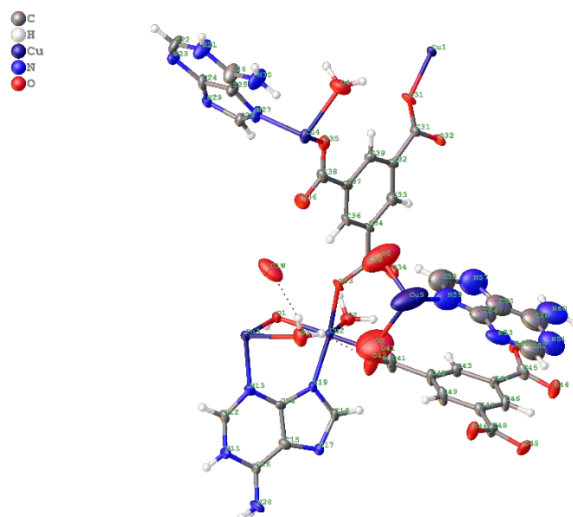


Figure 13. Asymmetric unit of **SION-10** viewed along axis *b*.

Table 3. Crystal data and structure refinement for **SION-10**.

Identification code	SION-10
Empirical formula	C _{32.02} H _{26.22} Cu _{4.4} N _{14.02} O _{18.09}
Formula weight	1176.42
Temperature/K	120.0
Crystal system	triclinic
Space group	P-1
a/Å	11.424(4)
b/Å	15.223(6)
c/Å	16.135(5)
α/°	98.306(5)
β/°	96.9310(10)
γ/°	111.263(5)
Volume/Å ³	2541.5(15)
Z	2
ρ _{calc} /g/cm ³	1.537
μ/mm ⁻¹	1.912
F(000)	1178.0
Crystal size/mm ³	0.065 × 0.04 × 0.02
Radiation	synchrotron (λ = 0.6889)
2θ range for data collection/°	2.518 to 54.676
Index ranges	-15 ≤ h ≤ 15, -20 ≤ k ≤ 20, -21 ≤ l ≤ 21
Reflections collected	34911
Independent reflections	12383 [R _{int} = 0.1104, R _{sigma} = 0.1143]
Data/restraints/parameters	12383/246/659
Goodness-of-fit on F ²	1.080
Final R indexes [I > 2σ (I)]	R ₁ = 0.0986, wR ₂ = 0.2700
Final R indexes [all data]	R ₁ = 0.1338, wR ₂ = 0.3197
Largest diff. peak/hole / e Å ⁻³	4.99/-2.47
CCDC	1547225

4.2.3. Breakthrough experiments for NH₃ capture

A stainless steel column (12 cm of length, 0.5 cm of internal diameter) was packed with 0.385 g of **SION-10** material. The column was activated under a pure He flow (20 mL/min) at 393 K overnight. The desired gas mixture (10 mL/min) was prepared *via* mass flow controllers to achieve a N₂/NH₃ (9:1) ratio. The breakthrough experiments were carried out at 303 K and 1 bar, by step changes from He to N₂/NH₃ flow mixtures. The relative amounts of gases passing through the column were monitored on a Mass Spectrometer Gas Analysis System (Pfeiffer Vacocon) detecting ion peaks at *m/z* 17 (NH₃), 28 (N₂), and 4 (He).

The NH₃/N₂ selectivity has been calculated using [Eq. 16](#).

$$S_{\text{NH}_3/\text{N}_2} = \frac{n_{\text{NH}_3}(0.1 \text{ bar})}{n_{\text{N}_2}(0.9 \text{ bar})} \quad (16)$$

where

$n_{\text{NH}_3}(0.1 \text{ bar})$ = amount of NH₃ adsorbed at its partial pressure of 0.1 bar (as the result of the integration of the breakthrough curve),

$n_{\text{N}_2}(0.9 \text{ bar})$ = amount of N₂ adsorbed at its partial pressure of 0.9 bar (equal to the absolute pressure at the point $p = 0.9 \text{ bar}$ of the N₂-sorption isotherm at 303 K).

4.3. Results and discussion

SION-10 was synthesised hydrothermally after mixing CuCO_3 with 1,3,5-benzenetricarboxylic acid (H_3btc) and adenine (9HAd). The crystals obtained were characterised by single-crystal X-ray diffraction (SCXRD). **SION-10** with the formula of $[\text{Cu}_4(\text{btc})_2(\text{Ade})(1\text{HAd})(\mu_3\text{-OH})(\text{H}_2\text{O})_3] \cdot 0.4[\text{Cu}(\text{Ade})_2(\text{H}_2\text{O})_4] \cdot 10.5(\text{H}_2\text{O})$ crystallises in the triclinic space group $P\bar{1}$, and comprises three components: *i.* a 3-dimensional host framework – $[\text{Cu}_4(\text{btc})_2(\text{Ade})(1\text{HAd})(\mu_3\text{-OH})(\text{H}_2\text{O})_3]$, *ii.* guest mononuclear complexes that are partially occupying the void channels within the host **SION-10** – $0.4[\text{Cu}(\text{Ade})_2(\text{H}_2\text{O})_4]$ (Figure 14), and *iii.* highly disordered guest H_2O solvent molecules. The host framework of **SION-10** is based on Cu-paddlewheel units, in which two Cu1 atoms are bridged by two deprotonated Ade^- ligands *via* an $\eta^1:\eta^1$ binding mode through their N3 and N9 atoms (Ade^- coloured in green – Figure 14a). The neutral 1HAd ligand is coordinated *via* N7 to the axial sites of the Cu-paddlewheel (1HAd coloured in orange – Figure 14a). The coordination of the paddlewheel is completed by the two bridging carboxylates from two crystallographically equivalent btc^{3-} ligands. The Cu-paddlewheel units are connected to each other *via* a tetranuclear Cu-cluster, $\text{Cu}_4(\mu_3\text{-OH})_2$ (Figure 14b), constructed from four Cu^{II} centres (two Cu2 and two Cu3) linked by two μ_3 -hydroxo groups. The presence of the $\mu_3\text{-OH}$ groups was confirmed by the bond valence sum calculation: $s = \sum(s_{ij}) = \sum[\exp(R_{ij} - d_{ij})/b]$, where $R_{ij} = 1.649$ for $\text{Cu}^{\text{II}}\text{-O}$, d_{ij} is the $\text{Cu}^{\text{II}}\text{-O}$ bond distances, $b = 0.37$. The value obtained was 1.23. For O, a value of 0–0.4 indicates H_2O , 1–1.4 indicates OH, and 1.8–2.2 indicates O^{2-} . All Cu2 and Cu3 display a square pyramidal coordination geometry. The apical positions of these pyramids are occupied by H_2O molecules coordinated to Cu^{II} through considerably long bonds (Cu2–O2 2.431(6) Å, Cu3–O3 2.424(6) Å). A single Cu4 atom, also with a square pyramidal coordination geometry, bonds to two btc^{3-} ligands (monodentate – yellow and bidentate – pink), one Ade^- and one H_2O molecule (Cu4–O4 2.211(0) Å – Figure 14c), and acts as a link between Cu-paddlewheel units and tetranuclear Cu-clusters. The host framework of **SION-10** displays an accessible volume of 37.9%, as determined by PLATON.⁶²

The cavities of the host **SION-10** framework are occupied by mononuclear complexes with the formula of $[\text{Cu}(\text{Ade})_2(\text{H}_2\text{O})_4]$ present with 80% partial occupancy (Figure 14d and Figure 17). The octahedrally coordinated Cu5 of the complex displays a Jahn–Teller distortion with two long Cu–N(Ade) bonds (2.226(17) Å), two long Cu–OH₂ bonds (2.24(2) Å), and two short Cu–OH₂ bonds (1.941(14) Å) (Figure 14d). The complex displays π – π stacking interactions between the pyrimidine ring of the Ade^- group and the phenyl ring of the btc^{3-} ligand with a distance of about 3.7 Å (Figure 18), and is involved in an array of hydrogen bonds that stabilise its position within the framework cavities (Figure 19). Our attempts to wash the Cu^{II} -complexes out were not successful, confirming that they cannot be removed from the host **SION-10** framework. Interestingly, molecular crystals of $\text{Cu}(\text{Ade})_2(\text{H}_2\text{O})_4$ are not known, and the theoretically predicted structure of this complex⁹² is markedly different from the one reported in this work. Thus, **SION-10** represents a typical example of a ship-in-a-bottle material. It is worth noting here that although the encapsulation of molecular species in the pores of a MOF is known,⁹³ the direct observation of them as a part of a refined crystal structure is rather rare.⁹⁴ The accessible volume of **SION-10** (with the complexes present within the channels) was found to be 20.3%,⁶² revealing that the complexes occupy nearly half of the accessible volume of the host-framework voids.

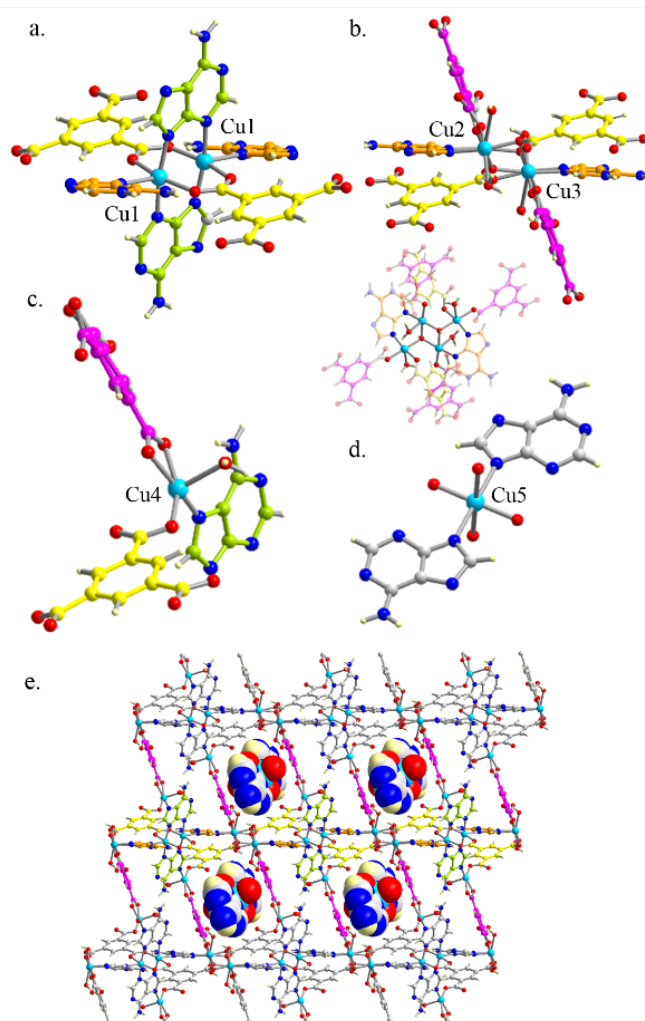


Figure 14. The structure of **SION-10** consists of: (a) Cu1-paddlewheel units which are linked to (b) Cu2Cu3 tetranuclear clusters $\text{Cu}_4(\mu_3\text{-OH})_2$ and c. mononuclear Cu4 to extend the structure in 3-dimensions. (d) and (e) The pores of the host **SION-10** accommodate guest mononuclear Cu5-complexes generating a material with ship-in-a-bottle structure. Atom colour code: C grey, H pale yellow, N blue, O red, Cu cyan.

The phase purity of **SION-10** was confirmed by powder X-ray diffraction (PXRD), scanning electron microscopy (SEM) and elemental analysis (EA), whereas the thermogravimetric (TGA) profile coupled with the variable-temperature (VT) PXRD study revealed the thermal stability of **SION-10**. The PXRD pattern of **SION-10** (Figure 15a) can be indexed to unit-cell parameters consistent with the parameters obtained from SCXRD. SEM images reveal only one type of crystal morphology (Figure 28). Elemental and inductively coupled plasma (ICP) analyses confirmed that the $[\text{Cu}(\text{Ade})_2(\text{H}_2\text{O})_4]$ complex is not 100% present within the pores as the composition of **SION-10** can fit to the formula derived from the SCXRD data (Table 4). FT-IR spectra show characteristic features originating from both ligands present in the structure of **SION-10** (Figure 25). The TGA profile of **SION-10** shows that the coordinated and guest H_2O molecules can be removed in the temperature range of 30–265 °C with the total loss of 20.8% (Figure 23). The weight loss observed in TGA is in good agreement with the weight loss calculated from the EA (20.0%). Above 250 °C a substantial decrease in crystallinity is observed from the VT PXRD study (Figure 20) and the decomposition of **SION-10** starts at 295 °C. As confirmed by PXRD (Figure 22) **SION-10** is stable in liquid water as well as in acidic and basic aqueous solutions, thus confirming its hydrolytic stability.

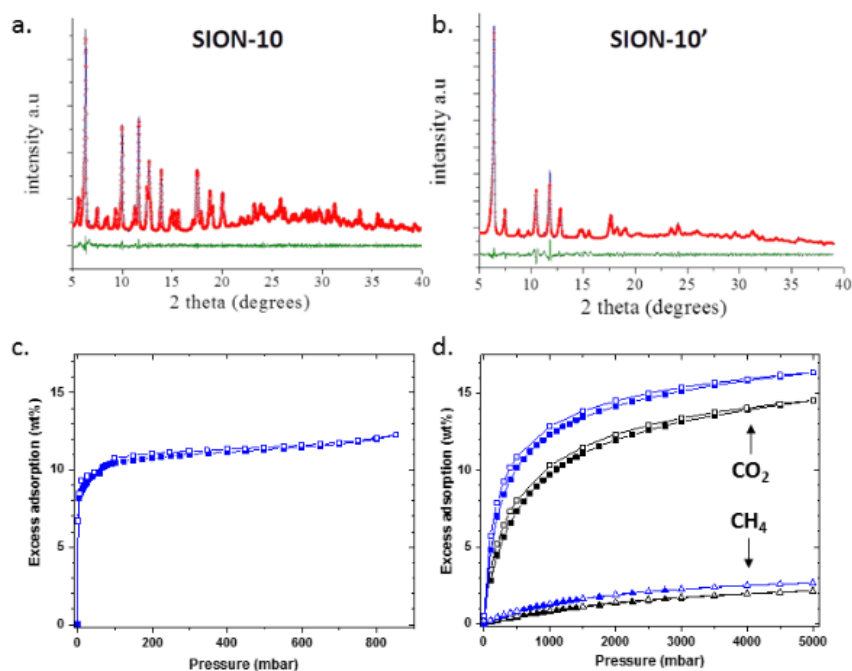


Figure 15. Le Bail fits of (a) **SION-10** (space group $P\bar{1}$, $a = 11.406(7)$ Å, $b = 15.483(6)$ Å, $c = 16.196(6)$ Å, $\alpha = 99.38(3)^\circ$, $\beta = 95.58(0)^\circ$, $\gamma = 112.31(7)^\circ$, $V = 2570.7$ Å³, $R_{wp} = 3.903\%$) and (b) **SION-10'** (space group $P\bar{1}$, $a = 11.269$ Å, $b = 15.560$ Å, $c = 15.962$ Å, $\alpha = 100.492^\circ$, $\beta = 98.126^\circ$, $\gamma = 112.396^\circ$, $V = 2475.7$ Å³, $R_{wp} = 4.74\%$) collected at 298 K using the Cu $K\alpha$. The blue plots represent the experimental data, the red dots show the refined Le Bail profiles while the green plots represent the difference between them. **SION-10'** is porous to: (c) N₂ at 77 K and 900 mbar and (d) CO₂ (top two plots) and CH₄ (bottom two plots) at 273 (blue plots) and 298 K (black plots) and 5000 mbar. In (c) and (d) full symbols represent adsorption, while the empty ones show the desorption.

The activated **SION-10'** was generated by heating the as-synthesized **SION-10** at 120 °C under vacuum (10^{-6} mbar). The weight loss of 19.8 % is consistent with the weight loss observed by TGA and EA. The PXRD pattern of **SION-10'** (Figure 15b) shows the retention of crystallinity and Le Bail fits revealed that the unit cell is contracted by 3.5% compared to the cell parameters of **SION-10**. When **SION-10'** is exposed to the atmosphere for 1–2 hours or is immersed in liquid H₂O (10 mins), **SION-10** can be recovered. This suggests that **SION-10'** with open Cu^{II} sites has high affinity for H₂O, and thus the re-coordination of H₂O molecules to Cu^{II} leads in the generation of the ordered **SION-10** structure.

SION-10' is permanently porous to N₂ at 77 K and 1 bar, exhibiting a reversible type I sorption behaviour characteristic for microporous materials (Figure 15c). Application of the Brunauer–Emmett–Teller (BET) model in the relative pressure p/p^0 range of 0.02–0.22 results in a surface area of ~300 m²/g. The calculated pore volume of **SION-10'** is 0.138 cm³/g, which is in good agreement with the pore volume derived from the single crystal data of the static structure of **SION-10** (0.132 cm³/g). **SION-10'** is porous to CO₂ and CH₄ at 273 and 298 K (type I isotherms, Figure 15d) and the isosteric heats of adsorption Q_{st} at zero coverage derived from the virial-type expression are 30.8 kJ/mol for CO₂ and 21.3 kJ/mol for CH₄.

Since the complexes do not block the porosity in **SION-10'** where open Cu^{II} are present, and both polar and non-polar molecules can diffuse in the accessible voids, we subjected **SION-10'** to NH₃ adsorption, with the NH₃ vapour generated by evaporation of a 25% ammonia solution at room temperature. Upon exposing the green powder of **SION-10'** to NH₃ vapour, a colour change was immediately noticed and the green colour changed to blue, whilst its shade deepened over a loading

period of 30 mins (Figure 16c, inset). The formula of **SION-10**→NH₃ (30 mins loading) corresponds to [Cu₄(btc)₂(Ade)(1HAde)(μ₃-OH)(NH₃)₃]·0.4[Cu(Ade)₂(NH₃)₄]·4(NH₃)·6.5(H₂O), revealing that the amount of chemisorbed NH₃ was 6.37 mmol/g (Table 4 and Figure 24). NH₃ molecules displace all H₂O ligands previously coordinated to Cu^{II}, and a part of non-coordinated H₂O guest molecules. In order to further evaluate the capability of **SION-10'** to selectively capture NH₃, we have performed a breakthrough experiment using a 10mL/min flow of N₂/NH₃ (9:1) gas mixture at 303 K (Figure 16a). At the NH₃ partial pressure of 0.1 bar **SION-10'** exhibited the adsorption capacity of 27.3 mmol/g. In a separate experiment, the adsorption capacity of **SION-10'** at the N₂ partial pressure of 0.9 bar and at 303 K was investigated (Figure 27). The amount of N₂ adsorbed (0.170 mmol/g) was significantly lower than that of NH₃, resulting in a NH₃/N₂ selectivity factor of 1440. This result is indicative of a selective and strong interaction of NH₃ molecules with **SION-10'** due to chemisorption (presence of active Cu^{II} centres) and physisorption (narrow pores of **SION-10'**), and places **SION-10'** among materials with the highest NH₃ capacity reported up to date.^{82, 84}

Interestingly, the colour change experienced by the NH₃ loaded **SION-10'** was also observed when the as-made **SION-10** was exposed to NH₃ vapours. The immersion of the blue **SION-10**→NH₃ in liquid water resulted in the isolation of a green material suggesting that **SION-10** could potentially be recovered. The PXRD patterns show that although the crystallinity of **SION-10**→NH₃ is reduced to a significant degree, the recovered material displays the same pattern as with **SION-10**, confirming the regeneration of **SION-10** (Figure 21). The FT-IR spectrum of **SION-10**→NH₃ (Figure 16b) shows a nearly identical pattern with that of **SION-10** with characteristic bands at 3400–3300 cm⁻¹ and 1640 cm⁻¹, corresponding to the N–H, O–H, and C=O stretching bands of the Ade⁻, the OH⁻ bridge/H₂O molecule, and the C=O of the btc³⁻ ligand, suggesting that despite the low crystallinity it has the same structural fingerprint as **SION-10**. To further investigate the impact of NH₃ uptake by **SION-10** and its regeneration, the UV/Vis diffuse reflectance spectra were collected (Figure 16c). The UV/Vis spectra revealed a blue-shift of ~70 nm of the Cu^{II} *d*–*d* transition band of **SION-10**→NH₃ compared to **SION-10**, suggesting the formation of new Cu–NH₃ bonds that are formed after the stronger-field NH₃ ligands substitute the weak-field H₂O ligands bound to Cu^{II} centres. The recovered **SION-10** displayed a comparable absorption band compared to the pristine **SION-10**, indicating that **SION-10** could be recycled, and we successfully performed three NH₃ adsorption-desorption NH₃ cycles (Figure 16c). Previous studies demonstrated that the presence of open metal sites within MOFs are key factors for the capture of NH₃. However, MOFs endowed with open metal sites were shown to reduce their porosity and crystallinity to a considerable extent when loaded with NH₃ vapours.⁸⁶ For **SION-10**, we strongly believe that the combination of narrow pores generated from the presence of the complexes, and the presence of active Cu^{II} sites are the key factors for the efficient capture of NH₃.

The substantial green-to-blue colour change was not observed with other gases (such as CO₂, N₂ and CH₄) suggesting that **SION-10** can also act as a selective detector for NH₃ vapour. When 5 mg of **SION-10** were exposed to controlled atmospheres of NH₃ with concentrations of 300 and 600 ppm, the shifts of the absorption bands were clearly observed (Figure 26), indicating the relatively high sensitivity of **SION-10** towards NH₃. In addition, the fast response time, i.e., immediate colour changes, ensures that **SION-10** can quickly detect the presence of NH₃ in the atmosphere. The high thermal and hydrolytic stability together with the uptake of NH₃, and its recyclability confirm that **SION-10** can be potentially used as a dual detector and adsorbent for NH₃.

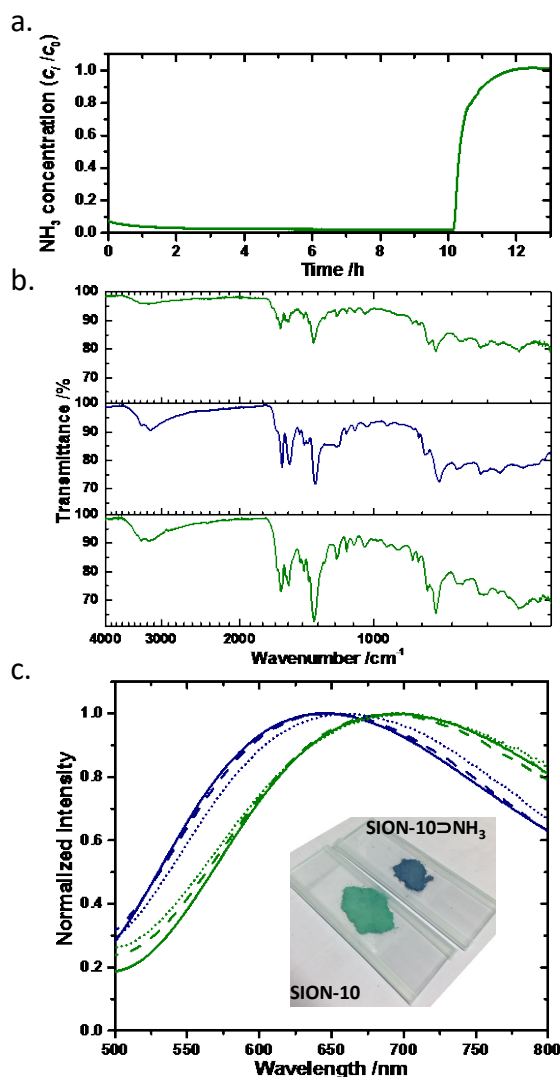


Figure 16. (a) Breakthrough profile of N_2/NH_3 (9:1) gas mixture at 303 K over **SION-10'**. (b) FT-IR spectra of the as-made **SION-10** (top), **SION-10 \supset NH₃** (middle) and recovered **SION-10** (bottom) upon immersion of **SION-10 \supset NH₃** in liquid H_2O , (c) UV/Vis spectra of **SION-10** (green plots) and **SION-10 \supset NH₃** (blue plots) and cycling NH_3 adsorption/desorption (first, second, and third uptake/regeneration cycles are shown in solid, dash, and dot lines, respectively). Inset: a photograph showing the colour difference between **SION-10** and **SION-10 \supset NH₃**.

4.4. Conclusions

In conclusion, we report the synthesis of a ship-in-a-bottle **SION-10** material that is stable in water, and upon activation it is porous to N_2 , CO_2 and CH_4 . The presence of the mononuclear Cu^{II} complexes decorate the pores of the host **SION-10'** with active Cu^{II} sites that allow NH_3 to be chemisorbed. **SION-10'** adsorbs up to a paramount value of 27.3 mmol of NH_3 per gram (chemisorption and physisorption) which is one of the highest NH_3 uptake reported to date. The high sensitivity and selectivity of **SION-10** towards NH_3 makes **SION-10** the first MOF that can quickly uptake NH_3 , and is easily regenerated and reused. In addition, it can detect NH_3 at concentrations as low as 300 ppm.

This work demonstrates a step forward towards the discovery of versatile, easily prepared and recyclable MOFs acting as dual detectors and adsorbents for NH_3 and further synthetic efforts in developing novel porous and water stable MOFs sensitive to NH_3 concentrations lower than 300 ppm.

4.5. Appendix

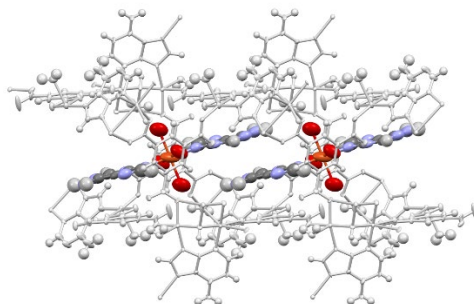


Figure 17. Arrangement of the $\text{Cu}(\text{Ade})_2(\text{H}_2\text{O})_4$ complexes entrapped within the channel of the host framework (marked in light grey) extending along the $[100]$ direction.

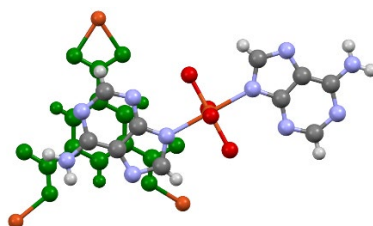


Figure 18. π - π stacking interaction between the pyrimidine ring of the Ade^- group and the phenyl ring of the btc^{3-} ligand (positioned below the Ade^-) depicted in green.

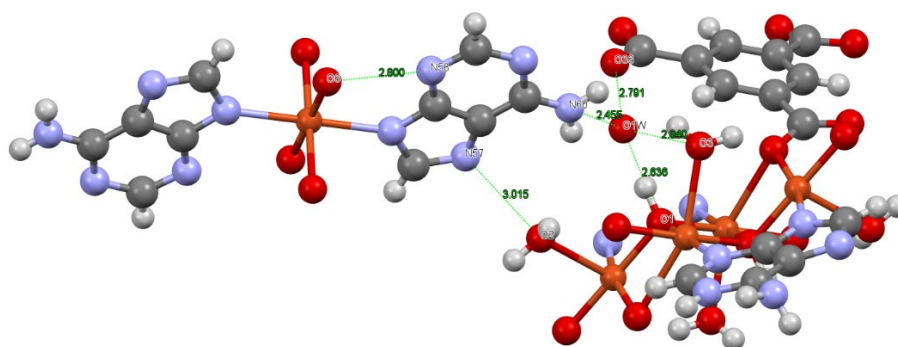


Figure 19. Structure of the $\text{Cu}(\text{Ade})_2(\text{H}_2\text{O})_4$ complex within the voids of **SION-10** and the array of hydrogen bonds stabilising its position. Lengths of H-bonds given in angstroms.

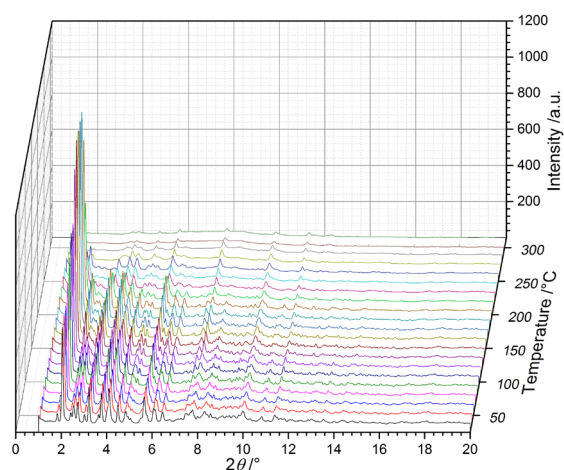


Figure 20. Variable-temperature PXRD pattern of **SION-10** recorded with synchrotron radiation ($\lambda = 0.50084 \text{ \AA}$).

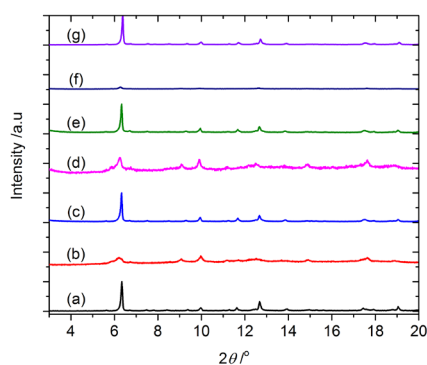


Figure 21. PXRD patterns of **SION-10** and **SION-10 \cdot NH₃** obtained from the recycling experiment, recorded with the Cu K_{α} radiation. (a) **SION-10** as made; (b) **SION-10** loaded with NH₃ in the first cycle; (c) **SION-10** recovered after the first loading cycle; (d) **SION-10** loaded with NH₃ in the second cycle; (e) **SION-10** recovered after the second loading cycle; (f) **SION-10** loaded with NH₃ in the third cycle; (g) **SION-10** recovered after the third loading cycle.

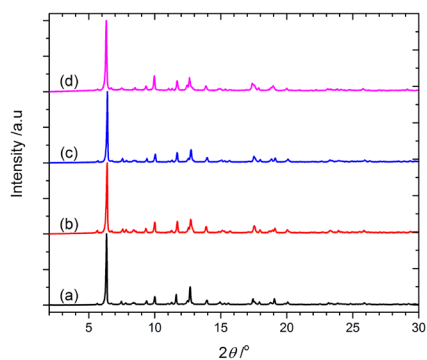


Figure 22. Hydrolytic stability testing of **SION-10**. PXRD patterns of: (a) as-made **SION-10**; (b) **SION-10** submerged in an acidic (pH = 4.0) buffer solution; (c) **SION-10** submerged in water; (d) **SION-10** submerged in a basic (pH = 9.4) buffer solution. $\lambda = 1.5418 \text{ \AA}$.

Table 4. Elemental analysis for **SION-10**, **SION-10'** and **SION-10 \rightarrow NH₃**.

Compound	Formula	Anal. Calcd	Experimental	Notes
SION-10	$[\text{Cu}_4(\text{btc})_2(\text{Ade})(1\text{HAde})(\mu_3\text{-OH})(\text{H}_2\text{O})_3] \cdot 0.4[\text{Cu}(\text{Ade})_2(\text{H}_2\text{O})_4] \cdot 10.5(\text{H}_2\text{O})$	C 28.27, H 3.66, N 14.43, Cu 20.6	C 27.72, H 3.69, N 13.86, Cu 20.9	Cu mass fraction obtained from ICP-MS.
SION-10'	$[\text{Cu}_4(\text{btc})_2(\text{Ade})(1\text{HAde})(\mu_3\text{-OH})] \cdot 0.4[\text{Cu}(\text{Ade})_2]$	C 35.35, H 1.78, N 18.03	C 33.22, H 2.35, N 17.17	
SION-10\rightarrowNH₃	$[\text{Cu}_4(\text{btc})_2(\text{Ade})(1\text{HAde})(\mu_3\text{-OH})(\text{NH}_3)_3] \cdot 0.4[\text{Cu}(\text{Ade})_2(\text{NH}_3)_4] \cdot 4(\text{NH}_3) \cdot 6.5(\text{H}_2\text{O})$	C 28.45, H 4.33, N 23.43	C 26.64, H 4.55, N 22.93	

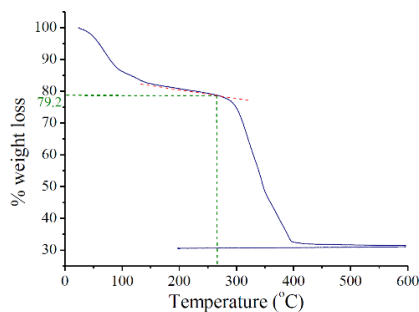


Figure 23. TGA profile of **SION-10**.

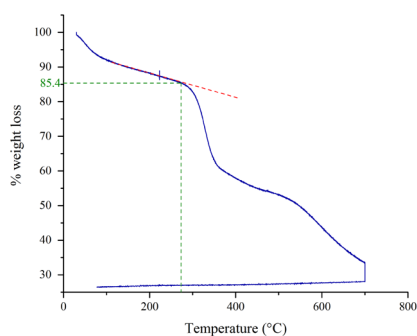


Figure 24. TGA profile of **SION-10 \rightarrow NH₃**.

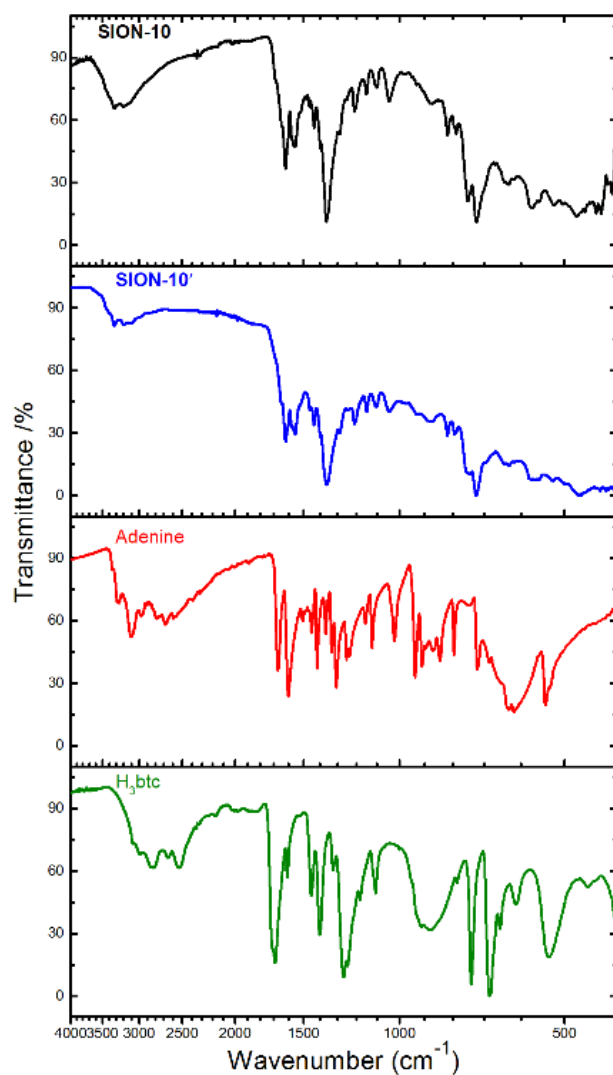


Figure 25. Fourier–transform infrared spectra of **SION-10** (black plots) and **SION-10'** (blue plots) compared to the spectra of HAdc (red plots) and H₃btc (green plots) ligands incorporated within the structure of the MOF. The spectra feature both N–H stretching at 3300 cm^{-1} , and C=O stretching at 1618 cm^{-1} , thus confirming the incorporation of both Ade[−] and btc^{3−} ligands into the framework.

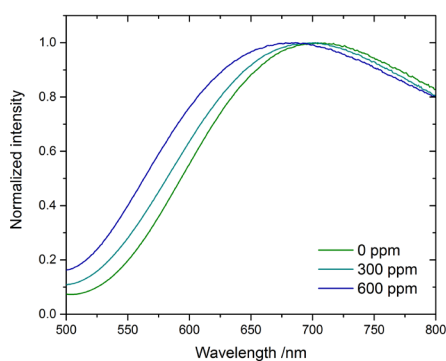


Figure 26. UV-Vis diffuse reflectance spectra of **SION-10** in atmospheres containing 0, 300 and 600 ppm of NH_3 .

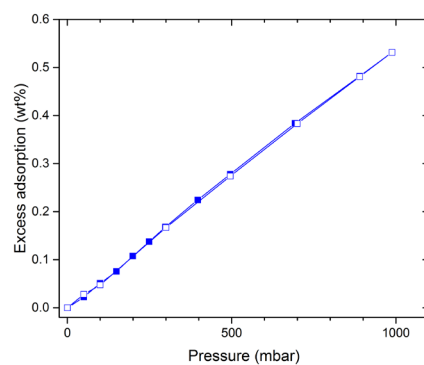


Figure 27. N₂-sorption isotherm at 303 K. Full squares denote the adsorption, while the empty ones – the desorption run.

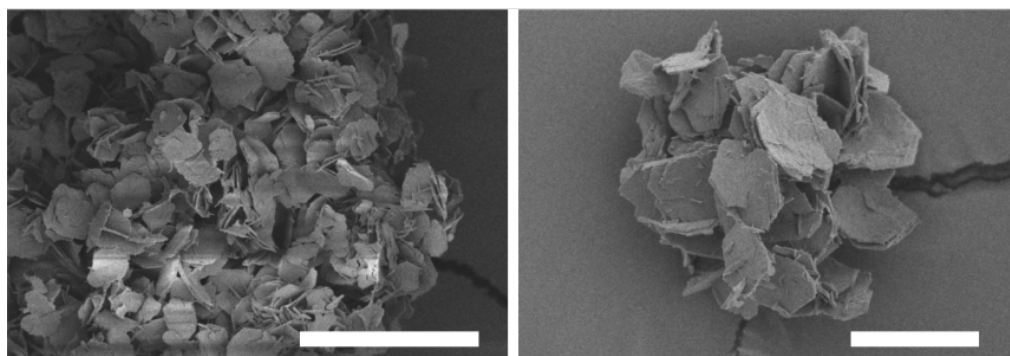


Figure 28. SEM images of **SION-10** showing the homogeneous morphology of microcrystals. Scale bars: 50 μm (left), 20 μm (right).

5. Protonation states and location of protonated N atoms of adenine in metal–organic frameworks

This chapter has been adapted from: A. Gladysiak, T. N. Nguyen, S. L. Anderson, P. G. Boyd, R. G. Palgrave, J. Bacsá, B. Smit, M. J. Rosseinsky, and K. C. Stylianou, *Inorg. Chem.*, **57**, 1888–1900, (2018).

My contribution to this work consisted in the SCXRD analysis of the discussed materials, analysis and plotting of the experimental data, database search, and participation in writing of the manuscript.

5.1. Introduction

Amongst the organic ligands used for the synthesis of MOFs, nucleobases present an attractive family of ligands that can be incorporated within the MOF structures.⁹⁵ This is due to their rigid structure and the large number of oxygen and nitrogen donor sites of different basicity; they are all readily available for metal coordination. In addition, nucleobases have the potential to form numerous complementary non-covalent interactions, including hydrogen bonds and π – π stacking, which can further be exploited in order to prepare stable MOFs, of which the components are held together by not only coordination bonds but also the cumulative effect of numerous supramolecular interactions.^{36d, 96} Canonical nucleobases are often classified into two subgroups based on their structures: purines (adenine and guanine) and pyrimidines (cytosine, thymine, and uracil). With the higher number of heteroatoms, the purine nucleobases are the better bridging ligands than the pyrimidine nucleobases, especially with adenine being extensively used for forming complexes and networks with transition metals.⁹⁷

Adenine (9HAde, [Figure 29](#)) is a rigid ligand with five potential coordination sites for metal binding, i.e., two imidazolate, two pyrimidinate N atoms, and an $-\text{NH}_2$ group. The basicity order of the N atoms is $\text{N9} > \text{N1} > \text{N7} > \text{N3} \gg \text{N10}$,⁹⁸ and the pK_a of 9HAde is 9.8. Due to the 9HAde's imidazolate functionality with the coordination bridging mode of $\mu_2\text{-N7,N9}$, several MOFs with zeolitic topologies have been reported.⁹⁹ However, due to the high versatility of adenine, which displays a variety of monodentate and bridging bidentate or tridentate metal coordination modes, an accurate prediction of Ade-based MOFs structures is often impossible. This, in fact, has been the impetus for the discovery of a large number of both porous and non-porous Ade-based MOFs with diverse structures and topologies that have been reported in the literature over the last few years.^{87a, 100} These MOFs have been shown to exhibit reversible hydrochromic behaviour,^{100o} CO_2/CH_4 selectivity,^{100g} tuneable porosity,^{100h, 100j, 100n} and properties such as mesoporosity with low densities, high surface areas and large pore volumes.^{100k} Application in controlled drug delivery has also been explored.^{100e}

Despite the high utility of adenine in MOF synthesis and due to the different possible protonation states of adenine (H_2Ade^+ , HAde^+ , and Ade^-), assigning the protonated N atoms and balancing the charge in crystal structures of many Ade-based MOFs is challenging, especially in complicated scaffolds. Exacting this information is vital to understand several properties of these materials, including acidity/basicity, catalytic cycles, and proton conductivity. The positions of H atoms are difficult to derive from X-ray diffraction data as H has the weakest X-ray scattering power among all elements. Neutron diffraction is more reliable in this context, although this technique requires special sample preparation methods and experimental instrumentation, which are not readily available in laboratories. Nevertheless, a rule of thumb for finding the location of protonated N atoms in heterocyclic compounds was postulated by Singh, stating that for six-membered rings, the C–N–C angle should fall in the range of $125 \pm 3^\circ$ for the protonated N atoms, and $116 \pm 3^\circ$ when the H-atom is

absent.¹⁰¹ Since the rule is mainly valid for non-coordinated heterocyclic compounds, its use in Ade-based MOFs is not straightforward. We combined X-ray photoelectron spectroscopy (XPS) with the C–N–C angles derived from single crystal X-ray diffraction (SCXRD) measurements, to determine the protonation states and to localise the protonated N-atoms of adenine in five Ade-based MOFs, which we referred to as **SION-31**, **SION-32**, **SION-33**, **SION-34** and **SION-35**. These materials are based on the transition metals Ni^{II}, Cu^{II} or Zn^{II}, adenine, and di-, tri- and tetra-carboxylate ligands. The different binding modes of adenine ligands within these materials will be discussed based on their crystal structures whereas their protonation states and the location of the protonated N atoms is reviewed through a detailed analysis of the XPS data and C–N–C angles.

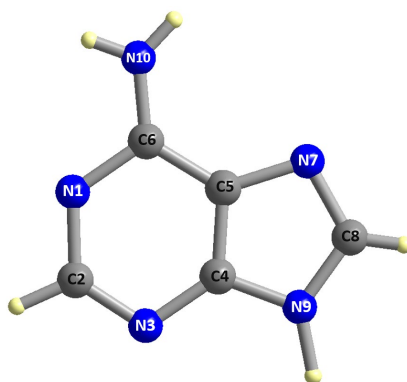


Figure 29. Structure of adenine (9HAde) protonated via N9. Colour scheme: grey, C; blue, N; and yellow, H.

5.2. Experimental section

5.2.1. Synthesis

The reagents, including adenine (9HAde), 1,3,5-benzenetricarboxylic acid (H₃btc), isophthalic acid (H₂ipa), 3,5-pyrazoledicarboxylic acid (H₃pzdc), 1,2,4,5-benzenetetracarboxylic acid (H₄btec), NiCO₃, CuCO₃, and ZnCO₃ were purchased from Sigma-Aldrich and used as received.

Synthesis of [Ni₂(btc)(Ade)(H₂O)₅]·3H₂O (SION-31**):** A mixture of NiCO₃ (71 mg, 0.6 mmol), H₃btc (63 mg, 0.30 mmol), 9HAde (40 mg, 0.30 mmol), and water (8 mL) were placed in a Teflon reactor. The mixture was heated at 160 °C for 4 days, and then gradually cooled to room temperature at a rate of 0.1 °C/min. Green plate type crystals of **SION-31** were obtained in 43 % yield (based on NiCO₃). Anal. Calcd for ([Ni₂(C₉H₃O₆)(C₅H₄N₅)(H₂O)₅](H₂O)₃): C 28.12, H 3.78, N 11.71; found: C 28.26, H 3.68, N 12.00.

Synthesis of [Ni(ipa)(3HAde)] (SION-32**):** The reaction conditions are similar to the ones described for **SION-31**, with the exception being that the molar ratio between NiCO₃:H₂ipa:9HAde is 3:2:3 (0.6 mmol NiCO₃). Green block-shape crystals of **SION-32** were obtained in 21 % yield (based on NiCO₃). Anal. Calcd for ([Ni(C₈H₄O₄)(C₅H₅N₅)]·(H₂O)_{0.2}): C 43.26, H 2.60, N 19.41; found: C 43.11, H 2.92, N 19.36.

Synthesis of [Ni₂(btec)(7HAde)₂(H₂O)₂]·4H₂O (SION-33**):** The reaction conditions are similar to the ones described for **SION-31**, with the exception being that the molar ratio between NiCO₃:H₄btec:9HAde is 2:3:3 (0.6 mmol NiCO₃). Green block crystals of **SION-33** were obtained in 38 % yield (based on NiCO₃). Anal. Calcd for ([Ni₂(C₁₀H₂O₈)(C₅H₅N₅)₂(H₂O)₂](H₂O)_{2.7}): C 33.30, H 2.96, N 19.42; found: C 33.38, H 2.68, N 19.51.

Synthesis of $[Cu_3(pzdc)_2(1HAde)(H_2O)_4]$ (SION-34): A mixture of $CuCO_3$ / H_3pzdc / $9HAde$ in a molar ratio of 1:1:1 (0.40 mmol $CuCO_3$) in 3 mL H_2O was heated at 120 °C for 36 hrs. Blue block crystals of **SION-34** were obtained in 35 % yield (based on $CuCO_3$). Anal. Calcd for $[Cu_3(C_5HN_2O_4)_2(C_5H_5N_5)(H_2O)_4] \cdot (H_2O)_{0.3}$: C 25.44, H 2.20, N 17.81; found: C 25.41, H 2.33, N 17.90.

Synthesis of $[Zn_2(btc)(Ade)(H_2O)_2]$ (SION-35): A mixture of $ZnCO_3$ (47mg, 0.40 mmol), H_3btc (84mg, 0.40 mmol), $9HAde$ (54mg, 0.40 mmol), and water (6 mL) was placed in a Teflon reactor. The mixture was heated at 150 °C for 72 hrs, and then gradually cooled to room temperature at a rate of 0.3 °C/min. Colourless needle crystals of **SION-35** were obtained in 22 % yield (based on $ZnCO_3$). Anal. Calcd for $[Zn_2(C_9H_3O_6)(C_5H_4N_5)(H_2O)_2] \cdot (H_2O)_{0.7}$: C 32.45, H 3.39, N 13.52; found: C 32.68, H 3.42, N 13.33.

5.2.2. Single-crystal X-ray diffraction

SCXRD data of **SION-31** was collected on a Bruker AXS SMART Apex equipped diffractometer with a CCD detector. The X-ray beam was generated using graphite monochromated Mo $K\alpha$ radiation from a molybdenum X-ray tube operating at 40 kV and 30 mA. A single crystal was immersed, picked with a polyimide loop which in turn was mounted on a goniometer. Diffraction data was collected at 100.0 K. Single crystals of **SION-32**, **SION-33**, **SION-34** and **SION-35** were measured using the synchrotron radiation at the European Synchrotron Radiation Facility, Beamline BM01. Suitable single crystals were selected and mounted onto the diffractometer equipped with a CCD area detector. The crystals were kept at 100.0 K during data collection. Using Olex2,⁹¹ their structures were solved with the ShelXT structure solution program using Intrinsic Phasing¹⁰² and refined with the ShelXL refinement package using Least Squares minimization.⁶⁰ Atomic positions were found from the difference–Fourier maps and refined anisotropically for all non-H atoms. Positions of aromatic H-atoms were refined using a riding model, while H atoms in methyl and hydroxy groups were refined as in idealised rotating groups. U_{iso} for H-atoms were set to 1.2 times U_{eq} of neighbouring atoms, and 1.5 times U_{eq} of atoms in terminating groups. Details on crystal structure refinement and experimental data for **SION-31**, **SION-32**, **SION-33**, **SION-34** and **SION-35** are listed in Table 11.

5.2.3. Powder X-ray diffraction

PXRD data of **SION-31**, **SION-32**, **SION-33**, **SION-34** and **SION-35** were collected with Cu $K\alpha$ radiation at 298 K. Their phase purity was confirmed by the comparison of the simulated PXRD patterns (derived from the Mercury software) to the experimental ones.

5.2.4. X-ray photoelectron spectroscopy

XPS spectra of **SION-31**, **SION-32**, **SION-33**, **SION-34** and **SION-35** were recorded on a Scienta ESCA 300 spectrometer located at the NCESS facility at Daresbury Laboratory, UK, which incorporated a rotating anode Al $K\alpha$ ($h\nu = 1486.6$ eV) X-ray source and had an effective instrument resolution of 400 meV. The spectrometer was calibrated regularly to set the Fermi edge of a silver reference sample at zero binding energy. Sample charging was compensated for using an electron flood gun. The binding energy scale was referenced using the adventitious carbon C1s peak which was set to 284.6 eV. Powder samples were prepared by pressing into indium foil, with care taken to ensure that no In signal was observed in the resulting spectra.

5.3. Results and discussion

5.3.1. Synthesis and characterisation

The syntheses of **SION-31**, **SION-32**, **SION-33**, **SION-34** and **SION-35** were all performed under hydrothermal reaction conditions, with the reactants being carbonate metal salts, adenine, and different carboxylate ligands in pure water. The molar ratios of the reactants were screened to obtain phase-pure products.

Green block type crystals of **SION-31** were formed as a pure phase, with the formula of $[\text{Ni}_2(\text{btc})(\text{Ade})(\mu_2\text{-H}_2\text{O})(\text{H}_2\text{O})_4]\cdot 3\text{H}_2\text{O}$ as determined by SCXRD (*vide infra*). This is well in agreement with the molar ratio of the reactants $\text{NiCO}_3\text{:H}_3\text{btc}\text{:}9\text{HAde}$ of 2:1:1 in the reaction. When H_2ipa , a dicarboxylic acid, is used instead of H_3btc , **SION-32** was formed, with the formula of $[\text{Ni}(\text{ipa})(3\text{HAde})]$. It is worth noting that the use of slight excess NiCO_3 and 9HAde (molar ratio of $\text{NiCO}_3\text{:H}_2\text{ipa}\text{:}9\text{HAde}$ of 3:2:3) is crucial to obtain the pure phase of **SION-32**. Similarly, in the case of **SION-33**, $[\text{Ni}_2(\text{bttec})(7\text{HAde})_2(\text{H}_2\text{O})_2]\cdot 4\text{H}_2\text{O}$, the slight excess of the tetracarboxylic acid H_4bttec and adenine (molar ratio of $\text{NiCO}_3\text{:H}_4\text{bttec}\text{:}9\text{HAde}$ of 2:3:3) is the key for the formation of the product.

Since different MOF structures were obtained with different carboxylate ligands, the metal ion and/or the carboxylate ligands were changed to further explore the versatility of this reaction scheme. **SION-34**, $[\text{Cu}_3(\text{pzdc})_2(1\text{HAde})(\text{H}_2\text{O})_4]$, formed when CuCO_3 and H_3pzdc were used while **SION-35**, $[\text{Zn}_2(\text{btc})(\text{Ade})(\text{H}_2\text{O})_2]$, was the product when ZnCO_3 was combined with H_3btc .

The bulk phase purity of **SION-31**, **SION-32**, **SION-33**, **SION-34** and **SION-35** was confirmed by PXRD, with both the theoretical and experimental X-ray powder diffraction patterns well in agreement (Figure 38). Their purity was further confirmed through elemental analysis (see experimental section) and SEM images (Figure 39, Figure 40 and Figure 41).

The thermal stability of **SION-31**, **SION-32**, **SION-33**, **SION-34** and **SION-35** was also investigated through TGA analysis. As illustrated in Figure 42, the TGA profiles of **SION-31**, **SION-32**, **SION-33**, **SION-34** and **SION-35** follow the same trend, showing an initial weight loss corresponding to the removal of the lattice H_2O molecules followed by the release of the metal bound H_2O molecules at higher temperature (Table 9). The weight loss in **SION-31** occurred in two steps: i. the first step corresponds to the loss of the guest H_2O molecules in the temperature range of 30–130 °C; ii. the second step is attributed to the loss of the coordinated H_2O molecules in the temperature range of 130–250 °C. A total weight loss of 22.5 % is in agreement with the loss calculated from elemental analysis (23.4 %). Decomposition of the framework starts at 400 °C. **SION-32** shows no weight loss as there are no H_2O molecules bound to the metal centre and the cavities are too small to accommodate any H_2O molecules. This is consistent with the elemental analysis as it was found that there are 0.2 H_2O guest molecules per formula unit comprising 0.4 % of the total weight of the structure. The TGA profile of **SION-32** shows its excellent stability up to 450 °C. The same profile for **SION-31** was also observed for **SION-33**. The final weight loss of 14.4 % is slightly larger than the one calculated from elemental analysis (11.3 %). TGA for **SION-34** shows that guest and coordinated H_2O molecules were removed in the temperature range of 30–280 °C with the total weight loss being 8.1 %. This weight loss observed in TGA is slightly lower than that calculated from elemental analysis (10.0 %). Decomposition of the framework starts at 295 °C. Finally, the TGA profile of **SION-35** shows that it is stable up to 210 °C, and in the temperature range of 210–370 °C the coordinated H_2O molecules are removed. The weight loss of 8.4 % is in agreement with the calculated proportion (9.1 %) of the H_2O molecules bound to Zn^{II} from the elemental analysis.

5.3.2. Single-crystal X-ray diffraction analysis

SION-31 crystallises in the monoclinic space group $P2_1/n$. The asymmetric unit (ASU) contains two symmetrically independent Ni^{II} environments (Ni1 and Ni2) which are linked via the btc and adenine ligands. Two carboxylate groups of the btc ligand coordinate to the Ni^{II} ions while the third site is free of any metal binding. Since the bond distances between the C and O atoms, C16–O9 and C16–O10, are comparable (1.263(3) Å and 1.273(3) Å, respectively) and intermediate between the values of 1.35 Å and 1.21 Å characteristic for respectively single and double $\text{C}(\text{sp}^2)\text{--O}$ bonds, this site is a deprotonated carboxylate group; i.e. the btc ligand is btc^{3-} . The charge is balanced with the adenine ligand in its anionic form Ade^- .^{34c} Two Ni1 ions are part of a dimeric unit, which is bridged by two Ade^- ligands via N3 and N9 and two $\mu_2\text{-H}_2\text{O}$ molecules to form a Ni-Ade secondary building unit (SBU) $[\text{Ni}_2(\text{Ade})_2(\text{H}_2\text{O})_4(\mu_2\text{-H}_2\text{O})_2]^{2+}$ (Figure 30a). The octahedral coordination sphere of each Ni1 ion is filled by two terminal H_2O ligands. The bond lengths of the $\text{Ni}\text{--O}_{\text{terminal H}_2\text{O}}$ bonds are 2.085(2) Å ($\text{Ni1}\text{--O2}$), 2.020(2) Å ($\text{Ni1}\text{--O3}$), whilst the bond lengths of the $\text{Ni}\text{--O}_{\text{bridging H}_2\text{O}}$ are 2.1793(17) Å and 2.1234(16) Å ($\text{Ni1}\text{--O1}$). These bond distances are consistent with those reported in the literature ($[\text{Ni}_2(\text{O}_2\text{CFcCO}_2)_2(2,2'\text{-bpy})_2(\mu_2\text{-OH}_2)_2]\cdot\text{CH}_3\text{OH}\cdot 2\text{H}_2\text{O}$:¹⁰³ $\text{Ni}\text{--OH}_2$ 2.107(9) / 2.138(3) Å, $[\text{Ni}_2(\text{H}_2\text{O})_4\text{bdptz}](\text{OTs})_4\cdot 2\text{CH}_3\text{OH}\cdot \text{H}_2\text{O}$:¹⁰⁴ $\text{Ni}\text{--OH}_2$ 2.159(1) / 2.170(4) Å), and are strikingly different from the bonds reported for bridging hydroxyl ligands (bis-(1,5-mesityl-3-nitroformazanato)-bis- μ -hydroxonickel:¹⁰⁵ $\text{Ni}\text{--OH}$ 1.890(7) / 1.884(4) Å). The Ni2 ion also adopts an octahedral coordination geometry, with one chelating and one monodentate btc^{3-} , one monodentate Ade^- via N7, and two terminal H_2O molecules as ligands (Figure 30b). **SION-31** consists of 2-dimensional sheets constructed by connecting the $[\text{Ni}_2(\text{Ade})_2(\text{H}_2\text{O})_4(\mu_2\text{-H}_2\text{O})_2]^{2+}$ units augmented at two extremities with Ni2 atoms (Figure 30a) via two deprotonated carboxylate groups of the btc^{3-} ligands (Figure 30c-d). The third carboxylate group of btc^{3-} forms H-bonds with guest and coordinated H_2O molecules. The non-coordinated H_2O molecules (O1W , O2W and O3W) are hydrogen bonded with the N1 atom of Ade^- and carboxylate O9, O11, and O12 atoms of btc^{3-} (O9, O11, and O12) ligands, ($\text{O1W}\cdots\text{N1}$ 2.712(3) Å, $\text{O1W}\cdots\text{O12}$ 3.025(3) Å, $\text{O2W}\cdots\text{O9}$ 2.801(3) Å, $\text{O3W}\cdots\text{O11}$ 2.618(3) Å), as well as with coordinated water molecules. The structure is close packed and exhibits no accessible voids.

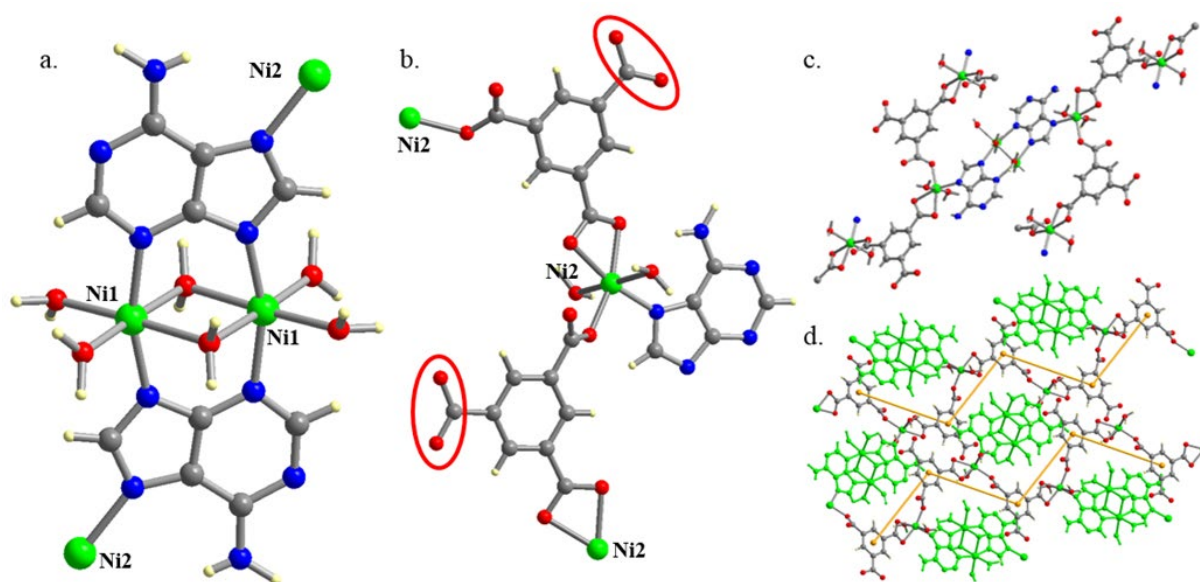


Figure 30. SION-31 (a) Depiction of the Ni-Ade secondary building unit (SBU) $[\text{Ni}_2(\text{Ade})_2(\text{H}_2\text{O})_4(\mu_2\text{-H}_2\text{O})_2]^{2+}$, with Ade^- acting as the bridging ligand via N3, N7 and N9, linking the Ni-Ade SBU with Ni2 . (b) Coordination environment of Ni2 ; the carboxylate group of btc^{3-} is not involved in coordination to Ni^{II} and is enclosed in a red ellipse. (c) Mono- and bi-dentate coordination modes of the btc^{3-} ligand. (d) The Ni-Ade SBU (coloured in green) connects the btc-based chains (orange zig-zag line) resulting in a 2-dimensional layered structure. Colour scheme: Ni, green; C, grey; O, red; N, blue and H, yellow.

Topological analysis with the program TOPOS reveals that the 2-dimensional sheets in **SION-31** form a hexagonal plane net (**hcb**),⁴³ containing vertices of degree 3 centred on the lone Ni²⁺ ions. The two dative bonds with H₂O are disregarded as they do not contribute to the underlying network connectivity. The chelating btc³⁻ carboxylate group, the monodentate carboxylate of a different btc³⁻ ligand, and the Ade⁻ N7 atom contribute as 'edges' incident on this node. The remaining chemical species, including the Ni-Ade SBU, are considered as 2-connected nodes in the topological description, and can therefore be reduced to a single edge in the **hcb** net (Figure 43).

SION-32 crystallises in the tetragonal space group $P4_2/nmc$. In the ASU, there is one Ni^{II} ion sitting on a special position with the Wyckoff site multiplicity reduced by a factor of 2, half deprotonated ipa²⁻ and one neutral 3HAde ligand (protonated via N3, *vide infra*). The 3HAde ligand is disordered as it assumes two equivalent orientations related to one another by a mirror plane. The coordination environment of Ni^{II} is of distorted octahedral geometry, with four O atoms from two chelating ipa²⁻ ligands and two N atoms from two disordered 3HAde ligands completing its coordination geometry (Figure 31a). Each of the 3HAde and ipa²⁻ ligands behave as a bridging linker between the Ni^{II} ions giving rise to a 2-dimensional layered structure (Figure 31b-c). The packing of the 2-dimensional layered structure of **SION-32** (Figure 31c) reveals that there is no accessible volume, as confirmed by the program PLATON.^{65, 106}

Topological analysis reveals that the 2-dimensional layers in **SION-32** form a square-lattice net (**sql**), which possesses single 4-connected nodes centred on the Ni^{II} atoms, while the ipa²⁻ and the 3HAde ligands represents the edges (Figure 44).

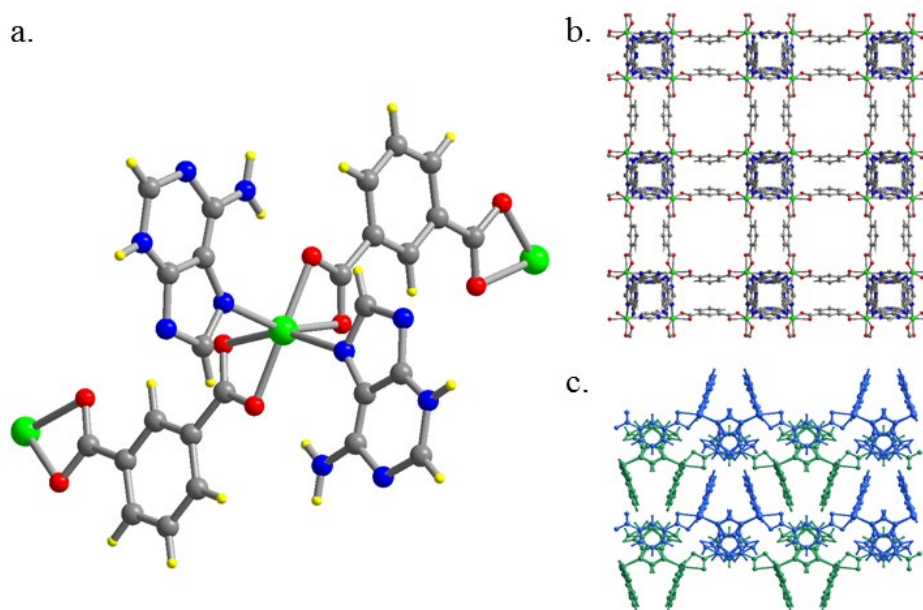


Figure 31. SION-32 (a) Illustration of the distorted octahedral coordination environment of Ni^{II} in **SION-32**; each Ni^{II} is coordinated by two ipa²⁻ and two 3HAde ligands, (b) The coordination of ipa²⁻ and 3HAde around Ni^{II} affords a 2-dimensional layered structure, (c) A single 2-dimensional sheet in **SION-32** along *a*-axis, showing that the orientation of ipa²⁻ and 3HAde around the Ni^{II} of the distorted octahedral coordination results in the generation of a close packed 2-dimensional layer. Colour scheme: Ni, green; C, grey; O, red; N, blue; and H, yellow.

SION-33 crystallises in the triclinic space group $P\bar{1}$. The ASU of **SION-33** consists of one Ni^{II} atom, one neutral 7HAde ligand (protonated via N7, *vide infra*), half the btec⁴⁻ ligand, one coordinated and

two guest H₂O molecules. The 7HAde ligand binds to two chemically equivalent Ni^{II} centres through N3 and N9. Two bridging 7HAde molecules coordinate on opposite sides of the Ni₂ unit forming a 'blade' dimer, [Ni₂(7HAde)₂(H₂O)₂]⁴⁺ (Figure 32a). Two symmetrically independent carboxylic groups of the btec⁴⁻ ligand bind to Ni^{II} in two distinct ways: the first one coordinates to both Ni^{II} atoms within the Ni₂ unit in a monodentate mode through O1, whereas the neighbouring carboxylate binds solely to one Ni^{II} atom through O4 (Figure 32b). A terminal coordinated H₂O molecule completes the octahedral coordination environment of Ni^{II}. The [Ni₂(7HAde)₂(H₂O)₂]⁴⁺ dimers connected into 1-dimensional chains extend along the *b*-axis (Figure 32c). The O3W water molecule links these chains along the [001] direction, through O3W⋯O2 (2.962(13) Å) and O3W⋯N10 (2.930(13) Å) hydrogen bonds to one such chain, and through N10⋯O3W (2.937(15) Å) H-bond to the parallel one. Along [100] there are hydrogen bonds linking subsequent Ni₂-chains directly (O1W⋯O4, 2.806(8) Å), and by means of the O2W water molecule (N7⋯O2W, 2.781(10) Å, and O2W⋯N1, 2.943(9) Å). Therefore, the array of hydrogen bonds combines 1D chains of [Ni₂(7HAde)₂(H₂O)₂]⁴⁺ units into a 3-dimensional supramolecular assembly. The packing and space filling representations of **SION-33** shows that it is not porous, which is further confirmed by PLATON.⁶⁵

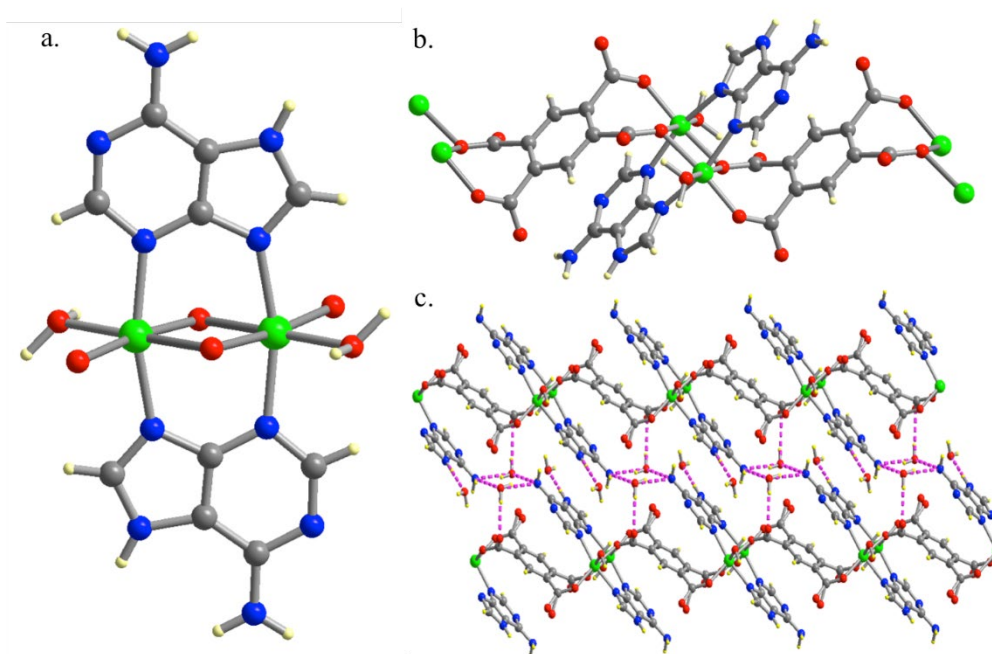


Figure 32. SION-33 (a) [Ni₂(7HAde)₂(H₂O)₂]⁴⁺ 'blade' dimer formed by the bridging coordination of 7HAde N9 and N3 atoms, (b) The coordination of btec⁴⁻ and 7HAde around the octahedrally coordinated Ni^{II} leads in the generation of 1-dimensional chains of **SION-33** along *b*-axis, and (c) Packing scheme viewed along the *a*-axis showing the 3-dimensional supramolecular structure; the array of hydrogen bonds between the framework N and O atoms and guest H₂O molecules is represented as magenta dashed bonds. Colour scheme: Ni, green; C, grey; O, red; N, blue and H, yellow.

SION-34 crystallises in the monoclinic space group *P2₁/c*. The ASU consists of three symmetrically independent Cu^I centres (Cu1, Cu2, and Cu3), two fully deprotonated pzdc³⁻ ligands, one neutral 1HAde ligand (protonated via N1, *vide infra*), and four coordinated H₂O molecules. Cu1 has a square planar geometry and is coordinated by one N9 atom from 1HAde, one pyrazolate N2 and one carboxylate O1 atom from the same pzdc³⁻ ligand, while the fourth position is occupied by one H₂O, with the Cu1–O1W bond distance of 1.920(2) Å (Figure 33a). Cu2 is five coordinated with a tetragonal pyramidal geometry. The equatorial positions of Cu2 are occupied by two carboxylate O atoms (O3

and O5) and two N atoms (N4 and N6) from two adjacent pzdc³⁻ ligands. The axial position is occupied by the O2W atom from a H₂O molecule with a bond distance of 2.323(2) Å (Figure 33a). Cu3 is also coordinated by five donor atoms, giving rise to a trigonal bipyramid coordination geometry. The coordination environment of Cu3 is provided by N12 and O7 atoms from the pzdc³⁻ ligand, one N7 from 1HAde and two O atoms, O3W and O4W from two distinct H₂O molecules (bond distances of 2.281(2) and 1.969(2) Å, respectively). As shown in the Figure 33a, the connection of Cu1–Cu2–Cu3 via the pzdc³⁻ and 1HAde affords a 1-dimensional chain extended along the crystallographic [201] direction. The adjacent 1-dimensional chains are interlocked by the π – π stacking interactions between the pyrimidine rings of 1HAde (distance between two 1HAde ligands: 3.231(4) Å) (Figure 33b), and by a system of hydrogen bonds to form a 3-dimensional supramolecular array. Water molecules O2W, O3W, and O4W, which protrude from the surface of a nearly planar 1D chain, serve as donors in a range of hydrogen bonds to the carboxylate O-atoms of the pzdc³⁻ ligands situated above and below the chain: O2W⋯O1, 3.028(3) Å; O2W⋯O7, 2.789(3) Å; O3W⋯O2, 2.719(3) Å; O3W⋯O6, 2.705(4) Å; O4W⋯O4, 2.677(3) Å. In addition, the pyrimidine N1 and amino N10 atoms of the 1HAde ligand provide the chain with linkage to the neighbouring chains in the perpendicular direction (N1⋯O8, 2.785(3) Å; N10⋯O8, 2.911(3) Å). The dense packing of **SION-34** indicates that it is non porous.

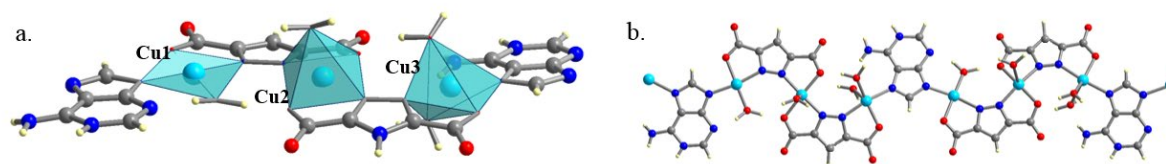


Figure 33. SION-34 (a) Coordination environment of Cu1 (square planar), Cu2 (tetragonal pyramidal) and Cu3 (trigonal bipyramid) in **SION-34**. 1HAde acts as a bridging ligand coordinated to Cu1 and Cu3 through N9 and N7 respectively. The orientation of 1HAde and pzdc³⁻ around Cu1, Cu2 and Cu3 affords a 1-dimensional chain. (b) Packing scheme showing the 3-dimensional supramolecular structure. Colour scheme: Cu, light blue; C, grey; O, red; N, blue; H, yellow.

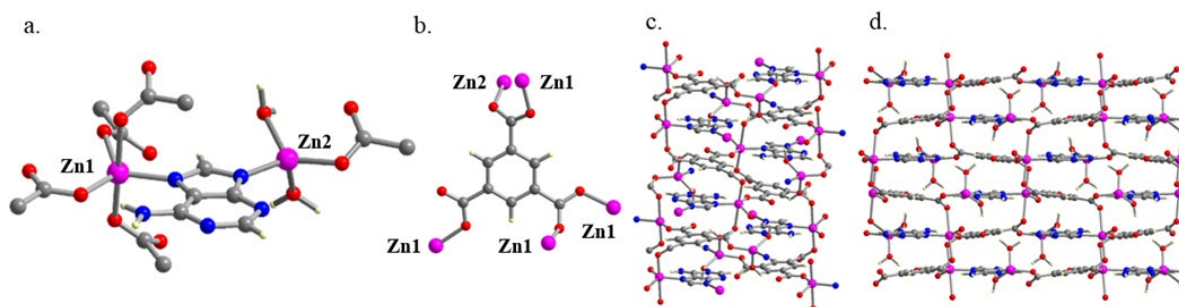


Figure 34. SION-35 (a) Coordination environments of Zn1 and Zn2; Zn1 holds a trigonal bipyramidal geometry and is coordinated via N7 of Ade⁻ and four O atoms from four adjacent btc³⁻ ligands; Zn2 is coordinated to N9 from Ade⁻, one O atom from btc³⁻ and two terminal H₂O molecules affording a distorted tetrahedral geometry, (b) Each btc³⁻ ligand is coordinated to five Zn^{II} ions, (c) and (d) The orientation of btc³⁻ and Ade⁻ (in a zig-zag fashion along c-axis and in a flat 2-dimensional layer along a- and b-axes) around Zn1 and Zn2 affords a 3-dimensional compact structure. Colour scheme: pink, Zn; grey, C; red, O; blue, N; and white, H.

SION-35 crystallises in the monoclinic space group $P2_1/c$. The ASU contains two independent Zn^{II} ions ($Zn1$ and $Zn2$), one btc^{3-} , one bidentate Ade^- , and two terminal H_2O ligands bound to $Zn2$. $Zn1$ ions adopt a trigonal bipyramidal geometry whereas $Zn2$ ions adopt a distorted tetrahedral coordination geometry. $Zn1$ and $Zn2$ are connected via the imidazolate N atoms, N7 and N9 respectively, of the Ade^- ligand (Figure 34a). The completion of the coordination sphere of $Zn1$ is provided by four carboxylate O atoms from four adjacent btc^{3-} ligands with monodentate binding mode (Figure 34a). Two terminal H_2O molecules are coordinated to $Zn2$ and the fourth position is occupied by a monodentate carboxylate O atom from the btc^{3-} ligand. These two specific coordination geometries of Zn^{II} present in **SION-35** are rarely observed in a single MOF.¹⁰⁷ Each btc^{3-} ligand is bound to five Zn^{II} atoms: four $Zn1$ and one $Zn2$ (Figure 34b). One carboxylate group of btc^{3-} is coordinated solely to $Zn1$ in a monodentate mode, whereas each of the other two groups is coordinated through a *syn-anti* coordination mode to two Zn^{II} – to two $Zn1$ and to both $Zn1$ and $Zn2$ (Figure 6b). Both btc^{3-} and Ade^- are packed in a zig-zag fashion along the *c*-axis and as in a flat 2-dimensional layer along the *b*- and *a*-axes (Figure 34c-d). Through the coordination of the carboxylate O-atoms of the btc^{3-} ligand with Zn ($Zn1-O4$: 2.373(3) Å and $Zn1-O1$: 2.113(3) Å) complemented by the system of hydrogen bonds, the Zn- Ade - btc layers are linked to each other propagating the structure into 3 dimensions. PLATON software reveals that there is no solvent accessible volume.⁶⁵

To determine the topology of **SION-35**, small rings consisting of no more than 8 covalent or dative bonds were identified in the material. This includes an 8-membered ring consisting of both $Zn1$ and $Zn2$ ions coordinated to two carboxylate groups from separate btc^{3-} ligands. This complex was reduced to a single node connected to 8 neighbours, including a 3-connected node representing the btc^{3-} ligand. The resulting 3,3,8-connected net has been reported in six previous structures as the '3,38T25' topology (Figure 45).⁴³

5.3.3. Investigation of the protonation states of adenine and location of the protonated N atoms

As previously mentioned, adenine can afford different protonation states, and it is often very challenging to accurately observe the presence of H atoms by elemental analysis or SCXRD. The protonation states of the adenine ligand within a MOF structure can sometimes be assigned based on the charge balance of the structure but the location of the protonated N atoms is not straightforward. XPS has been widely utilised as a reliable technique to assign protonation states of heterocyclic compounds.¹⁰⁸ This technique is based on the general observation that individual chemical environments/functional groups often exhibit similar ranges of binding energy values where the bonding or electronegativity is similar.¹⁰⁸ For example, the neutral 9HAde is expected to exhibit three photoemission N1s peaks corresponding to three different nitrogen environments, i.e., the one of the N1, N3, N7 atoms, as all of them have the same C=N-C environment, and therefore should have very similar binding energies, which are different from the ones of N9 (C-NH-C environment) and N10 (C-NH₂ environment). This prediction, in fact, was experimentally demonstrated by Feyer *et al.* when they studied the XPS spectra of 9HAde in the gas phase.¹⁰⁹ The N1s peaks from each N atom of adenine in the gas phase appear in the range of 398–402 eV. The three peaks correspond to N1, N3 and N7, while the other two peaks represent N9 or N10. The difference in the binding energies of the N atoms becomes less pronounced when the XPS spectrum of adenine is measured in the condensed phase, i.e., in the solid state, probably due to the influences of intermolecular interactions. Furukawa *et al.* recorded the XPS spectrum from a thick film ($>>1$ monolayer) of 9HAde on Cu(110); they fitted the N1s XPS spectrum with two components with binding energies of 399.3 eV (attributed to the imine nitrogen: N1, N3 and N7) and 400.6 eV (attributed to both protonated NH or NH₂ groups: N9 and N10).¹¹⁰ However the ratio of these two components was found to be 75:25, significantly different from the expected imine:amine ratio of 60:40. XPS measurement for 9HAde were repeated in the solid state, and we observed the same spectrum as reported by Furukawa *et al.* (Figure 35a), with a peak close to 399 eV and a high energy shoulder, and adapted the three component model that has been

successful for the gas phase. The three components represent N-environments with different numbers of N–H bonds. Component A represents imine nitrogen with no N–H bonds: N1, N3 and N7. Component B represents N9 which has one N–H bond, and component C represents N10 in the –NH₂ groups. Each component was modelled as Gaussian-Lorentzian peak. The area ratio of the components A:B:C was constrained according to the number of N atoms in 9HAde they comprised, i.e. to the ratio of 3:1:1. The full width at half maximum (FWHM) of all components was constrained to be equal in order to give a more physically realistic model. The neutral 9HAde compound was fitted with the model described, with the components A, B and C to be at binding energies of 398.49, 399.14, and 400.06 eV respectively (Figure 35a and Table 5). A difference in binding energies of 0.65 eV was observed between components A and B, and 1.57 eV between A and C. In the gas phase the corresponding differences in binding energies were 1.3 eV and 2.3 eV.¹⁰⁹ The model described, based on the chemical states expected in 9HAde, fits the experimental data well.

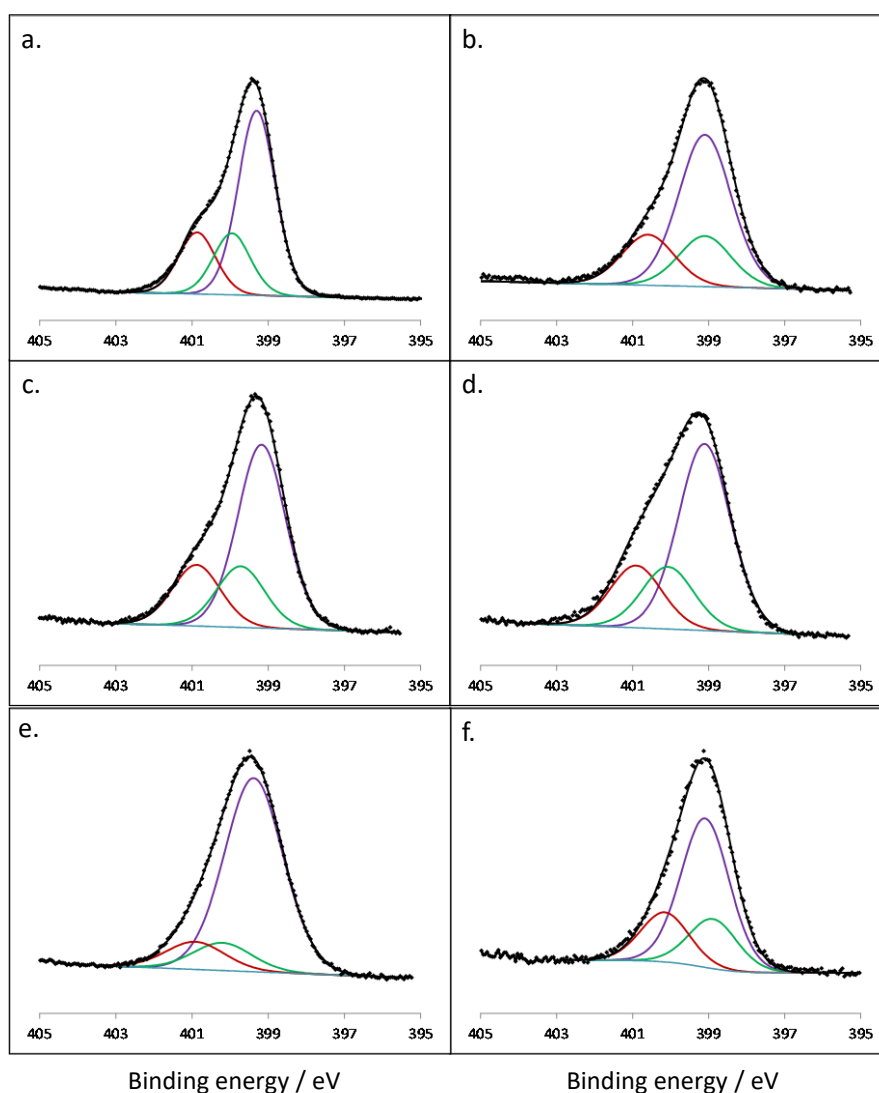


Figure 35. N1s photoelectron spectra of (a) neutral 9HAde, (b) **SION-31**, (c) **SION-32**, (d) **SION-33**, (e) **SION-34** and (f) **SION-35**, in the solid state. The peaks were fitted with the three components A:B:C. Colour scheme: Purple, component A (N1, N3 and N7); green, component B (N9); and blue, component C (N10) of adenine.

The XPS spectra of **SION-31**, **SION-32**, **SION-33**, **SION-34** and **SION-35** were subsequently collected, with 9HAd in the solid phase used to model the XPS spectra collected for each of these materials (Figure 35b-f). It should be noted that since the pzdc³⁻ ligand in **SION-34** contains different N atoms (two pzdc³⁻ ligands per Ade⁻ ligand, therefore four non-protonated N atoms per Ade⁻), these must also be included in the model for that material.¹¹¹ The binding energy of each of the fitted components for all materials was allowed to vary, and the refined values are tabulated in Table 5. It can be seen that in two cases, in **SION-31** and **SION-35**, the components A and B appear at very similar binding energies (<0.1 eV difference), whereas in **SION-32**, **SION-33** and **SION-34**, the separation was at least in the range of 0.3 eV. The appearance of these two components at the same binding energy were interpreted as the deprotonation of N9, bringing its binding energy down to coincide with the other deprotonated nitrogen environments N1, N3 and N7. On the other hand, separation between the components A and B suggests a loss of equivalence of chemical environments between one out of four following atoms: N1, N3, N7, or N9, and the remaining three. Therefore, the XPS data suggest that adenine is fully deprotonated and acts as an anionic ligand in **SION-31** and **SION-35**, whereas in **SION-32**, **SION-33**, **SION-34**, adenine is protonated, acting as a neutral ligand.

Table 5. Binding energies of fitted components for the N1s spectra. Components A, B and C were constrained to have the same FWHM, and the peak areas were constrained in the ratio A:B:C of 3:1:1.

	Binding Energy (eV) of Component		
	A	B	C
9HAd	398.49	399.14 (+0.65) ^α	400.06 (+1.57) ^α
SION-31	399.10	399.10 (+0.00) ^α	400.59 (+1.49) ^α
SION-32	399.17	399.49 (+0.32) ^α	400.58 (+1.41) ^α
SION-33	399.12	400.08 (+0.96) ^α	400.94 (+1.82) ^α
SION-34	399.04 ^β	400.69 (+1.65) ^α	400.69 (+1.65) ^α
SION-35	399.07	399.08 (+0.01) ^α	400.32 (+1.25) ^α

^α Values in brackets are the differences of binding energy from component A. ^β For **SION-34** the component A includes the N atoms in the pzdc³⁻ ligand.

At this point the structural questions for **SION-31** and **SION-35** are fully resolved: Ade⁻ is a fully deprotonated ligand, which is in agreement with the formulas provided with SCXRD, assuring the charge balance. However, the information gained by the XPS that **SION-32**, **SION-33** and **SION-34** structures contain a neutral HAd ligand is inconclusive, since the protonation of adenine may take place either on N1 or N3 for **SION-32** and **SION-34**, while the sites available in **SION-33** are N1 or N7.

First, the difference–Fourier maps of **SION-32**, **SION-33** and **SION-34** were examined and probed for additional electron density maxima. Since these structures are solved using synchrotron radiation diffraction data, the probability for peaks originating from H atoms appearing in the Fourier map was relatively high. Indeed, in case of **SION-33** and **SION-34** the Fourier maps revealed the location of H atoms. In **SION-33**, two electron density maxima were identified in the proximity of N7 (0.55 e-/Å³ 0.887 Å and 0.54 e-/Å³ 1.104 Å apart from this atom), and no maxima near N1. At the same time the peak of 0.75 e-/Å³ as far as 0.850 Å from N1 was found in the difference–Fourier map of **SION-34**, while again no peaks were found in the vicinity of N3. In both cases, N1 and N3 act as acceptors of H bonds from neighbouring guest water molecules, whose H atoms have also been localised in a similar way from the electron density map. However, the information obtained from the difference–Fourier map of **SION-32** did not allow for an unequivocal assignment of H atom positions, which might be due

to the disorder of adenine over two sites. Thus, an attentive consideration of adenine ligand geometry turned out to be necessary to determine the H-atom position in **SION-32**.

In order to substantiate our observations of different protonation states present in the adenine-based **SION-31**, **SION-32**, **SION-33**, **SION-34** and **SION-35**, and to resolve the problem of localisation of the protonated N-sites in **SION-32**, **SION-33**, and **SION-34**, we systematically studied the bond angles of adenine in these structures. As a reference, the observation made by Singh was used that in 6-membered rings of purine derivatives the C–N–C angles fall in the range of $125\pm3^\circ$ for the protonated N atoms, and of $116\pm3^\circ$ when the H atom is absent.¹⁰¹ For 5-membered rings, a similar relation states that if N7 is protonated, then this 5-membered ring is more symmetrical, whereas in case of deprotonation of N7, the C5–N7–C8 angle increases by $3.8\text{--}5^\circ$.¹¹² The respective bond angles for **SION-31**, **SION-32**, **SION-33**, **SION-34** and **SION-35** are listed in Table 6.

Table 6. Bond angles (in degrees) calculated from the crystal structures of **SION-31**, **SION-32**, **SION-33**, **SION-34** and **SION-35**.

	C2–N1–C6	C2–N3–C4	C5–N7–C8	C4–N9–C8
SION-31	119.8(2)	112.9(2) ^a	103.1(2) ^a	103.7(2) ^a
SION-32	118.1(13)	117.4(14)	110.2a,b	106.1a,b
SION-33	118.3(7)	111.5(8) ^a	106.5(7)	104.6(7) ^a
SION-34	124.6(3)	113.7(3)	102.9(3) ^a	103.2(3) ^a
SION-35	119.5(4)	112.0(4)	104.3(3) ^a	104.8(3) ^a

^a Metal coordinated to the N-atom. ^b No uncertainty, part of the idealised 5-membered ring.

A survey of the Cambridge Structural Database (CSD version 5.38)⁶⁶ was performed and from the 61 adenine-based MOF crystal structures deposited with the CSD (Table 10), the bond angle values were extracted, and presented in the form of histograms (Figure 36). In many cases, the protonation of N-sites of adenine is excluded, as they bind to the neighbouring metal centres by means of coordination bonds. In all other cases the N-sites of adenine were classified as protonated or non-protonated, and marked respectively as red and blue bars in Figure 36. For the N1 atom, the span of the C6–N1–C2 angle was found to equal $119\pm3^\circ$ for the deprotonated sites, and the only structure with this site protonated, [Cd(1HAde)(SO₄)],¹¹³ was reported with the bond angle of 124.095° (Figure 36a). Considering the bond angle values for **SION-31**, **SION-32**, **SION-33**, **SION-34** and **SION-35**, we observe that the C6–N1–C2 angle has similar values for **SION-31**, **SION-32**, **SION-33**, and **SION-35**, while such angle in **SION-34** is noticeably larger. Since the former group of angles fall in the range characteristic for deprotonated N1 sites, and the latter one is closer to the literature account on the N1 protonated adenine MOF, the data suggest that in **SION-31**, **SION-32**, **SION-33**, and **SION-35** the adenine ligand is N1 deprotonated, while in **SION-34** the adenine ligand is protonated through N1 (Table 6). No published structures were found to be protonated at the N3, and all C2–N3–C4 angles fall in the range of $112\pm2^\circ$ (Figure 36b). Respective angles for **SION-31**, **SION-33**, **SION-34** and **SION-35** also fall in this range, which confirms the deprotonation of adenine on N3 (Table 6). The respective angle for **SION-32**, however, is visibly larger (Table 6). No literature reference is available so we resorted to *ab initio* calculations to confirm the location of protonation. For **SION-32** and **SION-34**, i.e., the two MOFs where the protonation may take place on N1 or N3, we simulated and DFT optimised the respective N1 and N3 protonated structures, thus exploring all possibilities of protonation. The angles found in these DFT relaxed structures are listed in Table 7. Comparison between these data and the angles found experimentally (Table 6) confirms the N3 deprotonation of

adenine in **SION-34** (DFT: C2–N3–C4 of 114.46° in the N3 deprotonated and 117.52° in the N3 protonated structure; SCXRD: C2–N3–C4 of 113.7(3)°), and strongly suggests the protonation of **SION-32** on N3 (DFT: C2–N3–C4 of 113.97° in the N3 deprotonated and 117.03° in the N3 protonated structure; SCXRD: C2–N3–C4 of 117.7(13)°). In addition, the calculations report an energy difference of 15.4 kcal per mol of HAde residuals in favour of N3 protonation for **SION-32**. Meanwhile, in **SION-34** the N1 protonation is favoured by 13.3 kcal/mol, and its DFT-optimised angle distributions for N1 protonated (124.45°) and N3 deprotonated (114.46°) are closer to those reported for the structure in [Table 6](#). Thus based on insurmountable evidence, the adenine ligand in **SION-34** is N1 protonated, while in **SION-32** is clearly N3 protonated. We note that **SION-32** was previously reported as an N1 protonated structure,¹⁰⁶ however, in that study the complicated disorder of adenine was not fully resolved (probably due to the low quality of data recorded at room temperature), thus not allowing for the precise geometrical analysis. In terms of the 5-membered ring present in the adenine ligand of the CSD reported MOFs, two maxima in the distribution of the C5–N7–C8 angle were observed: the first one at 103±1° for the non-protonated, and the second one at 107±2° for the protonated N7 sites ([Figure 36c](#)). In the first case, an unexpectedly high value of this angle found at the non-protonated N7 site, 107.964°, originated from [Co₇(H₂O)₄(Ade)₂(μ₃-OH)₆(sip)₂],¹¹⁴ an example of structure with the adenine ligand disordered over two sites. In the second case, the structures with extremely high (114.52°, [Co₃(μ₆-TCPB)(μ₄-H₂TCPB)(7HAde)₂·H₂O]^{100o} and low (101.109°, [Cd(7HAde)₂Cl₂])¹¹⁵ C5–N7–C8 angle values turned out to have been reported with relatively high refinement indicators (*R*₁ = 12.7 % and 15.1 %, respectively). The C5–N7–C8 angle in **SION-33** is very close to the second maximum ([Table 6](#)), and DFT relaxation of the N7 protonated structure yields C5–N7–C8 and C6–N1–C2 angle values that agree well with the observed angles in the crystal structure ([Table 7](#)). The relative energy is 12.9 kcal/mol in favour of N7 vs N1 protonation. From this, we reason that the adenine ligand in **SION-33** is protonated on N7. Shift towards higher values in case of the N9 site protonation is also observed in the distribution of the C4–N9–C8 angles found in the reported structures ([Figure 36d](#)). The protonation states and coordination modes of adenine within the MOFs presented in this paper are shown schematically in [Figure 37](#), while the trends of adenine C–N–C bond angles revealed by us within the literature adenine-based MOFs are summarised in [Table 8](#). It should be noted that the statistical population considered in this survey was relatively small, which on the one hand indicates the need of use of supplementary methods (e.g. XPS and DFT) to unequivocally determine the protonation states of adenine in MOFs, but on the other hand highlights the demand for new adenine-based MOFs to be synthesised.

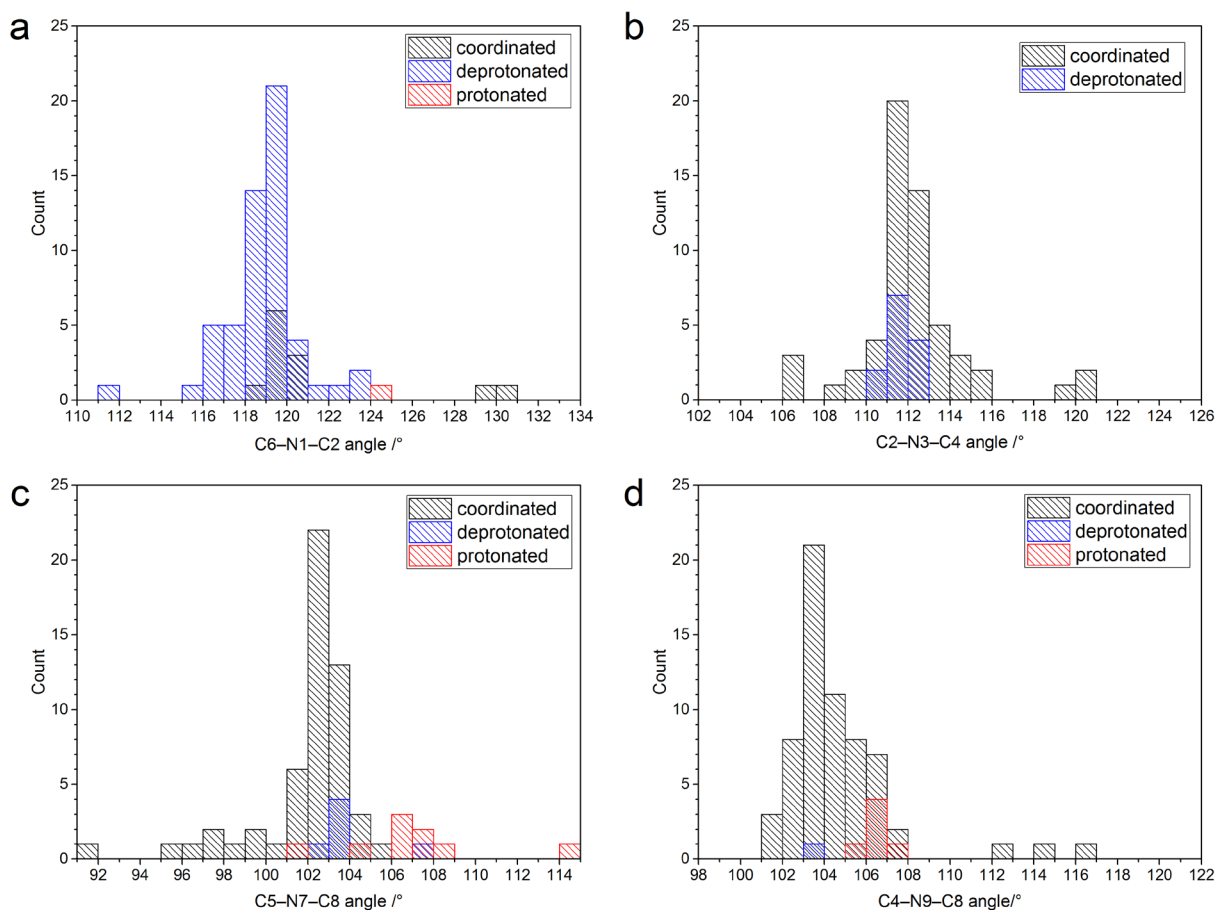


Figure 36. Distribution of the (a) C6–N1–C2, (b) C2–N3–C4, (c) C5–N7–C8, and (d) C4–N9–C8 bond angle values in the adenine based MOF structures found in the Cambridge Structural Database.

Table 7. Bond angles and relative energies of DFT optimised structures of **SION-32**, **SION-33**, and **SION-34** simulated with all probable protonation schemes. The energetically favoured site of N protonation is given in each ΔE column entry in parentheses.

	C6–N1–C2 (deg)	C2–N3–C4 (deg)	C5–N7–C8 (deg)	ΔE (kcal/mol)
SION-32 , N1-protonated	123.50	113.97		15.44 (N3)
SION-32 , N3-protonated	120.74	117.03		
SION-33 , N1-protonated	123.21		102.32	12.90 (N7)
SION-33 , N7-protonated	119.55		107.84	
SION-34 , N1-protonated	124.45	114.46		13.29 (N1)
SION-34 , N3-protonated	120.96	117.52		

Table 8. Regularities in the C–N–C angle values of adenine ligand within the adenine-MOF crystal structures reported in the literature.

	N site non-protonated	N site protonated
C2–N1–C6	119±4 °	124± 1°
C2–N3–C4	112±2 °	NA
C5–N7–C8	103±1 °	107±2 °
C4–N9–C8	103±1 °	106±1 °

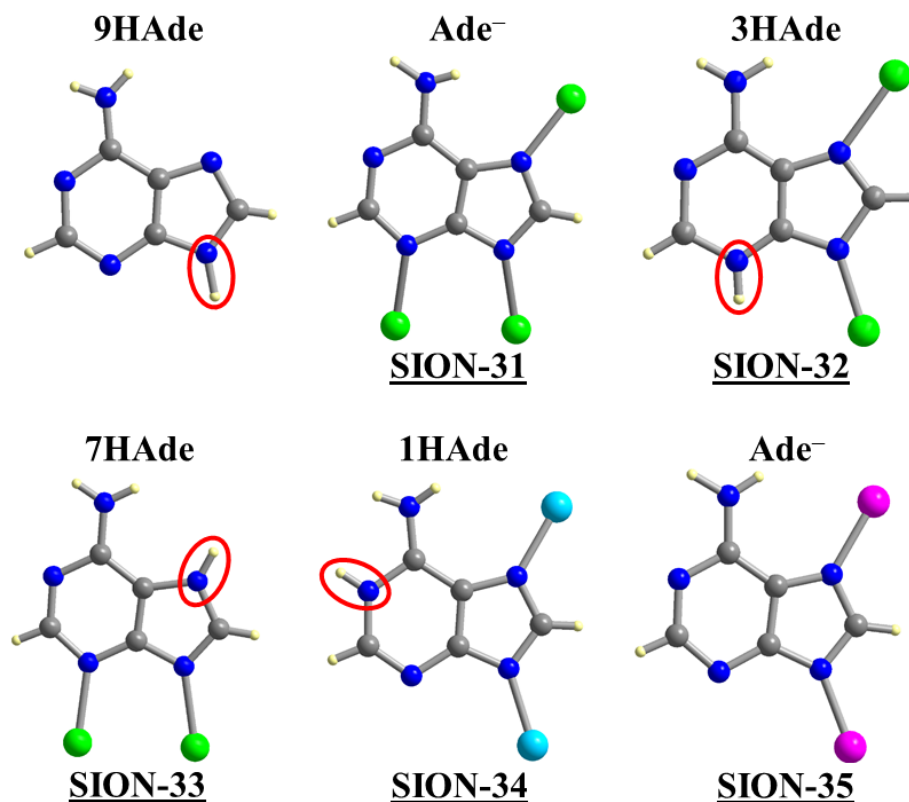


Figure 37. Protonation states and coordination modes of adenine within **SION-31**, **SION-32**, **SION-33**, **SION-34** and **SION-35**.

5.4. Conclusions

By varying the synthesis conditions, five adenine-based MOFs were isolated, and their crystal structures were solved using SCXRD. **SION-31** and **SION-32** were found to be 2-dimensional layered structures, **SION-33** and **SION-34** are based on 1-dimensional chains (or 3-dimensional supramolecular assemblies), while **SION-35** is a 3-dimensional compact framework. A variety of metal (Ni^{II} , Cu^{II} and Zn^{II}) coordination geometries as well as different coordination binding modes of the ligands used (H_3btc , H_2ipa , H_4btec , H_3pzdc , 9HAde) resulted in a range of structural topologies.¹¹⁶ The phase purity of each material was confirmed by PXRD, elemental analysis, and their thermal stability was checked by TGA.

Particular interest of our study has been drawn upon the coordination, protonation and location of protonated N atoms of adenine present in all materials presented herein. XPS has successfully been used to determine the protonation of adenine in **SION-31**, **SION-32**, **SION-33**, **SION-34** and **SION-35**. The N1s photoelectron peaks were deconvoluted to three components, and the binding energy shifts between them showed significantly different values in the spectra of fully deprotonated **SION-31** and **SION-35**, and those of protonated **SION-32**, **SION-33** and **SION-34**. The protonation sites of adenine, derived from the difference–Fourier maps, were further confirmed by the study of C–N–C bond angles supported by the literature survey. As previously observed by Singh, the protonation of a given N site gives rise to an increase of the adjacent C–N–C bond angle, which is further supported by the DFT calculations. This strategy can be utilised to other MOF materials with very complex formulas where the balance of the charge of the formula is proven to be challenging.

5.5. Appendix

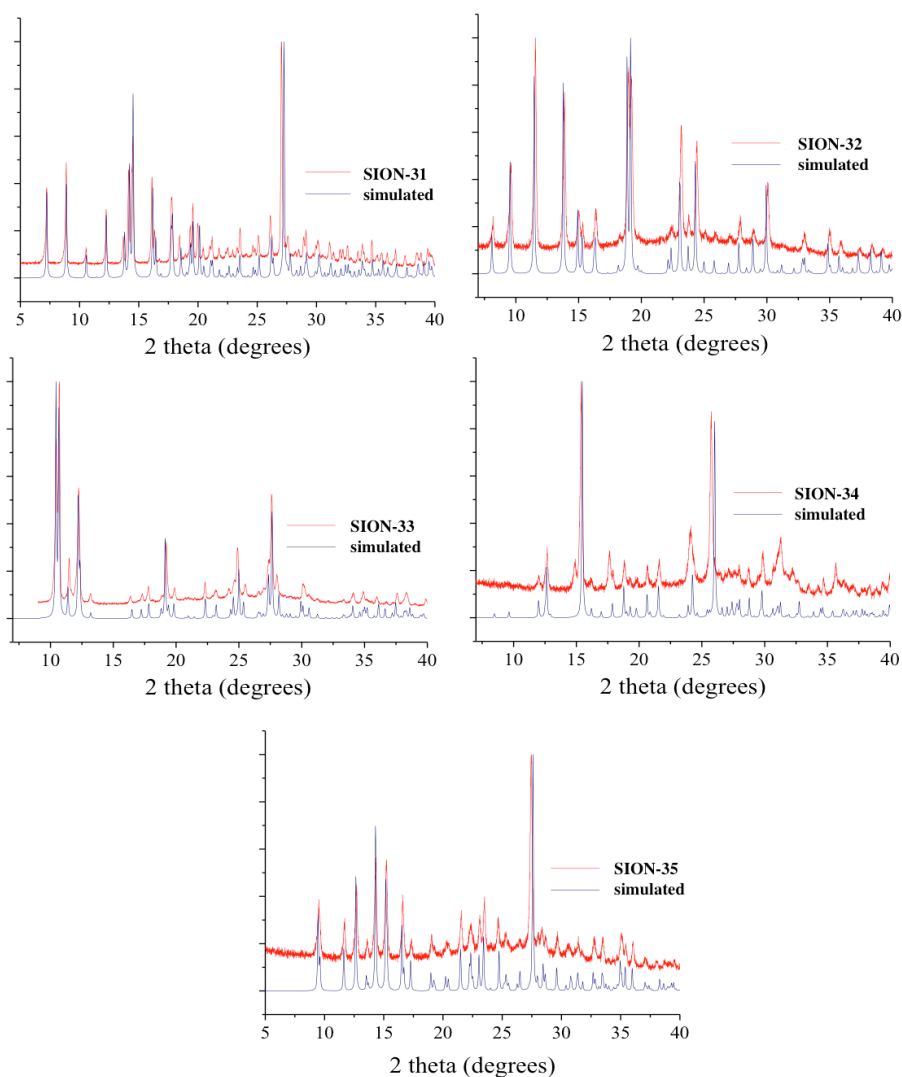


Figure 38. The comparison of the experimental (red) with the simulated PXRD (blue) for **SION-31**, **SION-32**, **SION-33**, **SION-34** and **SION-35** confirm that these frameworks can be isolated as phase pure.

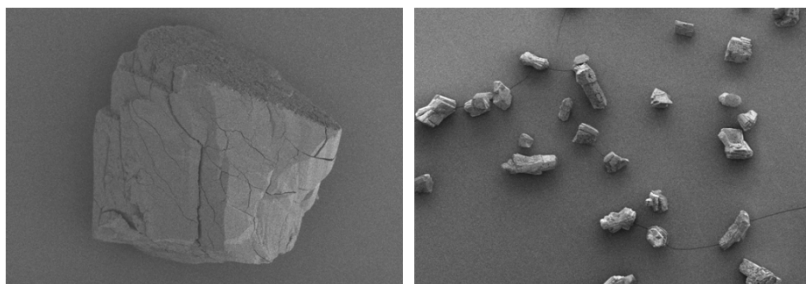


Figure 39. SEM images of **SION-31** showing the morphology of the isolated crystals and confirming the homogeneity of the material.

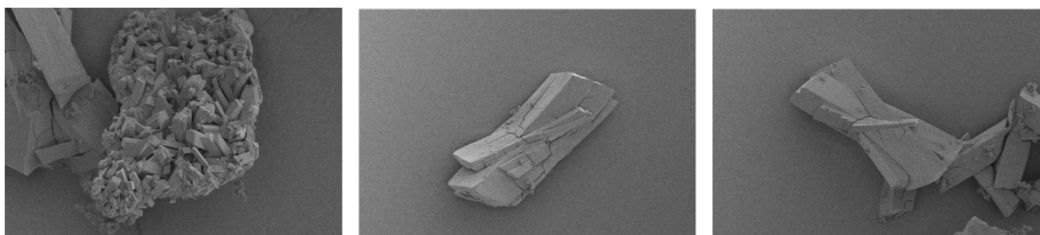


Figure 40. SEM of **SION-32** confirming the homogeneity of the bulk material.

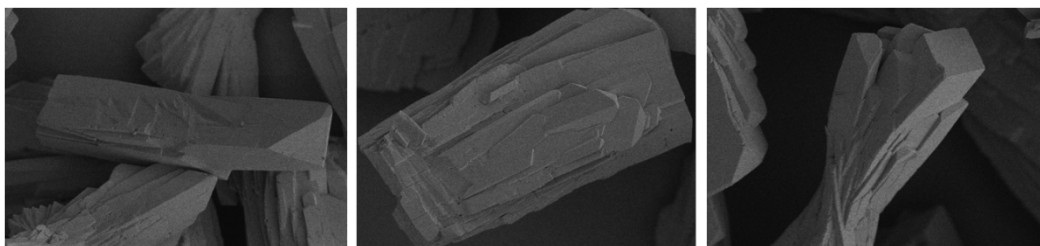


Figure 41. SEM images of **SION-35** revealing that the morphology of the crystals formed is based upon needles.

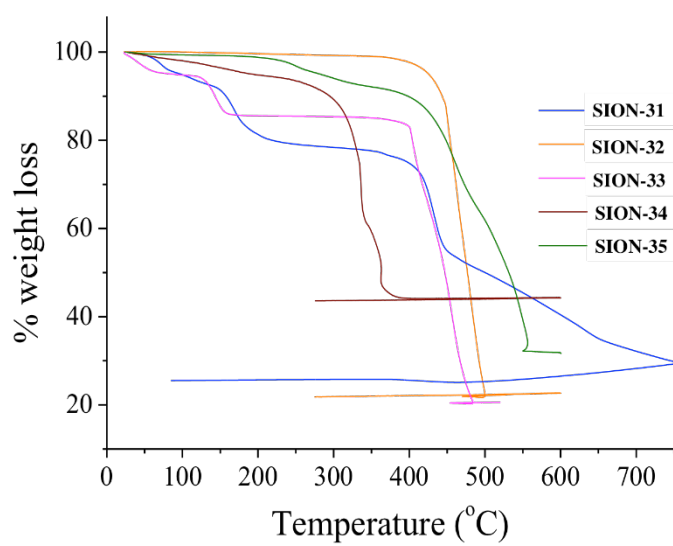


Figure 42. TGA data for **SION-31**, **SION-32**, **SION-33**, **SION-34** and **SION-35**.

Table 9. Summarised weight losses (corresponding to the guest and coordinated H₂O molecules) observed from TGA and elemental analysis and the temperature range that this loss occurs.

MOF	% weight loss corresponding to the loss of guest and bound to metal H ₂ O molecules (TGA)	Temperature of the loss of H ₂ O molecules (°C)	% weight loss corresponding to the loss of guest and bound to metal H ₂ O molecules (CHN analysis)
SION-31	22.5	30 – 250	23.4
SION-32	0.4	30 – 450	0.05
SION-33	14.4	30 – 165	11.3
SION-34	8.1	30 – 280	10.0
SION-35	8.4	210 – 370	9.1

Table 10. Reference codes of the entries from the Cambridge Structural Database containing adenine-based MOFs for which the C2–N1–C6, C2–N3–C4, C5–N7–C8, and C4–N9–C8 bond angles were calculated.

ANEHEI	EKEGUX	LAFSUH	TEJLOL
ANEHIM	ELOZOW	LAFTAO	TEPGUS
BEYRUU	GEFWOF	MEJQEZ	TOCJAY
BEYSAB	GEFXEW	MEJQID	TOCJEC
BEYSEF	HOYLEO	MEJQOJ	UNEZAP
BULZIS	HUWFIQ	NUDLAA	UXUZAP
BULZUE	INASAT	OKISEH	WIZDUG
CARCEE	INAVUQ	PUCFEZ	WIZFAO
COVJAA	INAWAX	QUFKEJ	WIZFES
COVJEE	IVILEG	QUFKIN	WUBLIQ
CUDPOI	IZUMUM	RUGKOV	WUNTIK
CUDPUO	IZUNAT	SAPBIW	WUVFIE
CUDQAV	KEBPEO	SEGCUD	XACZEH
CUDQEZ	KEBPOY	SIRGEG	YUVSUE
DUPVER	KEBPUE	SOLCUS	ZIWLLO
			ZUGDEM

Table 11. Crystal data and structure refinement for **SION-31**, **SION-32**, **SION-33**, **SION-34** and **SION-31**.

Identification code	SION-31	SION-32	SION-33	SION-34	SION-35
Empirical formula	C ₁₄ H ₂₃ N ₅ Ni ₂ O ₁₄	C ₁₃ H ₉ N ₅ NiO ₄	C ₁₀ H ₁₂ N ₅ NiO ₇	C ₁₅ H ₁₅ Cu ₃ N ₉ O ₁₂	C ₁₄ H ₁₁ N ₅ O ₈ Zn ₂
Formula weight	602.79	357.96	372.96	703.98	508.02
Temperature/K	100(2)	100	100	100	100
Crystal system	monoclinic	tetragonal	triclinic	monoclinic	monoclinic
Space group	P2 ₁ /n	P4 ₂ /nmc	P-1	P2 ₁ /c	P2 ₁ /c
a/Å	6.6387(10)	15.4355(4)	8.2247(14)	10.4204(2)	9.3730(3)
b/Å	19.882(3)	15.4355(4)	9.5117(16)	10.42630(10)	12.9344(4)
c/Å	15.682(2)	11.5831(3)	10.2269(17)	19.2543(3)	12.9133(3)
α/°	90	90	111.834(15)	90	90
β/°	99.066(2)	90	107.776(15)	94.1180(10)	99.761(2)
γ/°	90	90	100.449(14)	90	90
Volume/Å ³	2044.1(5)	2759.73(16)	666.7(2)	2086.51(6)	1542.87(8)
Z	4	8	2	4	4
ρ _{calc} /g/cm ³	1.959	1.723	1.858	2.241	2.187
μ/mm ⁻¹	1.931	1.658	1.51	3.123	3.179
F(000)	1240	1456	382	1404	1016
Crystal size/mm ³	0.40 × 0.30 × 0.20	0.1 × 0.02 × 0.02	0.07 × 0.03 × 0.02	0.06 × 0.05 × 0.02	0.1 × 0.02 × 0.01
Radiation	MoKα (λ = 0.71073)	synchrotron (λ = 0.7519)	synchrotron (λ = 0.72179)	synchrotron (λ = 0.71420)	synchrotron (λ = 0.72179)
2θ range for data collection/°	3.34 to 54.2	3.948 to 56.028	5.084 to 50.294	4.262 to 61.346	4.478 to 51.922
Index ranges	-8 ≤ h ≤ 8, 0 ≤ k ≤ 25, 0 ≤ l ≤ 20	-11 ≤ h ≤ 11, -18 ≤ k ≤ 18, -14 ≤ l ≤ 14	-9 ≤ h ≤ 9, -10 ≤ k ≤ 10, -11 ≤ l ≤ 11	-13 ≤ h ≤ 13, -14 ≤ k ≤ 14, -26 ≤ l ≤ 26	-10 ≤ h ≤ 10, -14 ≤ k ≤ 14, -15 ≤ l ≤ 15
Reflections collected	13334	11712	2360	15087	5730
Independent reflections	6990 [R _{int} = 0.0258, R _{sigma} = N/A]	1369 [R _{int} = 0.0546, R _{sigma} = 0.0219]	1197 [R _{int} = 0.0180, R _{sigma} = 0.0274]	4852 [R _{int} = 0.0299, R _{sigma} = 0.0301]	2186 [R _{int} = 0.0195, R _{sigma} = 0.0241]
Data/restraints/parameters	6990/29/384	1369/125/145	1197/79/156	4852/74/370	2186/102/264
Goodness-of-fit on F ²	1.058	1.176	1.083	1.093	1.051
Final R indexes [I>=2σ (I)]	R ₁ = 0.0355, wR ₂ = 0.0925	R ₁ = 0.0801, wR ₂ = 0.1753	R ₁ = 0.0852, wR ₂ = 0.2368	R ₁ = 0.0389, wR ₂ = 0.0910	R ₁ = 0.0369, wR ₂ = 0.0973
Final R indexes [all data]	R ₁ = 0.0437, wR ₂ = 0.0960	R ₁ = 0.0825, wR ₂ = 0.1763	R ₁ = 0.0879, wR ₂ = 0.2415	R ₁ = 0.0440, wR ₂ = 0.0937	R ₁ = 0.0408, wR ₂ = 0.0997
Largest diff. peak/hole/ e Å ⁻³	0.81/-0.71	0.93/-0.64	0.88/-1.07	1.10/-0.52	0.93/-0.87
CCDC	1574033	1576594	1576595	1576596	1576597

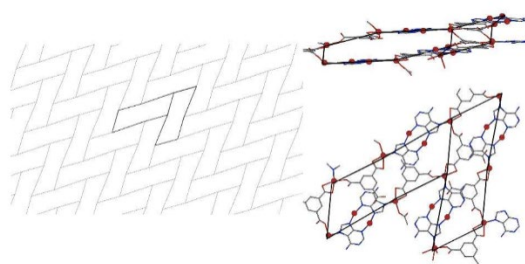


Figure 43. Topological analysis of **SION-31** revealed a *hcb* hexagonal plane net (6,3).

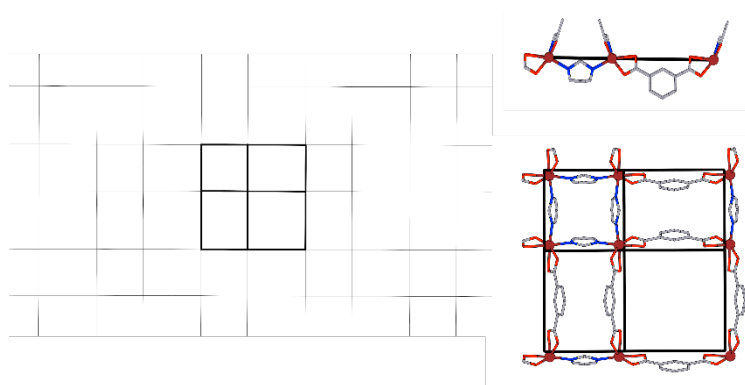


Figure 44. Topological analysis of **SION-32** revealed a *sql* tetragonal plane net.

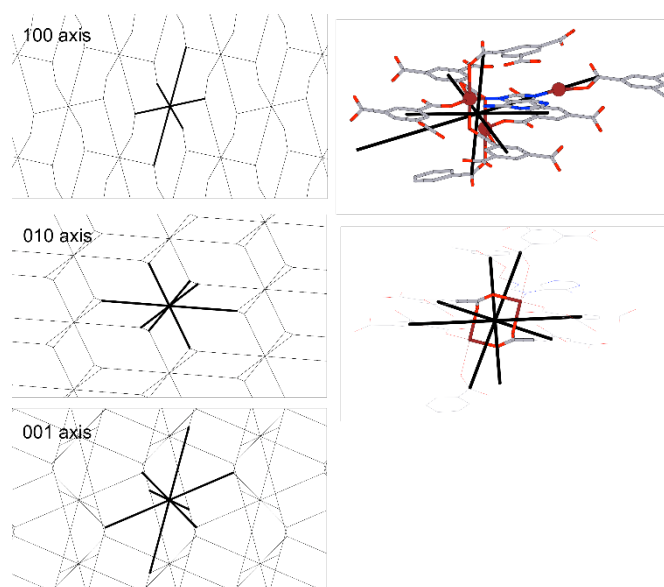


Figure 45. Topological analysis of **SION-35** revealed a 3,3,8-c net with stoichiometry $(3\text{-c})_2(3\text{-c})_2(8\text{-c})$; 3-nodal net. 8-coordinated vertex consists of two Zn atoms bridged by two carboxylate groups from separate BTC ligands. The remaining 3-coordinate vertices are located at the BTC ligands.

6. Tuneable CO₂/CH₄ separation performance in a bi-porous flexible Ca^{II}-based MOF

This chapter has been adapted from: A. Gladysiak, K. S. Deeg, I. Dovgaliuk, A. Chidambaram, K. Ordiz, P. G. Boyd, S. M. Moosavi, D. Ongari, J. A. R. Navarro, B. Smit, and K. C. Stylianou, *ACS Appl. Mater. Interfaces*, **10**, 36144–36156, (2018).

My contribution to this work consisted in the synthesis, SCXRD analysis, and characterisation of the discussed material, execution of the *in-situ* SCXRD and PXRD experiments using synchrotron radiation, analysis and plotting of the experimental data (including adsorption isotherms and breakthrough curves), and participation in writing of the manuscript.

6.1. Introduction

Efficient gas mixture separations are a continued challenge for the modern chemical industry. While classical separation techniques, including cryogenic distillation and low-temperature chemical absorption in aqueous alcoholamine and glycol derivatives solutions, are widely in use,¹¹⁷ they are energetically costly and present environmental issues, primarily due to the thermal solvent degradation and possible NO_x emission.¹¹⁸ Among different solutions being developed as alternatives to these techniques, pressure swing adsorption using a range of porous adsorbents, characterised by lower investment costs and lower complexity, is showing great promise.¹¹⁹

The removal of CO₂ from gas streams containing primarily CH₄ is one of the most important gas separation processes worldwide. Natural gas, an important fuel and chemical raw material, contains variable amounts of CO₂, typically 5–15%, but in some wells its content may reach 40%.¹²⁰ This percentage is normally higher in biogas, a mixture of gases produced by anaerobic fermentation of organic wastes (when these wastes originate from landfill deposits the term ‘landfill gas’ is used), and can reach 30–40%.¹²¹ Removal of CO₂ from these gases is necessary to meet both technological (lowering the risk of pipeline corrosion) and economic (raising the value of the gas being transported) standards.¹²² Nevertheless, engineering porous materials for CO₂/CH₄ separation is challenging due to the close similarity of these two molecules. They are both characterised by zero dipole moment, and their kinetic diameters (CO₂: 3.3 Å; CH₄: 3.8 Å)¹²³ and polarizabilities (CO₂: 2.63·10⁻⁴⁰ J⁻¹·C²·m²; CH₄: 2.60·10⁻⁴⁰ J⁻¹·C²·m²)¹²⁴ are comparable. Indeed, their quadrupole moments make the only appreciable difference between CO₂ ($q_{\text{CO}_2} = 13.4 \cdot 10^{-40} \text{ C}\cdot\text{m}^2$) and CH₄ ($q_{\text{CH}_4} = 0$)¹²³ in terms of physical properties. This is the reason why chemical interactions between the pore surface and an adsorbate are by far more exploited in separation processes. CO₂ is an inorganic acid anhydride, and its lone electron pairs are known to interact with open metal sites,¹²⁵ negatively charged species¹²⁶ and amines adsorbed on MOF surfaces.¹²⁷ On the other hand, CH₄ is chemically inert, and interacts with adsorbents only through weak dispersion interactions.¹²⁸

Capitalising on modular synthesis routes of MOFs, their structural tunability and possibility of pore functionalisation, many MOFs have been shown to efficiently separate gas mixtures. Bi-porous MOFs, in particular, have been shown to exhibit interesting behaviour especially for gas separations,¹²⁹ while bi-porous coordination networks have been studied for their interesting behaviour for separations¹³⁰ and storage of differing species.¹³¹ Such MOFs, only a handful of which have been reported, offer different chemical environments within a single material, leading to complex and varied structure-adsorbate chemical interactions that can be harnessed for gas separations and other applications.

Thus we emphasise the importance of fully understanding and characterizing such materials, as we have undertaken for the MOF introduced here.

In this account, we present the synthesis of a novel bi-porous MOF based on Ca^{II} and a tetracarboxylate ligand TBAPy^{4-} (Figure 46) featuring two chemically distinct types of pores: hydrophobic and hydrophilic. Owing to judicious choice of conditions, we gained access to both the fully activated material and the partially activated material with exclusively hydrophobic pores activated. The difference of the sorption behaviour of these materials was rationalised in terms of different molecular interactions between the partially or the fully activated material and CO_2 or CH_4 , and the selectivity of CO_2 over CH_4 was studied with breakthrough experiments.

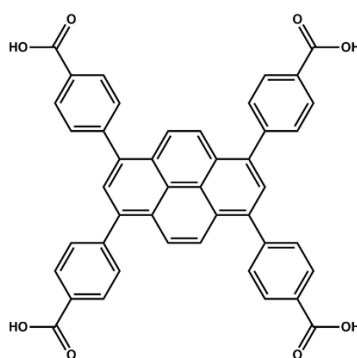


Figure 46. Structural formula of H_4TBAPy .

6.2. Experimental section

6.2.1. Synthesis of **SION-8**

The ligand, 1,3,6,8-tetrakis(*p*-benzoic acid)pyrene (H_4TBAPy), was synthesised using the procedure reported elsewhere.¹³² The reaction between 10 mg (0.0680 mmol) of $\text{CaCl}_2 \cdot 2\text{H}_2\text{O}$ and 10 mg (0.0146 mmol) of H_4TBAPy in the solution the solution composed of 2 mL of *N,N*-dimethylformamide (DMF), 1 mL of H_2O and 80 μL of HCl (techn., 32%) at 393 K for 72 hours resulted in 11.85 mg (0.0126 mmol, 86.0% yield) of $[\text{Ca}_2(\text{TBAPy})(\mu_2\text{-OH}_2)_2] \cdot 2\text{DMF}$ in the form of yellow block-shaped crystals suitable for single-crystal X-ray diffraction (SCXRD) analysis.

6.2.2. SCXRD analysis

The crystals were analysed with monochromatic synchrotron radiation on the single-crystal diffractometer equipped with a Pilatus2M 2-dimensional CCD detector at the BM01 Beamline of the ESRF.¹³³ The crystal structure was solved with SHELXT⁹⁰ and refined with SHELXL⁶⁰ programs implemented in the Olex2 program suite.⁹¹ Structure simplification and net classification was performed using the TOPOS Pro program suite.¹³⁴ Volume and electron count of the structural voids were calculated with the SQUEEZE procedure of the PLATON program suite;⁶² the excess electron density was further interpreted in terms of number of DMF molecules based on the number of electrons of a DMF molecule ($\text{C}_3\text{H}_7\text{NO}$, 40 e^-). The same program was also used to calculate the crystal-derived pore volume.

In an *in-situ* SCXRD experiment, a single crystal of **SION-8** was stuck onto the top of the glass fibre and enclosed in an environment cell constructed upon a sealed glass capillary connected to the

pressure control system. The experimental set-up was complemented with a temperature attachment allowing for flexible changes of temperature.

- a) During the stepwise activation experiment, vacuum, as low as 10^{-3} mbar, was achieved using a molecular vacuum pump. At each temperature point in the 300–400 K range the diffraction data were collected, which allowed for the structure solution and further refinement.
- b) During the variable-pressure (VP) experiments, increasingly higher pressures of N_2 (0–6000 mbar), CO_2 (0–14000 mbar), and CH_4 (0–5000 mbar) were exerted on a studied single crystal. Constant temperature was maintained (90 K for N_2 , and 300 K for CO_2 and CH_4), while the pressure was changed before each data collection point. Excess electron density found in the refined structures was interpreted in terms of number of gas molecules based on their electron counts (N_2 : 14 e^- , CO_2 : 20 e^- and CH_4 : 10 e^-).

6.2.3. VT and VP PXRD analysis and complementary bulk characterisation

Powder X-ray diffraction (PXRD) patterns were recorded using synchrotron radiation at BM01 and BM31 from SNBL (ESRF in Grenoble, France). The samples were packed into glass capillaries, and the PXRD patterns were measured at temperatures controlled with a Cryostream 700+ nitrogen blower. In the variable-temperature (VT) PXRD experiment ($\lambda = 0.75190$ Å) bulk powder of as-synthesised **SION-8** was heated at a rate of 5 K/min from 100 K to 500 K. In the VP PXRD experiment, the glass capillary was filled with **SION-8F** and attached to the gas system described above for single-crystal experiment. Le Bail fits were performed with the FullProf program suite,¹³⁵ wherein the unit-cell parameters were refined in the space group *Pbam*.

6.2.4. Sorption studies

Gravimetric gas sorption measurements were performed using the Intelligent Gravimetric Analyzer Instrument (IGA) from Hiden. Values of Q_{st} at zero loading were calculated from Henry's constants derived from the single-component adsorption isotherms recorded at different temperatures following a method published previously.⁷³

6.2.5. Breakthrough experiments

In a typical experiment, the **SION-8P** or **SION-8F** bulk powder was packed into a stainless steel column characterised by the length of 12 cm and internal diameter of 0.5 cm. Following the *in-situ* activation under the constant flow of helium, the fixed bed of the material was subjected to one of the CO_2/CH_4 gas mixtures at 1 bar and at a constant flow of 10 mL/min. Relative molar ratios of gases passing through the fixed bed were achieved with mass flow controllers, and the column was thermostated at a desired temperature. Composition of the outlet gas mixture was monitored with a Mass Spectrometer Gas Analysis System. Regeneration procedure was carried out before each new experiment. Adsorption capacities of **SION-8P** and **SION-8F** were calculated by integrating breakthrough curves following the procedure reported elsewhere.¹³⁶ Dynamic breakthrough selectivities α were calculated using the expression $\alpha = (q_{CO_2}/q_{CH_4})/(x_{CO_2}/x_{CH_4})$, where q = adsorption capacity (mmol/g), x = molar ratio, reported elsewhere.²⁵

6.3. Results and discussion

6.3.1. Crystal structure description

Self-assembly of Ca^{II} ions with the H_4TBAPy ligand in an acidified mixture of DMF and water gave rise to the crystallisation of $[\text{Ca}_2(\text{TBAPy})(\mu_2\text{-OH}_2)_2]\cdot 2\text{DMF}$, hereafter **SION-8**, in the orthorhombic space group $Pbam$, as deduced from SCXRD analysis (Table 16). The asymmetric unit comprises a quarter of fully deprotonated TBAPy^{4-} ligand, a half of a Ca^{II} atom (Ca1 sitting on a special position with the Wyckoff site multiplicity reduced by a factor of 2), and a half of H_2O molecule (Figure 53). The structure of **SION-8** is based on infinite 1-dimensional Ca-O chains extending along the a -axis (Figure 47a); O atoms in the chain originate from μ_2 -bridging water molecules and from carboxylate functionalities of the ligand. The chains are connected to each other via TBAPy^{4-} , which coordinates to Ca^{II} in $\eta^1:\eta^2$ bridging mode (Figure 47a): while O1 bonds to only one Ca1 atom, O2 is coordinated to two subsequent Ca1 atoms within the Ca-O chain. The overall coordination number of Ca^{II} is 8, and the geometry of its coordination environment can be described as biaugmented trigonal prism (Figure 54). Topologically, Ca atoms can be considered as 6-coordinated nodes (two Ca1-O2 links can be severed in order to make the ligands conceptually $\eta^1:\eta^1$ bridging), bridging H_2O molecules as 2-coordinated nodes simplified to 2-coordinating links, and TBAPy^{4-} ligands as 8-coordinated nodes. Following this description, the underlying net of **SION-8** is found to be of the *sea* type (Figure 55).

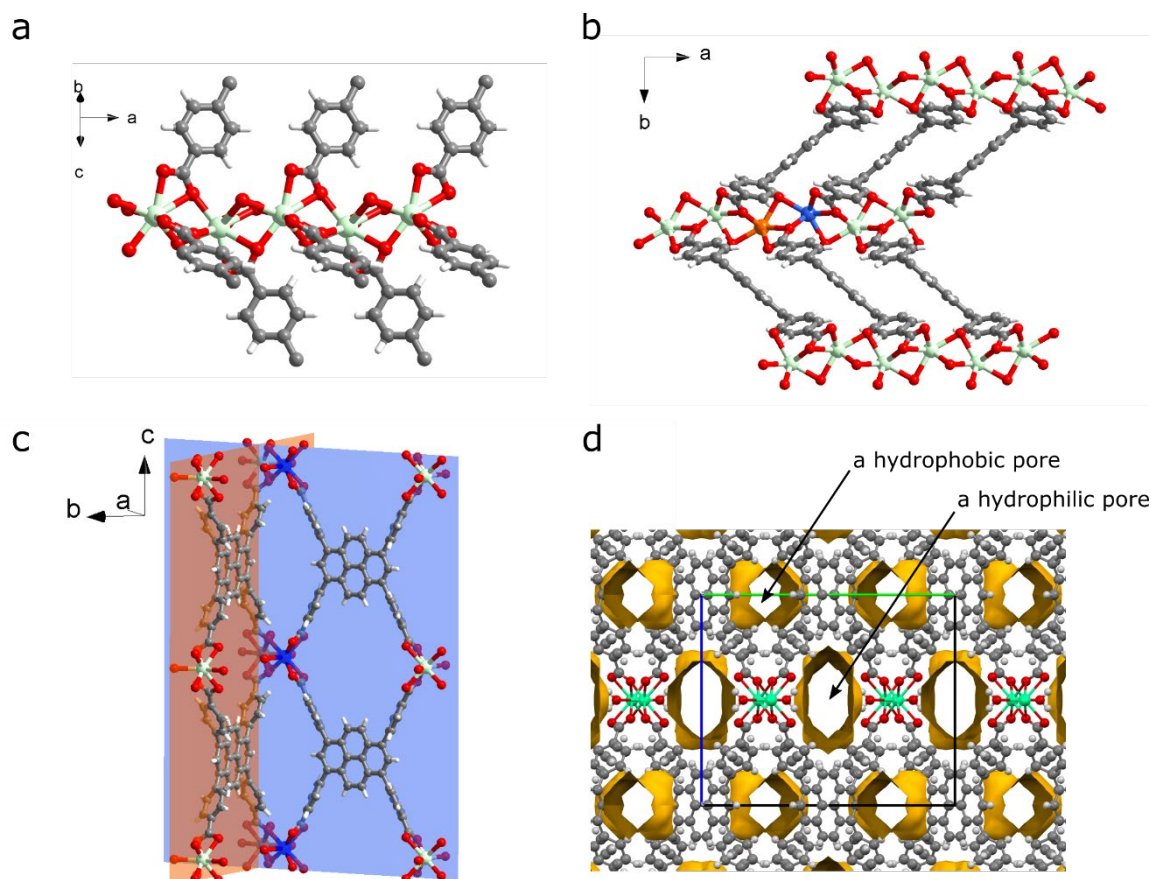


Figure 47. (a) A chain of alternating Ca-O atoms running along $[100]$. (b) Arrangement of the TBAPy^{4-} ligands relative to the Ca-O chains. View along $[001]$ features the close packing. Two consecutive Ca atoms are marked in blue and orange. (c) A dihedral angle between the planes of TBAPy^{4-} ligands bound to two subsequent Ca atoms (marked in blue and orange) of 80.06° . (d) Tubular structural voids extending along the $[100]$ direction, marked as gold surfaces, occupying 24.8% of the unit-cell volume. The unit-cell contour, with b and c edges coloured in green and blue, respectively, is outlined. Colour code: C grey, H white, O red, Ca light green.

When two TBAPy⁴⁻ ligands are attached to the same Ca1 atom (marked in orange in Figure 47c) with both O2 and O3 atoms, their planar pyrene cores are parallel to each other. At the same time, when sets of such ligands are coordinated to two subsequent Ca atoms of the Ca–O chain (accordingly marked in blue and orange in Figure 47c), they form an angle of 80.06°. This leads to the close-packed array of atoms in the (001) plane (Figure 47b) with the distance of 4.344 Å between two π -stacked TBAPy⁴⁻ ligands.

However, in a perpendicular direction, the crystal packing is much looser. Infinite structural voids, depicted in Figure 47d, run through the entire crystal in parallel with the Ca–O chains. Responsible for the formation of these voids is the rectangular shape of the TBAPy⁴⁻ ligand, with the pyrene core in the centre, and carboxylate groups situated far from it (Figure 46). From the structural analysis, we learn that the chemical character of two symmetrically inequivalent channels running across the structure of **SION-8** is highly anisotropic. The voids located at the positions with $x, \frac{1}{4}, 0$ coordinates are predominantly exposed to the lateral sides of TBAPy⁴⁻ ligands, namely the pyrene cores and benzoate rings, which clearly endows them with *hydrophobic* character. The cross section of these voids is 5.4 Å × 6.2 Å, excluding van der Waals radii, and the contribution from one such void to the unit-cell volume equals 105.5 Å³ (4.6%). On the other hand, the channels situated at $x, 0, \frac{1}{2}$ (5.9 Å × 10.0 Å large in cross section with the volume of 180 Å³ corresponding to 7.8% of the unit cell) in addition to the pyrene cores and benzoate rings, are also surrounded by O-atoms of the Ca–O chains and coordinated H₂O molecules, which allows us to refer to them as to *hydrophilic* pores. This observation is of high importance since only a few examples of MOFs with chemically distinctive pore types have been reported in the literature,^{131b, 137} and making practical use of them, e.g., by taking up mutually incompatible molecules,^{131a} selective recognition of alcohol molecules,¹³⁸ or alternating the gas sorption properties¹³⁹, has been achieved only in a handful of them. More widely encountered are MOFs with chemically distinct types of nanocages.¹⁴⁰ We note that in one unit cell of **SION-8** there are two hydrophilic and two hydrophobic pores (Figure 47d) accounting together for 571 Å³ (24.8%) of its volume.

6.3.2. Bulk characterisation

The phase purity of bulk **SION-8** was confirmed through Le Bail fit of the PXRD pattern recorded with synchrotron radiation (Figure 48a). The PXRD pattern is retained upon the immersion of **SION-8** in water (Figure 56), proving its hydrolytic stability. The IR spectrum of **SION-8**, and in particular stretching vibrations of carbonyl group at 1590 cm⁻¹ and an intense absorption band of extended aromatic ring at 1411 cm⁻¹ (Figure 57), corroborate the incorporation of TBAPy⁴⁻ ligand into the framework. Moreover, the broad band corresponding to the stretching vibrations of the carboxylic acid hydrogen at 3000 cm⁻¹, present in the spectrum of H₄TBAPy, is absent upon formation of **SION-8**, confirming that the TBAPy⁴⁻ ligand is coordinated to Ca^{II}. The spectrum of **SION-8** also contains a weak signal at 1649 cm⁻¹ originating from guest DMF molecules. TGA revealed an insight into the thermal stability of **SION-8** (Figure 48b). The TGA profile of **SION-8** does not show an abrupt drop of mass, but instead, the mass loss is realised in several steps. We can associate the two initial segments of the TGA profile to the release of guest DMF molecules residing within the pores; since the mass loss is not smooth in this region, we raise the hypothesis (see below for the experimental evidence) that this release is stepwise: the DMF molecules trapped in the hydrophobic pores are removed first (below 520 K), while those remaining in the hydrophilic pores are removed at higher temperatures, up to 590 K. The decomposition of **SION-8** occurs only once the coordinated H₂O molecules are removed between 590 K and 670 K, suggesting their vital role in maintaining the framework integrity. The experimental mass loss values match those based on the formula derived from SCXRD, [Ca₂(TBAPy)(μ_2 -OH₂)₂] \cdot 2DMF (Table 12). The stepwise release of DMF molecules from the pores of **SION-8**, as strongly suggested by the TGA, prompted us to study the gradual activation of this material in an *in-situ* SCXRD experiment.

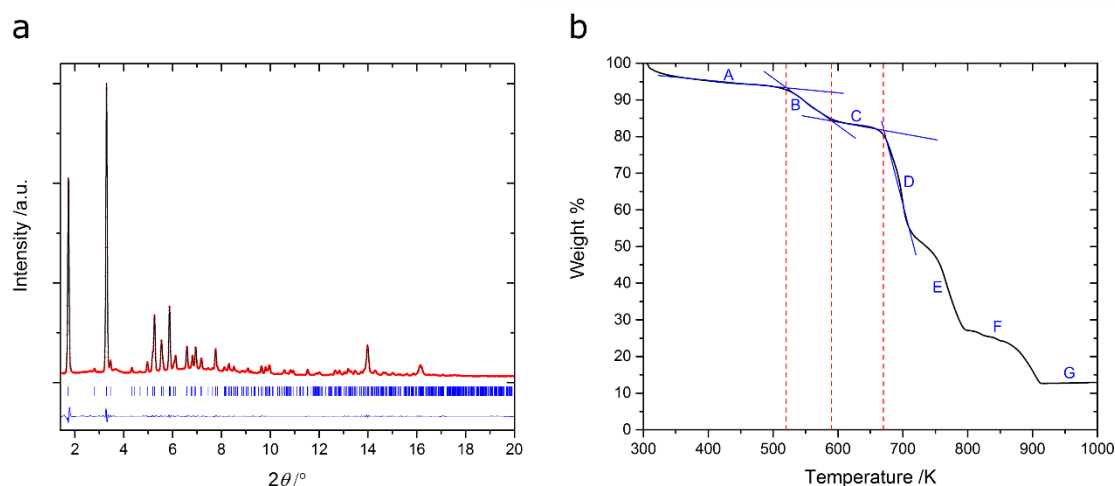


Figure 48. (a) PXRD Le Bail refinement of **SION-8** (space group *Pbam*: $R_p = 3.65\%$, $R_{wp} = 3.41\%$, $a = 6.92670(9)$ Å, $b = 20.415(3)$ Å, $c = 16.572(2)$ Å; $\lambda = 0.50084$ Å). The black plots represent the experimental data, the red dots show the refined Le Bail profiles, while the blue plots represent the difference between them. Reflection positions are marked in blue. (b) Thermogravimetric analysis of **SION-8**. Carrier gas: air. Letters A–G refer to the segments described in Table 12.

Table 12. Gradual decrease of mass of a sample of **SION-8** recorded in the TGA experiment compared to the values based on the formula derived from SCXRD.

Segment	Upper limit	Loss of mass observed from TGA	Loss of mass calculated from SCXRD	Description
A	520 K	7.2%	7.8%	DMF in the hydrophobic pores
B	590 K	7.9%	7.8%	DMF in the hydrophilic pores
C	670 K	4.3%	3.8%	bridging H ₂ O molecules
D, E, F	915 K			framework decomposition
G		87.0%	79.4%	mineralised sample

6.3.3. Stepwise activation

In order to further elucidate the gradual activation of **SION-8**, we designed an *in-situ* SCXRD experiment (see the details in the Experimental section) at BM01 (SNBL from ESRF). At high vacuum and at different temperatures, the **SION-8** structure was easily identified from all measurements, and the unit-cell volume and edge length changes are shown in Figure 49a and Figure 58. The pore volume and content (expressed in the units of e^-) were quantified and plotted in Figure 49b-c. Upon temperature increase, the volume as well as the residual e^- content of the hydrophilic pore are changed to a limited extent, despite the overall unit-cell volume increase from 2264 Å³ at 300 K to 2368 Å³ at 400 K as a consequence of thermal expansion. At the same time the hydrophobic pore, while increasing only slightly its volume of about 120 Å³, loses its excess electron density to a point that at 400 K it counts only 9 e^- . Comparing these results to the electron count of DMF, it is observed in this temperature range that the hydrophilic pore contains approximately 1 molecule of DMF, irrespective of temperature, while the hydrophobic pore loses its 1 molecule of DMF upon heating,

and at 400 K it is virtually empty. Therefore, at 400 K and under vacuum the selective *partial activation* of **SION-8**, limited solely to its hydrophobic pore, can be achieved (Figure 59). We note that on further heating, the single crystal of **SION-8** increased its mosaicity to a point that no sharp Bragg reflections could be recorded. The partially activated phase is referred to as **SION-8P**, while the phase where the pores of the framework are completely empty is named **SION-8F** (fully activated).

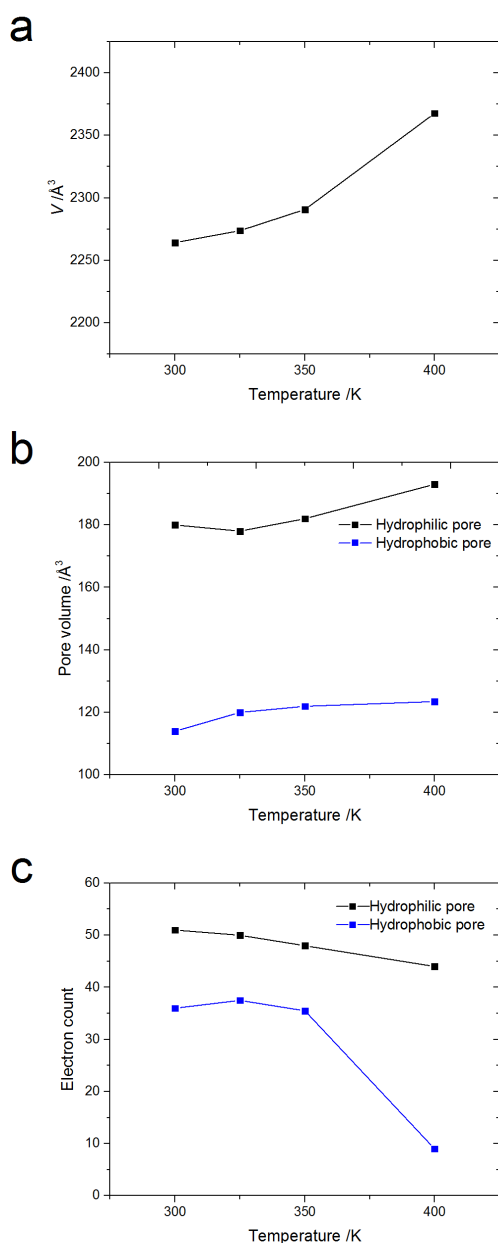


Figure 49. Stepwise activation of **SION-8** under vacuum investigated with SCXRD. (a) Volume V of the orthorhombic unit cell of **SION-8** plotted against temperature. (b) Volume of hydrophilic (black plots) and hydrophobic (blue plots) pores as calculated with SQUEEZE. (c) Excess electron density per pore found in both types of pores. Note that there are two hydrophobic and two hydrophilic pores in each unit cell.

6.3.4. Framework flexibility

Close examination of the crystal structure packing, described in the section 'Crystal structure description', prompted us to investigate the mechanical anisotropy of **SION-8**. The framework is composed of inorganic 1-dimensional Ca–O chains along the *a*-axis, and of organic moieties in two other directions, resulting in a structure similar to the wine-rack-like frameworks, known for their interesting elastic properties.¹⁴¹ Therefore it is anticipated that **SION-8** can be particularly inflexible along the *a*-axis, and much more flexible in the two perpendicular dimensions.

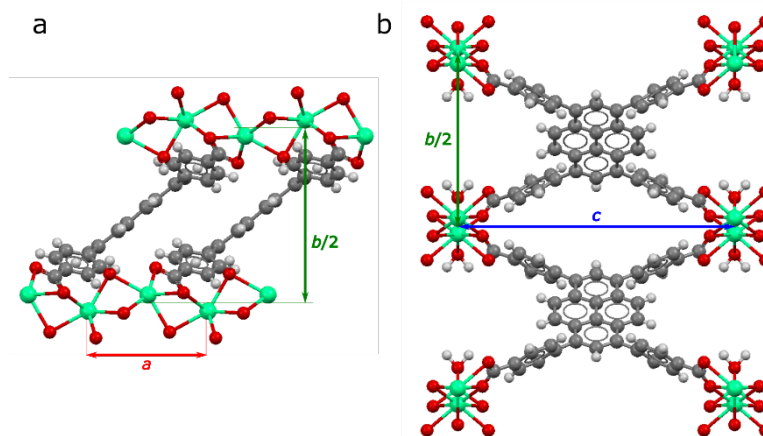


Figure 50. (a) View in the [001] plane and (b) view in the [100] plane of the crystal structure of **SION-8** highlighting the unit-cell parameters of different flexibilities.

The material is very stiff along the *a*-axis, the parameter *a* equalling the pitch of the zig-zag array of Ca atoms found in the 1-dimensional Ca–O chains (Figure 50a). Upon the influence of the external stimuli, this axis experiences hardly any change as within the Ca–O chains the Ca coordination polyhedra can undergo rotations or other deformations relative to one another, but they are particularly inflexible. A higher level of flexibility is exhibited by the parameter *c*, which represents the hydrophobic pore length (Figure 50b); however, as with the parameter *a*, it is dependent strictly on the geometry of Ca–O polyhedra. From the side of the ligand, this pore length is constrained by all-*sp*² hybridization of C atoms within TBAPy⁴⁻ which allows only some specific values of bond angles. Therefore the *c* dimension can be altered only to a certain extent. The polyhedra rotation can however have tremendous impact on the angle between the Ca–O chains and the TBAPy⁴⁻ ligand struts in the [001] plane (Figure 50a), which directly influences the *b* axis length. Moreover, even a slight deformation of Ca-based polyhedra can result in a considerable reorientation of TBAPy⁴⁻ in this plane, and since the Ca–O vs. TBAPy⁴⁻ angle can assume a wide range of values, **SION-8** exhibits the highest flexibility along the *b* axis.

6.3.5. Response of the structure to N₂, CO₂, and CH₄ adsorption and temperature changes

Structural flexibility may lead to drastic alterations of the adsorption capacity of a porous material. In particular, flexibility in a MOF can either improve or reduce its performance, mainly because of the impact on the pore size and shape.²⁹ For this reason, the flexibility of **SION-8** was studied as a function of the external gas pressure with SCXRD and PXRD chosen as experimental techniques to monitor the mechanical changes.

SCXRD was used first for two reasons: it provides information on the unit-cell parameter changes caused by the gas adsorption, and simultaneously it can give insights on how the external gas pressure influences the crystal structure. A single crystal of **SION-8P** was subjected to high pressures of N₂, CO₂, and CH₄ (see details in the Experimental section), and the corresponding crystal structures were solved and refined at each pressure point of these isotherms.

It was found that the gas molecules are adsorbed within the hydrophobic pores of **SION-8P**, but instead of assuming well-defined positions, they are heavily disordered; therefore, we turned to the integration of electron density as an adsorption probing tool. The amount of adsorbate was found to depend on the nature of the gas. At the studied conditions, a practically negligible amount of N₂ (Figure 60) is adsorbed in the pores, as we noticed no significant changes in the electron count within the structural voids. Similarly, upon increased external CH₄ pressure, an increase of 5.5 e⁻ of the integrated electron density within the hydrophobic pore is interpreted as the adsorption of less than 1 molecule of CH₄ in 1 hydrophobic pore (Figure 61). However, upon CO₂ adsorption, the excess electron count within the hydrophobic pores gradually increased by ~30 e⁻ (Figure 62). Therefore, each hydrophobic pore in **SION-8P**, once evacuated as a result of the activation process, can be filled with ~1.5 molecules of CO₂. The CO₂ adsorption within **SION-8P** monitored directly by SCXRD can be modelled with the Langmuir adsorption isotherm equation (Figure 63) resembling the isotherms recorded with the gravimetric method (*vide infra*).

Comparing the changes of the pore content induced by the external gas pressure with the concomitant evolution of the unit-cell dimensions (Figure 60, Figure 61 and Figure 62), it becomes clear that the most noticeable structural changes in **SION-8P** are exerted by CO₂. The influence of CO₂ on **SION-8P** is twofold: the uniform external pressure compresses the crystallites, and simultaneously, due to their porous nature, their pores are gradually filled with an increasing number of CO₂ molecules; as can be seen from the pressure dependence of the unit-cell volume (Figure 62), the second phenomenon prevails. When the external pressure of CO₂ is increased, the parameter *a* elongates to a small extent and the parameter *b* to a considerable extent, while the unit-cell dimension *c* shrinks, and the magnitude of these deformations is analogous to that anticipated and described above. The process is linked to an overall appreciable increase in volume of both the hydrophobic and the hydrophilic pores. These data are representative, since the same trends are observed when crystalline powder of **SION-8F** is subjected to CO₂, and the unit-cell parameters are derived from *in-situ* recorded PXRD patterns (Figure 64).

Analogous response is exhibited by the as-made **SION-8** material when subjected to still another external stimulus, namely variable temperature (Figure 51). Initially the pores of the material are filled with non-coordinated DMF molecules, and upon heating, the unit cell experiences the uniform changes of its volume and edge lengths. However, in the 325–360 K temperature range the unit-cell volume drops by 1.0% on heating, which we associate with the partial desolvation and generation of **SION-8P**.^{26b} This structural change is anisotropic as it is primarily realised along the *b* axis. After this transition, the desolvated structure changes monotonically in the same manner as before the transition, which turns out to be irreversible (once the solvent molecules are released from the pores, the mechanical response of the framework is not impeded by any factor). We therefore reason that in order to accommodate guest species within its pores, **SION-8** shrinks along *c*, elongates to a significant extent along *b*, and stays virtually invariant along *a*, which stays in line with the anticipation of the framework's flexibility described above. Ultimately, flexibility of **SION-8** greatly enhances its uptake of guest molecules. Virtually the same structural mechanisms play a role upon an increased external pressure of CO₂ (Figure 51) – in order to accommodate CO₂ gas molecules, **SION-8** anisotropically enhances its volume. In this respect, the behaviour of **SION-8** resembles that of Co(bdp)¹²⁸ and MIL-53(Cr),¹⁴² although in both of these cases the accommodation of additional gas molecules is realised upon phase transitions towards the forms of higher capacity, rather than through continuous structural changes within the same phase.

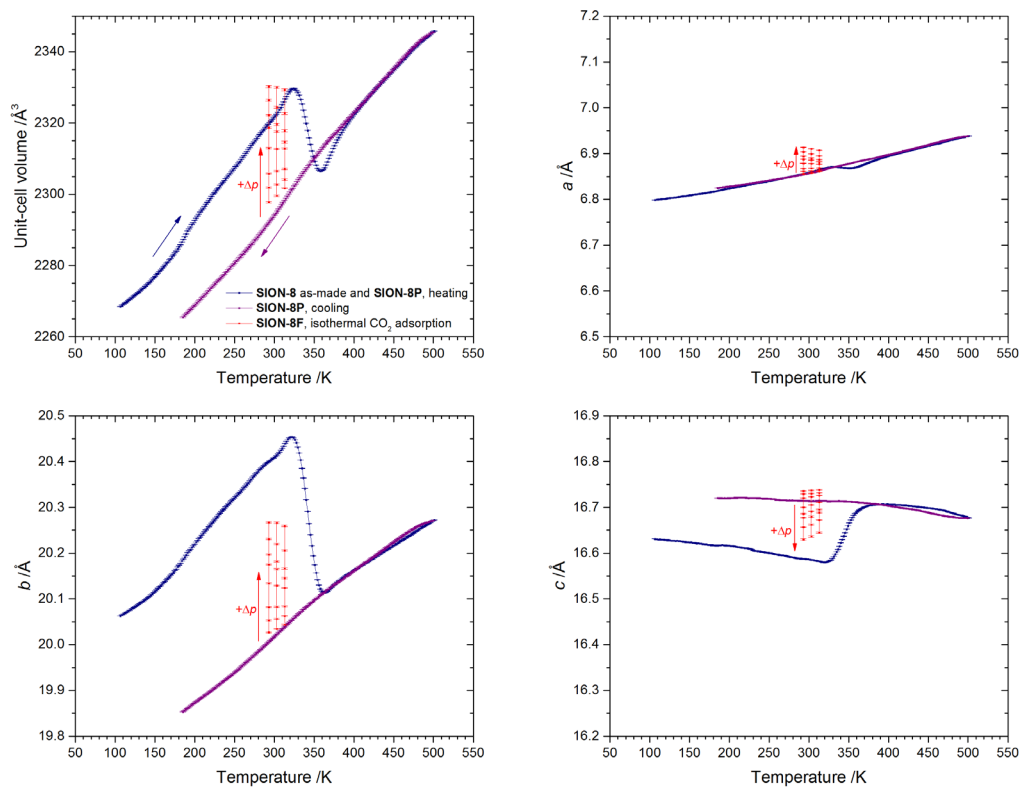


Figure 51. Unit-cell volume and parameters a , b , and c derived from Le Bail fits of the VT PXRD patterns. Fully solvated **SION-8** undergoes a 1.0% unit-cell compression at 325–360 K upon heating (blue plots), associated with the transformation to **SION-8P**. The cooling run (purple plots) does not show an analogous feature. Isothermal data for **SION-8F** at different pressures of CO_2 (Fig. S17) are overlaid in red.

6.3.6. Single-component N₂, CO₂, and CH₄ adsorption

Adsorption of different gases – N₂, CO₂, and CH₄ – in the hydrophobic pores of **SION-8P**, observed in the *in-situ* SCXRD experiment, prompted us to study further the sorption properties of the bulk material. First, we activated the powdered sample of **SION-8** using the previously discussed conditions for 8 hours, and measured the N₂-sorption isotherm at 77 K (Figure 52a). The mass loss observed prior to the isotherm collection is in agreement with the loss observed from TGA and crystallographic analysis (Table 13). Application of the Brunauer–Emmett–Teller (BET) model resulted in the surface area estimate of 174 m²/g, while the calculated pore volume of 0.0826 cm³/g was comparable to the one derived from the crystal structure. As expected, **SION-8** does not lose crystallinity upon activation and subsequent N₂ adsorption (Figure 65).

Table 13. Comparison between the two sets of activation conditions leading to two activation stages, **SION-8P** and **SION-8F**.

	SION-8P	SION-8F
Activation conditions	403 K, vacuum, 8 hours	solvent exchanged to acetone 463 K, vacuum, 8 hours
Observed loss of mass	8.7%	15.5%
Loss of mass calculated from TGA	7.2%	15.1%
Loss of mass calculated from the molecular formula	7.8%	15.6%
Pore volume derived from the isotherm	0.0826 cm ³ /g	0.2280 cm ³ /g
Pore volume derived from the crystal structure	0.0724 cm ³ /g	0.2164 cm ³ /g
BET surface area	174 m ² /g	509 m ² /g

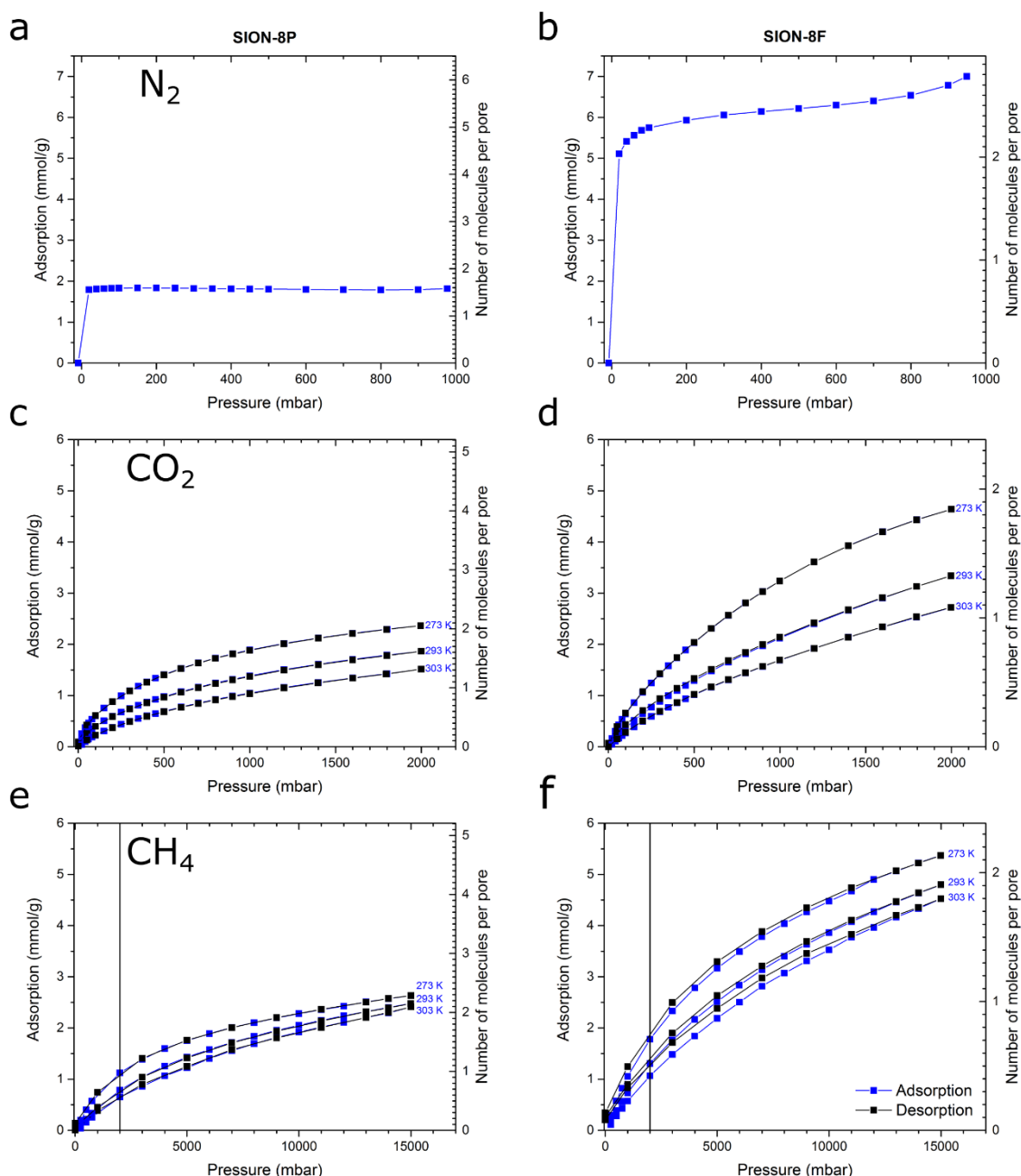


Figure 52. Experimental N_2 -adsorption isotherm of **SION-8P** (a) and of **SION-8F** (b) at 77 K; experimental CO_2 -adsorption isotherms of **SION-8P** (c) and of **SION-8F** (d) at 273 K, 293 K and 303 K; experimental CH_4 -adsorption isotherms of **SION-8P** (e) and of **SION-8F** (f) at 273 K, 293 K and 303 K. Vertical line in the panels e and f represents the pressure of 2000 mbar.

SION-8F, *i.e.* the *fully activated* phase in which both types of pores are emptied and available for gas adsorption, was achieved in the bulk by exploring another set of activation conditions – sample immersed in acetone for 3 days and subsequently outgassed at 463 K for 8 hours with a membrane vacuum pump – as evidenced by the comparison between the measured and calculated values of loss of mass and pore volume (Table 13). Moreover, the values of N_2 uptake (Figure 52b) and of BET surface area (Table 13) were found to be threefold of those recorded for **SION-8P**.

Therefore, by changing the activation conditions, we gained access to two bulk materials of different sorption properties. Most importantly, we observed that the isotherms collected on **SION-8P** were reproducible: due to the strong interactions between DMF and the hydrophilic pore, its evacuation was efficiently delayed while the hydrophobic pore was already activated. **SION-8P** and **SION-8F** were additionally tested for CO₂ and CH₄ adsorption at 273 K, 293 K and 303 K (Figure 52c-f); in both cases the sorption performance of **SION-8F** was nearly two times that of **SION-8P**. Based on the pore volume determined from SCXRD at 300 K (Figure 49) and the molecular volume of CH₄,¹⁰⁶ one hydrophobic pore of **SION-8** can theoretically accommodate ~1.7 molecules of CH₄, while one hydrophilic pore has a maximum capacity of ~2.8 molecules of CH₄ (therefore, the average equals ~2.3 molecules). Simultaneously, from single-component adsorption isotherms at 303 K and 15000 mbar (Figure 52e-f), we observed a preference for the pores to be occupied by 2.0 molecules of CH₄ in the hydrophobic pore (**SION-8P**), and by an average of 1.8 molecules of CH₄ per pore in **SION-8F**. This provides qualitative confirmation that the actual size of the pores is the limiting factor of CH₄ adsorption capacity. A similar conclusion can be drawn for the adsorption of CO₂.¹⁴³

The isosteric heats of adsorption Q_{st} calculated from the experimental isotherms reflect the energy of interaction between the studied gas species and the pore surface in **SION-8P** and **SION-8F** (Table 14). In **SION-8P** we associate the Q_{st} with the energy of interaction between the gas and the hydrophobic pore. In **SION-8F**, however, interactions between gas and both types of pores, the hydrophobic and the hydrophilic one, contribute to the overall Q_{st} (the energy of the gas–hydrophilic pore interaction is not experimentally available). CO₂ interacts more strongly with the pores than does CH₄ in both materials. This opens up a possibility to use **SION-8** in CO₂/CH₄ separations. Furthermore, in **SION-8P** the interaction between CO₂ and the pores is 1.3 times stronger than the analogous interaction of CH₄; in **SION-8F** this ratio increases to 1.5. Consequently, the CO₂/CH₄ separation is expected to be more efficient with **SION-8F**.

Table 14. Isosteric heats of adsorption Q_{st} at zero loading calculated from CH₄ and CO₂ adsorption isotherms recorded at different temperatures for **SION-8P** and **SION-8F**. Values in kJ/mol.

	SION-8P (only hydrophobic pores accessible)	SION-8F (both pores accessible)
CH ₄	21.4	16.0
CO ₂	28.4	23.4

6.3.7. CO₂/CH₄ separation

Prompted by the significantly different isosteric heats of adsorption derived from single-component adsorption isotherms, the CO₂/CH₄ separation performance of **SION-8P** and **SION-8F** was further investigated with breakthrough experiments, which provide additional information on the adsorption kinetics as compared with the equilibrium isotherms. A range of different CO₂/CH₄ gas mixtures were tested, with the focus on 90% CH₄ and 10% CO₂ (model composition of acid natural gas), and on 50% CH₄ and 50% CO₂ (model composition of biogas). As can be seen from the recorded breakthrough curves (Figure 66), at each condition, CH₄ was released from the chromatographic column first, followed by CO₂ after a certain retention time spanning from several seconds to minutes. Adsorption capacities of **SION-8P** and **SION-8F** were calculated by integrating breakthrough curves (Table 17), and were further used for the calculation of CO₂/CH₄ dynamic breakthrough selectivities α summarised in Table 15. In all cases α is higher than 1, implying that indeed in contact with the CO₂/CH₄ mixture, **SION-8P** and **SION-8F** selectively adsorb CO₂ over CH₄. The CO₂/CH₄ separation is more efficient at lower concentrations of CO₂, which require lower adsorbed amounts of CO₂ for an equally efficient separation, and at lower temperature, which favours the increase in CO₂ adsorption

capacity more as compared to that of CH₄ (Table 17). The better performance of **SION-8F** compared to **SION-8P**, increased by 40% in the case of a mixture of 90% CH₄ and 10% CO₂ at 323 K, and nearly 3-fold for the same gas mixture at 273 K (Table 15), is a consequence of different CO₂/CH₄ Q_{st} ratios exhibited by these materials. **SION-8F** showed the best separation performance towards the mixture composed of 90% of CH₄ and 10% of CO₂, and it decreased towards more moderate values with the increased concentrations of CO₂. Similar dependence of the selectivity on the CO₂/CH₄ mixture composition was previously found in other materials selective to CO₂, e.g. in MIL-101(Al)-NH₂,¹⁴⁴ MIL-53(Al)-NH₂,¹⁴⁵ and CCP-1.¹⁴⁶ We note that the values of selectivities derived from breakthrough curves arise from practical separation processes, in contrast to the selectivities calculated from single-component isotherms, which reflect the idealised situation, and should only be used as upper-level approximations. Therefore, the comparison of the separation performance of **SION-8** can be made where the selectivity of materials was calculated through the breakthrough experiments (Table 18). With its CO₂/CH₄ dynamic breakthrough selectivity of 2.34 towards the 50% CH₄ and 50% CO₂ gas mixture at 303 K, **SION-8F** performs similarly well compared to other MOFs based on ligands with aromatic groups exposed to the pore surfaces (e.g., MOF-508b, $\alpha = 3$;¹⁴⁷ MIL-101(Cr), $\alpha = 3.6$),^{136b} however MOFs containing unobstructed amino functionalisation (e.g., MIL-101(Al)-NH₂, $\alpha = 6.3$;¹⁴⁴ MIL-53(Al)-NH₂, $\alpha = 45$)¹⁴⁵ or negatively charged SiF₆²⁻ groups within the pores (e.g., SIFSIX-2-Cu-i, $\alpha = 51$)¹²⁶ perform better. Nevertheless, **SION-8** has a tuneable separation performance, which to the best of our knowledge has not been reported earlier.

Table 15. CO₂/CH₄ dynamic breakthrough selectivities α for **SION-8F** and **SION-8P** calculated from the integration of the respective breakthrough curves recorded at 273 K, 303 K, and at 323 K, and at a range of CO₂/CH₄ relative molar ratios.

SION-8F					
	10% CH ₄ , 90% CO ₂	25% CH ₄ , 75% CO ₂	50% CH ₄ , 50% CO ₂	75% CH ₄ , 25% CO ₂	90% CH ₄ , 10% CO ₂
273 K	2.16	2.16	3.09	5.42	5.45
303 K	1.69	1.73	2.34	3.16	3.71
323 K	1.49	1.55	1.62	1.94	1.98

SION-8P					
	10% CH ₄ , 90% CO ₂	25% CH ₄ , 75% CO ₂	50% CH ₄ , 50% CO ₂	75% CH ₄ , 25% CO ₂	90% CH ₄ , 10% CO ₂
273 K	1.10				2.11
303 K	1.01			1.41	1.47
323 K					1.38

6.4. Conclusions

SION-8, a novel bi-porous MOF endowed with two chemically contrasting structural pores, the hydrophobic and the hydrophilic, was successfully synthesised and fully characterised with diffraction, spectroscopic, and thermogravimetric methods. By judiciously altering the activation conditions, two functional materials were obtained: the partially-activated **SION-8P** and the fully-activated **SION-8F**. Due to their distinct pore environments, **SION-8P** and **SION-8F** showed different adsorption properties towards N₂, CO₂, and CH₄, and the size of the available pores was found to be the limiting factor for gas adsorption. Intrinsic structural flexibility, exhibited by **SION-8** primarily along the *b*-axis, was found

responsible for the structural adjustments allowing for the accommodation of guest solvent and gas molecules. The tuneable CO₂/CH₄ separation performance was tested with breakthrough experiments at 1 bar and expressed in terms of the CO₂/CH₄ dynamic breakthrough selectivity factors α . At 273 K, **SION-8P** showed α of 2.11 towards the gas mixture composed of 90% CH₄ and 10% CO₂, while the respective value for **SION-8F** reached 5.45. A significant contrast between the values of Q_{st} in the two chemically different pores constitutes the rationale behind the different dynamic breakthrough selectivity factors in both materials. The discovery of **SION-8** and the link between the macroscopic properties and the underlying chemistry of this material bring us closer to the rational design of new materials that can be used for a plethora of applications such as natural gas purification and other energy-related separations.

6.5. Appendix

Table 16. Crystal data and structure refinement for **SION-8**.

Identification code	SION-8
Empirical formula	C ₂₅ H ₂₀ CaO ₆ N
Formula weight	470.50
Temperature/K	100
Crystal system	orthorhombic
Space group	<i>Pbam</i>
<i>a</i> /Å	6.88590(11)
<i>b</i> /Å	20.0624(4)
<i>c</i> /Å	16.6453(4)
α /°	90
β /°	90
γ /°	90
Volume/Å ³	2299.51(8)
<i>Z</i>	4
ρ_{calc} / g/cm ³	1.359
μ /mm ⁻¹	0.281
<i>F</i> (000)	980.0
Crystal size/mm ³	0.14 × 0.1 × 0.03
Radiation	synchrotron (λ = 0.7153)
2 θ range for data collection/°	4.086 to 50.81
Index ranges	$-8 \leq h \leq 6, -23 \leq k \leq 23, -19 \leq l \leq 16$
Reflections collected	14679
Independent reflections	2064 [R_{int} = 0.0294, R_{sigma} = 0.0140]
Data/restraints/parameters	2064/82/170
Goodness-of-fit on F^2	1.916
Final <i>R</i> indexes [$\geq 2\sigma(I)$]	R_1 = 0.1024, wR_2 = 0.3739
Final <i>R</i> indexes [all data]	R_1 = 0.1053, wR_2 = 0.3805
Largest diff. peak/hole / e Å ⁻³	2.23/−0.54
CCDC	1846814

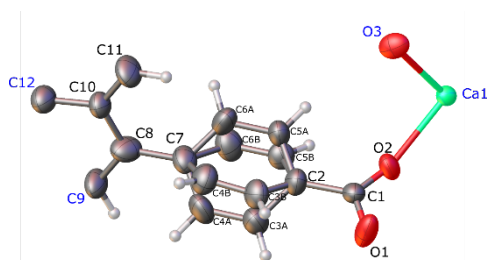


Figure 53. Asymmetric unit of **SION-8**. Atoms Ca1, O3, C9, and C12 (captioned in blue) are located at the special positions with the Wyckoff site multiplicity reduced by a factor of 2, while atoms C3, C4, C5, and C6 are disordered over two distinct positions.

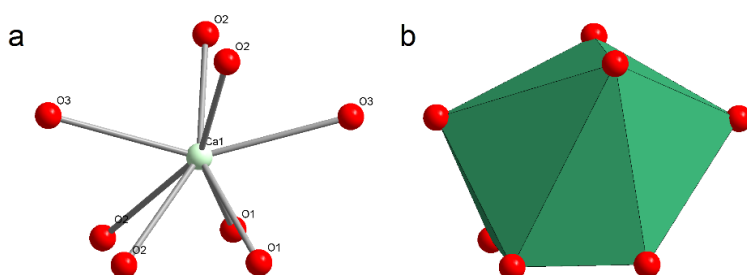


Figure 54. Coordination environment of the Ca1 atom in the structure of **SION-8**. (a) Atoms present in the first coordination shell of Ca1. (b) Coordination geometry described as biaugmented trigonal prism.

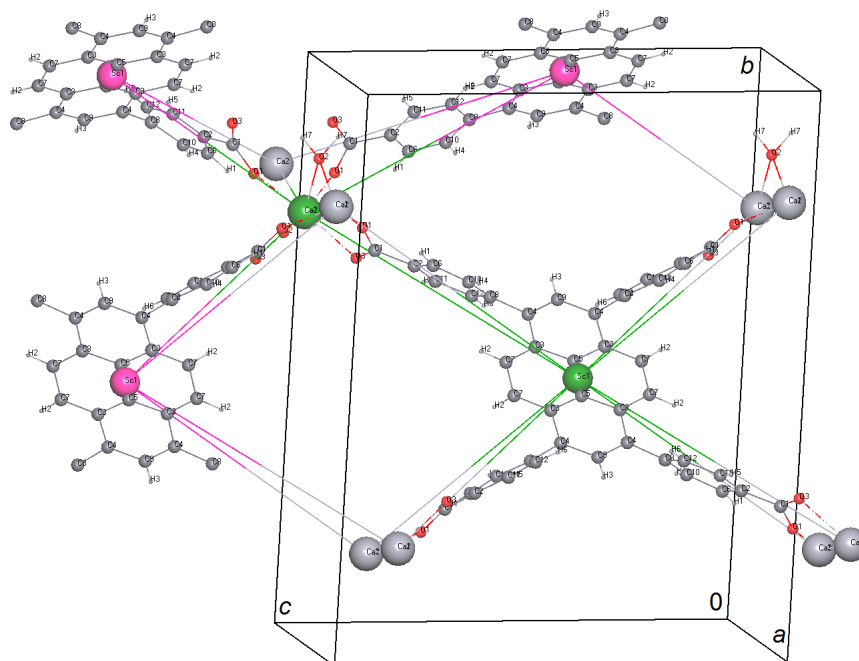


Figure 55. **SION-8** and its underlying **sea** net topology. The **sea** net is 2-nodal 6,8-coordinated with the (6-c)₂(8-c) stoichiometry and Schläfli symbol (3⁴.4¹².5⁴.6³)(3⁴.4⁴.5⁴.6³)₂. The 8-coordinated node marked as 'Sc1' represents the centre of the TBAPy⁴⁻ ligand. The Ca atom constitutes the 6-coordinated node connected to two neighbouring Ca nodes and four imminent 'Sc1' (TBAPy⁴⁻) nodes. The full coordination of two selected nodes, one 8-c and one 6-c, marked in green, is depicted. The contour of the unit cell is outlined in black.

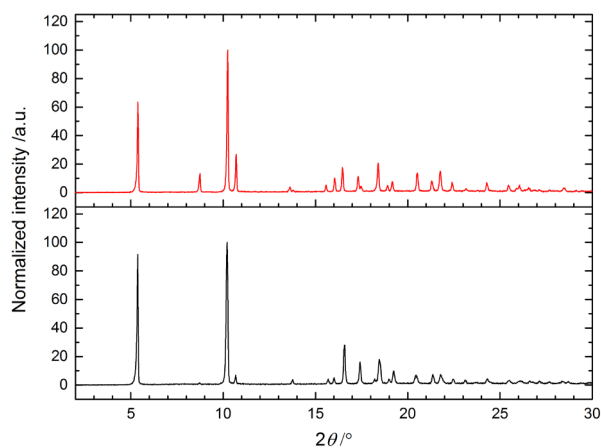


Figure 56. Powder pattern (recorded with Cu K α radiation) of **SION-8** before (top red plots) and after (bottom black plots) the immersion of the powder in pure H₂O for 24 h.

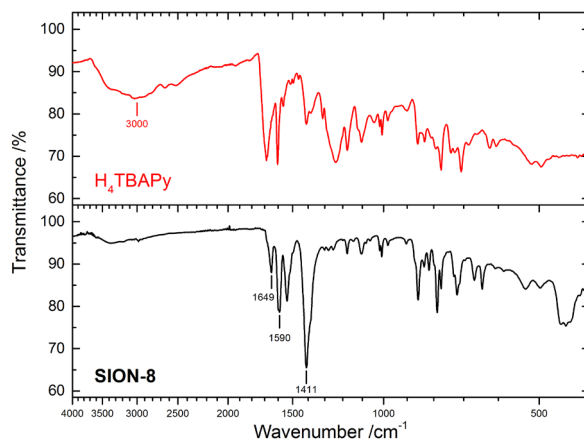


Figure 57. Infrared spectrum of **SION-8** (bottom black plots) compared to the spectrum of H₄TBAPy ligand (top red plots). Characteristic peaks mentioned in the Discussion are captioned.

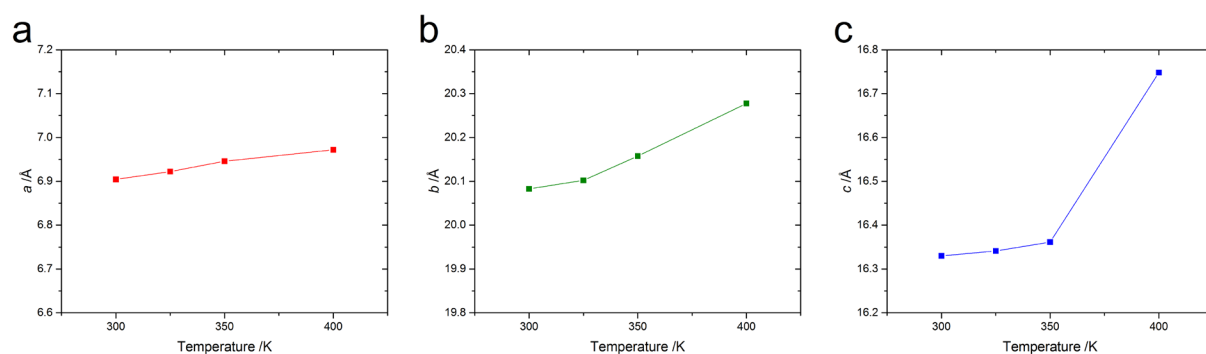


Figure 58. Parameters a (a), b (b), and c (c) of the orthorhombic unit cell of **SION-8** during activation under vacuum plotted against temperature.

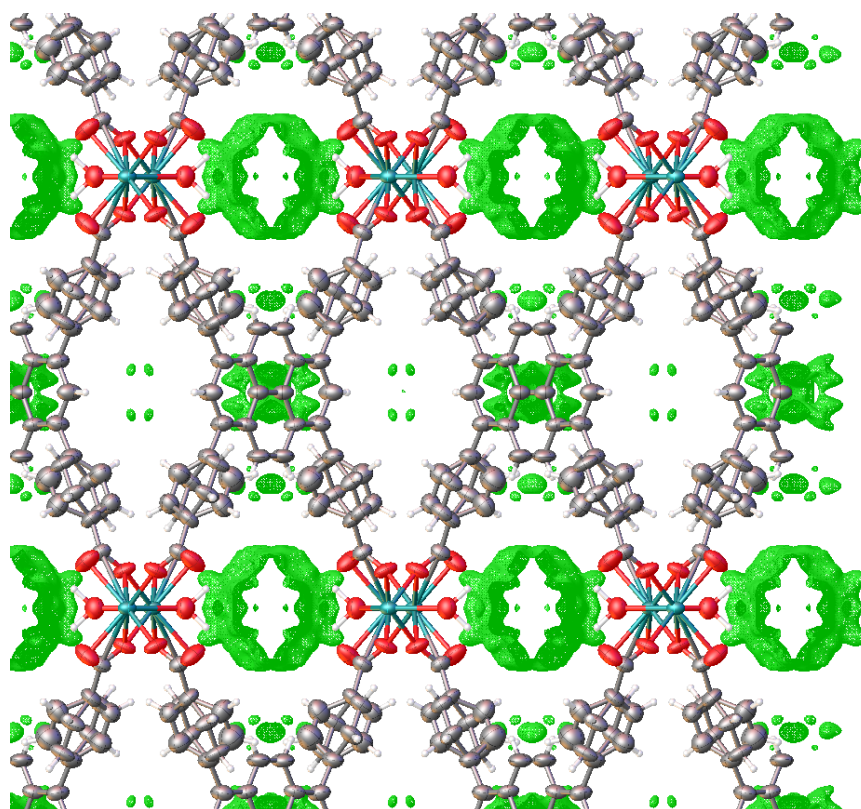


Figure 59. Difference-Fourier map of the crystal structure of **SION-8** at 400 K and under vacuum drawn with the program Olex2. The excess electron density map is represented in the wire style at the $0.5 \text{ e}^-/\text{\AA}^3$ level with the 0.1 \AA resolution. View along $[100]$.

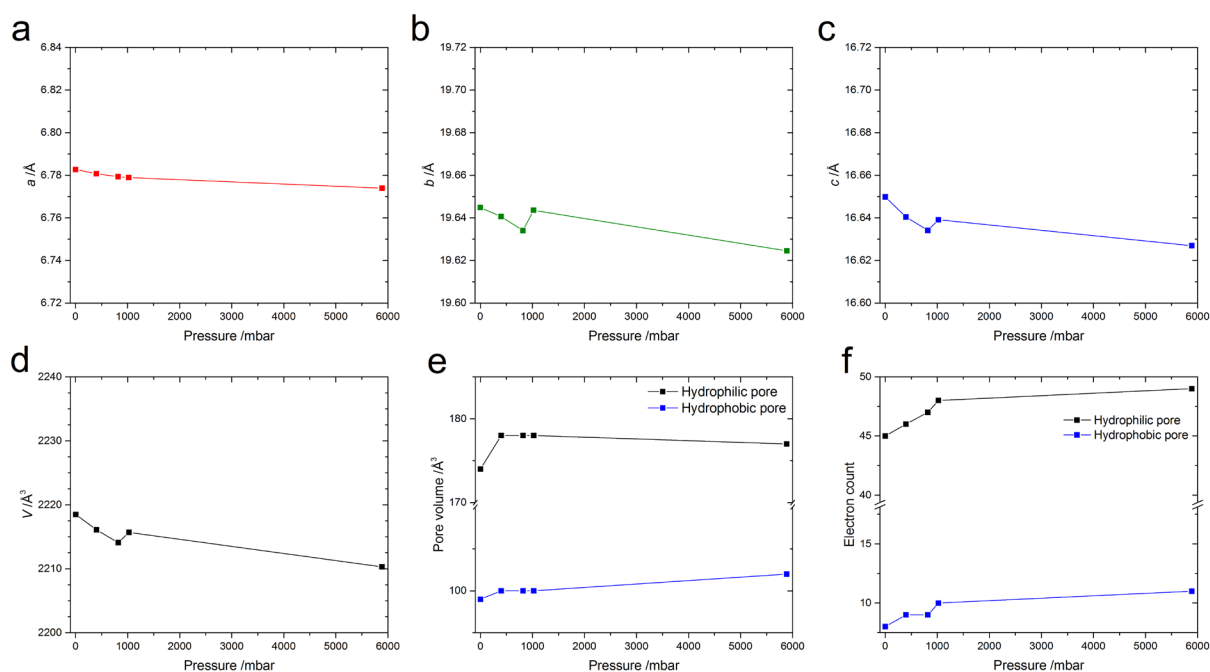


Figure 60. Structural parameters of **SION-8** plotted against pressure of nitrogen. (a-d) Unit-cell parameters a , b , c and V . (e) Volume of hydrophilic (black plots) and hydrophobic (blue plots) pores as calculated with SQUEEZE. (f) Excess electron density per pore found in both types of pores. Isotherm measured at $T = 90 \text{ K}$.

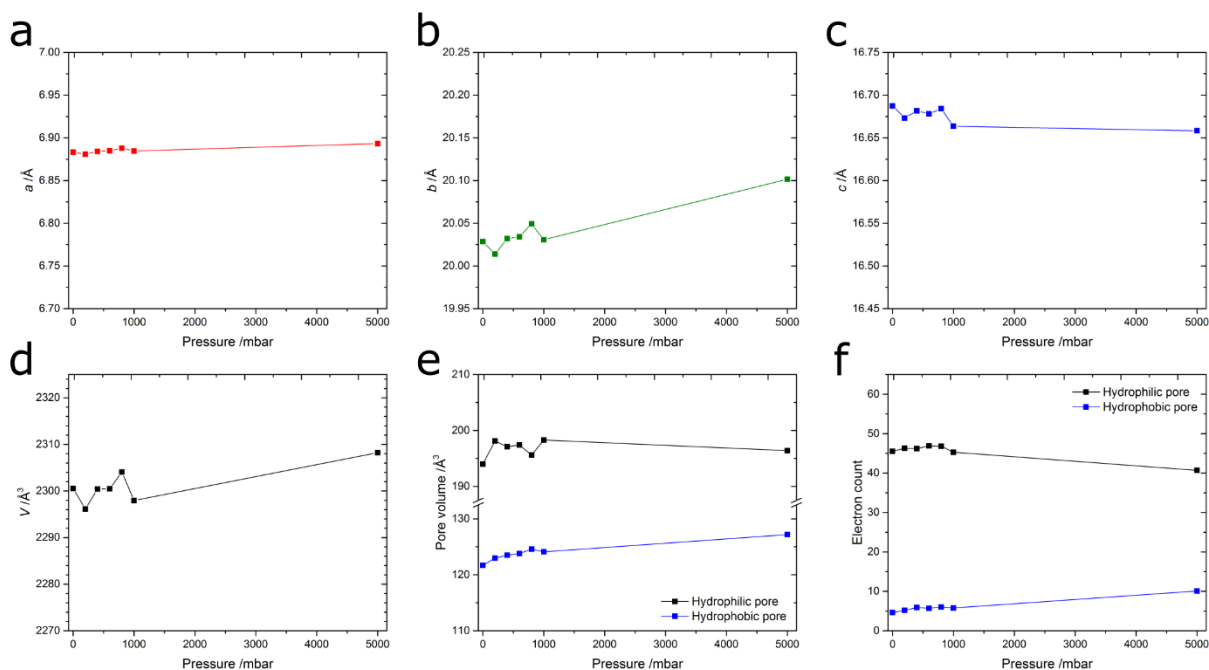


Figure 61. Structural parameters of **SION-8** plotted against pressure of methane. (a-d) Unit-cell parameters a , b , c and V . (e) Volume of hydrophilic (black plots) and hydrophobic (blue plots) pores as calculated with SQUEEZE. (f) Excess electron density per pore found in both types of pores. Isotherm measured at $T = 300$ K.

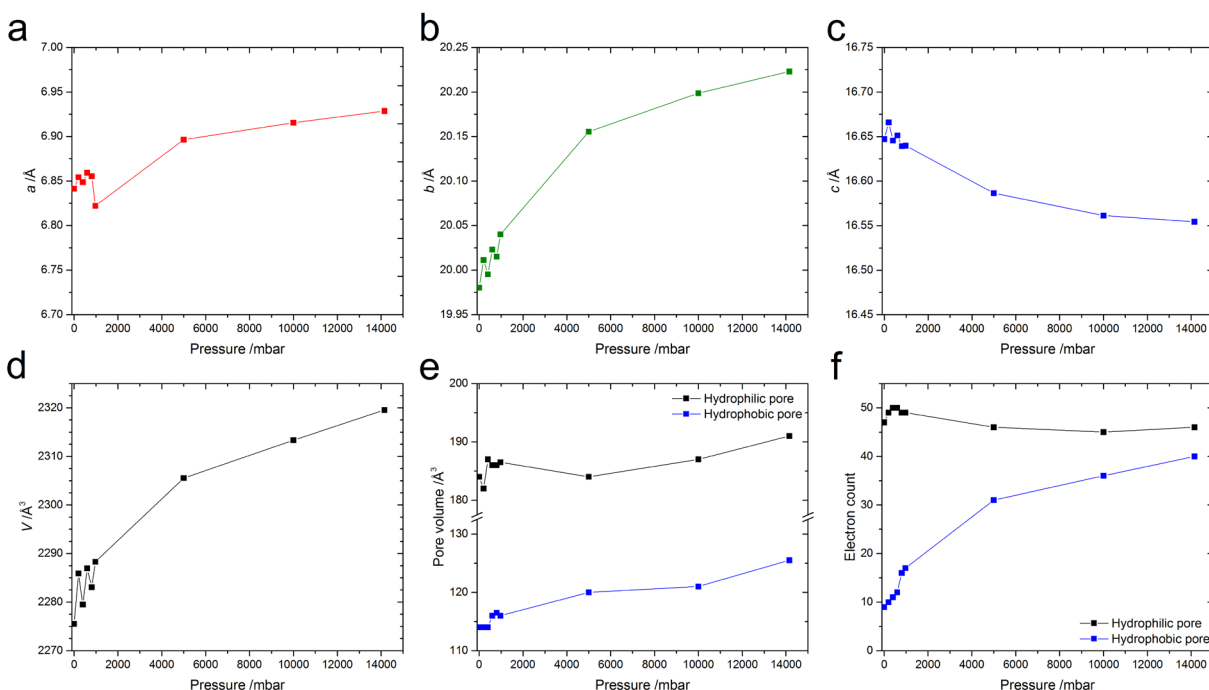


Figure 62. Structural parameters of **SION-8** plotted against pressure of carbon dioxide. (a-d) Unit-cell parameters a , b , c and V . (e) Volume of hydrophilic (black plots) and hydrophobic (blue plots) pores as calculated with SQUEEZE. (f) Excess electron density per pore found in both types of pores. Isotherm measured at $T = 300$ K.

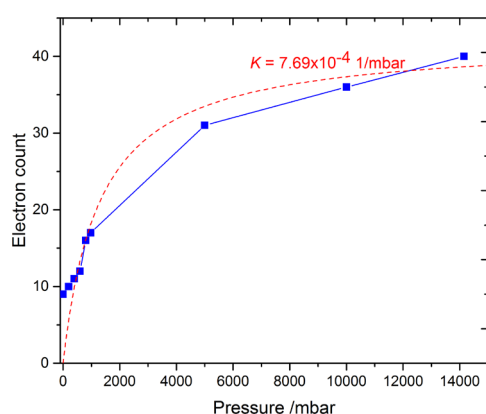


Figure 63. Excess electron density found in the hydrophobic pore plotted against the pressure of CO₂ (blue plots) fitted to the Langmuir model (dashed red line).

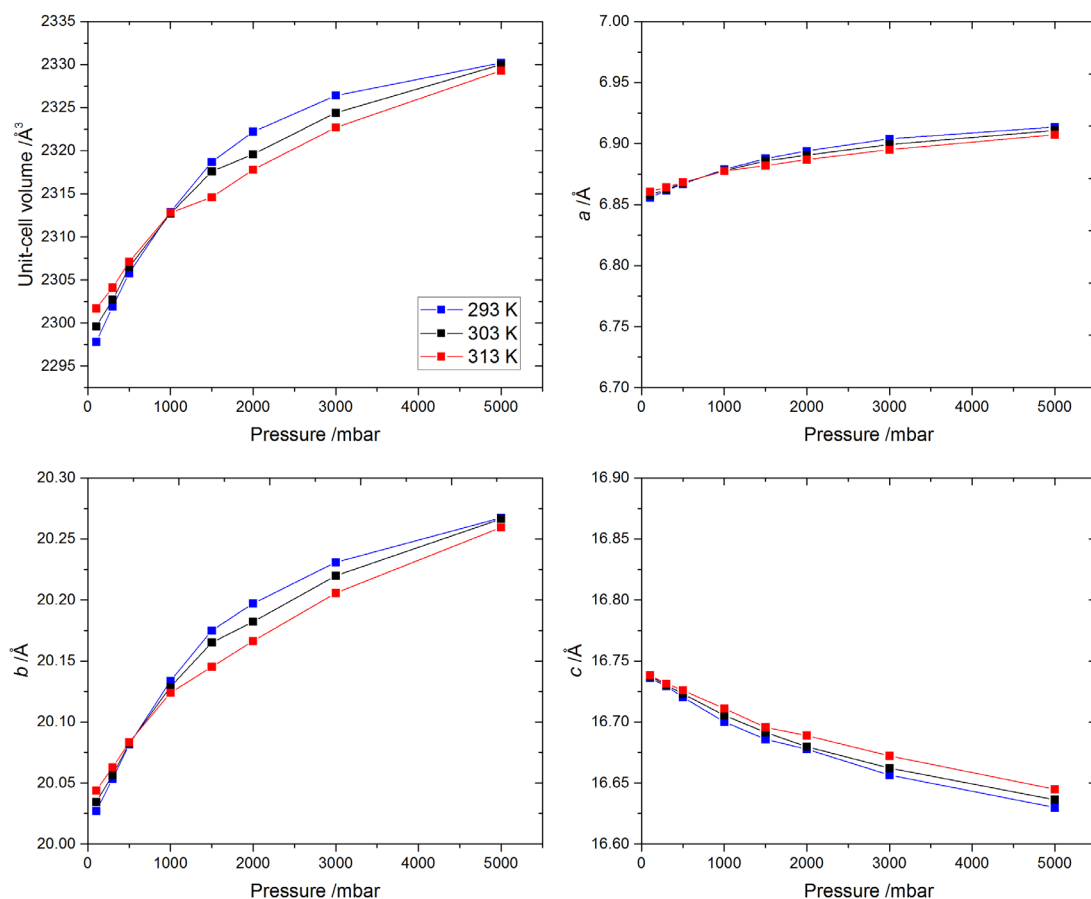


Figure 64. Unit-cell volume and parameters a , b , and c of **SION-8F** derived from the Le Bail fits to the PXRD patterns recorded during the *in-situ* CO₂-loading experiment ($\lambda = 0.72179 \text{ Å}$).

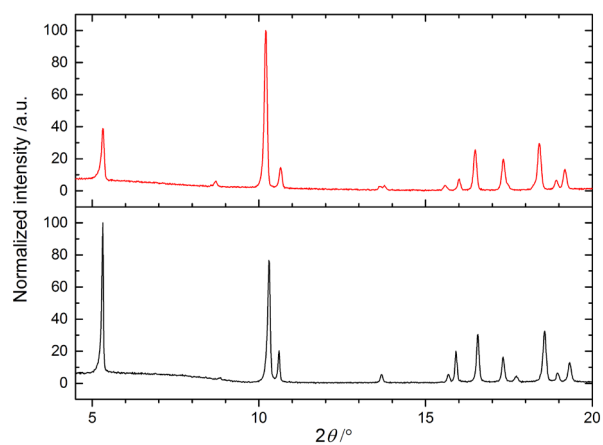
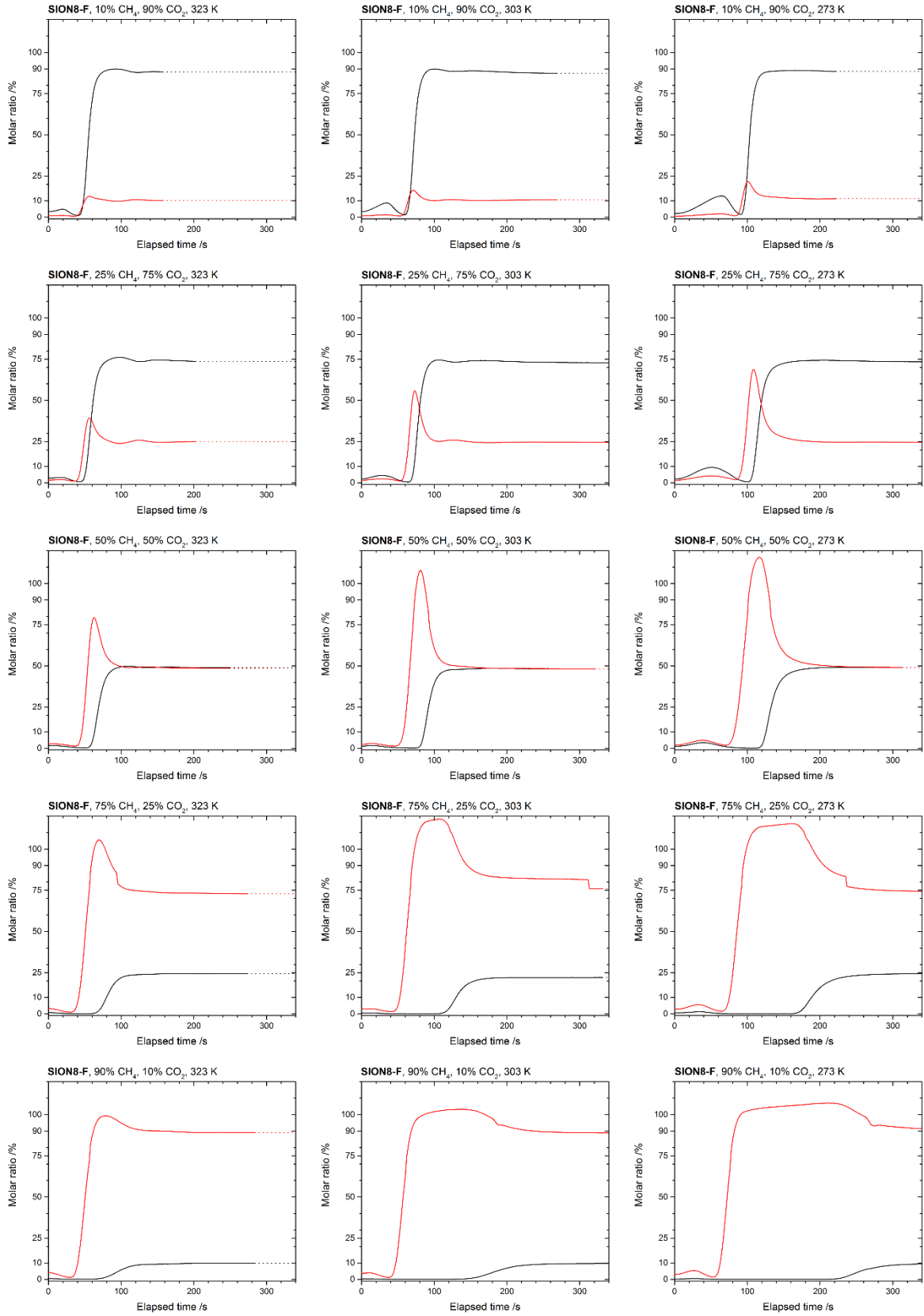


Figure 65. Powder pattern (recorded with Cu K α radiation) of a sample of **SION-8** before (top red plots) and after (bottom black plots) the adsorption experiment. No loss in crystallinity is clearly visible.



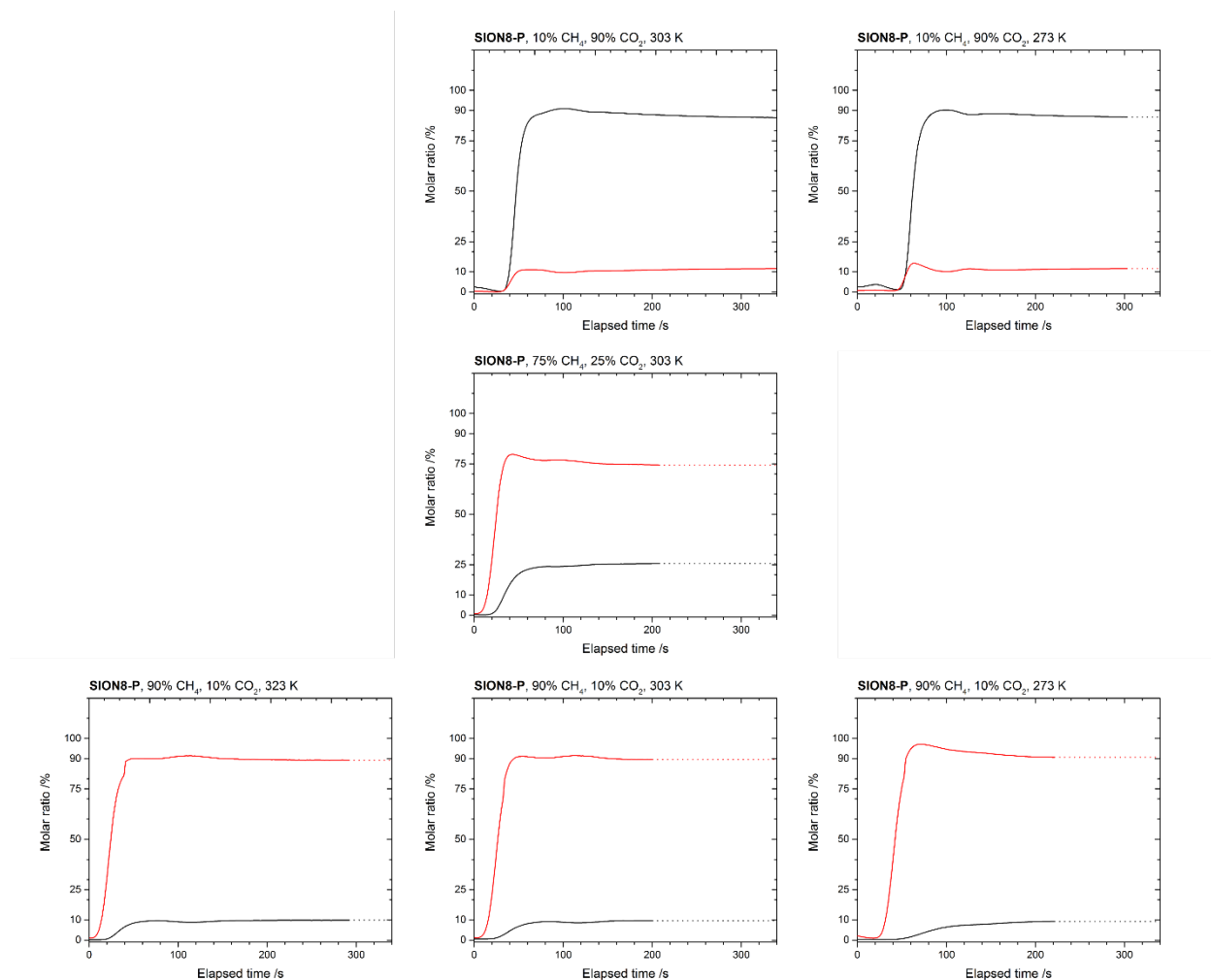


Figure 66. Breakthrough curves for **SION-8F** and **SION-8P** recorded at 273 K, 303 K and 323 K, and at different compositions of CO₂/CH₄ gas mixtures. Colour code: CO₂; black, CH₄; red.

Table 17. Adsorption capacities of **SION-8P** and **SION-8F** calculated by integrating breakthrough curves. Values in mmol/g.

SION-8F										
	10% CH ₄ , 90% CO ₂		25% CH ₄ , 75% CO ₂		50% CH ₄ , 50% CO ₂		75% CH ₄ , 25% CO ₂		90% CH ₄ , 10% CO ₂	
	CO ₂	CH ₄	CO ₂	CH ₄	CO ₂	CH ₄	CO ₂	CH ₄	CO ₂	CH ₄
273 K	1.92	0.10	1.89	0.29	1.46	0.47	1.08	0.60	0.56	0.92
303 K	1.38	0.09	1.35	0.26	0.98	0.56	0.64	0.61	0.37	0.90
323 K	1.00	0.07	0.88	0.19	0.69	0.43	0.43	0.67	0.19	0.88

SION-8P										
	10% CH ₄ , 90% CO ₂		25% CH ₄ , 75% CO ₂		50% CH ₄ , 50% CO ₂		75% CH ₄ , 25% CO ₂		90% CH ₄ , 10% CO ₂	
	CO ₂	CH ₄	CO ₂	CH ₄	CO ₂	CH ₄	CO ₂	CH ₄	CO ₂	CH ₄
273 K	1.57	0.16							0.30	1.29
303 K	1.11	0.12					0.39	0.83	0.18	1.13
323 K									0.16	1.03

Table 18. MOFs exhibiting the CO₂/CH₄ separation performance determined with breakthrough experiments reported in the literature.

Material	CO ₂ /CH ₄ feed ratio	Temp. [K]	Pressure [bar]	CO ₂ capacity [mmol/g]	CH ₄ capacity [mmol/g]	CO ₂ /CH ₄ dynamic selectivity	Reference
Al-BDC calcinated	0.50/0.50	303	1			10.5	148
Al-BDC calcinated	0.50/0.50	303	2			12.3	148
CCP-1	0.50/0.50	298	2			2	146
CPO-27-Ni	0.50/0.50	303	1			15	149
CPO-27-Co	0.50/0.50	303	1			12	149
CPO-27-Zn	0.50/0.50	303	1			9	149
Cu-BTC	0.25/0.75	303	1	1.2	0.6	6.6	136a
Cu-BTC	0.50/0.50	303	1	2.0	0.4	5.6	136a
Cu-BTC	0.75/0.25	303	1	3.0	0.2	6.6	136a
Mg-MOF-74	0.20/0.80			2.02	≈0	close to infinite	150
MIL-100(Fe)	0.50/0.50	303		1.49	0.28	5.3	136b
MIL-100(Fe), 50% RH	0.50/0.50	303		3.75	0.23	16.3	136b
MIL-100(Fe)	0.20/0.80	303		0.87	1.21	2.9	136b
MIL-101(Cr)	0.50/0.50	303		2.44	0.54	4.5	136b
MIL-101(Cr), 50% RH	0.50/0.50	303		1.37	0.37	3.7	136b
MIL-101(Cr)	0.15/0.85	303		1.67	1.80	3.7	136b
MIL-101(Al)-NH ₂	0.15/0.85	298	1	0.8		66.3	144
MIL-101(Al)-NH ₂	0.30/0.70	298	1	1.0		34.7	144
MIL-101(Al)-NH ₂	0.40/0.60	298	1	1.1		14.2	144
MIL-101(Al)-NH ₂	0.50/0.50	298	1	1.2		6.3	144
MIL-101(Cr)	0.30/0.70	298	1			7.5	144
MIL-101(Cr)	0.50/0.50	298	1			3.6	144
MIL-53(Al)-NH ₂	0.50/0.50	303	1	0.83	≈0	'almost infinite'	151, revised by 145
MIL-53(Al)-NH ₂	0.90/0.10	303	1			59	145
MIL-53(Al)-NH ₂	0.70/0.30	303	1			23	145
MIL-53(Al)-NH ₂	0.50/0.50	303	1	1.3	0.04	45	145
MIL-53(Al)-NH ₂	0.30/0.70	303	1			90	145
MIL-53(Al)-NH ₂	0.10/0.90	303	1			213	145
MIL-53(Al,PVA)	0.50/0.50	303	1	1.3	0.2	7	152
MIL-53(Al,PVA)	0.25/0.75	303	1	0.65	0.5	3.9	152
MIL-53(Al,PVA)	0.47/0.53	303	1	1.3	0.25	6.6	152
MIL-53(Al,PVA)	0.75/0.25	303	1	1.5	0.08	6.2	152
MIL-53(Cr)	0.25/0.75	303	1			13	153
MOF-508b	0.50/0.50	303	1	0.19	0.17	3	147
SIFSIX-2-Cu-i	0.50/0.50	298	1		3.14	51	126
STA-12-Ni	0.50/0.50	303	1			6	149
α-[Zn(bcba)]	0.10/0.90	298	1	0.35	0.11	2.9	154
α-[Zn(bcba)]	0.40/0.60	298	1	0.25	0.38	2.3	154
β-[Zn(bcba)]	0.10/0.90	298	1	0.15	0.50	32	154
β-[Zn(bcba)]	0.40/0.60	298	1	0.07	1.20	29	154
ZJNU-54	0.50/0.50	298	1.01	2.19		5.2	140a

7. Permanent adsorption of iodine by a pyrene-based MOF resulting in an enhancement of electrical conductivity

This chapter has been adapted from: A. Gladysiak, T. N. Nguyen, M. Spodaryk, J.-H. Lee, J. B. Neaton, A. Züttel, and K. C. Stylianou, *Chem. Eur. J.*, **25**, 501–506, (2019).

My contribution to this work consisted in the synthesis, iodine loading, SCXRD analysis, and characterisation of the discussed material, analysis and plotting of the experimental data, and participation in writing of the manuscript.

7.1. Introduction

Radioactive isotopes of iodine, mainly ^{129}I and ^{131}I , are produced in nuclear-related processes and may accidentally be released into the atmosphere as witnessed in Fukushima and Chernobyl, constituting a major hazard to humans and the environment. The ^{131}I has a radioactive decay half-life of ~ 8 days, emits β^- and γ rays, and concentrates in the thyroid gland of the person exposed to the radioactive source causing thyroid cancer. The ^{129}I isotope is much longer lived, with a half-life of 15.7 million years, and poses a long-term disposal risk. Capturing radioactive iodine is therefore necessary for safe nuclear waste storage.¹⁵⁵

Wet scrubbing and the use of solid adsorbents are two general methods for iodine capture, with the latter being often preferred since it does not require the use of highly corrosive liquids.¹⁵⁵ The benchmark solid adsorbents for radioactive iodine capture is the silver (Ag)-exchanged zeolitic mordenite, with an average I_2 adsorption capacity of $\sim 100\text{--}130\text{ mg g}^{-1}\text{mordenite}$ at high temperatures ($150\text{--}200\text{ }^\circ\text{C}$).¹⁵⁵⁻¹⁵⁶ In recent years, metal–organic frameworks (MOFs), which are crystalline materials formed by linking metal ions or metal clusters with multi-topic organic ligands,¹⁵⁷ have emerged as promising adsorbents for I_2 capture due to their high porosity¹⁵⁸ and chemical tuneability.¹⁵⁹ For example, our group has previously reported a high I_2 vapour uptake by HKUST-1 and ZIF-8, and their composites with polymers, reaching $538\text{ mg g}^{-1}\text{HKUST-1}$ at $75\text{ }^\circ\text{C}$.¹⁶⁰ The Nenoff group and the Thallapally group have studied the adsorption of I_2 on HKUST-1 and SBMOFs, respectively, in the presence of humidity.¹⁶¹ However, the degradation of these MOFs in water, and the leaching of I_2 from the I_2 -loaded MOFs when they are in contact with water and common organic solvents give rise to considerable concerns regarding the potential of these MOFs for I_2 capture. The I_2 leaching is thought to be due to the weak interaction between the I_2 molecules with the pore surface of the MOF.

Herein, we report that the MOF **SION-8**¹⁶² can efficiently capture I_2 vapour at both room temperature and at $75\text{ }^\circ\text{C}$. The strategy for I_2 capture is based on the well-known donor–acceptor interaction between pyrene and I_2 .¹⁶³ We will present single-crystal X-ray diffraction (SCXRD), impedance spectroscopy, and gravimetric studies as well as van der Waals-corrected density functional theory (vdW-corrected DFT) calculations to elucidate the location and interaction between I_2 and the pyrene-decorated pore surface of **SION-8**.

7.2. Experimental section

7.2.1. Synthesis of **SION-8** and iodine loading

The reaction between 10 mg (0.0680 mmol) of $\text{CaCl}_2 \cdot 2\text{H}_2\text{O}$ and 10 mg (0.0146 mmol) of H_4TBAPy (prepared using a previously reported procedure)¹³² in the solution composed of 2 mL of *N,N*-dimethylformamide (DMF), 1 mL of H_2O and 80 μL of HCl (techn., 32%) at 120 °C for 72 h resulted in 11.85 mg (0.0126 mmol, 86.0% yield) of $[\text{Ca}_2(\text{TBAPy})(\mu_2\text{-OH}_2)_2] \cdot 2\text{DMF}$ (**SION-8**) in the form of single crystals.¹⁶²

The crystals of **SION-8** were introduced into an open vial, which in turn was enclosed in a glass vessel containing solid iodine. The vial containing **SION-8** was repeatedly weighted to determine the increase of the mass of the sample. The procedure was repeated *i.* at room temperature and *ii.* at 75 °C. Anal. Calcd for $[\text{Ca}_2(\text{TBAPy})(\mu_2\text{-OH}_2)_2] \cdot 1.4 \text{ DMF} \cdot 1.5 \text{ I}_2$: C 45.30, H 2.82, N 1.53; found: C 45.36, H 2.86, N 1.52.

7.2.2. Single-crystal X-ray diffraction analysis

A high-quality single crystal of **SION-8** $\cdot\text{I}_2$ was mounted onto a PILATUS@SNBL diffractometer at the BM01 beamline (European Synchrotron Radiation Facility, Grenoble, France),¹³³ and probed with X-rays ($\lambda = 0.72179 \text{ \AA}$). Preliminary exposures confirmed the singularity of the crystal. Reflection intensities were measured using the PILATUS2M detector. The crystal was kept at 100(2) K during data collection. Raw data were processed with CrysAlisPro (v. 1.171.38.43) program suite,¹⁶⁴ and the empirical absorption correction was performed using spherical harmonics, implemented in SCALE3 ABSPACK scaling algorithm. Crystal structure was solved with the SHELXT structure solution program using Intrinsic Phasing,¹⁰² and refined with the SHELXL refinement package using least-squares minimization,⁶⁰ implemented in the Olex2 program suite.⁹¹ Contribution of the disordered solvent molecules found in the structural voids to the measured structure factors was quantified with the SQUEEZE procedure of the PLATON program suite.⁶² Solvent accessible volume of 571 \AA^3 (24.8%) (probe radius 1.2 \AA) was calculated with the program MERCURY (v. 3.10.1).⁶⁸ The difference in the radii of the vibration ellipsoids of atoms I1 and I2 along the bond between them of 0.00021 \AA^2 was calculated with the program PLATON (v. 120716).¹⁶⁵

Unit-cell parameters derived from the SCXRD study were used as a starting point of the full profile decomposition of the powder XRD pattern of **SION-8** $\cdot\text{I}_2$. Fitting was performed using the FullProf program suite.¹³⁵ Le Bail-refined unit-cell parameters were $a = 6.8361(2) \text{ \AA}$, $b = 20.3071(7) \text{ \AA}$, $c = 16.5648(6) \text{ \AA}$, space group *Pbam*, $\lambda = 0.72179 \text{ \AA}$.

7.2.3. Impedance spectroscopy measurements

Conductivity of **SION-8** $\cdot\text{I}_2$ was investigated using electrochemical impedance spectroscopy (EIS). The measurements were performed on potentiostat/galvanostat PGSTAT302N with FRA32M module (Metrohm Autolab). Impedance spectra of the powder samples pressed into 8 mm diameter (thickness of 0.6–0.65 mm) pellets were measured in the range of working frequencies from 1 Hz to 1 MHz. The measurement frequency range is built using a logarithmic distribution. The voltage modulation amplitude was set to 10 mV. Pressed powder samples were investigated in home-designed conductivity cell with copper contacts previously plated with gold in order to assure their chemical stability during measurements. In order to achieve a sufficient contact between powder particles the measurements were carried out under the pressure of 1990 kG/cm^2 . The impedance spectra were obtained in the range of temperatures of 5–23 °C.

7.3. Results and discussion

SION-8 was synthesised from the self-assembly of Ca^{II} ions with the TBAPy^{4-} ligand in an acidified mixture of DMF and water, giving rise to single crystals of $[\text{Ca}_2(\text{TBAPy})(\mu_2\text{-OH}_2)_2]\cdot 2\text{DMF}$. **SION-8** crystallises in the orthorhombic space group *Pbam*, and its structure is based on 1-dimensional Ca-O chains extending along the *a*-axis interlinked by the fully deprotonated TBAPy^{4-} . Structural analysis reveals two symmetrically inequivalent channels across the structure of **SION-8**, one of which is exposed to the lateral sides of the TBAPy^{4-} ligands and hence possesses a hydrophobic character, whilst the other one is surrounded by the O-atoms of the Ca-O chains and coordinated H_2O molecules which endow it with a more hydrophilic character. The phase purity of **SION-8** was confirmed by powder X-ray diffraction (PXRD).

When the partially activated single crystals of **SION-8** were exposed to I_2 vapour at room temperature, the yellow colour of the crystals slowly turned to black purple. After 72 h of I_2 loading, a single crystal was picked to investigate its structure with SCXRD (Table 19). **SION-8** $\rightarrow\text{I}_2$ conserves the original framework connectivity of **SION-8** (Figure 67a). I_2 molecules were found to be located within the pores of the framework, with an average of 0.405 I_2 molecules in each hydrophobic pore; simultaneously, the hydrophilic pores are occupied by the disordered DMF solvent molecules. The formula of this material sums up to $[\text{Ca}_2(\text{TBAPy})(\text{H}_2\text{O})_2]\cdot\text{DMF}\cdot 0.81\text{I}_2$. Both atoms of the I_2 molecule, named I1 and I2, are located at special positions with the Wyckoff site multiplicity reduced by a factor of 2, while their site occupancy factor refines to 0.405(9). The I1–I2 distance equals 2.73(2) Å, which is comparable to the I–I separations reported in other crystal structures (Figure 71). The I_2 molecule is nearly perpendicular to one pyrene core of TBAPy^{4-} and nearly parallel to the neighbouring one with the shortest $\text{I}_2\text{--TBAPy}^{4-}$ distance of 3.609(15) Å (Figure 67b). Visualisation of the crystal structure of **SION-8** $\rightarrow\text{I}_2$ may suggest the existence of infinite $(\text{--I--I--})_n$ chains; however, since the I1 and I2 atom sites are not fully occupied, such chains are probably not formed.

The shapes of anisotropic displacement ellipsoids of I1 and I2 seem intricate; however, they conform to the ‘rigid-bond postulate’.¹⁶⁶ The difference in the radii of the vibration ellipsoids of atoms I1 and I2 along the bond between them of 0.00021 Å² is situated below the limit imposed by the Hirshfeld test (0.001 Å²).¹⁶⁷ Substantial improvement of refinement indicators when an I_2 molecule is introduced into the crystal structure (Table 20) makes still another argument in favour of the occurrence of I_2 molecules in the hydrophobic pores of **SION-8**. Further improvement of *R*-factors on squeezing⁶² indicates the presence of heavily disordered DMF molecules in the hydrophilic pores. However, the results of squeezing of the ‘bare’ and the I_2 -containing structure are virtually the same.

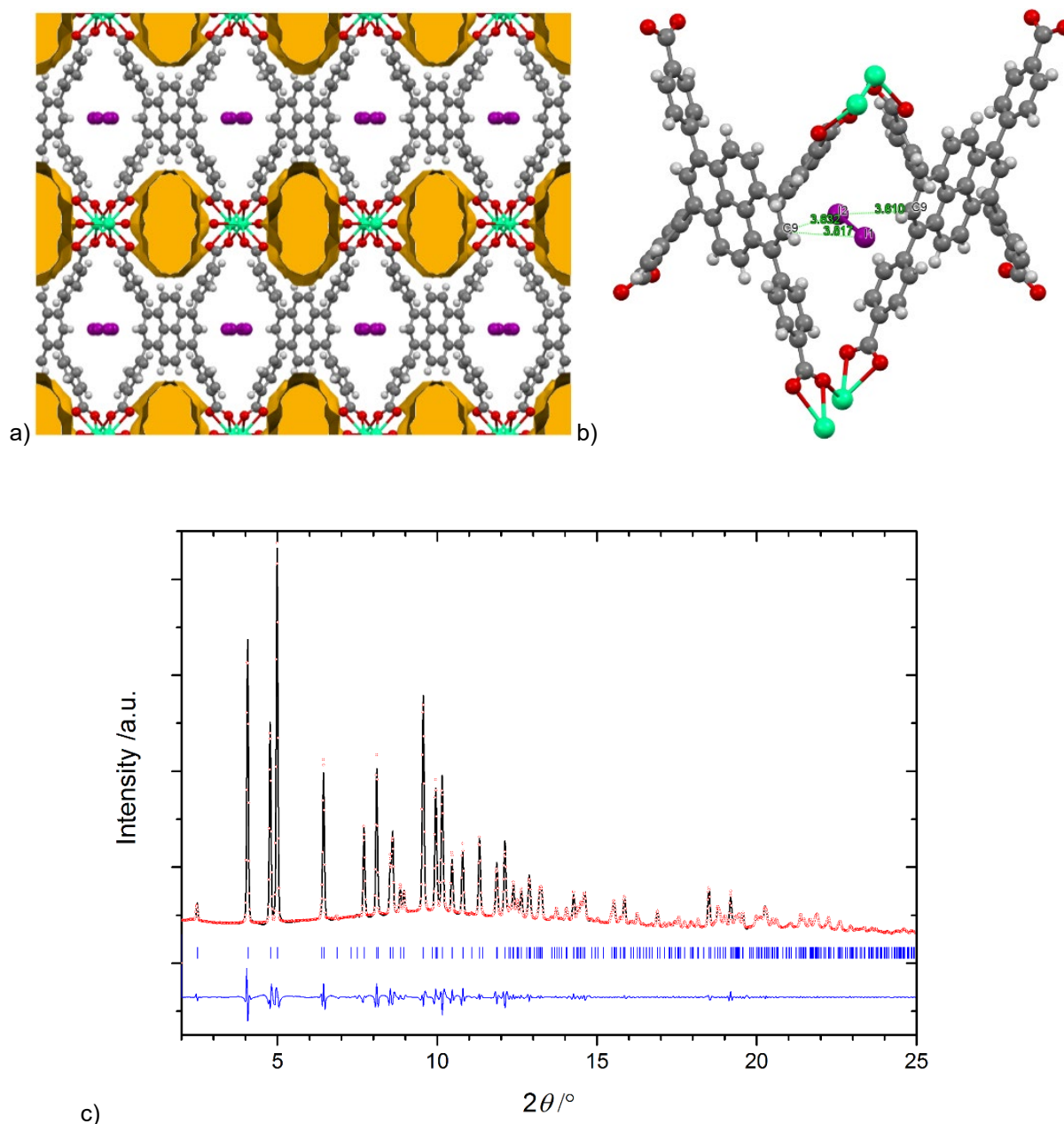


Figure 67. (a) Crystal structure of **SION-8I₂** viewed along the *a*-axis. Atom color code: green, Ca; purple, I; red, O; grey, C; white, H. Disordered solvent-containing structural voids have been depicted as gold surfaces. (b) Localization of the I₂ molecule within the hydrophobic pore of **SION-8**. Precise values of the highlighted closest I₂–TBAPy⁴⁻ distances are: I2–C9 = 3.609(15) Å, I2–C9' = 3.64(2) Å, I1–C9' = 3.817(18) Å. (c) PXRD Le Bail refinement of **SION-8I₂** (space group *Pbam*: $R_p = 2.09\%$, $R_{wp} = 2.78\%$; $a = 6.8361(2)$ Å, $b = 20.3071(7)$ Å, $c = 16.5648(6)$ Å, $\lambda = 0.72179$ Å). Experimental data are shown as black plots, the refined Le Bail profiles as red dots, and the difference between them as blue plots. Reflection positions are marked with blue.

Inspired by the results of the crystallographic analysis, we investigated the time-dependent adsorption of I₂ vapour in the partially activated powder samples of **SION-8** at room temperature and at 75 °C. The I₂ adsorption can be visually observed as the yellow powder of **SION-8** quickly turns its colour to black purple. The PXRD pattern of the I₂-loaded sample is comparable with the one of **SION-8** (Figure 67c), with the Bragg reflections remaining at the same positions although the intensity of several of them is lower (Figure 72). The decrease of the PXRD peaks' intensity is probably due to the I₂

molecules being incommensurate with the periodicity of the framework, and is also often observed in other guest@MOF systems.^{36d, 168} As shown in Figure 68, at room temperature, I₂ is relatively quickly adsorbed and the uptake capacity reaches 34 wt% (340 mg g⁻¹_{MOF}) after 200 hours. The adsorption rate is then decreased, and by 1000 hours, the total adsorption is 46 wt% (460 mg g⁻¹_{MOF}). This corresponds to 1.6 I₂ molecules per formula unit of **SION-8**, which is matched by the result of the elemental analysis (see the Experimental section). Since adsorption is an exothermic process, the equilibrium I₂ loading at 75 °C is shifted towards the substrates (compared with the case of room temperature) with the total adsorption of 25 wt% (250 mg g⁻¹_{MOF}). On the other hand, at 75 °C, the adsorption reaches saturation in a much shorter time, already after 2.5 h. Interestingly, when fully activated **SION-8** is used instead of the partially activated material, virtually the same adsorption figure was obtained, suggesting a preference of non-polar I₂ molecules to occupy solely the hydrophobic pores (Figure 73). The rate of adsorption at 75 °C is in fact five times greater than that of HKUST-1 crystalline powder, as 1 gram of HKUST-1 adsorbs ~100 mg I₂ after 5 hours.¹⁶⁰ This also suggests that **SION-8** has high affinity towards I₂, most probably due to the strong interaction between the I₂ molecules and pyrene-decorated pore surface of **SION-8**. Based on our vdW-corrected DFT calculations which previously were shown to reliably quantify the host-guest interactions in MOF-based systems,¹⁶⁹ the computed I₂ binding energy is -73.2 kJ mol⁻¹ which is comparable to those found in other charge transfer MOF-I₂ complexes (MOFs with open metal sites).¹⁷⁰ More interestingly, washing the **SION-8**⊃I₂ powder with water or copious amounts of common organic solvents such as ethanol, toluene, and hexane gives rise to the release of only 5.0% of the captured I₂ (Figure 74).

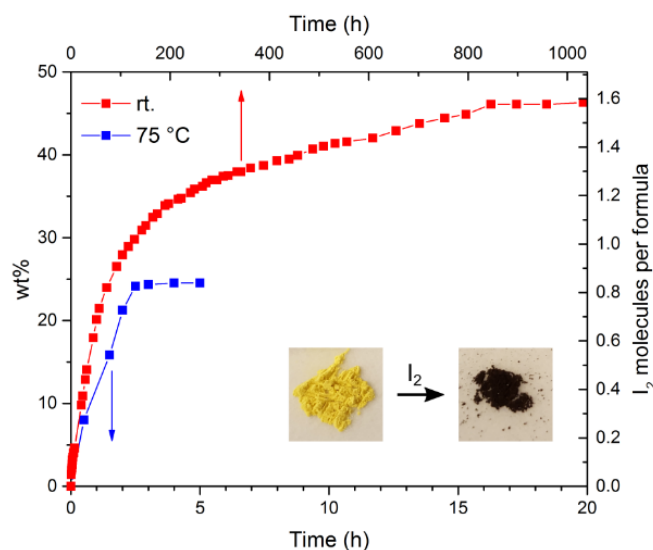


Figure 68. I₂ adsorption on partially activated **SION-8** at room temperature (red plots) and at 75 °C (blue plots). Note two different time scales for these processes. The inset comprises the photographs of **SION-8** and **SION-8**⊃I₂ powder samples.

Thermal stability of **SION-8**⊃I₂ was investigated with differential scanning calorimetry (DSC). Upon continuous heating, DSC profile of **SION-8**⊃I₂ featured a broad endothermic peak starting at 70 °C and centred at 140 °C (Figure 75). This peak, however, was absent when the sample was cooled down to room temperature and heated up again during the second thermal cycle. Therefore, we associate that peak to the endothermic desorption of I₂ from within the pores of **SION-8**⊃I₂. This result signifies that I₂ can be permanently captured by partially activated **SION-8** in a broad range of temperatures spanning from room temperature up to ca. 70 °C. ZrDMBD-I₂ exhibited a similar thermal stability (up to 90 °C), however, in that case I₂ could be released by washing the sample with 1,2-ethanedithiol.^{159a}

To investigate this interaction further, we first collected the diffuse reflectance spectra of **SION-8** and **SION-8**⊃I₂ (Figure 76). **SION-8** displays a broad and strong absorption in the 250–500 nm region, with the peak centred at ~400 nm, which can be attributed to the π – π^* transitions of the TBAPy^{4–} ligand. On the other hand, **SION-8**⊃I₂ absorbs light in a very broad range of the visible region with the low-energy photon absorption threshold extending far into the IR region, suggesting the occurrence of a charge transfer process that significantly lowers the bandgap energy of the material. Similar phenomenon was observed for other I₂@MOFs; for example, Hu *et al.* reported the MOF [Tb(Cu₄I₄)(ina)₃(DMF)] in which the I₂@[Tb(Cu₄I₄)(ina)₃(DMF)] displayed a broad absorption over the visible window and its bandgap is 1.5 eV lower than the one of the bare MOF.¹⁷¹ It is worth noting that the interaction of I₂ with aromatic compounds has been studied since the 1940s and the hypothesis was that I₂ has an abnormally high dielectric polarization in these liquids and forms complexes of solvent-I⁺I[–].¹⁷² In the case of pyrene (and other highly aromatic compounds), the donor–acceptor charge transfer between the pyrene molecule and I₂ leads to a high electrical conductivity of the pyrene–I₂ complex compared to its individual components.¹⁶³ Inspired by this study, we then performed the electrochemical impedance spectroscopy measurements on **SION-8** and **SION-8**⊃I₂. The powders of the samples were pressed into pellets and placed in a home-designed conductivity cell. The impedance spectra were obtained in the range of temperatures of 5–23 °C (Figure 77). As can be observed in Figure 69, **SION-8**⊃I₂ displays electrical conductivity that increases with increasing temperature and reaches $\sigma = 5.3 \times 10^{-6}$ S/cm at 23 °C. This value is comparable to those reported for other I₂@MOFs,^{171, 173} although the latter were obtained from a variety of different methods;¹⁷⁴ similar in size increase of electrical conductivity was also reported for other MOF charge transfer complexes, namely by utilising fullerenes and TCNQ as electron acceptors.¹⁷⁵ In contrast to the semiconducting behaviour of the I₂-captured sample, **SION-8** is an insulator ($\sigma < 10^{-9}$ S/cm) and the semi-circular impedance spectrum for this material could not be obtained. We note that the frequency range covered by our electrochemical impedance spectroscopy measurements (from 1 Hz to 1 MHz) was not capable of capturing the electronic conductivity, the latter becoming significant only in the GHz region. Therefore, we reason that either iodide or polyiodide ions, or even polarised I₂ molecules could be responsible for the measured electrical conductivity, however, we were unable to resolve the question which species indeed caused the electrical conductivity increase. The fact of significant electrical conductivity of **SION-8**⊃I₂ seems incontestable based on our measurements, however, no conclusion can be drawn on the sheer nature of the charge carriers.

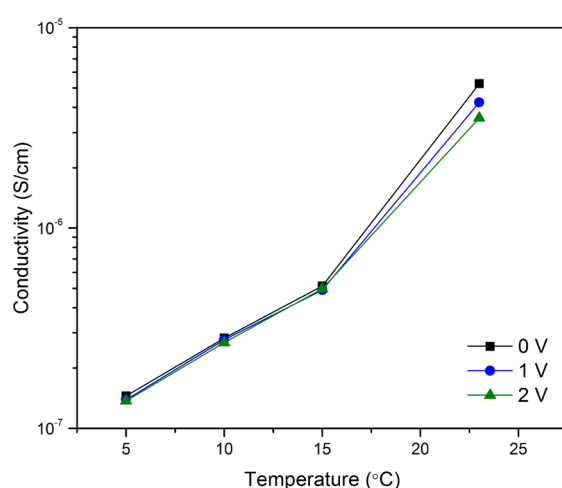


Figure 69. Electrical conductivity as a function of temperature collected on **SION-8**⊃I₂.

To further confirm the charge transfer interaction between the framework of **SION-8** and I_2 , DFT calculations were performed. Figure 70 shows the computed total and partial density of states (DOS) of the two structures. Since the contribution of Ca s and p orbitals to the projected DOS is negligible within the energy window shown in Figure 70, this contribution was excluded. As shown in Figure 70a, the valence band maximum (VBM) and conduction band minimum (CBM) levels of **SION-8** are mainly composed of C 2p character, and the calculated DFT-vdW-DF-cx band gap is 2.08 eV. For **SION-8** $\rightarrow I_2$, interestingly, the CBM states are characterized by the I p character. As illustrated in Figure 70b, the I 5p–I 5p antibonding states are located above the VBM level. Due to this, the band gap is significantly reduced to 0.48 eV. Although DFT is known to underestimate the band gap,¹⁷⁶ it can often predict the trends in band gap.¹⁷⁷ Given the extended nature of both the C p and I p states along the pore direction, we expect the trend in the DFT-vdW-DF-cx band gap to be consistent with experiment in this case as well. This smaller band gap has in turn impact on the increase of the conductivity of **SION-8** $\rightarrow I_2$ compared to **SION-8**.

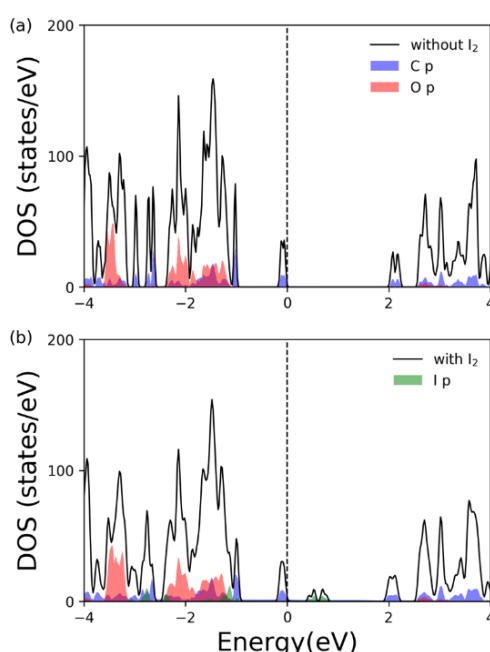


Figure 70. Computed total density of states (DOS, depicted as the black contour) and partial charge density (PDOS, coloured as a function of contributing element) of C, O and I atoms of (a) **SION-8** (b) **SION-8** $\rightarrow I_2$

7.4. Conclusions

In summary, we report a pyrene-based MOF that can adsorb I_2 vapour with high capacity. The strong interaction between I_2 and the pyrene-based ligand of **SION-8** is due to the donor–acceptor charge transfer between them, and manifested by the changes in the photophysical and electrical properties of the MOF. This leads to the incarceration of I_2 within the MOF’s cavity, suggesting the potential of **SION-8** for capturing radioactive I_2 .

Atomic-level ordering of I_2 molecules within the mutually parallel hydrophobic pores of **SION-8** extending across the entire crystal allows another potential application of **SION-8** $\rightarrow I_2$. I_2 is a molecule characterised by a high molecular mass, and therefore it is expected to exhibit a high refractive index. A material consisting in a single-crystal thin film of **SION-8** $\rightarrow I_2$ would have a highly anisotropic refractive index: very high along the ordered I_2 chains, and significantly lower in a perpendicular

direction. Furthermore, engineering a thin film would considerably reduce light absorptivity of the material, the latter growing exponentially with the thickness. Both these characteristics are key for the construction of an efficient light polariser, or polaroid, an optical filter that lets light waves of a specific polarisation pass through, while blocking light waves of other polarisations. Use of polarisers is widespread in liquid-crystal displays and various optical set-ups. Practical realisation of this concept, however, would require the advanced technology of growing sufficiently large thin films of the single-crystal quality followed by efficient partial activation and I₂ loading without loss of monocrystallinity.

7.5. Appendix

Table 19. Crystal data and structure refinement for **SION-8-I₂**.

Identification code	SION-8_I2
Empirical formula	C _{23.5} H _{16.5} CaI _{0.86} N _{0.5} O _{5.5}
Formula weight	542.77
Temperature/K	100.0
Crystal system	orthorhombic
Space group	Pbam
a/Å	6.9388(3)
b/Å	20.8110(7)
c/Å	16.5100(3)
α/°	90
β/°	90
γ/°	90
Volume/Å ³	2384.10(14)
Z	4
ρ _{calc} /g/cm ³	1.512
μ/mm ⁻¹	1.458
F(000)	1082.0
Crystal size/mm ³	0.07 × 0.05 × 0.02
Radiation	synchrotron (λ = 0.72179)
2θ range for data collection/°	3.976 to 50.878
Index ranges	-7 ≤ h ≤ 7, -24 ≤ k ≤ 24, -19 ≤ l ≤ 19
Reflections collected	7582
Independent reflections	1841 [R _{int} = 0.0280, R _{sigma} = 0.0259]
Data/restraints/parameters	1841/43/146
Goodness-of-fit on F ²	2.216
Final R indexes [I ≥ 2σ (I)]	R ₁ = 0.1563, wR ₂ = 0.4513
Final R indexes [all data]	R ₁ = 0.1622, wR ₂ = 0.4624
Largest diff. peak/hole / e Å ⁻³	1.80/-0.62
CCDC	1865814

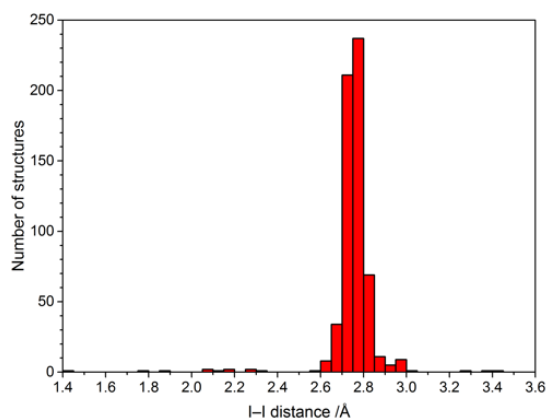


Figure 71. Distribution of the I-I distances derived from the 602 crystal structures containing an I₂ molecule found in the Cambridge Structural Database (version 5.39).⁶⁶

Table 20. Indicators of different steps of **SION-8**⊃I₂ crystal structure refinement.

	<i>R</i> ₁
structure with I ₂	17.59%
structure without I ₂	34.39%
structure without I ₂ , squeezed	15.14%
structure with I ₂ , squeezed	15.73%

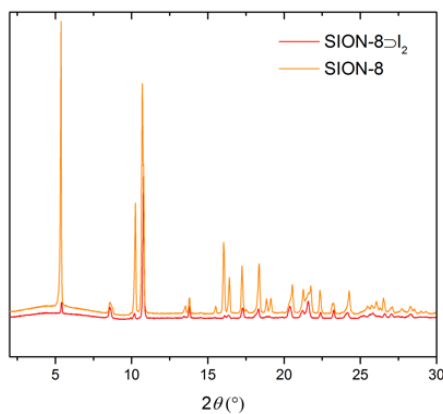


Figure 72. PXRD pattern of the parent **SION-8** (orange plots) and iodine-adsorbed **SION-8**⊃I₂ (red plots).

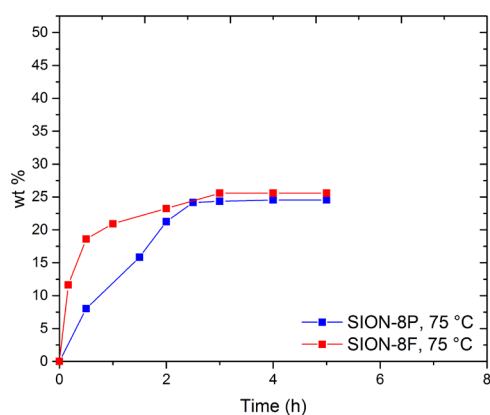


Figure 73. Comparison between the mass increase exhibited by the partially activated **SION-8** (blue plots) and that by the fully activated **SION-8** (red plots) upon vapour I_2 adsorption at 75 °C. Both materials reach the saturation at ca. 25 wt%.

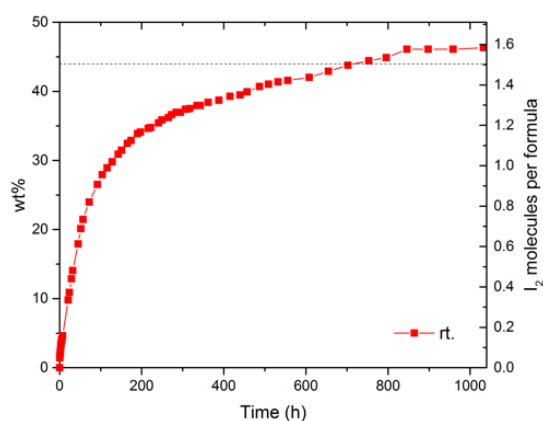


Figure 74. Mass increase of a sample of **SION-8** exposed to I_2 vapours for 1000 h. After the I_2 adsorption experiment, the sample of **SION-8** was washed with 40 mL of ethanol, followed by 40 mL of hexane and 40 mL of acetone. At the beginning of the first washing the filtrate was brown (due to the dissolution of I_2 physically adsorbed on the surface of the solid), and soon it turned to colourless. Washings with hexane and acetone did not give rise to the solvent colour change. At the same time the colour of the solid being washed remained black purple. It underwent a negligible (–5.0 wt%) mass drop which is marked in the figure with a dashed black line.

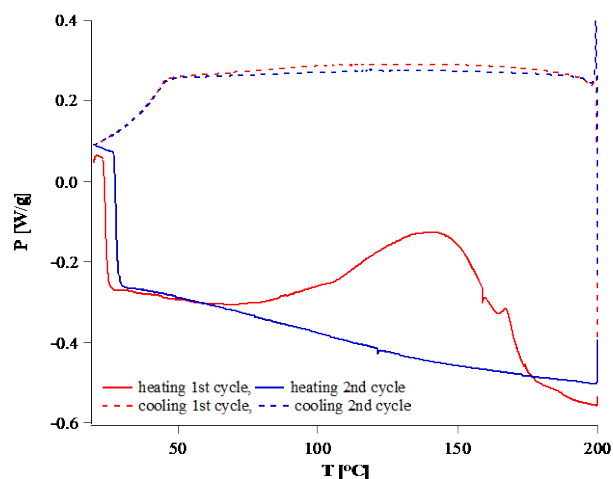
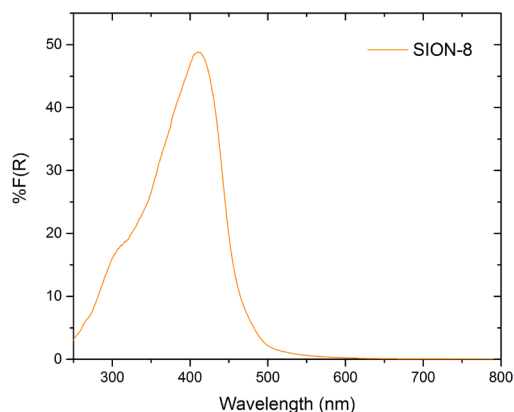
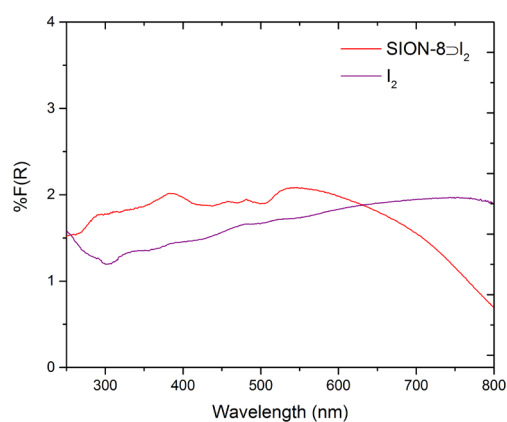


Figure 75. DSC profile of **SION-8-I₂**. The endothermic peak is present during the first heating cycle, which is associated to the I₂ desorption, while during the second heating cycle that peak is absent. The measurement was performed with a high pressure DSC 827e instrument from Mettler Toledo. The sample was measured in a standard aluminium pan with a pin (40 µL) at ambient pressure. The heating power of the sample was measured from 20 °C to 200 °C with the heating rate of 5 °C/min and cooled down with the same rate; this procedure was repeated twice.



a)



b)

Figure 76. UV/vis diffuse reflectance spectra of (a) **SION-8** and (b) **SION-8-I₂** compared to the spectrum of I₂.

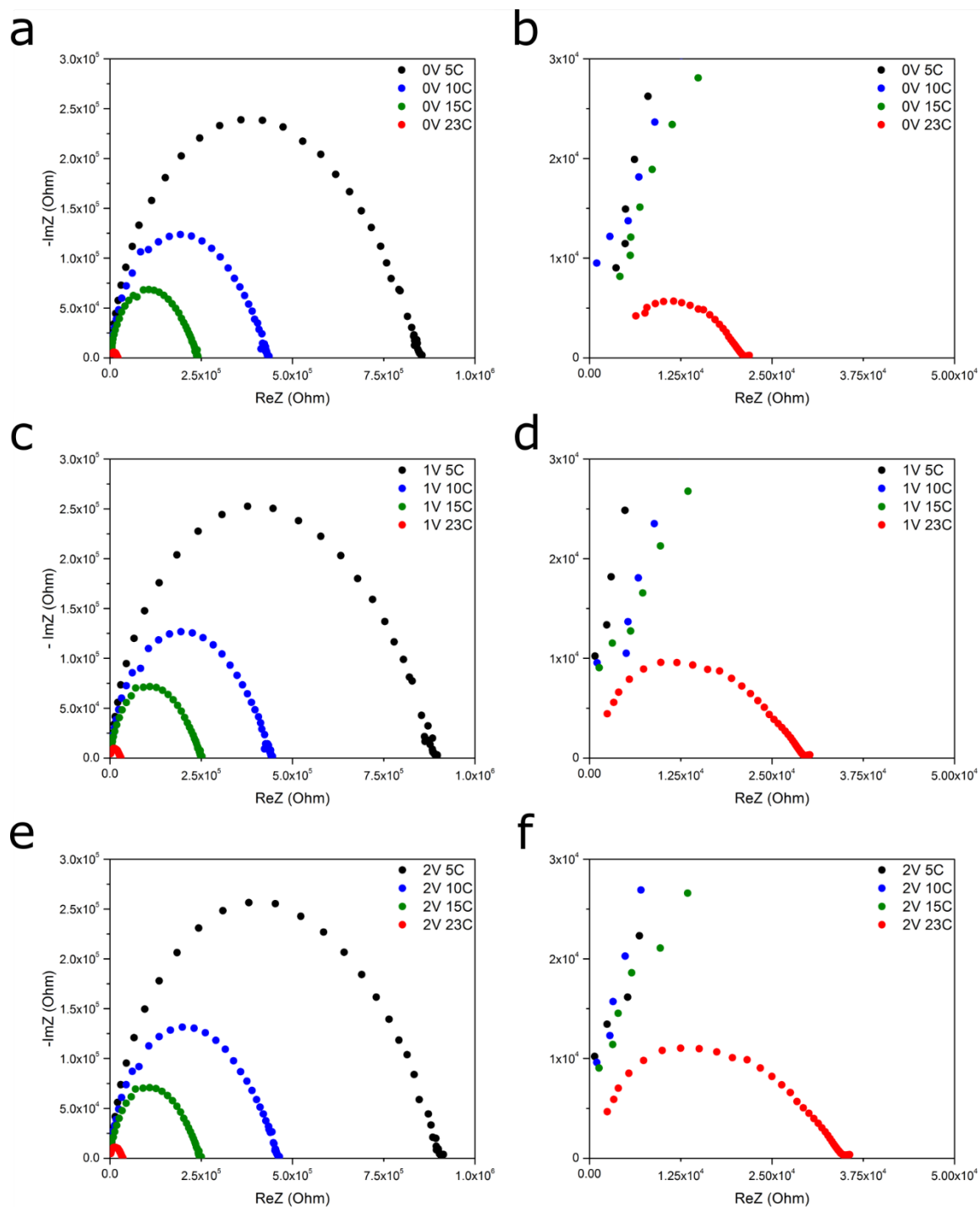


Figure 77. Impedance spectra collected for **SION-8I₂** at 5, 10, 15 and 23 °C. (a) Voltage used: 0 V. (b) Voltage used: 0 V, close-up. (c) Voltage used: 1 V. (d) Voltage used: 1 V, close-up. (e) Voltage used: 2 V. (f) Voltage used: 2 V, close-up.

8. Temperature-dependent interchromophoric interaction in a porous pyrene-based metal–organic framework

This chapter has been adapted from: A. Gladysiak, T. N. Nguyen, R. Bounds, A. Zacharia, G. Itskos, J. A. Reimer, and K. C. Stylianou, *Chem. Sci.*, **10**, 6140–6148, (2019).

My contribution to this work consisted in the synthesis, SCXRD analysis, topological analysis, and characterisation of the discussed material, execution of the *in-situ* SCXRD experiment using synchrotron radiation, analysis and plotting of the experimental data (including VT fluorescence spectra), and participation in writing of the manuscript.

8.1. Introduction

Interchromophoric interactions play a crucial role in the optical properties of materials that are assembled from multiple chromophores. For non-interacting chromophores, after photoexcitation, the excited electron can simply relax to the ground state via fluorescence and/or via non-radiative processes such as internal conversion and intersystem crossing. When the chromophores are coupled, e.g. when they are positioned in proximity to each other and with a suitable orientation, however, an excited chromophore can pair up with a nearby unexcited chromophore to form an excimer (excited dimer), which often displays emission that is markedly different than the one of the chromophore itself.¹⁷⁸ When the components of the interacting chromophores are of different chemical identity, the entity is called exciplex (excited complex). Excimers and exciplexes have found numerous applications. They can be used to estimate the distance between biomolecules grafted with organic chromophores,¹⁷⁹ while their application in chemical sensing or luminescent thermometry has also been widely studied.¹⁸⁰ In addition, while embedded in a polymeric matrix, they can serve as wavelength switchable microlasers.¹⁸¹

Among fluorescent organic compounds, pyrene and its derivatives are canonical examples that display excimer fluorescence, which is often a structureless emission band in high-concentration solutions. When the solution is diluted, the structured emission band at lower wavelengths originating from the unassociated monomer becomes more dominant as the interaction between the pyrene chromophores is diminishing.¹⁸² This principle of interchromophoric interaction is also applied for pyrene and its derivatives in the solid state.¹⁸³ Apparently, if this interaction can be finely controlled, materials with desired optical properties can be rationally designed. In fact, efforts in investigating the interchromophoric interaction in pyrene-based organic and inorganic solid materials have been noticed.¹⁸⁴ For the latter, recent focus is on pyrene-based metal–organic frameworks (MOFs).^{132, 162, 185}

MOFs are crystalline materials which often exhibit high porosity and structural tuneability,^{23, 186} and can be synthesised in a wide range of topologies.¹⁸⁷ They have found numerous applications, including methane storage,¹⁸⁸ heterogeneous catalysis¹⁸⁹ as well as temperature,¹⁹⁰ pressure,^{35f, 191} and chemical sensing.^{190, 192} Optical properties of MOFs, such as their UV/vis absorption, are known to be finely tuneable by external stimuli, e.g. chemical species,¹⁹³ temperature¹⁹⁴ or pressure.¹⁹⁵ The fluorescence of MOFs has been equally intensely investigated.¹⁹⁶ This arises from the fact that in many instances, the usefulness of MOF materials stems from their fluorescence emission, which in turn is heavily dependent on the interactions between the chromophores. Excimer emission of MOF materials due to interchromophoric interactions have been observed in several cases.^{180a, 180b, 197} In particular, the extent of the interchromophoric interaction in several MOFs was found to be topology-

dependent as each MOF displayed different concentration, distance, and mutual orientation of the ligands.^{184c, 184d} However, it is still unclear how the interchromophoric interaction can be controlled within each porous material; therefore, this is still an attractive platform for further investigation, and is the topic of this chapter.

Herein, we report a porous MOF, named **SION-7**, based on Mg^{II} and H₄TBAPy (1,3,6,8-tetrakis(*p*-benzoic acid)pyrene). The intensity and position of the fluorescence emission band of **SION-7** is temperature-dependent, with a structured emission spectrum characteristic for pyrene-derivative monomers at low temperature, which gradually transforms to a structureless red-shifted emission spectrum when the temperature is increased, indicating the presence of excimers due to interchromophoric interaction. Ex-situ variable-temperature (VT) single-crystal X-ray diffractometry (SCXRD) studies were performed providing insights into the relationship between the structure and the temperature-dependent interaction between the pyrene moieties, and will be discussed in detail.

8.2. Experimental section

8.2.1. Procedures and materials

All manipulations were performed under aerobic conditions using chemicals and solvents as received without further purification. The compound H₄TBAPy was synthesised using a previously reported procedure.¹³²

8.2.2. Synthesis of **SION-7**

With the chemical formula of [Mg_{1.5}(HTBAPy)(H₂O)₂] \cdot 3DMF, **SION-7** was synthesised from the reaction of 10.0 mg (0.0390 mmol) of Mg(NO₃)₂ \cdot 6H₂O and 10.0 mg (0.0146 mmol) of H₄TBAPy in a mixture composed of 5.0 mL of *N,N*-dimethylformamide (DMF), 1.0 mL of H₂O and 80 μ L of HCl (techn., 32%) held at 393 K for 72 hours. Block-shape single crystals of **SION-7** suitable for SCXRD analysis were obtained in a 47.8% yield (6.8 mg). The activated sample, **SION-7a**, was prepared by heating the dried powdered sample of **SION-7** at 403 K under dynamic vacuum for 8 hours.

8.2.3. Single-crystal X-ray diffraction

A high-quality single crystal of **SION-7** was isolated from the mother liquor, and mounted onto the PILATUS@SNBL diffractometer at the BM01 beamline (European Synchrotron Radiation Facility, Grenoble, France).¹³³ The crystal was kept at 100 K, probed with X-rays, and the intensities of Bragg reflections were recorded with the PILATUS2M detector. Raw data were processed with CrysAlisPro (v. 1.171.38.43) program suite,¹⁶⁴ and the empirical absorption correction was performed using spherical harmonics, implemented in SCALE3 ABSPACK scaling algorithm. Crystal structure was solved with the SHELXT structure solution program using Intrinsic Phasing,¹⁰² and refined with the SHELXL refinement package using least-squares minimisation,⁶⁰ implemented in the Olex2 program suite.⁹¹ Structure simplification and net classification was performed using the TOPOS Pro program suite.¹³⁴ Crystal structure-derived pore volume as well as contribution of the disordered solvent molecules found in the structural voids to the measured structure factors were quantified with the solvent mask procedure implemented in Olex2.⁶³ The integrated electron density found in the pores was interpreted in terms of number of DMF molecules by comparison to the electron count of the latter (C₃H₇NO, 40 e⁻).

Variable-temperature (VT) SCXRD measurements were performed by modifying the abovementioned procedure. The temperature was controlled with a Cryostream 700+ nitrogen blower. Full sphere of

reflections was recorded at each temperature point, and the corresponding crystal structures were further solved and refined. Eventually, crystal structure of **SION-7** was determined at 100, 150, 200, 250, 270, 293, 310, 330, and 350 K on heating and subsequent cooling.

8.2.4. Other characterisation techniques

Powder X-ray diffraction (PXRD) patterns were recorded using synchrotron radiation at the BM31 beamline (ESRF, Grenoble, France). In the in-situ VT PXRD experiment bulk powder of the as-synthesised **SION-7** was packed into a glass capillary and heated at a rate of 3 K/min from room temperature to 600 K. The Le Bail fit of the pattern recorded at room temperature was performed with the FullProf program suite.¹³⁵

Thermogravimetric analysis (TGA) was performed with the TGA Q500 instrument on a sample heated at a constant rate of 5 K/min with air acting as carrier gas.

Gravimetric gas sorption measurements were performed using the Intelligent Gravimetric Analyzer Instrument (IGA) from Hiden.

¹³C CP-MAS solid-state NMR spectra were recorded at a 700 MHz spectrometer with a rotor spinning frequency of 8 kHz. The density functional theory (DFT)-based code CASTEP was used to calculate the predicted chemical shifts.

Fourier-transform infrared (FT-IR) spectra were recorded on a Perkin Elmer Spectrum Two FT-IR spectrometer.

Diffuse reflectance UV/vis spectra were recorded on a Perkin Elmer Lambda 950 S spectrometer.

VT fluorescence spectra were recorded in the 80–450 K temperature range in steps of 10 K (80–200 K range) or 25 K (200–450 K range), as well as in the 80–200 K temperature range in steps of 10 K, covering the range of wavelengths of 415–720 nm, using the excitation wavelength of 405 nm. In addition, the fluorescence spectra were expressed in the RGB coordinates using the Commission internationale de l'éclairage (CIE)-1931 standard. Fluorescence decays monitoring the peak emission were fitted with double-exponentials yielding weighted average lifetimes.

8.3. Results and discussion

8.3.1. Synthesis and crystal structure analysis

The synthesis of **SION-7** was performed under solvothermal reaction conditions. Mg²⁺ was chosen to form the MOF as it is diamagnetic and does not cause the quenching of fluorescence often observed with paramagnetic metal ions. The presence of a small amount of HCl is critical for the reaction and it is believed to act as the reaction modulator that facilitates crystal growth by adjusting the reaction kinetics. The molar ratios of the reactants were screened to obtain the phase-pure product. The synthesis procedure is slightly different to that previously reported,¹⁹⁸ therefore, the formulae of the resultant MOFs differ.

The structure of **SION-7** was revealed from the SCXRD measurement. **SION-7** crystallises in the triclinic space group $P\bar{1}$. The asymmetric unit comprises one partially protonated HTBAPy³⁻ ligand, two Mg atoms (one of which sits on a special position with the Wyckoff site multiplicity reduced by a factor of 2), and two coordinated H₂O molecules (Figure 83). **SION-7** is a 2-dimensional structure in which Mg–O trinuclear clusters (Figure 78a) link pairs of mutually parallel HTBAPy³⁻ ligands into infinite layers (Figure 78b). In the third dimension, the clusters form supramolecular chains along the *a*-axis held together by hydrogen bonds (Figure 84). Within each of these clusters, Mg1 assumes the

central position (it is localised on an inversion centre), Mg₂ is present in form of two symmetrical equivalents, and both Mg₁ and Mg₂ adopt an octahedral coordination geometry with the coordination number 6 (Figure 78a). Such clusters are not uncommon in the coordination chemistry of magnesium.¹⁹⁹ Four HTBAPy³⁻ positioned in the middle of the Mg₃-cluster use both their carboxylate O-atoms to bind to Mg₁ and Mg₂ through the $\eta^1:\eta^1$ -bridging mode, while the other four HTBAPy³⁻ ligands are η^1 -coordinated to Mg₂ through a single carboxylate O-atom (Figure 78c). Analogous types of positions are assumed by coordinated H₂O molecules, with two of them in the middle of the Mg₃-cluster being $\eta^1:\eta^1$ -bridging and two others at its extremities being η^1 -coordinated. In addition, HTBAPy³⁻ ligands η^1 -coordinated to Mg₂ are bound with strong hydrogen bonds to the bridging H₂O molecules (Figure 85). Pairs of HTBAPy³⁻ ligands are linked covalently by coordination bonds (Figure 78d); the 2D layers, in turn, are stacked on the top of one another with non-covalent (H-bonds, π - π stacking and van der Waals) interactions. The layered structure of **SION-7** can be topologically interpreted considering the Mg₃-clusters as 8-coordinated nodes, and HTBAPy³⁻ ligands as 4-coordinated nodes. This interpretation leads in the **4,8L15** net described by the Schläfli symbol of (4²⁰.6⁸)(4⁶)₂ (Figure 78e and Figure 86).²⁰⁰ The structure of **SION-7** contains infinitely propagating structural voids, and two distinct pores, pore 1 and pore 2 (Figure 78f), account for the total of 41.1% of the unit cell's volume and accommodate three heavily disordered DMF molecules.

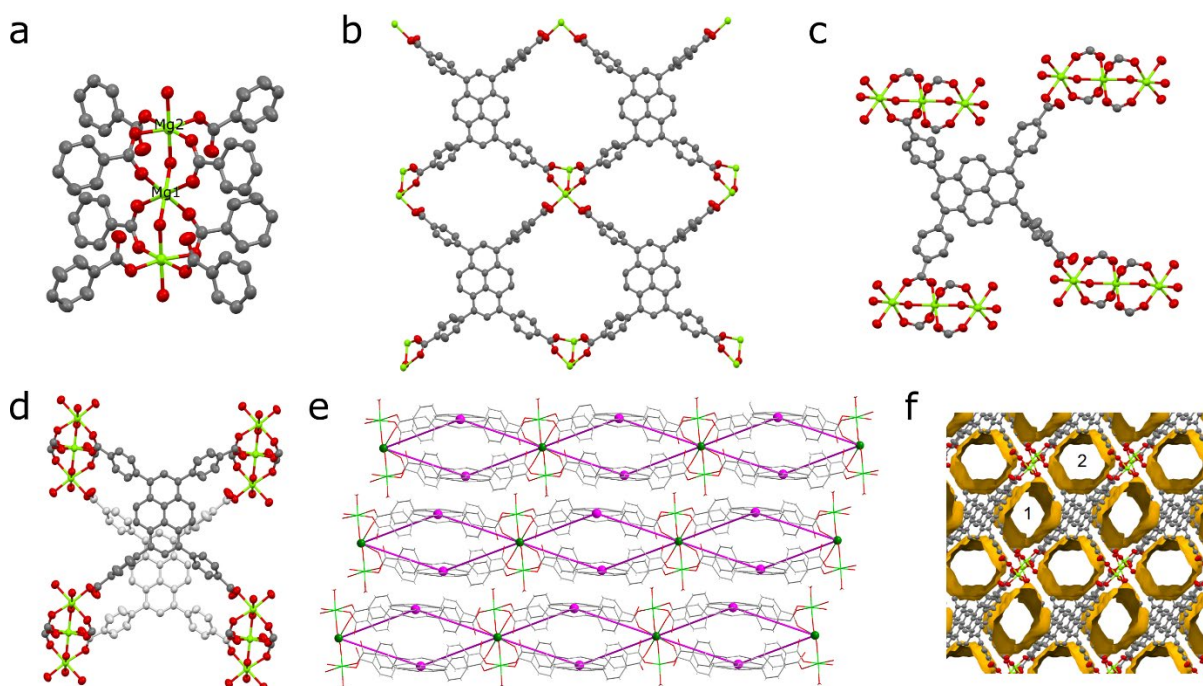


Figure 78. (a) Centrosymmetrical Mg₃-cluster constituting the structure of **SION-7**. Mg₁, positioned in its middle, sits on an inversion centre, while Mg₂ is on a general position. (b) Top part of a 2-dimensional layer constructed from HTBAPy³⁻ ligands joined together by Mg₃-clusters. (c) Coordination environment of an HTBAPy³⁻ ligand with $\eta^1:\eta^1$ -bridging and η^1 -coordination modes. (d) A pair of HTBAPy³⁻ ligands linked by a Mg₃-cluster viewed parallel to the pyrene cores (the ligand positioned in the bottom is shown in pale grey). Offset of pyrene cores is noticeable. (e) 2-dimensional layers viewed along the [1 $\bar{1}$ 0] direction overlaid with the topological scheme of the underlying **4,8L15** net. (f) The system of structural voids, including pore 1 and pore 2, viewed along the *a*-axis. Colour code: C, black; O, red; Mg, light green; 4-c node, purple; 8-c node, green. H atoms are omitted for clarity.

8.3.2. Thermal stability and phase transitions

Le Bail fit confirmed the phase purity of **SION-7** (Figure 87). The structure of **SION-7** is retained on heating up to 456 K, as inferred from in-situ VT PXRD measurements (Figure 79a). At this temperature a phase transition occurs towards **SION-7a** endowed with a markedly different powder pattern. Significant change of periodicity shown by PXRD indicates a structural rearrangement taking place upon the phase transition. The phase transition temperature of 456 K is also registered by the TGA: this is the point up to which all three guest DMF molecules are released in a gradual way (Figure 88). Therefore, we reason that **SION-7a** is the activated form of **SION-7**, i.e. the one of the same chemical composition, but with solvent-free pores. This is further confirmed by the gravimetric sorption measurements, which show that **SION-7a** is porous to N₂ at 77 K and 1 bar, and CH₄ (Figure 89), and its BET surface area amounts to 580 m²/g. The structure-derived pore volume (0.30 cm³/g) is consistent with the pore volume obtained from the N₂-adsorption isotherm (0.22 cm³/g). Additionally, the ¹³C CP-MAS solid-state NMR spectrum of the as-made **SION-7**, successfully predicted with the DFT-based CASTEP code, displays the same resonances as the spectrum of the activated **SION-7a** does (Figure 79b), and the FT-IR spectra of **SION-7** and **SION-7a** are nearly identical (Figure 90), hence upon activation the chemical identity of the material is retained. This activation, however, is irreversible as submersion of **SION-7a** in liquid DMF does not lead to the regeneration of **SION-7** (confirmed by PXRD). **SION-7a** is stable on heating up to around 700 K, when the framework decomposition starts (TGA, Figure 88). In-situ activation at elevated temperatures under vacuum leads to the breakdown of single crystals of **SION-7** (Figure 91), thus preventing us from the study of **SION-7a** with SCXRD.

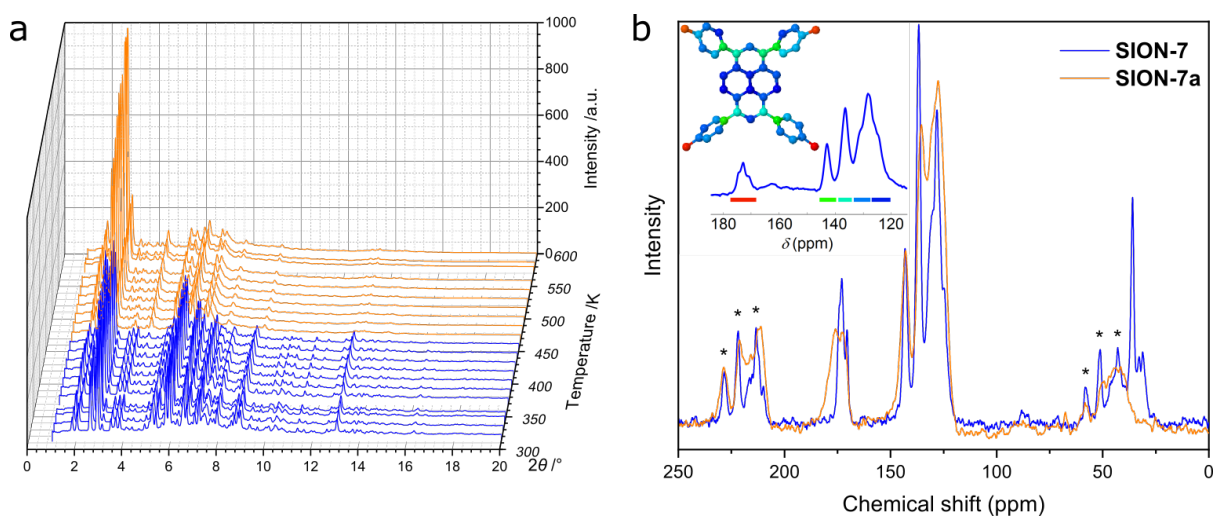


Figure 79. (a) VT PXRD patterns recorded from **SION-7** on heating. Significant changes in the positions and intensities of the Bragg peaks at 456 K marking the phase transition towards **SION-7a** are clearly noticeable. (b) ¹³C CP-MAS solid-state NMR spectrum of **SION-7a** compared to that of **SION-7**. Asterisks refer to spinning sidebands. Peak assignment: 170–180 ppm: carbonyl C of HTBAPy³⁻, 161.8 ppm: carbonyl C of DMF,²⁰¹ 120–145 ppm: aromatic C (pyrene core and phenylene rings) of HTBAPy³⁻, 30.6 and 35.7 ppm: alkyl C of DMF.²⁰¹ The inset illustrates the DFT-calculated resonances and their assignment to the structure.

8.3.3. Optical properties

Bulk **SION-7** powder has a pale yellow colour, which manifests itself in a diffuse reflectance UV/vis spectrum as a broad peak centred at 413 nm. Upon activation, the colour of **SION-7a** changes to deep yellow, which is also reflected by a slight shift of the absorption band towards a maximum at 434 nm (Figure 92). By exciting **SION-7** near its absorption maximum at rt. results in a fluorescence emission with a broad peak centred at around 500 nm and with the calculated quantum yield of 1.59(2)%. The shift observed in the UV/vis diffuse reflectance spectra of **SION-7** and **SION-7a** as well as the widely studied fluorescent properties of the pyrene molecule and its derivatives prompted us to thoroughly investigate the emission of **SION-7** using VT fluorescence spectroscopy.^{192c, 202}

8.3.4. Temperature-dependent interchromophoric interaction

Solid-state fluorescence emission spectra of **SION-7** measured in the 80–450 K temperature range on heating and cooling are presented in Figure 80a. At 80 K, **SION-7** exhibits a broad fluorescence spectrum including distinctly structured bands at 440 nm and 465 nm, characteristic for the π – π^* transitions of pyrene-derived monomers.¹⁸² Upon heating, this emission decreases in intensity and the structureless emission bands characteristic of the excimer become more dominant. At 450 K, the excimer emission with the peak at 525 nm can be observed. A similar transition was reported in thin films of high-temperature polymorph of pyrene,²⁰³ but not in a bulk solid material. This result clearly demonstrates the varying degree of interchromophoric interaction within **SION-7** as a function of temperature. On subsequent cooling, the monomer spectrum is not recovered, but instead the excimer emission enhances its intensity and blue-shifts its peak to 505 nm at 80 K (Figure 80a). CIE-1931 chromaticity diagram of the **SION-7** fluorescence shows the gradual transition of the emission colour from blue at low temperatures to yellow-green at higher temperatures (Figure 80c and Figure 93). Although MOFs responding to external pressure²⁰⁴ and chemical species²⁰⁵ alter the colour of their fluorescence to a similarly strong extent, such drastic changes occurring in MOFs as a function of temperature are relatively rare.²⁰⁶ Further heating and cooling of the material gives a very similar emission and intensity profile as in the first thermal sequence (Figure 94a, c, e), in which the fluorescence intensity always decreases upon heating, but is brought back to the initial values on cooling (Figure 94b, d, f). This is expected since at higher temperatures more vibrational levels are available, and hence more non-radiative decay processes can occur. Emission lifetimes of **SION-7** at different temperatures within the first thermal sequence are summarised in Table 21. It is apparent that upon heating, the increased population of excimers leads to the lengthening of the fluorescence dynamics. This observation is in agreement with a previous report in which the excimer formation in pyrene-based MOFs enhances the lifetime of the emissive excited states as compared to the free linker.^{184c}

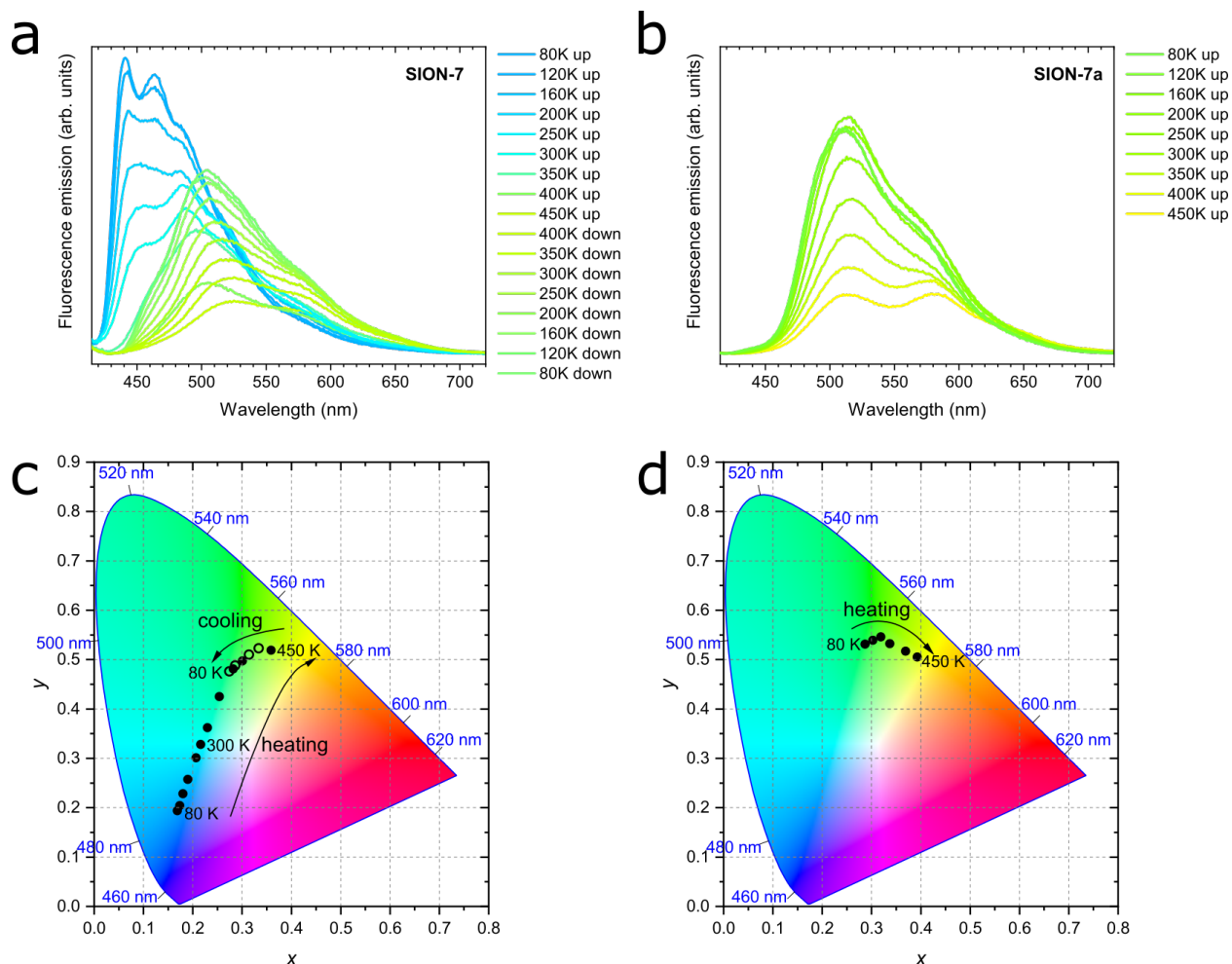


Figure 80. (a) Fluorescence spectra of **SION-7** measured in the 80–450 K temperature range on heating and cooling. (b) Fluorescence spectra of **SION-7a** measured in the 80–450 K temperature range on heating. In both panels the colours of the curves represent the perception of a given spectrum by human colour vision, as determined with the CIE-1931 standard. $\lambda_{\text{ex}} = 405$ nm. (c) CIE-1931 chromaticity diagram displaying the colour coordinates (x,y) of the fluorescence from **SION-7** during heating (filled circles) and cooling (empty circles) in the 80–450 K temperature range. (d) CIE-1931 chromaticity diagram of the fluorescence from **SION-7a** during heating from 80 to 450 K.

Due to the phase transition observed when **SION-7** is activated and transforms into **SION-7a**, the fluorescence emission of **SION-7a** was also investigated. Like **SION-7** in the second and third thermal sequences, **SION-7a** exhibits a similar featureless excimer emission in the entire 80–450 K temperature range, and the emission profiles are reversible for at least three cycles of heating and cooling (Figure 80b and Figure 95). The colour of the fluorescence changes from yellow-green back and forth to yellow (Figure 80d and Figure 96). The immersion of **SION-7a** in DMF does not lead to the recovery of the monomer emission of the resultant material (Figure 97).

Table 21. Average fluorescence lifetimes of **SION-7** at different temperatures upon heating and cooling.

Temperature (K)	Average Lifetime (ns)	
	Heating 80–450 K	Cooling 450–80 K
100	2.08	4.55
200	2.31	4.23
450	2.72	2.72

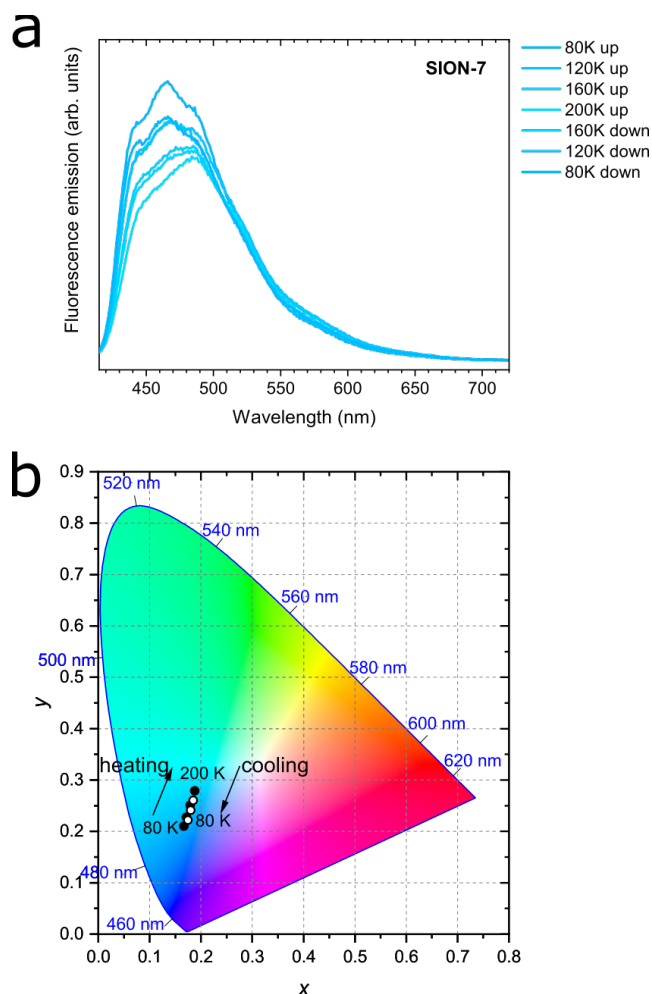


Figure 81. (a) Fluorescence spectra of **SION-7** measured in the 80–200 K temperature range on heating and cooling. (b) CIE-1931 chromaticity diagram of the fluorescence from **SION-7** during heating (filled circles) and cooling (empty circles) in the 80–200 K temperature range.

Interestingly, while kept in a relatively wide temperature range of 80–200 K, as-made **SION-7** displays structured monomer-like spectrum, which red-shifts and decreases in intensity when the temperature is increased, and blue-shifts and increases in intensity when the temperature is decreased (Figure 81a and Figure 98). Its colour changes reversibly from deep to light blue, but never surpasses the left bottom part of the CIE-1931 chromaticity diagram (Figure 81b and Figure 99). Therefore, by keeping the material in a low-temperature range, monomer emission from **SION-7** can be retained.

To elucidate the excimer formation in **SION-7**, VT SCXRD measurements were performed. As previously described, the structure of **SION-7** consists of 2-dimensional layers of pairs of HTBAPy³⁻ ligands joined together by Mg₃-clusters non-covalently stacked on the top of one another (Figure 78c). Interestingly, the pyrene core planes spacing within the Mg₃-bound layers (4.752 Å in the initial crystal structure measured at 100 K) is greater than the spacing between planes of pyrene cores originating from two subsequent layers (3.561 Å). Since also the offset between the succeeding pyrene cores is greater within the layers than in between of them (Figure 82a and Figure 100a, b), we reason that the pyrene cores originating from two consecutive 2-dimensional layers interact with each other to give the excimer fluorescence. This spacing increases with temperature (by 0.24 Å in the 100–400 K temperature range; Figure 100c), and amounts to slightly higher values than the sum of the van der Waals radii of C (3.54 Å).²⁰⁷ However, this observation only explains the excimer emission in **SION-7a** and in **SION-7** during the second and third thermal sequence, but does not explain the monomer emission exhibited by the as-made **SION-7**. The clarification comes from the analysis of the pore content as a function of temperature. As aforementioned, there are two types of pores within the structure of **SION-7**, pore 1 and pore 2. Pore 1, situated at x, 0, 0.5, is at the initial stage at 100 K filled with ca. 2 DMF molecules, while pore 2, with the fractional coordinates of x, 0.5, 0, encloses ca. 1 DMF molecule. As the temperature is increased, the total pore content changes to a limited extent up to 330 K, and at this temperature a dramatic decrease in electron count inside pore 1 takes place (Figure 82b). Above this point and on subsequent cooling, the content of this pore stays virtually invariant as it now comprises ca. 1 molecule of DMF. Simultaneously, the content of pore 2 amounts to ca. 1 DMF molecule throughout the entire thermal cycle (Figure 82b), and the pore content analysis is consistent with the TGA result (Figure 88). It is reasonable that extra DMF molecules in pore 1 impede the pyrene–pyrene interactions hindering the formation of an excimer, which can be formed and show up in the emission spectra solely once the guest solvent molecules are released. Therefore, fluorescence of **SION-7** is a physical phenomenon which is strongly dependent on the presence of the guest solvents, in analogy to spin crossover in Fe₂(azpy)₄(NCS)₄,²⁰⁸ and compressibility in Zn(niba)₂(OH)₂.²⁰⁹ Another structural feature that explains the excimer formation is the level of extended π – π conjugation of the aromatic rings. Within each HTBAPy³⁻ excimer, the pyrene cores are parallel to each other, while the phenylene rings attached to them are positioned in a much less regular manner. As the temperature is increased, the values of dihedral angles between the phenylene rings originating from the neighbouring HTBAPy³⁻ within the excimer (captioned as C20–C40 and C30–C50 in Figure 82a) decrease: <C20C40 drops from 13.86° at 100 K at the beginning of the thermal cycle to 9.85° at 350 K, while the corresponding initial and final values for <C30C50 are 34.72° and 4.37°, respectively (Figure 82c). This implies that the phenylene rings effectively become more parallel towards each other (a dihedral angle of 0° would signify a perfect parallelism), thus the interaction between them is more favourable. Moreover, the dihedral angles between the pyrene core and the phenylene rings within each HTBAPy³⁻ ligand change in a multidirectional way with temperature (the angles C20–pyrene and C30–pyrene increase, C40–pyrene stays virtually invariant, while C50–pyrene decreases, Figure 82d), which may explain why slight changes in the fluorescence shift and intensity are still observed even after **SION-7** undergoes the transition towards the excimer state. Superimposing the images of HTBAPy³⁻ derived from the structures at 100 K and 305 K emphasises the multidirectional way of phenylene–pyrene dihedral angle changes in the discussed temperature range (Figure 82e).

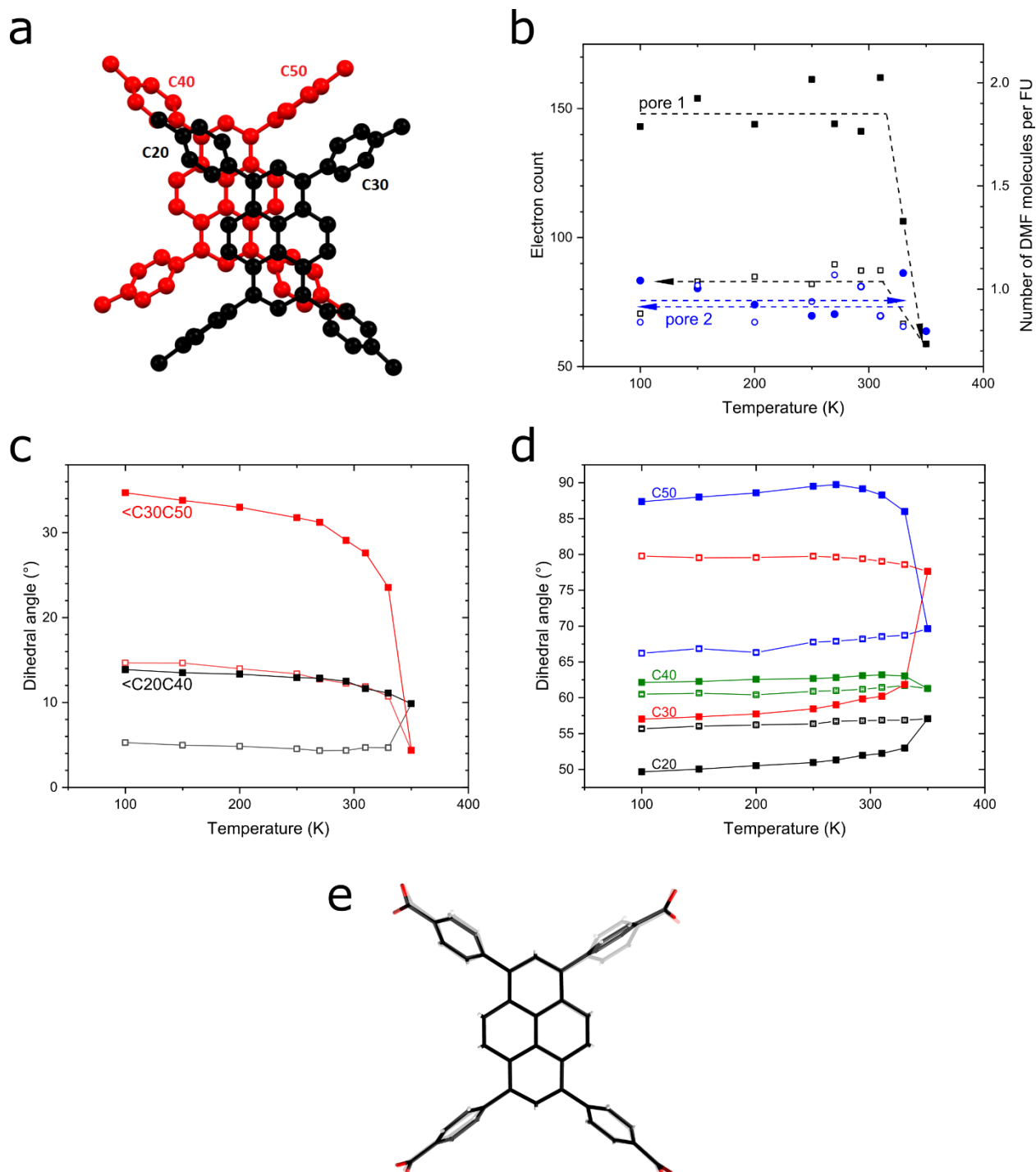


Figure 82. (a) A pair of HTBAPy³⁻ ligands originating from two neighbouring 2-dimensional layers, forming an excimer. Phenylene rings are captioned. (b) Content of pore 1 and pore 2 of **SION-7** expressed as electron count (left vertical axis) and the corresponding number of DMF molecules per formula unit (right vertical axis). (c) Dihedral angles between the phenylene rings originating from the neighbouring HTBAPy³⁻ within the excimer plotted as a function of temperature. (d) Dihedral angles between the pyrene core and the phenylene rings within each HTBAPy³⁻ ligand. Full and empty symbols denote the heating and cooling regimes, respectively. (e) Superposition of the images of HTBAPy³⁻ derived from the structures at 100 K (opaque wireframe) and 350 K (bold wireframe).

8.4. Conclusions

SION-7, a MOF synthesised from the self-assembly of Mg^{2+} and H_4TBAPy , was found to be a platform suitable for an in-depth study of the interactions between pyrene derivative chromophores incorporated into the metal-organic framework. Noteworthy, it was found that the interchromophoric interactions in a pyrene-based MOF do not depend solely on the framework topology and the linker concentration, but can also be tuned by external stimuli. In particular, temperature was shown to dramatically change the mutual orientation of HTBAPy^{3-} ligands (enhanced parallelism of the phenylene rings originating from two neighbouring layers of HTBAPy^{3-} ligands plus multidirectional change of the phenylene–pyrene dihedral angles at elevated temperatures) and the pore content of **SION-7** (at 100 K pore 1 is filled with approx. 2 DMF, and pore 2 with approx. 1 such molecule; upon heating up to 350 K, the content of these pores changes to approx. 1 and 1 DMF molecule, respectively), which entails crucial changes in the fluorescence emission (a structured monomer emission at low temperatures transforms to a structureless excimer emission at high temperatures). Another important conclusion of this work is that the presence of simple guest molecules such as solvents plays an important role in the fluorescence emission of pyrene-based MOFs, and shall not be overlooked in future studies. Our study opens a new dimension for controlling the optical properties of porous materials since the colour of their emission can be regulated without the need of introducing additional chemical species. When integrated to a substrate, e.g. in form of a thin film, **SION-7** could potentially serve as a temperature sensor for cryogenic environments; when temperatures higher than cryogenic were attained, such a sensor would dramatically change its colour.

8.5. Appendix

Table 22. Crystal data and structure refinement for **SION-7** at 100 K.

Identification code	SION_T100
Empirical formula	C ₁₀₆ H ₉₆ Mg ₃ O ₂₆ N ₆
Formula weight	1942.81
Temperature/K	100.0
Crystal system	triclinic
Space group	P-1
a/Å	11.2723(4)
b/Å	14.4121(5)
c/Å	15.9112(5)
$\alpha/^\circ$	81.410(3)
$\beta/^\circ$	77.802(3)
$\gamma/^\circ$	77.284(3)
Volume/Å ³	2450.19(15)
Z	1
$\rho_{\text{calc}}/\text{cm}^3$	1.317
μ/mm^{-1}	0.112
F(000)	1018.0
Crystal size/mm ³	0.18 × 0.11 × 0.08
Radiation	synchrotron ($\lambda = 0.7142$)
2 θ range for data collection/ $^\circ$	4.154 to 63.946
Index ranges	-16 ≤ h ≤ 16, -18 ≤ k ≤ 18, -23 ≤ l ≤ 23
Reflections collected	18468
Independent reflections	9526 [$R_{\text{int}} = 0.0176$, $R_{\text{sigma}} = 0.0311$]
Data/restraints/parameters	9526/6/503
Goodness-of-fit on F^2	1.086
Final R indexes [$ I \geq 2\sigma(I)$]	$R_1 = 0.0701$, $wR_2 = 0.2070$
Final R indexes [all data]	$R_1 = 0.0726$, $wR_2 = 0.2105$
Largest diff. peak/hole / e Å ⁻³	0.50/-0.48
CCDC	1897075

Table 23. Crystal data and structure refinement for **SION-7** at 350 K.

Identification code	SION_T350
Empirical formula	C _{96.38} H _{67.56} Mg ₃ N _{2.79} O _{22.79}
Formula weight	1702.28
Temperature/K	350
Crystal system	triclinic
Space group	P-1
a/Å	11.4034(5)
b/Å	14.6274(5)
c/Å	16.1091(7)
$\alpha/^\circ$	80.439(3)
$\beta/^\circ$	77.037(4)
$\gamma/^\circ$	75.856(3)
Volume/Å ³	2521.50(19)
Z	1
$\rho_{\text{calc}}/\text{cm}^3$	1.121
μ/mm^{-1}	0.097
F(000)	884.0
Crystal size/mm ³	0.18 × 0.11 × 0.08
Radiation	synchrotron ($\lambda = 0.7142$)
2 θ range for data collection/ $^\circ$	3.772 to 63.59
Index ranges	-16 ≤ h ≤ 16, -18 ≤ k ≤ 18, -23 ≤ l ≤ 23
Reflections collected	18816
Independent reflections	9688 [$R_{\text{int}} = 0.0255$, $R_{\text{sigma}} = 0.0507$]
Data/restraints/parameters	9688/6/503
Goodness-of-fit on F^2	1.238
Final R indexes [$I \geq 2\sigma(I)$]	$R_1 = 0.1059$, $wR_2 = 0.3011$
Final R indexes [all data]	$R_1 = 0.1120$, $wR_2 = 0.3093$
Largest diff. peak/hole / e Å ⁻³	0.67/-0.43
CCDC	1897076

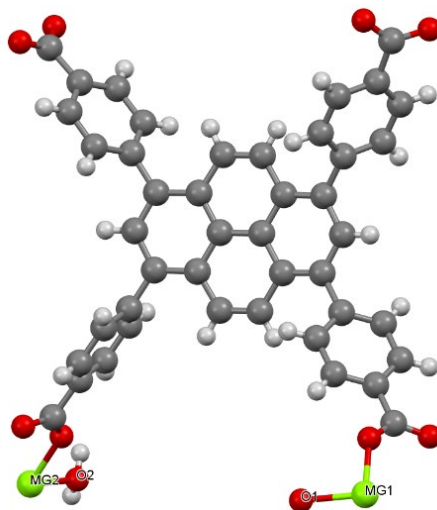


Figure 83. Symmetrically independent part of the unit cell of **SION-7**. Apart from one HTBAPy³⁻ ligand this comprises two Mg-atoms (of which Mg1 sits on a special position with the Wyckoff site multiplicity reduced by a factor of 2), and O1 and O2 oxygen atoms belonging to two coordinated H₂O molecules. Some H-atoms could not be localised.

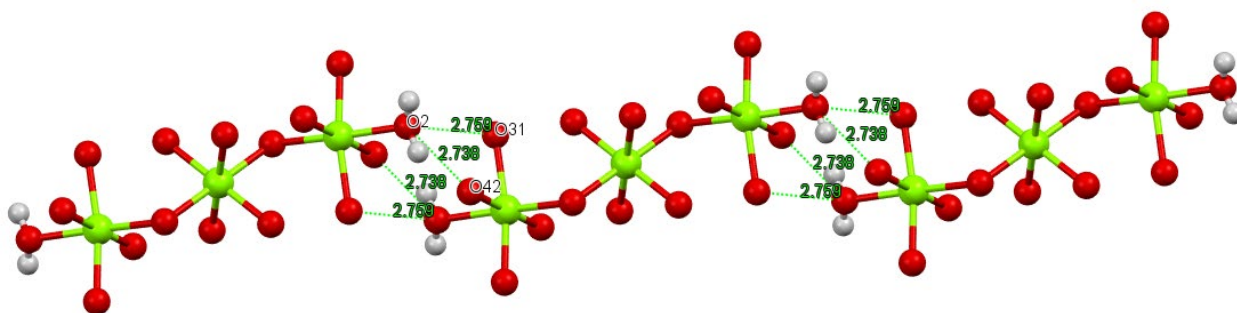


Figure 84. A supramolecular chain formed by the extension of Mg₃-clusters along the *a*-axis by means of the hydrogen bonds O2...O31 (2.759 Å) and O2...O42 (2.738 Å).

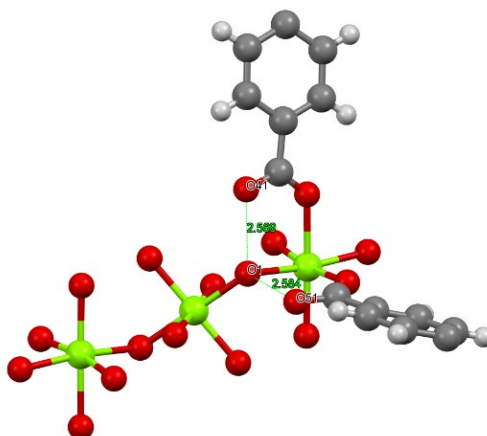


Figure 85. Chemical environment of the O1 bridging atom within the Mg₃-cluster; numbers refer to the lengths (expressed in Å) of the corresponding hydrogen bonds. It is plausible that the H atom of the partially protonated HTBAPy³⁻ ligand is disordered and shared by two protonated carboxylate groups bound with hydrogen bonds to the bridging H₂O molecule.

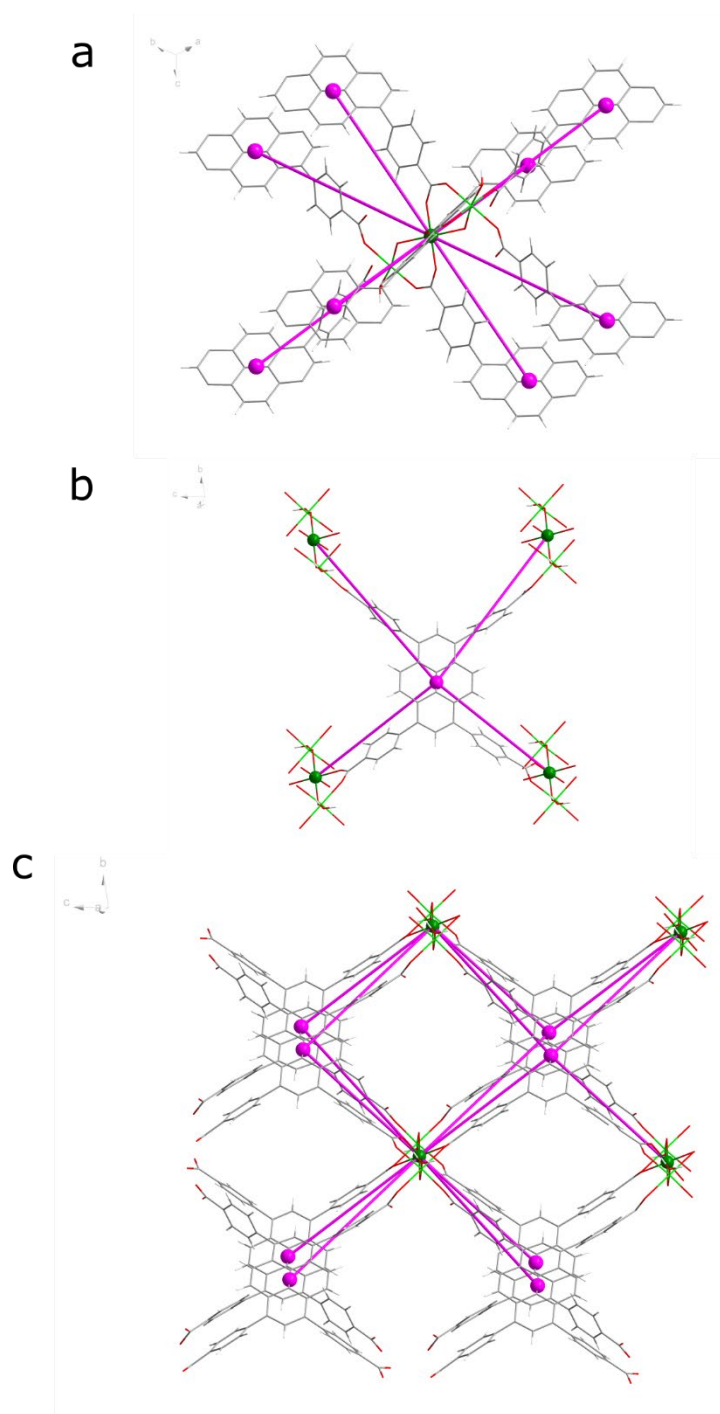


Figure 86. **SION-7** topologically interpreted as a 4,8-c net. (a) Mg_3 -cluster (green sphere) interpreted as an 8-c node. (b) HTBAPy^{3-} (purple sphere) interpreted as a 4-c node. (c) Fragment of the $(4^{20}.6^8)(4^6)_2$ underlying net viewed approximately along the a -axis.

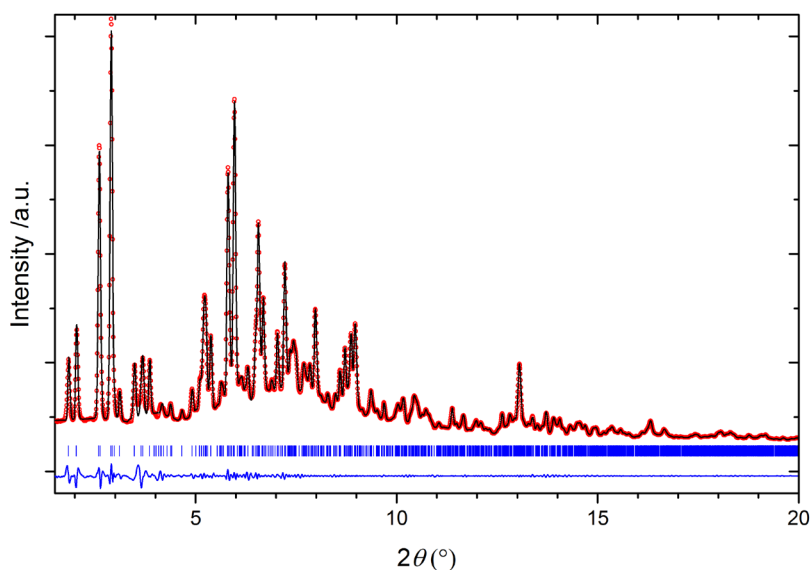


Figure 87. Le Bail refinement of the **SION-7** PXRD pattern recorded with synchrotron radiation at rt. (space group $P\bar{1}$: $R_p = 4.01\%$, $R_{wp} = 4.26\%$; $a = 11.3514(2)$ Å, $b = 14.4851(4)$ Å, $c = 15.9534(4)$ Å, $\alpha = 81.2688(14)^\circ$, $\beta = 77.8212(19)^\circ$, $\gamma = 76.5933(13)^\circ$; $\lambda = 0.50084$ Å). The red dots represent the experimental data, the black plots show the refined Le Bail profiles, while the blue plots represent the difference between them. Reflection positions are marked in blue.

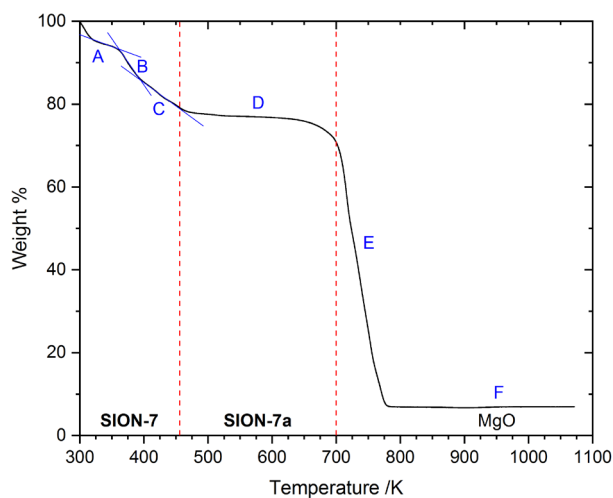


Figure 88. TGA of **SION-7**. Steps A (up to 360 K, -6.6 wt%), B (360–395 K, -7.8 wt%) and C (395–456 K, -7.6 wt%) can each be approximated to 7.7 wt% loss of the framework, which, based on the formula, corresponds to the mass of 1 DMF molecule. Subsequent phase transitions at 456 K and 700 K are marked with dashed red lines. At 800 K, the remaining 6.8 wt% correspond to the entirely mineralised magnesium oxide residue (6.2 wt%). Since this analysis predicts a full desolvation of **SION-7**, no ions are expected to reside within the pores. Therefore, it is inferred that the singly protonated form of the ligand, HTBAPy^{3-} , constitutes the framework of **SION-7**.

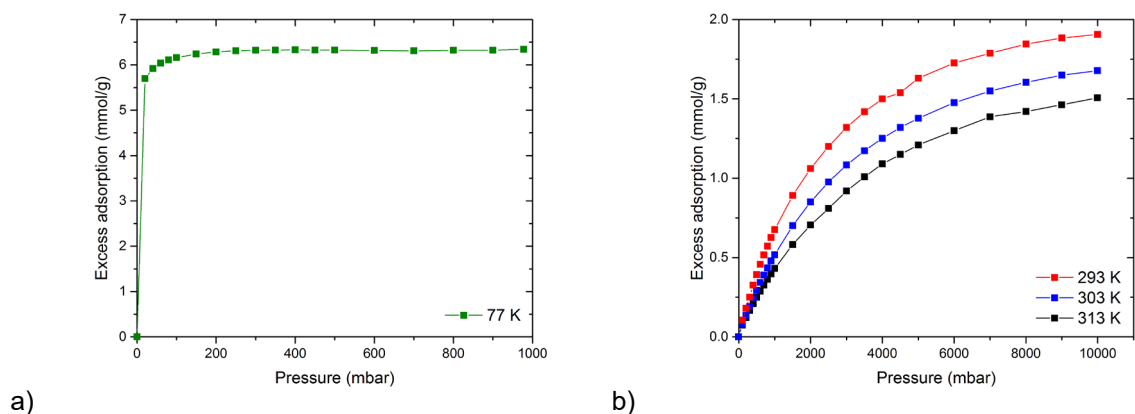


Figure 89. (a) N₂-adsorption type-I isotherm of **SION-7a** recorded at 77 K. Activation conditions: heating at 403 K under dynamic vacuum for 8 hours. The recorded weight loss (25.1%) is consistent with the weight loss derived from the TGA (24.3 wt%) and from the formula (26.3 wt%). (b) CH₄-adsorption type-I isotherms of **SION-7a** recorded at 293 K, 303 K, and 313 K.

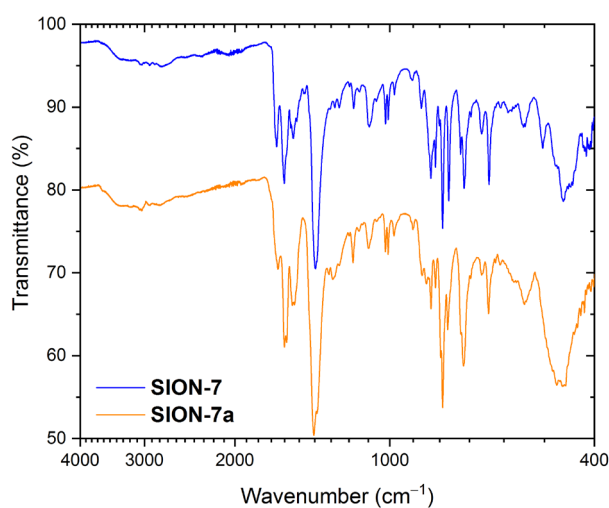


Figure 90. FT-IR spectra of **SION-7** (blue plots) compared to those of **SION-7a** (orange plots). Occurrence of the same bands in the spectra indicate the presence of identical functional groups in the respective solid materials. The spectrum of **SION-7a** is offset by -15%.



Figure 91. Optical photographs of a single crystal of **SION-7** enclosed in an environment cell (a), and subjected to the vacuum of 10^{-3} mbar and the temperature above 350 K (b). As the single crystal shatters, the study of **SION-7a** with SCXRD proved impossible.

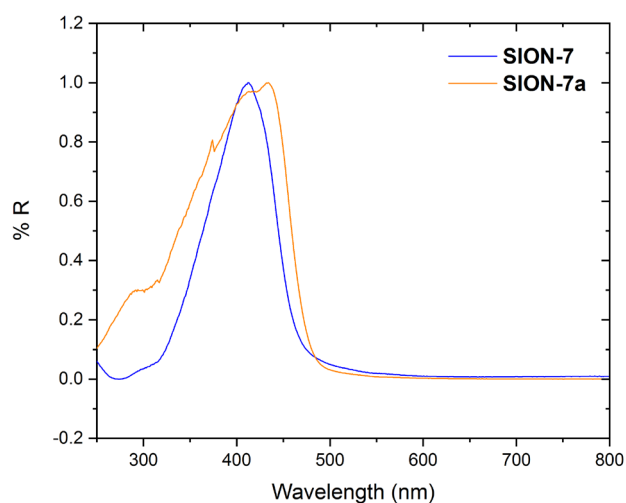


Figure 92. Diffuse reflectance UV/vis spectra of **SION-7** and **SION-7a**. The spectra have been normalised for an easier comparison.

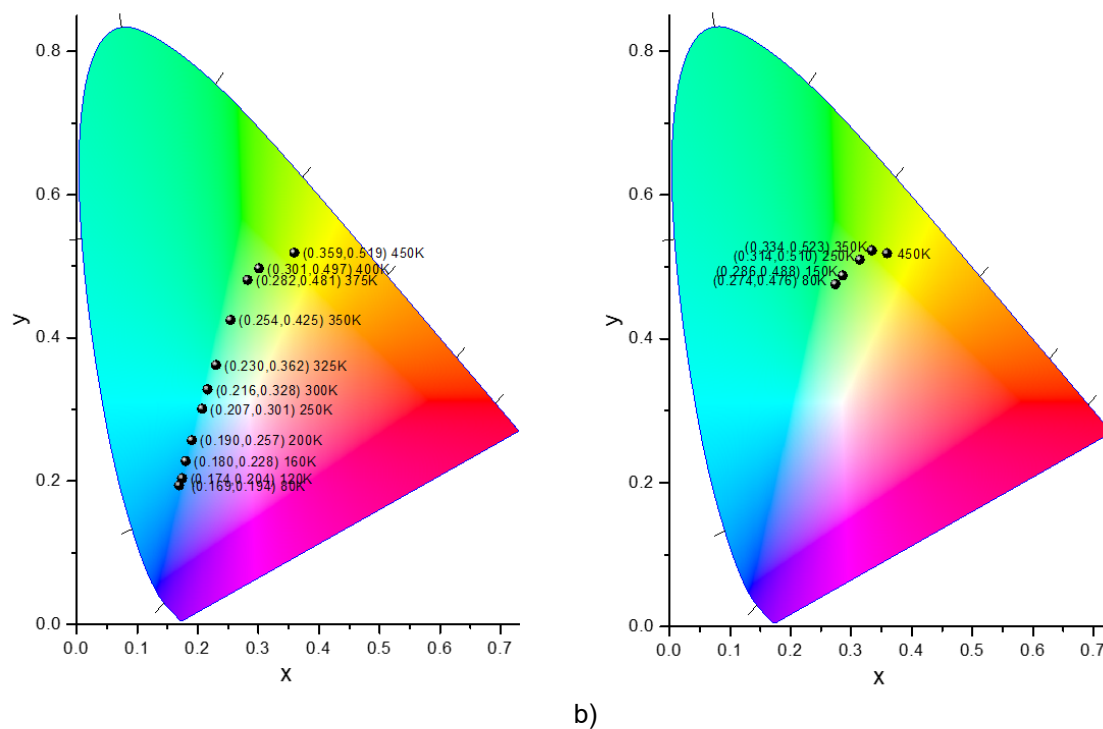


Figure 93. CIE-1931 chromaticity diagram of the fluorescence from **SION-7** (a) on heating in the 80–450 K temperature range, and (b) on cooling in the 450–80 K temperature range.

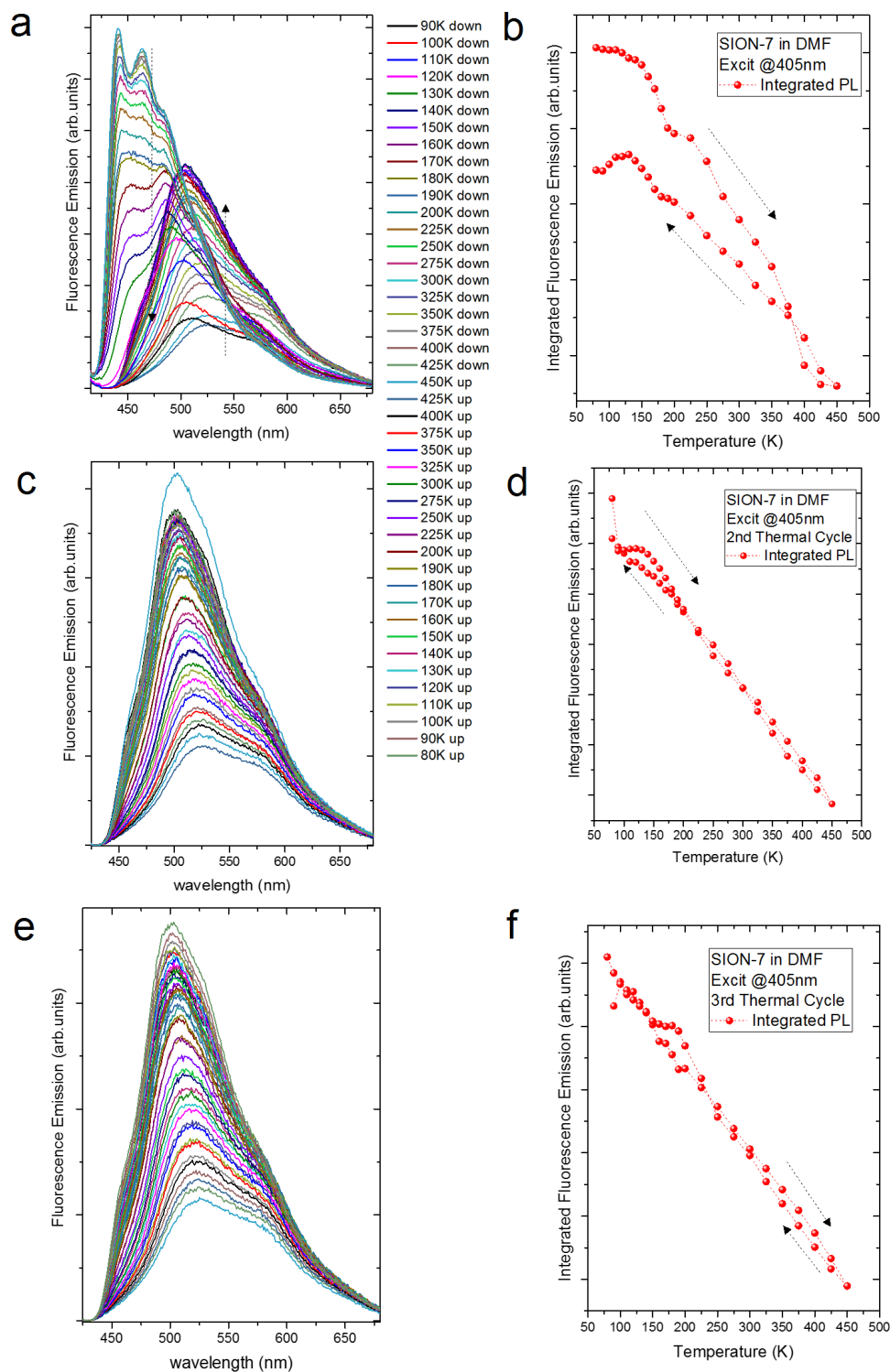


Figure 94. Fluorescence spectra of **SION-7** measured in the 80–450 K temperature range on heating and cooling: (a) first thermal cycle, (c) second thermal cycle, (e) third thermal cycle. Integrated fluorescence intensity of **SION-7** in the 80–450 K temperature range on heating and cooling: (b) first thermal cycle, (d) second thermal cycle, (f) third thermal cycle.

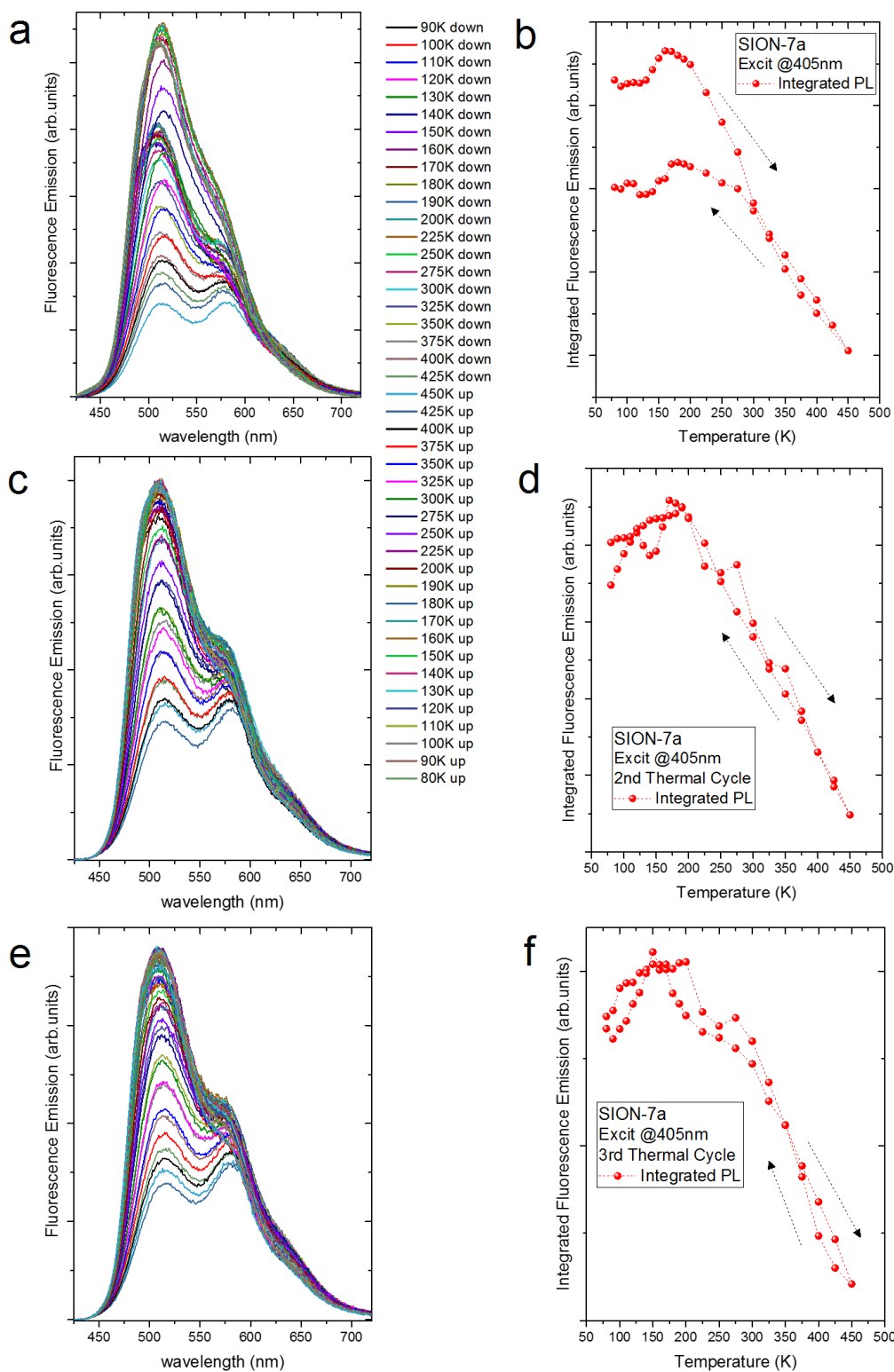


Figure 95. Fluorescence spectra of **SION-7a** measured in the 80–450 K temperature range on heating and cooling: (a) first thermal cycle, (c) second thermal cycle, (e) third thermal cycle. Integrated fluorescence intensity of **SION-7a** in the 80–450 K temperature range on heating and cooling: (b) first thermal cycle, (d) second thermal cycle, (f) third thermal cycle.

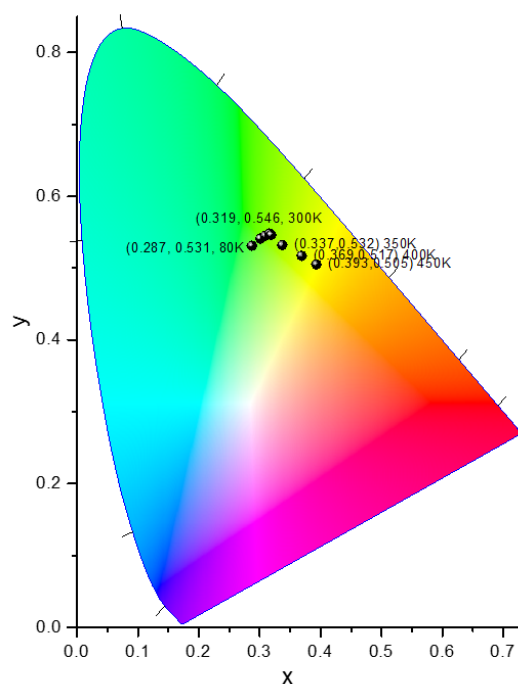


Figure 96. CIE-1931 chromaticity diagram of the fluorescence from **SION-7a** on heating in the 80–450 K temperature range.

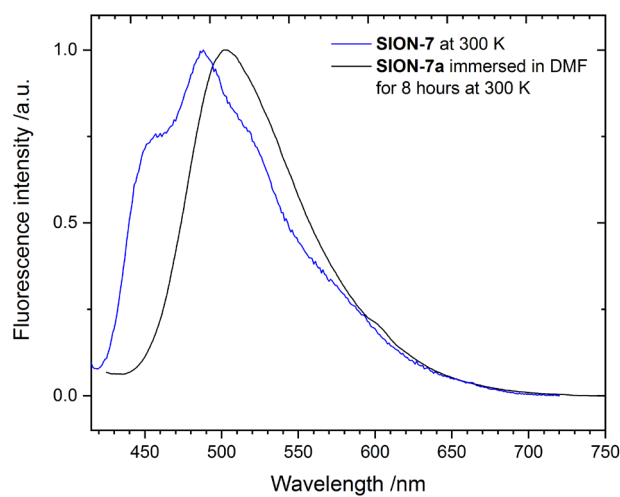


Figure 97. Fluorescence spectrum of as-made **SION-7** measured at 300 K during the first heating cycle (blue plots) and that of the **SION-7a** immersed in DMF for 8 hours, filtered, dried in air and measured at 300 K (black plots). Lack of the low-wavelength feature in the second spectrum confirms that the monomer emission is not recovered.

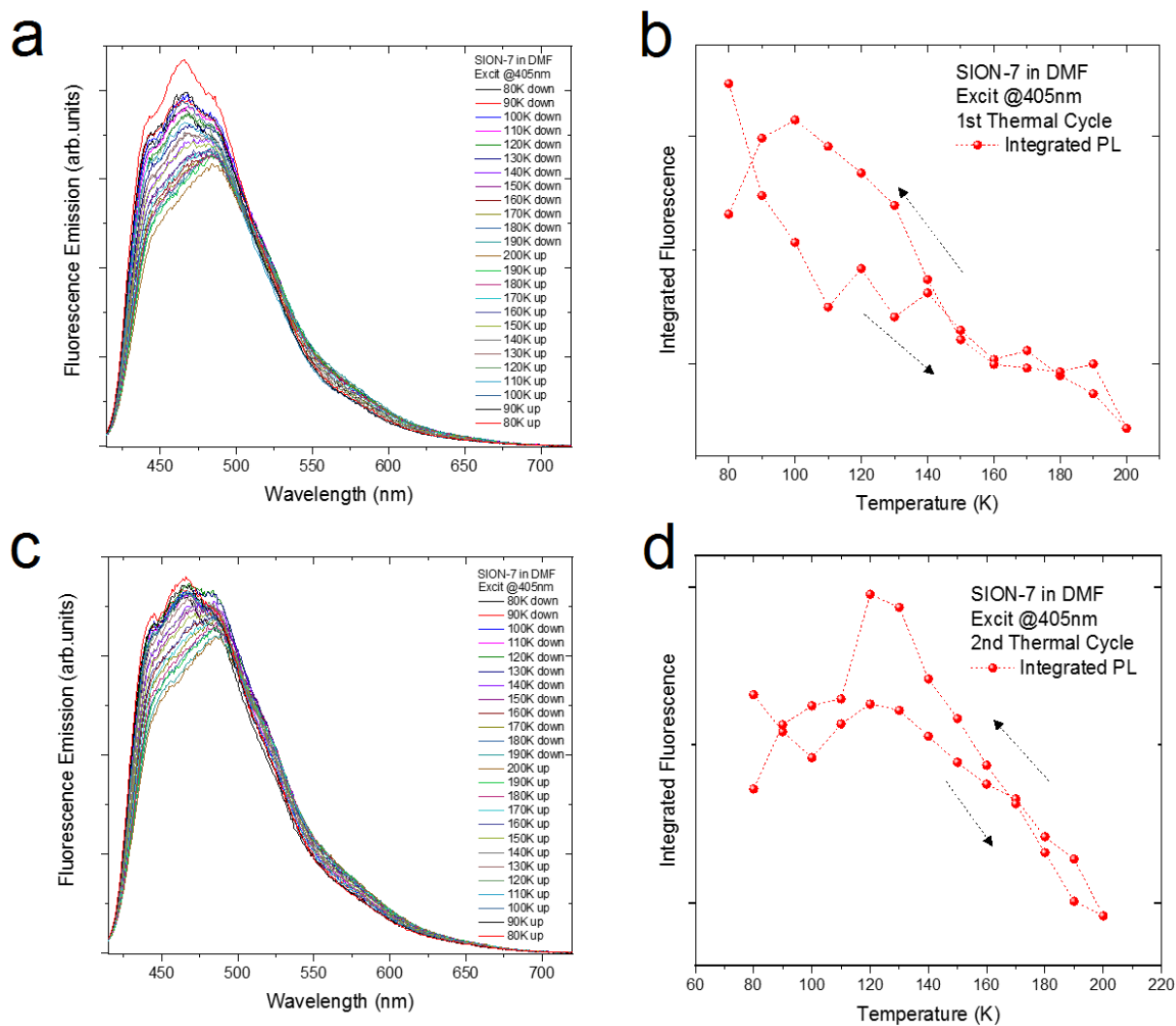


Figure 98. Fluorescence spectra of **SION-7** measured in the 80–200 K temperature range on heating and cooling: (a) first thermal cycle, (c) second thermal cycle. Integrated fluorescence intensity of **SION-7** in the 80–200 K temperature range on heating and cooling: (b) first thermal cycle, (d) second thermal cycle.

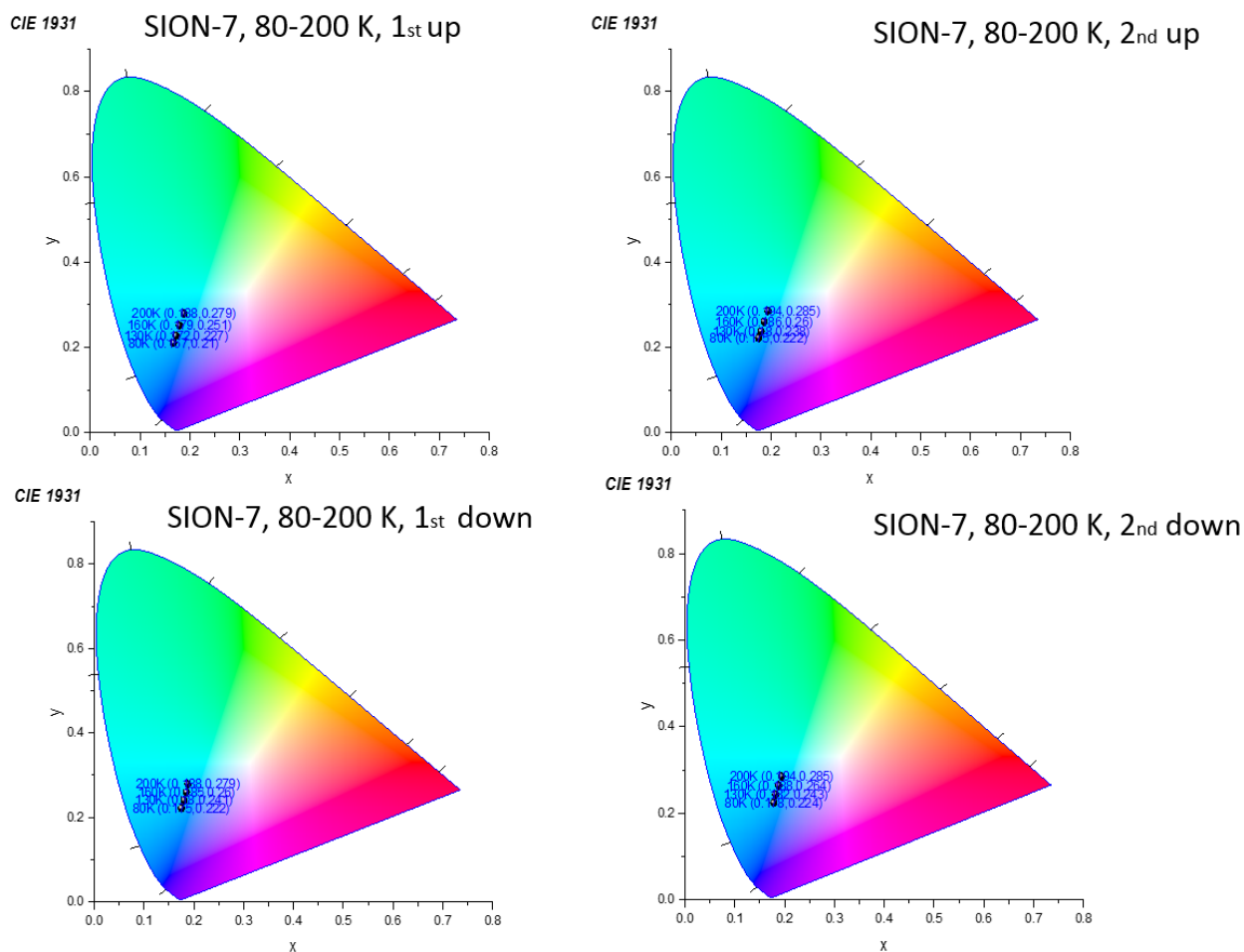


Figure 99. CIE-1931 chromaticity diagram of the fluorescence from **SION-7** on heating and cooling in the 80–200 K temperature range during the first and second thermal cycle.

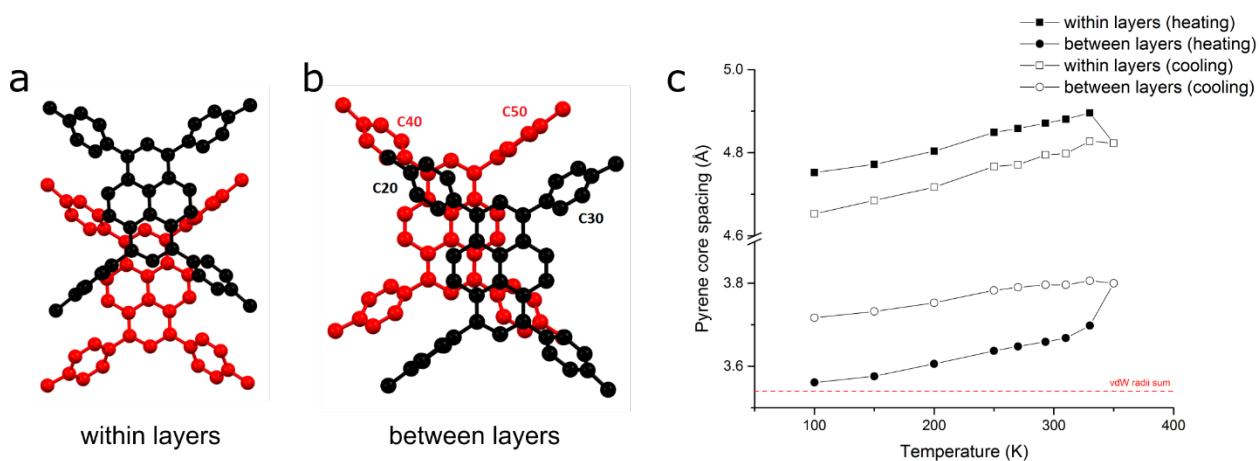


Figure 100. A pair of HTBAPy³⁻ ligands originating from (a) the same and (b) two neighbouring 2-dimensional layers of the ligands joined together by Mg₃-clusters. (c) Evolution of the pyrene core planes spacing with temperature.

9. Guest-dependent negative thermal expansion in a lanthanide-based metal–organic framework

This chapter has been adapted from: A. Gladysiak, S. M. Moosavi, L. Sarkisov, B. Smit, and K. C. Stylianou, *CrystEngComm*, **21**, 5292–5298, (2019).

My contribution to this work consisted in the SCXRD analysis, topological analysis, and characterisation of the discussed material, execution of the *in-situ* VT SCXRD experiments using synchrotron radiation, analysis and plotting of the experimental data, and participation in writing of the manuscript.

9.1. Introduction

Negative thermal expansion (NTE) is a counterintuitive property of certain materials that contract in at least one direction upon heating.²¹⁰ Recently, a number of materials, including metal–organic frameworks (MOFs) exhibiting a wide range of NTE effects have been reviewed.²¹¹ Aside from scientific curiosity and purely academic motivation to explain NTE phenomena on a fundamental level, interest in these materials is also driven by their potential applications in numerous fields where precise control over the thermal expansion is of supreme importance, *i.e.* electronic and optical devices as well as energy-related technologies.²¹² In these applications, materials exhibiting NTE can be combined with much more common materials endowed with overall positive thermal expansion (PTE) to form a composite whose size over a given temperature range does not change; in other words, it displays zero thermal expansion (ZTE).²¹³ Such approach minimises the temperature-induced strains, which may lead to improper performance or, in an extreme case, to an exfoliation and severe damage of the system.

There are numerous ways how the NTE effect is explained. Open-framework materials, in vast majority of cubic symmetry, derive their NTE from thermal population of low-energy transverse vibrational modes. ZrW_2O_8 , an emblematic example of such frameworks, features a cubic lattice of metal ions M^{n+} interlinked by O^{2-} bridges. At increasing temperatures, the transverse vibrations of the M–O–M linkages bring the metal ions closer together within the lattice, resulting in an overall volumetric contraction, *i.e.* an NTE in three orthogonal directions.²¹⁴ In many instances, the increased population of transverse vibrational modes is concomitant with distortions of edge-sharing polyhedra, as in the case of ScF_3 ,²¹⁵ LiBeBO_3 ,²¹⁶ and ReO_3 -type compounds.²¹⁷ Identical in terms of mechanism, but differing in magnitude, the NTE effect was equally found in inorganic cyanides, $\text{Zn}(\text{CN})_2$ and $\text{Cd}(\text{CN})_2$,²¹⁸ nitrides,²¹⁹ as well as in MOFs including HKUST-1,²²⁰ interpenetrated $\text{Cu}_3(\text{btb})_2$,²²¹ MOF-5,²²² and MIL-68(In).²²³ In turn, graphite and $\text{Ni}(\text{CN})_2$ were reported to display a relatively rare biaxial NTE effect.²²⁴

In many instances, the NTE effect becomes more evident as a material approaches a phase transition.²²⁵ An emblematic example of such a behaviour is PbTiO_3 perovskite, which exhibits increasingly stronger NTE effect near its ferroelectric–paraelectric phase transition.²²⁶ NTE observed exclusively below the magnetic ordering temperature in CuO and MnF_2 ²²⁷ is reminiscent of the Invar effect, *i.e.* virtual vanishing of thermal expansion in Fe–Ni and Fe–Pt alloys on approach towards the magnetic ordering temperature.²²⁸ Noteworthy is, however, that thermal expansion coefficients are in general temperature-dependent, and significant differences in their values as a function of temperature can be observed even if no phase transition takes place.²²⁹

Materials in which significant framework flexibility is responsible for the NTE constitute another large family. Most of these materials have symmetry lower than cubic, and exhibit NTE only in one specific direction, while the higher magnitude of PTE in two other directions gives rise to the overall positive volume thermal expansion. Inorganic framework materials (e.g., $\text{Ag}_3[\text{Co}(\text{CN})_6]$),²³⁰ molecular aggregates ($\text{CD}_3\text{OD}\cdot\text{D}_2\text{O}$)²³¹ and most importantly MOFs (HMOF-1, $\text{Zn}(\text{ISN})_2$, $\text{InD}(\text{BDC})_2$, FJI-H11-R, $\text{Zn}(\text{eim})_2$ and $\text{Cd}(\text{eim})_2$)²³² owe their NTE to their intrinsic flexibility.

Thermal expansion behaviour of NTE materials can be influenced by the incorporation of guest molecules.²³³ The introduction of guest molecules can involve the change in magnitude of thermal expansion coefficient,²³⁴ reversing the sign thereof,^{234c, 234d, 235} or even the appearance of a new phase endowed with a markedly different thermal expansion.^{234c, 236} Interesting examples of mechanisms leading to the guest-dependent thermal expansion involve the substitution of a halide counterion,²³⁷ inserting helium into the structural cavities by means of hydrostatic pressure,²³⁸ or intercalation with lithium ions,²³⁹ while adsorption of molecular species causing the change of the thermal expansion behaviour was predicted computationally.²⁴⁰

To further advance the field of materials exhibiting NTE, new strategies are required to be developed. An attractive suggestion comes from the field of coordination chemistry, where materials with diverse bonding topologies and chemistries show anomalous thermal and mechanical properties.²⁴¹ In particular, while it is widely known that transition metal complexes adopt only some discrete coordination numbers and preferred coordination geometries, lanthanide (Ln) ions, with their 4f orbitals buried inside the atomic core and well shielded by the filled 5s and 5p sub-shells, adopt a variety of coordination numbers and geometries, dominated by the steric effects of the ligands.²⁴² Assembling such complexes into 3D polymers may give rise to a concerted response of the solid upon temperature increase, leading to anomalous thermal phenomena.

Herein, we combine the two approaches: (i) the assembly of a 3D framework and guest molecules together with (ii) the incorporation of Ln-atoms into a 3D structure, to access to a material endowed with a switchable NTE effect. In previous works, only the thermal expansion of Ln-based MOFs having charged particles (counterions) as guests was investigated,²⁴³ thus precluding the possibility of guest evacuation. The presently discussed Ln-based MOF, named **SION-2**, exhibits a high magnitude of NTE effect while it incorporates solvent guest molecules, however, once desolvated, it displays a significantly weaker NTE effect. The direction of NTE is also altered upon desolvation. Below we describe the origin of this effect studied with single-crystal X-ray diffractometry.

9.2. Experimental section

SION-2 was crystallised following the previously reported procedure.²⁴⁴ A high-quality single crystal of **SION-2** was isolated from the reaction mixture. It was mounted on a PILATUS@SNBL single-crystal X-ray diffractometer at the BM01 Swiss-Norwegian Beamline (ESRF, Grenoble, France).¹³³ Preliminary exposures confirmed the singularity of the crystal. Reflection intensities were measured using the PILATUS2M detector. Raw data were processed with CrysAlisPro program suite,²⁴⁵ and the empirical absorption correction was performed using spherical harmonics, implemented in SCALE3 ABSPACK scaling algorithm. The structures were solved by the direct method and refined by the full-matrix least-squares method on F^2 with anisotropic thermal parameters for all non-hydrogen atoms. SHELXT and SHELXL programs,^{60, 102} implemented in the Olex2 program suite,⁹¹ were used for this purpose. Least-square refinement involved using the restraints on displacement parameters of some atoms. Positions of H atoms within the benzene rings and molecules of DMF were refined using the riding model, while H atoms within the hydroxyl groups were refined as in idealised rotating groups. U_{iso} for non-terminal H atoms were set to 1.2 times U_{eq} of neighbouring atoms, and for terminal H atoms – 1.5 times U_{eq} of neighbouring atoms. The experiment was initially performed at 100 K, and then repeated in the 100–380 K temperature range at 20 K intervals on heating, and then in the 380–

100 K temperature range on cooling. In the 100–340 K temperature range, one non-coordinated DMF molecule was localised within the cavities of the main $[\text{Tb}_2(\text{DHBDC})_3(\text{DMF})_4]$ framework; its disorder was refined as assuming two positions of inequivalent occupancy; moreover, displacement parameters and interatomic distances in both components of the disorder were constrained. In the 260–340 K temperature range, the disorder of one of the coordinated DMF molecules was also refined as assuming two positions of inequivalent occupancy. In the 360–380 K temperature range, the contribution of the heavily disordered DMF molecules found in the structural voids of **SION-2** to the measured structure factors was quantified with the Olex2 solvent masking procedure:⁶² at 360 K the integrated excess electron density of 27 e^- was found to correspond to 0.675 DMF molecules per unit cell, while at 380 K the electron count equalled 0. Coefficients of thermal expansion were calculated using the program PASCAL (Principal Axis Strain Calculator).²⁴⁶ Topological simplification and net classification was performed using the TOPOS Pro program suite.¹³⁴

9.3. Results and discussion

SION-2, $[\text{Tb}_2(\text{DHBDC})_3(\text{DMF})_4] \cdot 2\text{DMF}$ ($\text{DHBDC}^{2-} = 2,5\text{-dihydroxybenzene-1,4-dicarboxylate}$, $\text{DMF} = N,N\text{-dimethylformamide}$), crystallises in the triclinic space group $P\bar{1}$. Its framework is constructed upon Tb^{III}_2 binuclear clusters interlinked through three types of DHBDC^{2-} ligands: one η^2 chelating and two distinct $\eta^1:\eta^1$ bridging ligands. The Tb^{III}_2 clusters and all types of DHBDC^{2-} ligands are centrosymmetric as they lie about inversion centres. The DMF molecules coordinated to the Tb^{III} metal centres, and those occupying the structural voids (guest molecules), are present in the structure of **SION-2** in a ratio of 2:1. Tb^{III} atoms are 8-coordinated and display a square antiprismatic coordination geometry. **SION-2** has recently been assigned to the **xah** net topology,²⁴⁴ but it can be further simplified to the $\alpha\text{-Po}$ type, **pcu** net (Figure 101 and Figure 103) by regarding the Tb^{III}_2 clusters as a single node rather than as two separate nodes.

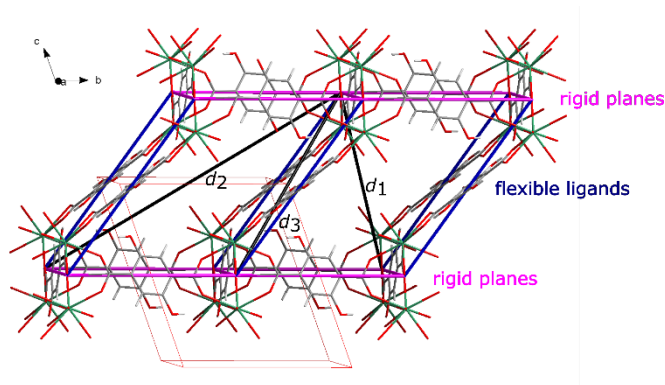


Figure 101. Crystal structure of **SION-2** and the contour of its unit cell outlined with the nodes of the underlying **pcu** net (centres of the Tb^{III}_2 clusters) overlaid. Distances d_1 , d_2 , and d_3 are a function of the unit-cell parameters. DMF molecules have been omitted for clarity.

The thermal expansion of **SION-2** was studied with variable-temperature single-crystal X-ray diffractometry (VT SCXRD) using synchrotron radiation. While heated in the 100–340 K temperature range, **SION-2** experiences a continuous unit-cell volume expansion with no phase transitions (Table 25). The thermal expansion of **SION-2** is heavily anisotropic with the β and c parameters expanding to the largest extent, and at 340 K equalling respectively 104.3% and 103.6% of their initial values. The thermal expansion coefficients $\alpha_i = (1/\ell)d\ell/dT$ calculated with respect to the three principal axes X_1 , X_2 , and X_3 ,²⁴⁷ revealed an NTE along X_1 , a moderate PTE along X_2 , and a significant PTE along X_3 .

(Table 24 and Figure 104). **SION-2** exhibits NTE along X_1 with $\alpha_1 = -153(6) \text{ MK}^{-1}$, which is the highest value among all lanthanide-based MOFs reported to date. Ammonium metal formate framework $[\text{NH}_2\text{NH}_3][\text{Tm}(\text{HCOO})_4]$ was shown to display a slightly weaker NTE effect of $\alpha_3 = -120 \text{ MK}^{-1}$ over a narrower 100–180 K temperature range,^{243a} while the effect in $[\text{NH}_2\text{CHNH}_2][\text{Er}(\text{HCOO})_4]$ was weaker by one order of magnitude ($\alpha_2 = -7 \text{ MK}^{-1}$) in the 60–300 K temperature range.^{243b}

The principal axes X_1 , X_2 , and X_3 nearly coincide with the face diagonals of parallelepipeds forming the primitive α -Po net. d_1 is defined as the shorter diagonal of the parallelogram formed by two η^2 -chelating and two O2,O4-bridging DHBDC²⁻ ligands, d_2 as the longer diagonal of this parallelogram, and d_3 as the shorter diagonal of the parallelogram formed by two η^2 -chelating and two O3,O6-bridging DHBDC²⁻ ligands (Figure 102 and Figure 103; the O atom numbering refers to the scheme in the originally published crystal structure). Due to the fact that the nodes of the *pcu* net occupy special 1g positions of the triclinic unit cell (0, $\frac{1}{2}$, $\frac{1}{2}$), the lengths of d_1 , d_2 , and d_3 can be directly inferred from the adequate unit-cell parameters (Figure 105). The change of these distances as a function of temperature is presented in Figure 106. The distance d_1 shortens to a significant extent, while d_2 increases slightly, and d_3 increases by 0.77 Å in the 100–340 K temperature range. Expressing the progression of these distances in the percentage scale (Figure 102b) emphasises the same temperature-induced trends as observed in the case of principal axis lengths (Figure 102a). For the purpose of comparison, the coefficients of thermal expansion of the distances d_1 , d_2 , and d_3 were also calculated, and reported in Table 24. During the heating run, in the 100–340 K temperature range, they reflect the same trends as the coefficients derived along the principal axes. During the subsequent cooling, in the 340–100 K temperature range, however, the change of d_1 , d_2 , and d_3 with temperature is markedly different. The most significant, yet lower in value, PTE is observed along d_3 , d_1 displays a moderate PTE, while weak NTE is observed along d_2 .

Geometrically, **SION-2** can be considered as constructed by planes of Tb^{III}_2 clusters interconnected with O2,O4- and O3,O6-bridging DHBDC²⁻ ligands (horizontal layers in Figure 101). Multiple coordination bonds constituting these planes (O atoms of carboxylate groups of DHBDC²⁻ bind simultaneously to two Tb^{III} atoms within a Tb^{III}_2 unit) should in theory provide the planes with a certain inflexibility upon temperature increase as any potential change of position of one O atom in the coordination shell of the first Tb^{III} atom ought to involve a concerted change of the second O coordinated to the neighbouring Tb^{III} (Figure 107a). On the other hand, the Tb^{III} -bridging DHBDC²⁻ planes are linked together with chelating DHBDC²⁻ ligands; they coordinate to the same Tb^{III} with both carboxylate O atoms (in a manner similar to a ball-and-socket linkage endowed with a considerable rotational freedom), so change of their position with respect to the Tb^{III}_2 cluster should not be constrained (Figure 107b).

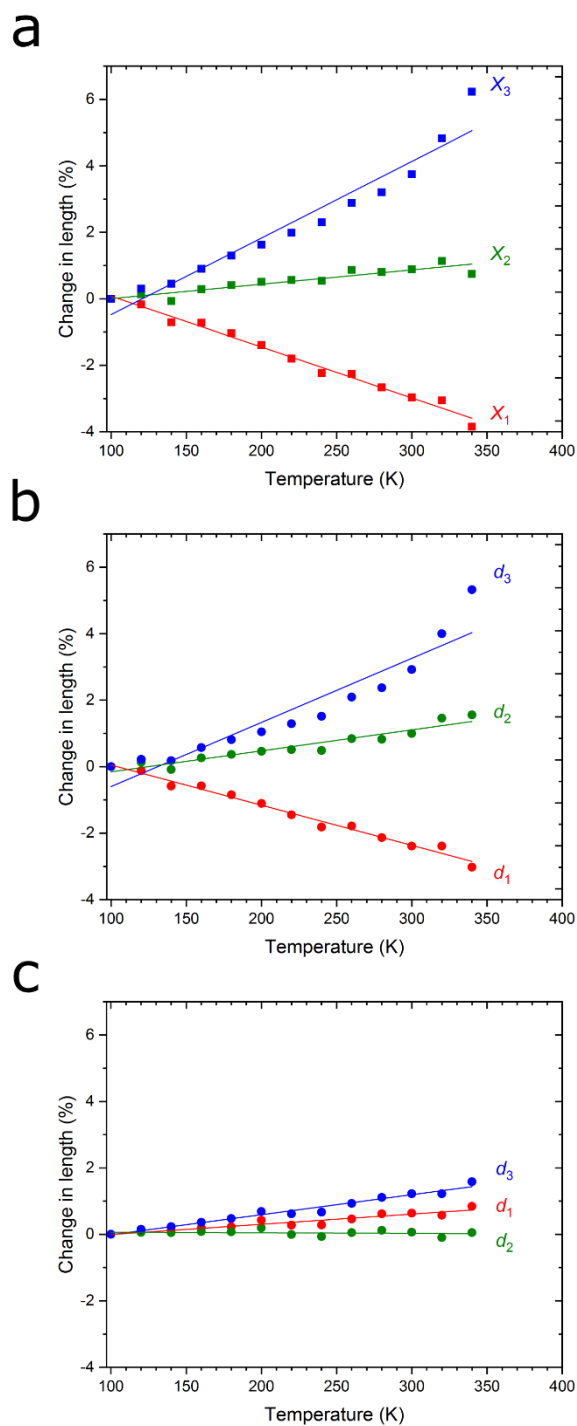


Figure 102. (a) Percentage change in lengths of the principal axes X_1 , X_2 , and X_3 of **SION-2** as a function of temperature. (b) Percentage change in distances d_1 , d_2 , and d_3 in the 100–340 K temperature range on heating. (c) Percentage change in distances d_1 , d_2 , and d_3 in the 340–100 K temperature range on cooling. The coefficients α of thermal expansion (Table 24) are effectively the average slopes of these curves marked with solid lines.

Table 24. Coefficients α of thermal expansion determined experimentally along three principal axes X_1 , X_2 , and X_3 in the 100–340 K temperature range during the heating regime, and coefficients α of thermal expansion of the distances d_1 , d_2 , and d_3 in the 100–340 K temperature range during the heating and cooling regimes. The volumetric coefficient of thermal expansion during the heating regime is $\alpha_V = +144(16) \text{ MK}^{-1}$.

100–340 K, heating			
Axis	$\alpha \text{ (MK}^{-1}\text{)}$	Distance	$\alpha \text{ (MK}^{-1}\text{)}$
$X_1 \cong [\overline{0.83} \ 0.13 \ \overline{0.54}] \cong [\overline{513}]$	$-158(6)$	d_1	$-121(4)$
$X_2 \cong [0.34 \ 0.89 \ 0.29] \cong [131]$	$+31(11)$	d_2	$+63(5)$
$X_3 \cong [\overline{0.58} \ 0.07 \ 0.81] \cong [\overline{203}]$	$+280(40)$	d_3	$+190(20)$
340–100 K, cooling			
		Distance	$\alpha \text{ (MK}^{-1}\text{)}$
		d_1	$+32(2)$
		d_2	$-4(2)$
		d_3	$+61(2)$

To provide more insights, VT SCXRD measurements were further analysed with full-matrix least-squares refinement. Derivation of specific conformational parameters helped elucidate the NTE effect in many previous cases.^{223, 232c, 232d, 248} In **SION-2**, as the temperature is increased, the Tb^{III} –bridging DHBDC²⁻ planes slide on the top of each other while the angle between the chelating DHBDC²⁻ and the planes decreases (Figure 108). In particular, the slide is realised in such a way that the distance d_1 shortens considerably, and the distance d_2 lengthens as the temperature is increased, leading to respectively NTE along d_1 and PTE along d_2 . It is highly probable that in an extreme case, the slide of the Tb^{III} –bridging DHBDC²⁻ planes may lead to a mutual connection of Tb^{III}_2 clusters into 1D Tb –O chains. The chemical transformation of **SION-2** into another Tb -based MOF, $[\text{Tb}_2(\text{DHBDC})(\text{DOBDC})\cdot(\text{DMF})_2]$, (**SION-1**, where $\text{DOBDC}^{2-} = 2,5\text{-dioxidobenzene-1,4-dicarboxylate}$), which realises this scenario, was reported previously.²⁴⁴

The least-square refinement also provides insights about the structural changes occurring at 380 K. A decrease of 12.7% of the unit-cell volume in the 360–380 K temperature range (Figure 109a,b and Table 26) is accompanied by the significant reduction of the void volume (from 17.7% of the unit-cell volume at 360 K to 12.7% at 380 K, Figure 110) and content (at 360 K, non-coordinated DMF molecules become highly disordered, contributing to the diffuse electron density corresponding to 0.675 DMF molecules per unit cell, and at 380 K they vanish, Figure 111). Once desolvated, the crystal of **SION-2** exhibits a strikingly different thermal expansion pattern. The slide of the rigid Tb^{III} –bridging DHBDC²⁻ planes is reversed (Figure 108), however, the geometry of this slide is different compared to the heating run. Two closest Tb^{III}_2 cluster originating from two subsequent rigid planes come closer to each other as the temperature is lowered, which results in PTE along d_1 . In turn, the distance d_2 lengthens on cooling, which is reflected by a small, yet definitely negative coefficient of thermal expansion of d_2 . In the direction perpendicular to both d_1 and d_2 , the result of heating is analogous to that of cooling, since during both temperature ramps the strongest PTE is observed along d_3 .

Interestingly, whenever the crystal of **SION-2** is kept in a relatively low-temperature regime (not higher than 300 K), the changes in unit-cell parameters are quasi-reversible (Figure 109c,d and Table 27). Although the changes in principal axes lengths do not follow exactly the same scheme upon cooling and heating in the 100–300–100 K temperature range, the unit-cell volume change shows no hysteresis. This observation emphasises the impact of presence or absence of guest DMF molecules on the thermal expansion coefficients of **SION-2**.

9.4. Conclusions

Thermal expansion of a Ln-based MOF having labile solvent guest molecules within the structural voids was experimentally studied for the first time. When heated in the 100–340 K temperature range, **SION-2** exhibits a uniaxial negative thermal expansion along X_1 with $\alpha_1 = -153(6) \text{ MK}^{-1}$, which manifests itself as a slide of rigid Tb^{III} –bridging DHBDC^{2-} planes interconnected with mobile chelating DHBDC^{2-} ligands on the top of each other, as observed from the VT SCXRD measurements. This phenomenon, however, occurs only when the DMF guest molecules are present within the structural voids. Once heated up to 380 K, the crystal loses all non-coordinated solvent, which is accompanied by a significant reduction of the void size. Upon subsequent cooling, the thermal expansion of the crystal is markedly different. The slide of the rigid Tb^{III} –bridging DHBDC^{2-} planes is reversed, however, the progression of d_1 and d_2 distances (lying approximately along the respective X_1 and X_2 principal axes) with temperature is contrary compared to the heating run. Consequently, a weak NTE of $-4(2) \text{ MK}^{-1}$ is observed along d_2 on cooling in the 340–100 K temperature range. The example of **SION-2** can trigger further research efforts in this field, and so Ln-based MOFs endowed with mobile guest species entrapped in the structural voids can establish themselves as a novel unique class of materials exhibiting strong and tuneable NTE effects.

9.5. Appendix

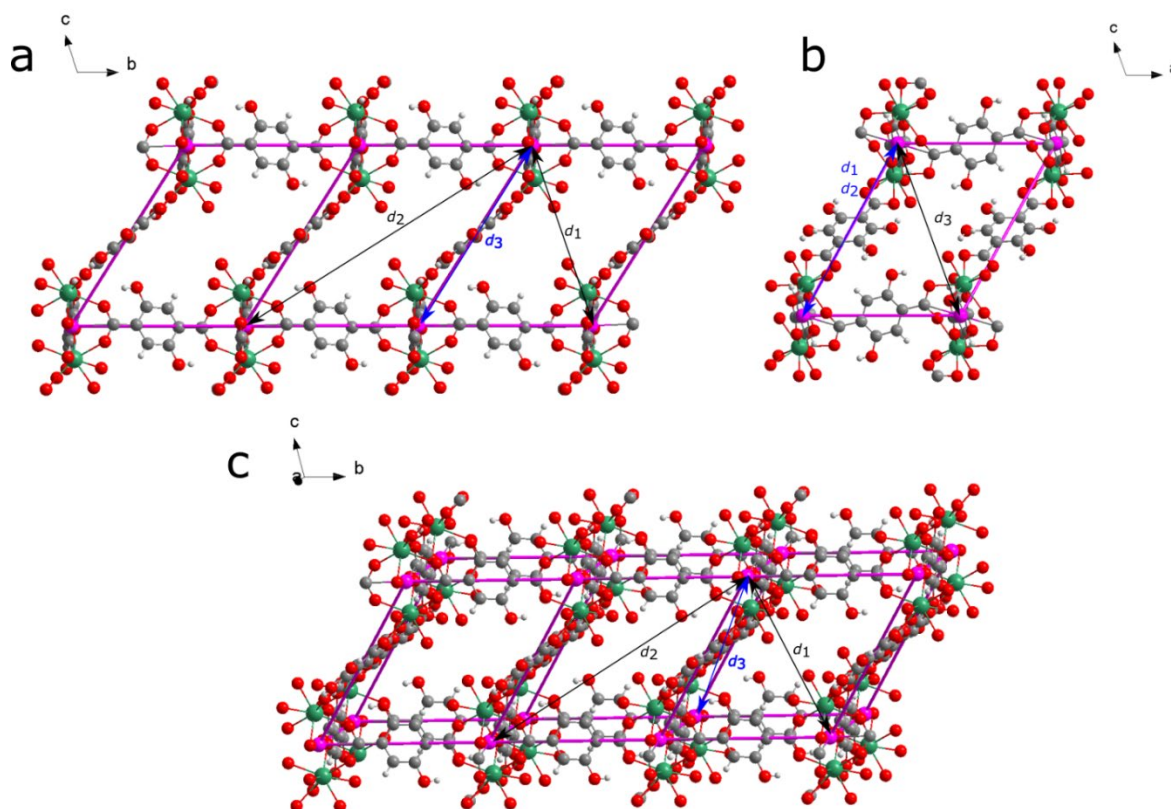


Figure 103. Crystal structure of **SION-2** overlaid with its topological description. Tb_2 clusters act as 6-coordinated nodes, while DHBDC^{2-} ligands are 2-coordinating links. Distances d_1 , d_2 , and d_3 , localised within the crystal structure of **SION-2** are approximately collinear with the principal axes X_1 , X_2 , and X_3 respectively, markedly different from the crystallographic axes a , b , and c . Distances d_1 , d_2 , and d_3 marked in black are in the plane of the picture, while those marked in blue extend out of that plane. (a) View along a -axis, (b) View along b -axis (c) View along an intermediate direction. Coordinated and non-coordinated DMF molecules have been omitted for clarity.

Table 25. Edge lengths, angles, and volumes of the triclinic unit cell of **SION-2** determined from SCXRD measurements in the 100–340 K temperature range.

T (K)	a (Å)	b (Å)	c (Å)	α (°)	β (°)	γ (°)	V (Å ³)
100	10.5096(6)	10.9768(4)	12.5019(6)	104.759(4)	107.340(5)	97.380(4)	1298.23(12)
120	10.5156(6)	10.9858(4)	12.5290(6)	104.707(4)	107.578(5)	97.265(4)	1301.80(12)
140	10.4937(6)	10.9559(4)	12.5321(6)	104.652(4)	107.923(4)	97.114(4)	1294.06(12)
160	10.5194(6)	10.9889(4)	12.5734(6)	104.589(4)	108.172(5)	96.992(4)	1304.34(12)
180	10.5256(6)	10.9947(5)	12.6032(6)	104.523(4)	108.540(5)	96.829(4)	1306.91(13)
200	10.5213(5)	10.9954(5)	12.6323(5)	104.438(4)	108.872(4)	96.664(4)	1307.93(11)
220	10.5190(6)	10.9933(5)	12.6565(5)	104.317(4)	109.262(4)	96.536(4)	1307.83(12)
240	10.5121(6)	10.9835(5)	12.6782(5)	104.175(4)	109.639(4)	96.452(4)	1305.96(12)
260	10.5371(6)	11.0161(5)	12.7345(5)	104.005(5)	109.918(4)	96.448(4)	1317.37(12)
280	10.5333(6)	11.0035(5)	12.7511(5)	103.784(5)	110.271(4)	96.437(4)	1315.34(12)
300	10.5445(7)	11.0141(6)	12.7860(8)	103.484(6)	110.657(6)	96.517(5)	1319.52(16)
320	10.5861(8)	11.0497(6)	12.8741(9)	103.021(6)	111.134(7)	96.698(5)	1335.67(19)
340	10.5964(10)	11.0355(7)	12.9523(13)	102.131(7)	112.002(9)	97.133(6)	1338.1(2)

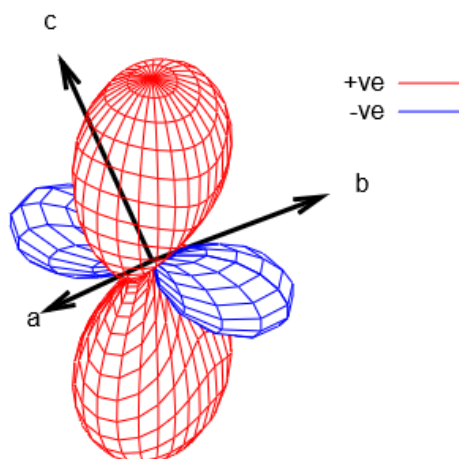


Figure 104. Graphical representation of the coefficients of thermal expansion of **SION-2** in the form of an expansivity indicatrix.

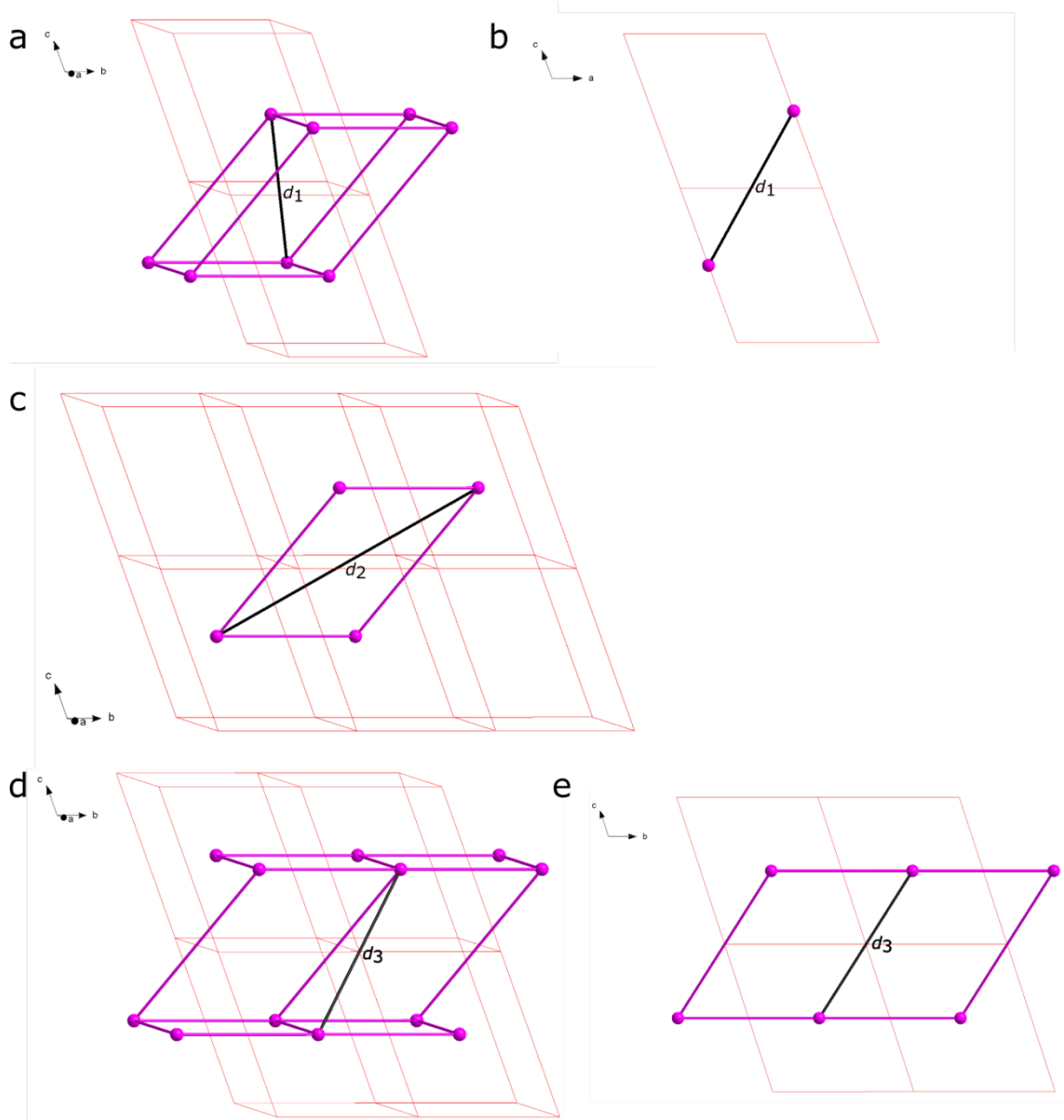


Figure 105. (a) Localisation of the distance d_1 within the unit cell of **SION-2**. (b) From the projection onto the ac plane (both nodes involved are situated at $y = 0.5$) and the law of cosines it is inferred that

$$d_1 = \sqrt{a^2 + c^2 - 2ac \cos(180^\circ - \beta)}$$

(c) Localisation of the distance d_2 within the unit cell of **SION-2**. This distance is not parallel to any face of the unit cell, so in order to calculate its value the general formula for the interstitial distance can only be applied

$$d_2 = \sqrt{a^2 + 4b^2 + c^2 + 4ab \cos \gamma + 4bc \cos \alpha + 2ac \cos \beta}$$

(d) Localisation of the distance d_3 within the unit cell of **SION-2**. (e) From the projection onto the bc plane (both nodes involved are situated at $x = 0$) and the law of cosines it is inferred that

$$d_3 = \sqrt{b^2 + c^2 - 2bc \cos(180^\circ - \alpha)}$$

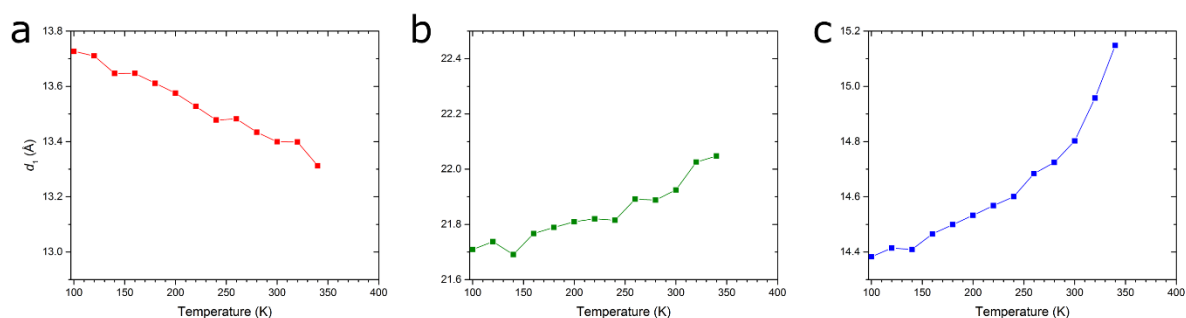


Figure 106. Change of the absolute values of the distances (a) d_1 , (b) d_2 , and (c) d_3 as a function of temperature.

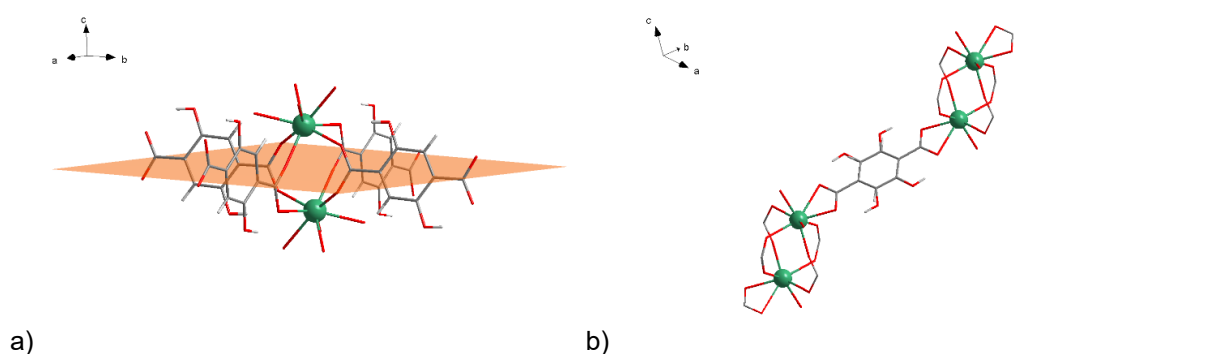


Figure 107. (a) A Tb^{III}₂ unit bound simultaneously to four DHBDC²⁻ ligands via O2,O4- and O3,O6-bridging endowing the 2-dimensional planes (marked in orange) with an inflexibility. (b) η^2 -chelating DHBDC²⁻ ligands, the position of which with respect to the Tb^{III}₂ cluster is not constrained.

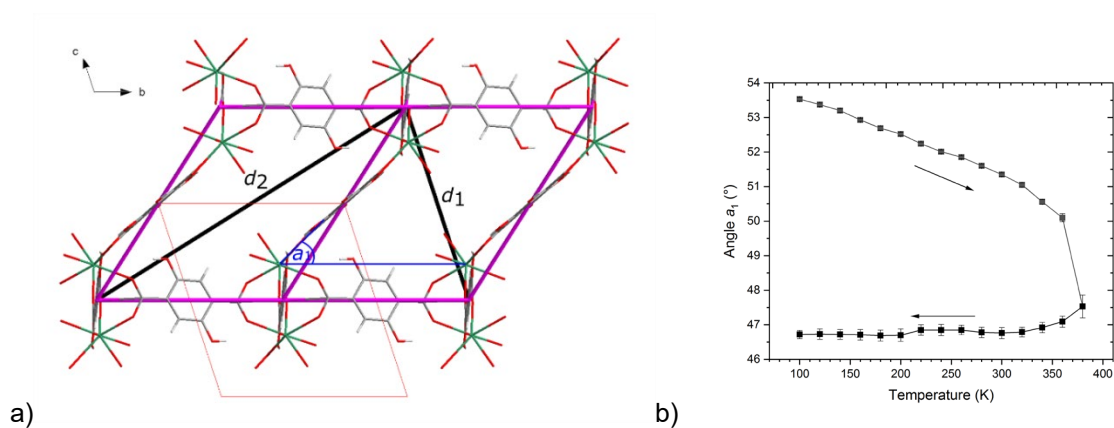


Figure 108. (a) Angle a_1 representing the inclination of the η^2 -chelating DHBDC²⁻ ligands with respect to the rigid Tb^{III}-bridging DHBDC²⁻ planes. (b) Progression of a_1 as a function of temperature. The arrows indicate the heating and the cooling regime.

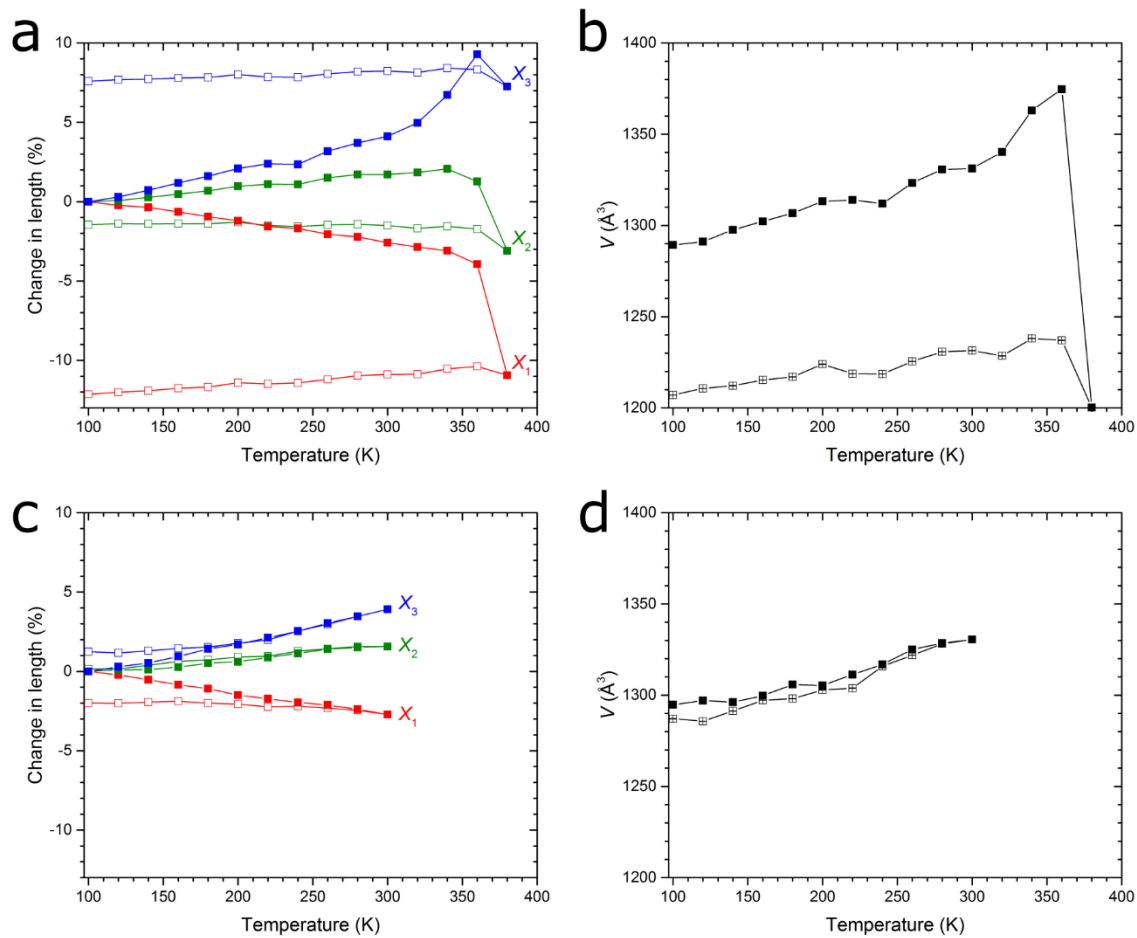


Figure 109. (a) Percentage change in lengths of the principal axes X_1 , X_2 , and X_3 and (b) absolute change of the unit-cell volume of **SION-2** in the 100–380–100 K temperature range. (c) Percentage change in lengths of the principal axes X_1 , X_2 , and X_3 and (d) absolute change of the unit-cell volume of **SION-2** in the 100–300–100 K temperature range. Full symbols denote the heating, while the empty ones – the cooling regime.

Table 26. Edge lengths, angles, and volumes of the triclinic unit cell of **SION-2** determined from SCXRD measurements in the 100–380–100 K temperature range on heating and cooling.

T (K)	<i>a</i> (Å)	<i>b</i> (Å)	<i>c</i> (Å)	α (°)	β (°)	γ (°)	<i>V</i> (Å ³)
100	10.4740(6)	10.9218(3)	12.5171(6)	104.803(4)	107.218(5)	97.441(4)	1289.29(12)
120	10.4785(6)	10.9262(3)	12.5373(6)	104.797(4)	107.481(5)	97.272(4)	1291.14(12)
140	10.4969(6)	10.9385(6)	12.5755(6)	104.753(4)	107.766(5)	97.097(4)	1297.59(12)
160	10.5112(6)	10.9539(3)	12.6033(6)	104.720(4)	108.142(5)	96.856(4)	1302.25(12)
180	10.5222(6)	10.9713(3)	12.6332(6)	104.684(4)	108.521(5)	96.635(4)	1306.79(12)
200	10.5396(6)	10.9909(3)	12.6702(6)	104.581(4)	108.915(5)	96.463(4)	1313.17(12)
220	10.5391(6)	10.9954(3)	12.6924(6)	104.471(4)	109.276(5)	96.350(4)	1313.97(12)
240	10.5332(6)	10.9940(3)	12.6843(6)	104.463(4)	109.319(5)	96.339(4)	1311.94(12)
260	10.5588(6)	11.0205(3)	12.7641(6)	104.174(4)	109.941(5)	96.235(4)	1323.30(12)
280	10.5792(6)	11.0356(4)	12.8087(7)	103.932(4)	110.274(5)	96.262(4)	1330.70(13)
300	10.5785(6)	11.0332(4)	12.8359(7)	103.661(4)	110.638(5)	96.324(4)	1331.17(13)
320	10.6017(6)	11.0500(4)	12.9005(7)	103.241(4)	111.115(5)	96.457(4)	1340.32(13)
340	10.659(6)	11.1024(5)	13.0304(7)	102.405(4)	111.874(5)	96.904(5)	1363.06(13)
360	10.6975(7)	11.1103(5)	13.1588(7)	100.742(4)	112.996(6)	98.049(5)	1374.72(16)
380	10.5363(13)	11.0128(19)	11.6445(19)	96.840(14)	111.826(13)	101.636(12)	1200.2(4)
360	10.6634(8)	11.1405(7)	11.6932(8)	96.751(5)	111.604(7)	101.562(6)	1237.09(17)
340	10.6765(7)	11.1609(5)	11.6592(6)	96.727(4)	111.531(5)	101.572(5)	1238.04(14)
320	10.6527(6)	11.1484(5)	11.6012(6)	96.768(4)	111.444(5)	101.555(5)	1228.50(13)
300	10.6648(6)	11.1682(5)	11.5897(6)	96.799(4)	111.386(5)	101.528(4)	1231.44(13)
280	10.6648(6)	11.1779(5)	11.5682(6)	96.856(4)	111.320(5)	101.494(4)	1230.79(13)
260	10.6565(6)	11.1667(5)	11.5332(6)	96.830(4)	111.282(5)	101.473(4)	1225.52(12)
240	10.6376(6)	11.1560(5)	11.4941(5)	96.866(4)	111.213(5)	101.459(4)	1218.61(12)
220	10.6410(6)	11.1651(5)	11.4787(5)	96.891(4)	111.171(5)	101.441(4)	1218.75(12)
200	10.6568(6)	11.1912(5)	11.4798(5)	96.941(4)	111.109(5)	101.425(4)	1223.97(12)
180	10.6430(6)	11.1747(5)	11.4401(5)	96.900(4)	111.066(5)	101.426(4)	1216.96(12)
160	10.6385(6)	11.1794(5)	11.4206(5)	96.941(4)	111.003(5)	101.423(4)	1215.30(12)
140	10.6338(6)	11.1768(5)	11.3943(5)	96.944(4)	110.943(5)	101.428(4)	1212.19(12)
120	10.6311(6)	11.1791(5)	11.3767(5)	96.958(4)	110.894(5)	101.421(4)	1210.69(12)
100	10.6219(6)	11.1750(5)	11.3531(5)	96.985(4)	110.840(5)	101.422(4)	1207.05(12)

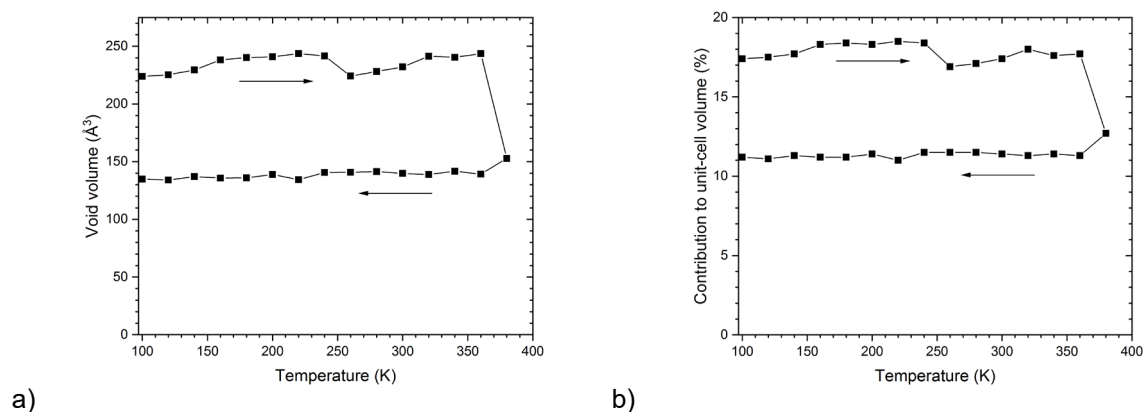


Figure 110. Volume of the structural voids found in the crystal structure of **SION-2** expressed (a) as absolute values (in \AA^3) and (b) as a contribution to the overall unit-cell volume. Void volume was calculated by the VOIDS procedure of the program MERCURY. In the 100–340 K temperature range on heating, non-coordinated DMF molecules were manually removed before running the void volume calculation. The arrows indicate the heating and the cooling regime.

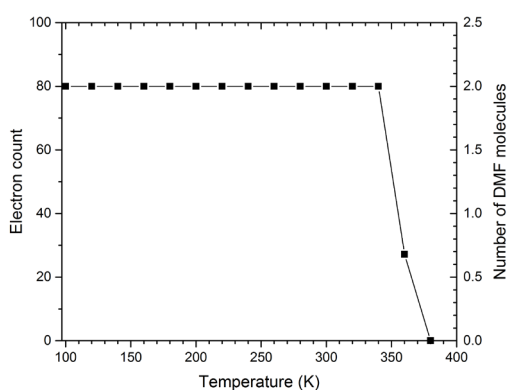


Figure 111. Content of the structural voids of **SION-2** plotted against temperature (in K) expressed in terms of integrated electron density. Electron count of 80 e^- (full occupancy of two DMF molecules per unit cell) was arbitrarily assigned to all temperatures up to 340 K, while last two data points were quantified with the SQUEEZE algorithm within the PLATON program suite.

Table 27. Edge lengths, angles, and volumes of the triclinic unit cell of **SION-2** determined from SCXRD measurements in the 100–300–100 K temperature range on heating and cooling.

T (K)	<i>a</i> (Å)	<i>b</i> (Å)	<i>c</i> (Å)	α (°)	β (°)	γ (°)	<i>V</i> (Å ³)
100	10.4901(6)	10.9330(4)	12.5332(6)	104.772(4)	107.209(5)	97.408(4)	1294.77(12)
120	10.4964(6)	10.9385(4)	12.5536(6)	104.754(4)	107.472(5)	97.243(4)	1297.06(12)
140	10.4935(6)	10.9365(4)	12.5654(6)	104.745(4)	107.751(5)	97.071(4)	1296.23(12)
160	10.5049(6)	10.9483(4)	12.5894(6)	104.711(4)	108.121(5)	96.845(4)	1299.70(12)
180	10.5212(6)	10.9697(4)	12.6243(6)	104.673(4)	108.498(5)	96.634(4)	1305.86(12)
200	10.5170(6)	10.9737(4)	12.6400(7)	104.625(4)	108.862(5)	96.467(4)	1305.32(13)
220	10.5312(7)	10.9923(4)	12.6777(7)	104.523(4)	109.210(5)	96.348(4)	1311.33(14)
240	10.5442(7)	11.0078(4)	12.7133(7)	104.373(4)	109.552(5)	96.258(5)	1316.85(14)
260	10.5653(7)	11.0256(4)	12.7629(7)	104.186(4)	109.902(6)	96.216(5)	1325.00(14)
280	10.5735(7)	11.0298(5)	12.7995(8)	103.973(4)	110.249(6)	96.219(5)	1328.50(15)
300	10.5777(7)	11.0325(5)	12.8313(7)	103.730(4)	110.611(6)	96.270(5)	1330.55(15)
280	10.5752(7)	11.0347(4)	12.7898(7)	103.907(4)	110.295(6)	96.254(5)	1328.15(14)
260	10.5621(7)	11.0272(5)	12.7404(7)	104.100(4)	109.996(6)	96.262(5)	1321.94(14)
240	10.5494(7)	11.0166(5)	12.6931(7)	104.218(4)	109.725(6)	96.289(5)	1315.81(14)
220	10.5180(7)	10.9930(5)	12.6295(7)	104.362(4)	109.454(5)	96.321(5)	1303.87(14)
200	10.5216(7)	10.9951(5)	12.5999(7)	104.415(4)	109.242(5)	96.365(5)	1302.88(14)
180	10.5127(7)	10.9902(5)	12.5596(7)	104.502(4)	109.035(5)	96.406(5)	1298.11(14)
160	10.5162(7)	10.9943(5)	12.5325(7)	104.547(4)	108.870(5)	96.440(5)	1297.23(14)
140	10.5041(6)	10.9869(5)	12.4908(7)	104.614(4)	108.718(5)	96.465(5)	1291.33(14)
120	10.4901(6)	10.9817(5)	12.4553(7)	104.682(4)	108.602(5)	96.492(5)	1285.72(14)
100	10.4999(6)	10.9917(5)	12.4405(7)	104.682(4)	108.544(5)	96.491(5)	1287.09(15)

10. Outlook

Six research projects presented in the current thesis showed the practical realisation of the structure-to-application approach in the investigation of novel materials. MOFs, with their unprecedented structural versatility, proved to be an excellent platform for the design of new materials aimed at desired applications. Based on the structure of the newly synthesised MOFs, revealed with success using the diffraction techniques, a range of potential applications was postulated. Furthermore, the adjustment of the native MOF structures (partial or complete activation, introduction of extra guest species, temperature change) led in dramatic alterations of the characteristics of the studied materials. This, in turn, allowed for the postulation that these MOFs can find some even more specific applications (tuneable CO₂/CH₄ separation, radioactive iodine capture, thermofluorochromic sensors). In this way, it was demonstrated that the modified bottom-up approach of materials discovery is an efficient method of accessing novel materials for targeted applications. It was also shown that MOFs can compete with, and in many cases outperform the currently available functional materials.

It is not unsafe to state that MOFs will continue to attract attention of researchers who wish to bring the findings of fundamental research to everyday-life application. Advancement of the experimental techniques and constant growth of the quantity of the experimental data available will allow the design of new original experiments and drawing more binding conclusions. Now, as the field of MOFs is attaining its maturity, many exciting discoveries will surely come to light.

References

- O. M. Yaghi, M. J. Kalmutzki and C. S. Diercks, in *Introduction to Reticular Chemistry: Metal-Organic Frameworks and Covalent Organic Frameworks*, John Wiley & Sons, 2019.
- K. A. Hofmann and F. Küspert, *Z. Anorg. Chem.*, 1897, **15**, 204-207.
- J. H. Rayner and H. M. Powell, *J. Chem. Soc.*, 1952, 319-328.
- T. Hasegawa, S.-i. Nishikiori and T. Iwamoto, *Chem. Lett.*, 1985, **14**, 1659-1662.
- S.-i. Nishikiori, T. Hasegawa and T. Iwamoto, *J. Inclus. Phenom. Mol.*, 1991, **11**, 137-152.
- Y. Kinoshita, I. Matsubara and Y. Saito, *B. Chem. Soc. Jpn.*, 1959, **32**, 741-747.
- (a) Y. Kinoshita, I. Matsubara, T. Higuchi and Y. Saito, *B. Chem. Soc. Jpn.*, 1959, **32**, 1221-1226; (b) Y. Kinoshita, I. Matsubara and Y. Saito, *B. Chem. Soc. Jpn.*, 1959, **32**, 1216-1221.
- (a) B. F. Hoskins and R. Robson, *J. Am. Chem. Soc.*, 1989, **111**, 5962-5964; (b) B. F. Hoskins and R. Robson, *J. Am. Chem. Soc.*, 1990, **112**, 1546-1554.
- A. F. Wells, *Three-Dimensional Nets and Polyhedra*, Wiley-Interscience, New York, 1977.
- M. J. Zaworotko, *Chem. Soc. Rev.*, 1994, **23**, 283-288.
- R. W. Gable, B. F. Hoskins and R. Robson, *J. Chem. Soc. Chem. Commun.*, 1990, 762-763.
- B. F. Abrahams, B. F. Hoskins, D. M. Michail and R. Robson, *Nature*, 1994, **369**, 727-729.
- O. M. Yaghi and H. Li, *J. Am. Chem. Soc.*, 1995, **117**, 10401-10402.
- O. M. Yaghi, G. Li and H. Li, *Nature*, 1995, **378**, 703-706.
- H. Li, M. Eddaoudi, T. L. Groy and O. M. Yaghi, *J. Am. Chem. Soc.*, 1998, **120**, 8571-8572.
- H. Li, M. Eddaoudi, M. O'Keeffe and O. M. Yaghi, *Nature*, 1999, **402**, 276-279.
- (a) O. M. Yaghi, M. O'Keeffe, N. W. Ockwig, H. K. Chae, M. Eddaoudi and J. Kim, *Nature*, 2003, **423**, 705-714; (b) H. Furukawa, K. E. Cordova, M. O'Keeffe and O. M. Yaghi, *Science*, 2013, **341**, 1230444.
- (a) S. M. Auerbach, *Handbook of Zeolite Science and Technology*, New York : Dekker, New York, 2003; (b) A. K. Cheetham, G. Férey and T. Loiseau, *Angew. Chem., Int. Ed.*, 1999, **38**, 3268-3292.
- (a) G. Férey, *Chem. Soc. Rev.*, 2008, **37**, 191-214; (b) A. J. Fletcher, K. M. Thomas and M. J. Rosseinsky, *J. Solid State Chem.*, 2005, **178**, 2491-2510.
- K. J. Saunders, *Organic Polymer Chemistry: An Introduction to the Organic Chemistry of Adhesives, Fibres, Paints, Plastics, and Rubbers*, Springer Netherlands, 2013.
- (a) E. J. Carrington, I. J. Vitorica-Yrezabal and L. Brammer, *Acta Cryst. Sect. B*, 2014, **70**, 404-422; (b) W. M. Bloch, N. R. Champness and C. J. Doonan, *Angew. Chem., Int. Ed.*, 2015, **54**, 12860-12867.
- O. K. Farha, I. Eryazici, N. C. Jeong, B. G. Hauser, C. E. Wilmer, A. A. Sarjeant, R. Q. Snurr, S. T. Nguyen, A. Ö. Yazaydin and J. T. Hupp, *J. Am. Chem. Soc.*, 2012, **134**, 15016-15021.
- H. Furukawa, N. Ko, Y. B. Go, N. Aratani, S. B. Choi, E. Choi, A. Ö. Yazaydin, R. Q. Snurr, M. O'Keeffe, J. Kim and O. M. Yaghi, *Science*, 2010, **329**, 424-428.
- H. Furukawa, Y. B. Go, N. Ko, Y. K. Park, F. J. Uribe-Romo, J. Kim, M. O'Keeffe and O. M. Yaghi, *Inorg. Chem.*, 2011, **50**, 9147-9152.
- K. Sumida, D. L. Rogow, J. A. Mason, T. M. McDonald, E. D. Bloch, Z. R. Herm, T.-H. Bae and J. R. Long, *Chem. Rev.*, 2012, **112**, 724-781.
- (a) M. P. Suh, H. J. Park, T. K. Prasad and D.-W. Lim, *Chem. Rev.*, 2012, **112**, 782-835; (b) Y. He, W. Zhou, G. Qian and B. Chen, *Chem. Soc. Rev.*, 2014, **43**, 5657-5678.
- (a) S.-L. Li and Q. Xu, *Energy Environ. Sci.*, 2013, **6**, 1656-1683; (b) A. Schoedel, Z. Ji and O. M. Yaghi, *Nat. Energy*, 2016, **1**, 16034.
- (a) M. Klimakow, P. Klobes, A. F. Thünemann, K. Rademann and F. Emmerling, *Chem. Mater.*, 2010, **22**, 5216-5221; (b) J.-R. Li, R. J. Kuppler and H.-C. Zhou, *Chem. Soc. Rev.*, 2009, **38**, 1477-1504.
- M. Witman, S. Ling, S. Jawahery, P. G. Boyd, M. Haranczyk, B. Slater and B. Smit, *J. Am. Chem. Soc.*, 2017, **139**, 5547-5557.
- (a) S. S. Y. Chui, S. M. F. Lo, J. P. H. Charmant, A. G. Orpen and I. D. Williams, *Science*, 1999, **283**, 1148; (b) N. L. Rosi, J. Kim, M. Eddaoudi, B. Chen, M. O'Keeffe and O. M. Yaghi, *J. Am. Chem. Soc.*, 2005, **127**, 1504-1518; (c) K. S. Park, Z. Ni, A. P. Côté, J. Y. Choi, R. Huang, F. J. Uribe-Romo, H. K. Chae, M. O'Keeffe and O. M. Yaghi, *Proc. Natl. Acad. Sci. U. S. A.*, 2006, **103**, 10186; (d) P. Horcajada, S. Surblé, C. Serre, D.-Y. Hong, Y.-K. Seo, J.-S. Chang, J.-M. Grenèche, I. Margiolaki and G. Férey, *Chem. Commun.*, 2007, 2820-2822.
- (a) J. Su and J. Chen, *MOFs of Uranium and the Actinides*, Springer Berlin Heidelberg, Berlin, Heidelberg, 2015; (b) S. Kaskel, *The Chemistry of Metal-Organic Frameworks: Synthesis, Characterization, and Applications*, Wiley-VCH Verlag, Weinheim, 2016.
- (a) F. A. Almeida Paz, J. Klinowski, S. M. F. Vilela, J. P. C. Tomé, J. A. S. Cavaleiro and J. Rocha, *Chem. Soc. Rev.*, 2012, **41**, 1088-1110; (b) K. Shen, M. Zhang and H. Zheng, *CrystEngComm*, 2015, **17**, 981-991.
- H. Deng, S. Grunder, K. E. Cordova, C. Valente, H. Furukawa, M. Hmadeh, F. Gándara, A. C. Whalley, Z. Liu, S. Asahina, H. Kazumori, M. O'Keeffe, O. Terasaki, J. F. Stoddart and O. M. Yaghi, *Science*, 2012, **336**, 1018.
- (a) Y.-B. Huang, J. Liang, X.-S. Wang and R. Cao, *Chem. Soc. Rev.*, 2017, **46**, 126-157; (b) A. H. Chughtai, N. Ahmad, H. A. Younus, A. Laypkov and F. Verpoort, *Chem. Soc. Rev.*, 2015, **44**, 6804-6849; (c) M. Ranocchiari and J. A. van Bokhoven, *Phys. Chem. Chem. Phys.*, 2011, **13**, 6388-6396; (d)

- J. Lee, O. K. Farha, J. Roberts, K. A. Scheidt, S. T. Nguyen and J. T. Hupp, *Chem. Soc. Rev.*, 2009, **38**, 1450-1459.
35. (a) L. E. Kreno, K. Leong, O. K. Farha, M. Allendorf, R. P. Van Duyne and J. T. Hupp, *Chem. Rev.*, 2012, **112**, 1105-1125; (b) Z. Hu, B. J. Deibert and J. Li, *Chem. Soc. Rev.*, 2014, **43**, 5815-5840; (c) S. E. Miller, M. H. Teplensky, P. Z. Moghadam and D. Fairen-Jimenez, *Interface Focus*, 2016, **6**, 20160027; (d) D. Wang, Q. Tan, J. Liu and Z. Liu, *Dalton Trans.*, 2016, **45**, 18450-18454; (e) X. Liu, W. Fu and E. Bouwman, *Chem. Commun.*, 2016, **52**, 6926-6929; (f) M. Andrzejewski and A. Katrusiak, *J. Phys. Chem. Lett.*, 2017, **8**, 279-284; (g) M. D. Allendorf, C. A. Bauer, R. K. Bhakta and R. J. Houk, *Chem. Soc. Rev.*, 2009, **38**, 1330-1352.
 36. (a) G. W. Peterson, M. R. Destefano, S. J. Garibay, A. Ploskonka, M. McEntee, M. Hall, C. J. Karwacki, J. T. Hupp and O. K. Farha, *Chem. Eur. J.*, 2017, **23**, 15913-15916; (b) E. Barea, C. Montoro and J. A. R. Navarro, *Chem. Soc. Rev.*, 2014, **43**, 5419-5430; (c) L. M. Rodríguez-Albelo, E. López-Maya, S. Hamad, A. R. Ruiz-Salvador, S. Calero and J. A. R. Navarro, *Nat. Commun.*, 2017, **8**, 14457; (d) A. Gładysiak, T. N. Nguyen, J. A. R. Navarro, M. J. Rosseinsky and K. C. Stylianou, *Chem. Eur. J.*, 2017, **23**, 13602-13606; (e) R. J. Drouot, K. Otake, A. J. Howarth, T. Islamoglu, L. Zhu, C. Xiao, S. Wang and O. K. Farha, *Chem. Mater.*, 2018, **30**, 1277-1284; (f) Y. Liu, A. J. Howarth, N. A. Vermeulen, S.-Y. Moon, J. T. Hupp and O. K. Farha, *Coord. Chem. Rev.*, 2017, **346**, 101-111.
 37. L. R. Mingabudinova, V. V. Vinogradov, V. A. Milichko, E. Hey-Hawkins and A. V. Vinogradov, *Chem. Soc. Rev.*, 2016, **45**, 5408-5431.
 38. W. Zhang and R. G. Xiong, *Chem. Rev.*, 2012, **112**, 1163-1195.
 39. (a) A. D. Katsenis, E. K. Brechin and G. S. Papaefstathiou, in *Encyclopedia of Inorganic and Bioinorganic Chemistry*, John Wiley & Sons, Ltd, 2011; (b) M. Kurmoo, *Chem. Soc. Rev.*, 2009, **38**, 1353-1379; (c) M. Kurmoo, *Chem. Soc. Rev.*, 2009, **38**, 1353-1379.
 40. (a) L. Sun, M. G. Campbell and M. Dincă, *Angew. Chem., Int. Ed.*, 2016, **55**, 3566-3579; (b) P. Ramaswamy, N. E. Wong and G. K. Shimizu, *Chem. Soc. Rev.*, 2014, **43**, 5913-5932; (c) S. Horike, D. Umeyama and S. Kitagawa, *Acc. Chem. Res.*, 2013, **46**, 2376-2384; (d) A. Morozan and F. Jaouen, *Energy Environ. Sci.*, 2012, **5**, 9269.
 41. S. R. Batten, in *Metal-organic frameworks: design and application*, ed. L. R. MacGillivray, John Wiley & Sons, 2010.
 42. R. Robson, *J. Chem. Soc. Dalton Trans.*, 2000, 3735-3744.
 43. V. A. Blatov, A. P. Shevchenko and D. M. Proserpio, *Cryst. Growth Des.*, 2014, **14**, 3576-3586.
 44. M. O'Keeffe, M. A. Peskov, S. J. Ramsden and O. M. Yaghi, *Acc. Chem. Res.*, 2008, **41**, 1782-1789.
 45. S. R. Batten and R. Robson, *Angew. Chem., Int. Ed.*, 1998, **37**, 1460-1494.
 46. *Reticular Chemistry Structure Resource*, <http://rcsr.anu.edu.au/>.
 47. A. J. Howarth, A. W. Peters, N. A. Vermeulen, T. C. Wang, J. T. Hupp and O. K. Farha, *Chem. Mater.*, 2016, **29**, 26-39.
 48. (a) D. K. Kumar, A. Das and P. Dastidar, *Cryst. Growth Des.*, 2007, **7**, 2096-2105; (b) B.-C. Tzeng, H.-T. Yeh, T.-Y. Chang and G.-H. Lee, *Cryst. Growth Des.*, 2009, **9**, 2552-2555.
 49. K. S. Min and M. P. Suh, *J. Am. Chem. Soc.*, 2000, **122**, 6834-6840.
 50. N. Stock and S. Biswas, *Chem. Rev.*, 2012, **112**, 933-969.
 51. A. Rabenau, *Angew. Chem., Int. Ed. Engl.*, 1985, **24**, 1026-1040.
 52. J. Klinowski, F. A. Almeida Paz, P. Silva and J. Rocha, *Dalton Trans.*, 2011, **40**, 321-330.
 53. W. Liu, L. Ye, X. Liu, L. Yuan, X. Lu and J. Jiang, *Inorg. Chem. Commun.*, 2008, **11**, 1250-1252.
 54. (a) M. Li and M. Dincă, *J. Am. Chem. Soc.*, 2011, **133**, 12926-12929; (b) H. Al-Kutubi, J. Gascon, E. J. R. Sudhölter and L. Rassaei, *ChemElectroChem*, 2015, **2**, 462-474.
 55. P. J. Beldon, L. Fábíán, R. S. Stein, A. Thirumurugan, A. K. Cheetham and T. Friščić, *Angew. Chem.*, 2010, **122**, 9834-9837.
 56. N. A. Khan and S. H. Jung, *Coord. Chem. Rev.*, 2015, **285**, 11-23.
 57. (a) E. S. Fedorov, *Zap. Mineral. Obch.*, 1891, **28**, 1-146; (b) A. M. Schönflies, *Theorie der Kristallstruktur*, Gebr. Bornträger, Berlin, 1891.
 58. *International Tables for Crystallography, 6th Edition, Volume A, Space-Group Symmetry*, Wiley, Weinheim, 2016.
 59. *International Tables for Crystallography, 3rd Edition, Volume C, Mathematical, Physical and Chemical Tables*, Wiley, Weinheim, 2004.
 60. G. Sheldrick, *Acta Cryst. Sect. C*, 2015, **71**, 3-8.
 61. V. Petříček, M. Dušek and L. Palatinus, *Z. Kristallogr.*, 2014, **229**, 345.
 62. A. Spek, *Acta Cryst. Sect. C*, 2015, **71**, 9-18.
 63. P. van der Sluis and A. L. Spek, *Acta Cryst. Sect. A*, 1990, **46**, 194-201.
 64. S. R. Hall, F. H. Allen and I. D. Brown, *Acta Cryst. Sect. A*, 1991, **47**, 655-685.
 65. A. L. Spek, *J. Appl. Crystallogr.*, 2003, **36**, 7-13.
 66. C. R. Groom, I. J. Bruno, M. P. Lightfoot and S. C. Ward, *Acta Cryst. Sect. B*, 2016, **72**, 171-179.
 67. V. Pecharsky and P. Zavalij, *Fundamentals of Powder Diffraction and Structural Characterization of Materials*, Springer Science+Business Media LLC, New York, 2009.
 68. C. F. Macrae, I. J. Bruno, J. A. Chisholm, P. R. Edgington, P. McCabe, E. Pidcock, L. Rodriguez-Monge, R. Taylor, J. van de Streek and P. A. Wood, *J. Appl. Crystallogr.*, 2008, **41**, 466-470.
 69. J. F. Watts and J. Wolstenholme, *An introduction to surface analysis by XPS and AES*, Wiley-VCH, 2003.

70. P. Atkins and J. de Paula, *Physical Chemistry*, 8th edn., W. H. Freeman and Company, New York, 2006.
71. K. S. W. Sing, *Pure Appl. Chem.*, 1982, **54**, 2201-2218.
72. S. Brunauer, P. H. Emmett and E. Teller, *J. Am. Chem. Soc.*, 1938, **60**, 309-319.
73. A. Soleimani Dorcheh, D. Denysenko, D. Volkmer, W. Donner and M. Hirscher, *Micropor. Mesopor. Mat.*, 2012, **162**, 64-68.
74. *Occupational Safety and Health Guideline for Ammonia*, <http://www.cdc.gov/niosh/docs/81-123/pdfs/0028-rev.pdf>.
75. in *The MAK-Collection for Occupational Health and Safety*, Wiley-VCH Verlag GmbH & Co. KGaA, 2002.
76. *Nitrogen (Fixed) – Ammonia. Mineral Commodity Summary*, U.S. Geological Survey, 2017.
77. R. Rademacher and K. Kim, *Int. J. Refrig.*, 1996, **19**, 61-69.
78. R. Lan and S. Tao, *Front. Energ. Res.*, 2014, **2**, 1-4.
79. I. Lundström, A. Spetz, F. Winqvist, U. Ackelid and H. Sundgren, *Sensor. Actuat. B Chem.*, 1990, **1**, 15-20.
80. A. L. Kukla, Y. M. Shirshov and S. A. Piletsky, *Sensor. Actuat. B Chem.*, 1996, **37**, 135-140.
81. A. Qajar, M. Peer, M. R. Andalibi, R. Rajagopalan and H. C. Foley, *Micropor. Mesopor. Mat.*, 2015, **218**, 15-23.
82. J. F. Van Humbeck, T. M. McDonald, X. Jing, B. M. Wiers, G. Zhu and J. R. Long, *J. Am. Chem. Soc.*, 2014, **136**, 2432-2440.
83. C. J. Doonan, D. J. Tranchemontagne, T. G. Glover, J. R. Hunt and O. M. Yaghi, *Nat. Chem.*, 2010, **2**, 235-238.
84. A. J. Rieth, Y. Tulchinsky and M. Dincă, *J. Am. Chem. Soc.*, 2016, **138**, 9401-9404.
85. (a) J. E. Mondloch, M. J. Katz, W. C. Isley III, P. Ghosh, P. Liao, W. Bury, G. W. Wagner, M. G. Hall, J. B. DeCoste, G. W. Peterson, R. Q. Snurr, C. J. Cramer, J. T. Hupp and O. K. Farha, *Nat. Mater.*, 2015, **14**, 512; (b) O. T. Wilcox, A. Fateeva, A. P. Katsoulidis, M. W. Smith, C. A. Stone and M. J. Rosseinsky, *Chem. Commun.*, 2015, **51**, 14989-14991; (c) J. B. DeCoste and G. W. Peterson, *Chem. Rev.*, 2014, **114**, 5695-5727.
86. (a) G. W. Peterson, G. W. Wagner, A. Balboa, J. Mahle, T. Sewell and C. J. Karwacki, *J. Phys. Chem. C*, 2009, **113**, 13906-13917; (b) M. J. Katz, A. J. Howarth, P. Z. Moghadam, J. B. DeCoste, R. Q. Snurr, J. T. Hupp and O. K. Farha, *Dalton Trans.*, 2016, **45**, 4150-4153.
87. (a) J. An, S. J. Geib and N. L. Rosi, *J. Am. Chem. Soc.*, 2009, **131**, 8376-8377; (b) J. An, S. J. Geib and N. L. Rosi, *J. Am. Chem. Soc.*, 2010, **132**, 38-39; (c) J. An and N. L. Rosi, *J. Am. Chem. Soc.*, 2010, **132**, 5578-5579.
88. (a) M. Leroux, N. Mercier, M. Allain, M.-C. Dul, J. Dittmer, A. H. Kassiba, J.-P. Bellat, G. Weber and I. Bezverkhyy, *Inorg. Chem.*, 2016, **55**, 8587-8594; (b) T. Grant Glover, G. W. Peterson, B. J. Schindler, D. Britt and O. Yaghi, *Chem. Eng. Sci.*, 2011, **66**, 163-170.
89. BrukerAXS Inc., Madison, Wisconsin, USA, 2009.
90. G. Sheldrick, *Acta Cryst. Sect. A*, 2015, **71**, 3-8.
91. O. V. Dolomanov, L. J. Bourhis, R. J. Gildea, J. A. K. Howard and H. Puschmann, *J. Appl. Crystallogr.*, 2009, **42**, 339-341.
92. H. Cheng, F. Huq and M. Farhad, *Asian J. Chem.*, 2005, **17**, 1532-1538.
93. (a) J. Juan-Alcañiz, J. Gascon and F. Kapteijn, *J. Mater. Chem.*, 2012, **22**, 10102-10118; (b) S. Rezaei, A. Landarani-Isfahani, M. Moghadam, S. Tangestaninejad, V. Mirkhani and I. Mohammadpoor-Baltork, *RSC Adv.*, 2016, **6**, 92463-92472; (c) M. B. Boroujeni, A. Hashemzadeh, A. Shaabani and M. M. Amini, *Appl. Organomet. Chem.*, 2017, e3715.
94. (a) M. Dincă, A. Dailly, Y. Liu, C. M. Brown, D. A. Neumann and J. R. Long, *J. Am. Chem. Soc.*, 2006, **128**, 16876-16883; (b) P. Manna, J. Debgupta, S. Bose and S. K. Das, *Angew. Chem., Int. Ed.*, 2016, **55**, 2425-2430; (c) C. Xu, D. Mochizuki, Y. Hashimoto, T. Honda, Y. Tsukahara, T. Yamauchi and Y. Wada, *Eur. J. Inorg. Chem.*, 2012, **2012**, 3113-3120; (d) R. Sen, S. Koner, A. Bhattacharjee, J. Kusz, Y. Miyashita and K.-I. Okamoto, *Dalton Trans.*, 2011, **40**, 6952-6960.
95. S. L. Anderson and K. C. Stylianou, *Coord. Chem. Rev.*, 2017, **349**, 102-128.
96. G. Beobide, O. Castillo, J. Cepeda, A. Luque, S. Pérez-Yáñez, P. Román and J. Thomas-Gipson, *Coord. Chem. Rev.*, 2013, **257**, 2716-2736.
97. (a) D. Choquesillo-Lazarte, M. del Pilar Brandi-Blanco, I. García-Santos, J. M. González-Pérez, A. Castiñeiras and J. Niclós-Gutiérrez, *Coord. Chem. Rev.*, 2008, **252**, 1241-1256; (b) S. Verma, A. K. Mishra and J. Kumar, *Acc. Chem. Res.*, 2010, **43**, 79-91.
98. P. X. Rojas-González, A. Castiñeiras, J. M. González-Pérez, D. Choquesillo-Lazarte and J. Niclós-Gutiérrez, *Inorg. Chem.*, 2002, **41**, 6190-6192.
99. F. Wang, Y.-X. Tan, H. Yang, H.-X. Zhang, Y. Kang and J. Zhang, *Chem. Commun.*, 2011, **47**, 5828-5830.
100. (a) J. P. García-Terán, O. Castillo, A. Luque, U. García-Couceiro, P. Román and L. Lezama, *Inorg. Chem.*, 2004, **43**, 4549-4551; (b) S. Das, C. Madhavaiah, S. Verma and P. K. Bharadwaj, *Inorg. Chim. Acta*, 2005, **358**, 3236-3240; (c) E.-C. Yang, H.-K. Zhao, B. Ding, X.-G. Wang and X.-J. Zhao, *New J. Chem.*, 2007, **31**, 1887-1890; (d) E.-C. Yang, H.-K. Zhao, Y. Feng and X.-J. Zhao, *Inorg. Chem.*, 2009, **48**, 3511-3513; (e) J. Y. An, S. J. Geib and N. L. Rosi, *J. Am. Chem. Soc.*, 2009, **131**, 8376-8377; (f) J. An, S. J. Geib and N. L. Rosi, *J. Am. Chem. Soc.*, 2010, **132**, 38-39; (g) K. C. Stylianou, J. E. Warren, S.

- Y. Chong, J. Rabone, J. Bacsa, D. Bradshaw and M. J. Rosseinsky, *Chem. Commun.*, 2011, **47**, 3389-3391; (h) S. Pérez-Yáñez, G. Beobide, O. Castillo, J. Cepeda, A. Luque, A. T. Aguayo and P. Román, *Inorg. Chem.*, 2011, **50**, 5330-5332; (i) F. Wang and Y. Kang, *Inorg. Chem. Commun.*, 2012, **20**, 266-268; (j) S. Pérez-Yáñez, G. Beobide, O. Castillo, J. Cepeda, M. Fröba, F. Hoffmann, A. Luque and P. Román, *Chem. Commun.*, 2012, **48**, 907-909; (k) O. K. Farha, I. Eryazici, N. C. Jeong, B. G. Hauser, C. E. Wilmer, A. A. Sarjeant, R. Q. Snurr, S. T. Nguyen, A. Ö. Yazaydin and J. T. Hupp, *J. Am. Chem. Soc.*, 2012, **134**, 15016-15021; (l) T. Li and N. L. Rosi, *Chem. Commun.*, 2013, **49**, 11385-11387; (m) T. Li, D.-L. Chen, J. E. Sullivan, M. T. Kozlowski, J. K. Johnson and N. L. Rosi, *Chem. Sci.*, 2013, **4**, 1746-1755; (n) T. Li, M. T. Kozlowski, E. A. Doud, M. N. Blakely and N. L. Rosi, *J. Am. Chem. Soc.*, 2013, **135**, 11688-11691; (o) I. Burneo, K. C. Stylianou, S. Rodríguez-Hermida, J. Juanhuix, X. Fontrodona, I. Imaz and D. Maspoch, *Cryst. Growth Des.*, 2015, **15**, 3182-3189; (p) J. An, O. K. Farha, J. T. Hupp, E. Pohl, J. I. Yeh and N. L. Rosi, *Nat. Commun.*, 2012, **3**, 604.
101. C. Singh, *Acta Cryst.*, 1965, **19**, 861-864.
102. G. Sheldrick, *Acta Cryst. Sect. A*, 2015, **71**, 3-8.
103. X. R. Meng, H. W. Hou, G. Li, B. X. Ye, T. Z. Ge, Y. T. Fan, Y. Zhu and H. Sakiyama, *J. Organomet. Chem.*, 2004, **689**, 1218-1229.
104. A. M. Barrios and S. J. Lippard, *J. Am. Chem. Soc.*, 1999, **121**, 11751-11757.
105. J. B. Gilroy, B. O. Patrick, R. McDonald and R. G. Hicks, *Inorg. Chem.*, 2008, **47**, 1287-1294.
106. H.-X. Huang, X.-Z. Tian, Y.-M. Song, Z.-W. Liao, G.-M. Sun, M.-B. Luo, S.-J. Liu, W.-Y. Xu and F. Luo, *Aust. J. Chem.*, 2012, **65**, 320-325.
107. S. T. Wu, L. Q. Ma, L. S. Long, L. S. Zheng and W. B. Lin, *Inorg. Chem.*, 2009, **48**, 2436-2442.
108. J. S. Stevens, S. J. Byard, C. A. Muryn and S. L. M. Schroeder, *J. Phys. Chem. B*, 2010, **114**, 13961-13969.
109. V. Feyer, O. Plekan, K. C. Prince, F. Šutara, T. Skála, V. Cháb, V. Matolín, G. Stenuit and P. Umari, *Phys. Rev. B*, 2009, **79**, 155432.
110. M. Furukawa, T. Yamada, S. Katano, M. Kawai, H. Ogasawara and A. Nilsson, *Surf. Sci.*, 2007, **601**, 5433-5440.
111. M. Wenkin, R. Touillaux and M. Devillers, *New J. Chem.*, 1998, **22**, 973-976.
112. G. L. Hardgrove, Jr, J. R. Einstein, B. E. Hingerty and C. H. Wei, *Acta Cryst. Sect. C*, 1983, **39**, 88-90.
113. A. K. Paul, U. Sanyal and S. Natarajan, *Cryst. Growth Des.*, 2010, **10**, 4161-4175.
114. E.-C. Yang, Z.-Y. Liu, L. Zhang, N. Yang and X.-J. Zhao, *Dalton Trans.*, 2016, **45**, 8134-8141.
115. Y. Song, X. Yin, B. Tu, Q. Pang, H. Li, X. Ren, B. Wang and Q. Li, *CrystEngComm*, 2014, **16**, 3082-3085.
116. (a) Z. Su, J. Fan, T.-a. Okamura, W.-Y. Sun and N. Ueyama, *Cryst. Growth Des.*, 2010, **10**, 3515-3521; (b) S. Bauer, C. Serre, T. Devic, P. Horcajada, J. Marrot, G. Férey and N. Stock, *Inorg. Chem.*, 2008, **47**, 7568-7576; (c) C. Volkringer, T. Loiseau, N. Guillou, G. Férey, M. Haouas, F. Taulelle, E. Elkaïm and N. Stock, *Inorg. Chem.*, 2010, **49**, 9852-9862.
117. G. T. Rochelle, *Science*, 2009, **325**, 1652-1654.
118. P. G. Cifre, K. Brechtel, S. Hoch, H. García, N. Asprion, H. Hasse and G. Scheffknecht, *Fuel*, 2009, **88**, 2481-2488.
119. D. M. Ruthven, *Principles of Adsorption and Adsorption Processes*, Wiley, New York, 1984.
120. A. J. Kidnay and W. R. Parrish, *Fundamentals of Natural Gas Processing*, Taylor & Francis, Boca Raton, 2006.
121. L. F. Gomez, R. Zacharia, P. Bénard and R. Chahine, *Adsorption*, 2015, **21**, 433-443.
122. R. W. Baker and K. Lokhandwala, *Ind. Eng. Chem. Res.*, 2008, **47**, 2109-2121.
123. D. M. D'Alessandro, B. Smit and J. R. Long, *Angew. Chem., Int. Ed.*, 2010, **49**, 6058-6082.
124. C. J. F. Böttcher and P. Bordewijk, *Theory of Electric Polarization*, Elsevier, Amsterdam, 1978.
125. (a) A. Biswas, M.-B. Kim, S.-Y. Kim, T.-U. Yoon, S.-I. Kim and Y.-S. Bae, *RSC Adv.*, 2016, **6**, 81485-81490; (b) Z. Li, X. Li, C. Chen, L. Zhou, Q. Guo, D. Yuan, H. Wan, J. Ding and G. Guan, *Eur. J. Inorg. Chem.*, 2018, **2018**, 194-202; (c) A. López-Olvera, E. Sánchez-González, A. Campos-Reales-Pineda, A. Aguilar-Granda, I. A. Ibarra and B. Rodríguez-Molina, *Inorg. Chem. Front.*, 2017, **4**, 56-64; (d) A. Masala, J. G. Vitillo, G. Mondino, C. A. Grande, R. Blom, M. Manzoli, M. Marshall and S. Bordiga, *ACS Appl. Mater. Interfaces*, 2017, **9**, 455-463; (e) B. Pato-Doldán, M. H. Rosnes and P. D. C. Dietzel, *ChemSusChem*, 2017, **10**, 1710-1719.
126. P. Nugent, Y. Belmabkhout, S. D. Burd, A. J. Cairns, R. Luebke, K. Forrest, T. Pham, S. Ma, B. Space, L. Wojtas, M. Eddaoudi and M. J. Zaworotko, *Nature*, 2013, **495**, 80-84.
127. (a) A. Demessence, D. M. D'Alessandro, M. L. Foo and J. R. Long, *J. Am. Chem. Soc.*, 2009, **131**, 8784-8786; (b) T. M. McDonald, J. A. Mason, X. Kong, E. D. Bloch, D. Gygi, A. Dani, V. Crocellà, F. Giordanino, S. O. Odoh, W. S. Drisdell, B. Vlaisavljevich, A. L. Dzubak, R. Poloni, S. K. Schnell, N. Planas, K. Lee, T. Pascal, L. F. Wan, D. Prendergast, J. B. Neaton, B. Smit, J. B. Kortright, L. Gagliardi, S. Bordiga, J. A. Reimer and J. R. Long, *Nature*, 2015, **519**, 303.
128. J. A. Mason, J. Oktawiec, M. K. Taylor, M. R. Hudson, J. Rodriguez, J. E. Bachman, M. I. Gonzalez, A. Cervellino, A. Guagliardi, C. M. Brown, P. L. Llewellyn, N. Masciocchi and J. R. Long, *Nature*, 2015, **527**, 357.
129. A. K. Chaudhari, S. Mukherjee, S. S. Nagarkar, B. Joarder and S. K. Ghosh, *CrystEngComm*, 2013, **15**, 9465-9471.

130. S. A. Sapchenko, D. G. Samsonenko, D. N. Dybtsev and V. P. Fedin, *Inorg. Chem.*, 2013, **52**, 9702-9704.
131. (a) O. Ohmori, M. Kawano and M. Fujita, *Angew. Chem.*, 2005, **117**, 1998-2000; (b) B. F. Abrahams, M. Moylan, S. D. Orchard and R. Robson, *Angew. Chem.*, 2003, **115**, 1892-1895.
132. K. C. Stylianou, R. Heck, S. Y. Chong, J. Bacsa, J. T. A. Jones, Y. Z. Khimyak, D. Bradshaw and M. J. Rosseinsky, *J. Am. Chem. Soc.*, 2010, **132**, 4119-4130.
133. V. Dyadkin, P. Pattison, V. Dmitriev and D. Chernyshov, *J. Synchrotron Radiat.*, 2016, **23**, 825-829.
134. V. A. Blatov, A. P. Shevchenko and D. M. Proserpio, *Cryst. Growth Des.*, 2014, **14**, 3576-3586.
135. J. Rodríguez-Carvajal, *Phys. B*, 1993, **192**, 55-69.
136. (a) L. Hamon, E. Jolimaître and G. D. Pirngruber, *Ind. Eng. Chem. Res.*, 2010, **49**, 7497-7503; (b) S. Xian, J. Peng, Z. Zhang, Q. Xia, H. Wang and Z. Li, *Chem. Eng. J.*, 2015, **270**, 385-392.
137. (a) A. K. Chaudhari, S. Mukherjee, S. S. Nagarkar, B. Joarder and S. K. Ghosh, *CrystEngComm*, 2013, **15**, 9465-9471; (b) P. Kanoo, K. L. Gurunatha and T. K. Maji, *J. Mater. Chem.*, 2010, **20**, 1322-1331; (c) K. C. Stylianou, J. Bacsa, D. Bradshaw and M. J. Rosseinsky, *Z. Anorg. Allg. Chem.*, 2014, **640**, 2123-2131; (d) S. Zang, Y. Su, C. Duan, Y. Li, H. Zhu and Q. Meng, *Chem. Commun.*, 2006, 4997-4999.
138. M. Kawano, T. Kawamichi, T. Haneda, T. Kojima and M. Fujita, *J. Am. Chem. Soc.*, 2007, **129**, 15418-15419.
139. M. I. Mohideen, B. Xiao, P. S. Wheatley, A. C. McKinlay, Y. Li, A. M. Slawin, D. W. Aldous, N. F. Cessford, T. Duren, X. Zhao, R. Gill, K. M. Thomas, J. M. Griffin, S. E. Ashbrook and R. E. Morris, *Nat. Chem.*, 2011, **3**, 304-310.
140. (a) J. Jiao, L. Dou, H. Liu, F. Chen, D. Bai, Y. Feng, S. Xiong, D. L. Chen and Y. He, *Dalton Trans.*, 2016, **45**, 13373-13382; (b) F. Chen, D. Bai, Y. Wang, D. Jiang and Y. He, *Mater. Chem. Front.*, 2017, **1**, 2283-2291.
141. A. U. Ortiz, A. Boutin, A. H. Fuchs and F.-X. Coudert, *J. Chem. Phys.*, 2013, **138**, 174703.
142. C. Serre, S. Bourrelly, A. Vimont, N. A. Ramsahye, G. Maurin, P. L. Llewellyn, M. Daturi, Y. Filinchuk, O. Leynaud, P. Barnes and G. Férey, *Adv. Mater.*, 2007, **19**, 2246-2251.
143. M. Hutchinson and M. Widom, *Comput. Phys. Commun.*, 2012, **183**, 1422-1426.
144. P. Serra-Crespo, E. V. Ramos-Fernandez, J. Gascon and F. Kapteijn, *Chem. Mater.*, 2011, **23**, 2565-2572.
145. S. Couck, E. Gobechiya, C. E. A. Kirschhock, P. Serra-Crespo, J. Juan-Alcañiz, A. M. Joaristi, E. Stavitski, J. Gascon, F. Kapteijn, G. V. Baron and J. F. M. Denayer, *ChemSusChem*, 2012, **5**, 740-750.
146. M. Giménez-Marques, N. Calvo Galve, M. Palomino, S. Valencia, F. Rey, G. Sastre, I. J. Vitorica-Yrezabal, M. Jiménez-Ruiz, J. A. Rodríguez-Velamazán, M. A. González, J. L. Jordá, E. Coronado and G. M. Espallargas, *Chem. Sci.*, 2017, **8**, 3109-3120.
147. L. Bastin, P. S. Bácia, E. J. Hurtado, J. A. C. Silva, A. E. Rodrigues and B. Chen, *J. Phys. Chem. C*, 2008, **112**, 1575-1581.
148. T. Sun, J. Hu, X. Ren and S. Wang, *Sep. Sci. Technol.*, 2015, **50**, 874-885.
149. E. J. García, J. P. S. Mowat, P. A. Wright, J. Pérez-Pellitero, C. Jallut and G. D. Pirngruber, *J. Phys. Chem. C*, 2012, **116**, 26636-26648.
150. D. Britt, H. Furukawa, B. Wang, T. G. Glover and O. M. Yaghi, *Proc. Natl. Acad. Sci. U. S. A.*, 2009, **106**, 20637-20640.
151. S. Couck, J. F. M. Denayer, G. V. Baron, T. Rémy, J. Gascon and F. Kapteijn, *J. Am. Chem. Soc.*, 2009, **131**, 6326-6327.
152. V. Finsy, L. Ma, L. Alaerts, D. E. De Vos, G. V. Baron and J. F. M. Denayer, *Micropor. Mesopor. Mat.*, 2009, **120**, 221-227.
153. L. Hamon, P. L. Llewellyn, T. Devic, A. Ghoufi, G. Clet, V. Guillermin, G. D. Pirngruber, G. Maurin, C. Serre, G. Driver, W. van Beek, E. Jolimaître, A. Vimont, M. Daturi and G. Férey, *J. Am. Chem. Soc.*, 2009, **131**, 17490-17499.
154. N.-Y. Huang, Z.-W. Mo, L.-J. Li, W.-J. Xu, H.-L. Zhou, D.-D. Zhou, P.-Q. Liao, J.-P. Zhang and X.-M. Chen, *CrystEngComm*, 2018.
155. B. J. Riley, J. D. Vienna, D. M. Strachan, J. S. McCloy and J. L. Jerden, *J. Nucl. Mater.*, 2016, **470**, 307-326.
156. (a) T. R. Thomas, B. A. Staples and L. P. Murphy, *Development of Ag⁰Z for Bulk ¹²⁹I Removal from Nuclear Fuel Reprocessing Plants and PbX for ¹²⁹I Storage*, 1978; (b) R. T. Jubin, *Organic Iodine Removal from Simulated Dissolver Off-gas Systems Utilizing Silver-exchanged Mordenite*, 1981.
157. (a) O. K. Farha and J. T. Hupp, *Acc. Chem. Res.*, 2010, **43**, 1166-1175; (b) H. Furukawa, K. E. Cordova, M. O'Keeffe and O. M. Yaghi, *Science*, 2013, **341**, 1230444; (c) M. L. Foo, R. Matsuda and S. Kitagawa, *Chem. Mater.*, 2014, **26**, 310-322.
158. X. Zhang, I. da Silva, H. G. W. Godfrey, S. K. Callear, S. A. Sapchenko, Y. Cheng, I. Vitorica-Yrezabal, M. D. Frogley, G. Cinque, C. C. Tang, C. Giacobbe, C. Dejoie, S. Rudić, A. J. Ramirez-Cuesta, M. A. Denecke, S. Yang and M. Schröder, *J. Am. Chem. Soc.*, 2017, **139**, 16289-16296.
159. (a) K. K. Yee, Y. L. Wong and Z. Xu, *Dalton Trans.*, 2016, **45**, 5334-5338; (b) A. S. Munn, F. Millange, M. Frigoli, N. Guillou, C. Falaise, V. Stevenson, C. Volkringer, T. Loiseau, G. Cibir and R. I. Walton, *CrystEngComm*, 2016, **18**, 8108-8114.
160. B. Valizadeh, T. N. Nguyen, B. Smit and K. C. Stylianou, *Adv. Funct. Mater.*, 2018, **28**, 1801596.
161. (a) D. F. Sava, K. W. Chapman, M. A. Rodriguez, J. A. Greathouse, P. S. Crozier, H. Zhao, P. J. Chupas and T. M. Nenoff, *Chem. Mater.*, 2013, **25**, 2591-2596; (b) D. Banerjee, X. Chen, S. S.

- Lobanov, A. M. Plonka, X. Chan, J. A. Daly, T. Kim, P. K. Thallapally and J. B. Parise, *ACS Appl. Mater. Interfaces*, 2018, **10**, 10622-10626.
162. A. Gładysiak, K. S. Deeg, I. Dovgaliuk, A. Chidambaram, K. Ordiz, P. G. Boyd, S. M. Moosavi, D. Ongari, J. A. R. Navarro, B. Smit and K. C. Stylianou, *ACS Appl. Mater. Interfaces*, 2018, **10**, 36144-36156.
 163. M. Kawabe, K. Masuda and J. Yamaguchi, *J. Phys. Soc. Jpn.*, 1968, **24**, 1281-1285.
 164. RigakuOxfordDiffraction, 1.171.38.43 edn., 2015.
 165. A. L. Spek, 120716 edn., 2016.
 166. M. Harel and F. L. Hirshfeld, *Acta Cryst. Sect. B*, 1975, **31**, 162-172.
 167. F. Hirshfeld, *Acta Cryst. Sect. A*, 1976, **32**, 239-244.
 168. (a) R. X. Yao, X. Cui, X. X. Jia, F. Q. Zhang and X. M. Zhang, *Inorg. Chem.*, 2016, **55**, 9270-9275; (b) S. S. Lobanov, J. A. Daly, A. F. Goncharov, X. Chan, S. K. Ghose, H. Zhong, L. Ehm, T. Kim and J. B. Parise, *J. Phys. Chem. A*, 2018, **122**, 6109-6117.
 169. J. H. Lee, R. L. Siegelman, L. Maserati, T. Rangel, B. A. Helms, J. R. Long and J. B. Neaton, *Chem. Sci.*, 2018, **9**, 5197-5206.
 170. G. Brunet, D. A. Safin, M. Z. Aghaji, K. Robeyns, I. Korobkov, T. K. Woo and M. Murugesu, *Chem. Sci.*, 2017, **8**, 3171-3177.
 171. Y.-Q. Hu, M.-Q. Li, Y. Wang, T. Zhang, P.-Q. Liao, Z. Zheng, X.-M. Chen and Y.-Z. Zheng, *Chem. Eur. J.*, 2017, **23**, 8409-8413.
 172. H. A. Benesi and J. H. Hildebrand, *J. Am. Chem. Soc.*, 1949, **71**, 2703-2707.
 173. (a) M.-H. Zeng, Q.-X. Wang, Y.-X. Tan, S. Hu, H.-X. Zhao, L.-S. Long and M. Kurmoo, *J. Am. Chem. Soc.*, 2010, **132**, 2561-2563; (b) S. Horike, M. Sugimoto, K. Kongpatpanich, Y. Hijikata, M. Inukai, D. Umeyama, S. Kitao, M. Seto and S. Kitagawa, *J. Mater. Chem. A*, 2013, **1**, 3675-3679; (c) D. Y. Lee, E. K. Kim, N. K. Shrestha, D. W. Boukhvalov, J. K. Lee and S. H. Han, *ACS Appl. Mater. Interfaces*, 2015, **7**, 18501-18507.
 174. L. Sun, S. S. Park, D. Sheberla and M. Dincă, *J. Am. Chem. Soc.*, 2016, **138**, 14772-14782.
 175. (a) S. Goswami, D. Ray, K.-i. Otake, C.-W. Kung, S. J. Garibay, T. Islamoglu, A. Atilgan, Y. Cui, C. J. Cramer, O. K. Farha and J. T. Hupp, *Chem. Sci.*, 2018, **9**, 4477-4482; (b) C. Schneider, D. Ukaj, R. Koerver, A. A. Talin, G. Kieslich, S. P. Pujari, H. Zuilhof, J. Janek, M. D. Allendorf and R. A. Fischer, *Chem. Sci.*, 2018.
 176. J. P. Perdew and M. Levy, *Phys. Rev. Lett.*, 1983, **51**, 1884-1887.
 177. J. L. Lyons and C. G. Van de Walle, *npj Comput. Mater.*, 2017, **3**, 12.
 178. N. J. Turro, V. Ramamurthy and J. C. Scaiano, *Principles of Molecular Photochemistry: An Introduction*, University Science Books, Sausalito, CA, 2009.
 179. G. K. Bains, S. H. Kim, E. J. Sorin and V. Narayanaswami, *Biochemistry*, 2012, **51**, 6207-6219.
 180. (a) W. Cho, H. J. Lee, G. Choi, S. Choi and M. Oh, *J. Am. Chem. Soc.*, 2014, **136**, 12201-12204; (b) D. Ananias, A. D. G. Firmino, R. F. Mendes, F. A. A. Paz, M. Nolasco, L. D. Carlos and J. Rocha, *Chem. Mater.*, 2017, **29**, 9547-9554; (c) R. Dalapati and S. Biswas, *Sensor. Actuat. B Chem.*, 2017, **239**, 759-767; (d) H. R. Fu, X. X. Wu, L. F. Ma, F. Wang and J. Zhang, *ACS Appl. Mater. Interfaces*, 2018, **10**, 18012-18020; (e) T. N. Nguyen, F. M. Ebrahim and K. C. Stylianou, *Coord. Chem. Rev.*, 2018, **377**, 259-306.
 181. C. Wei, M. Gao, F. Hu, J. Yao and Y. S. Zhao, *Adv. Opt. Mater.*, 2016, **4**, 1009-1014.
 182. T. Förster, *Angew. Chem., Int. Ed. Engl.*, 1969, **8**, 333-343.
 183. (a) J. Ferguson, *J. Chem. Phys.*, 1958, **28**, 765-768; (b) B. Stevens, *Spectrochim. Acta*, 1962, **18**, 439-448; (c) R. Seyfang, E. Betz, H. Port, W. Schrof and H. C. Wolf, *J. Lumin.*, 1985, **34**, 57-62; (d) F. M. Winnik, *Chem. Rev.*, 1993, **93**, 587-614.
 184. (a) G. J. McManus, J. J. Perry, M. Perry, B. D. Wagner and M. J. Zaworotko, *J. Am. Chem. Soc.*, 2007, **129**, 9094-9101; (b) S. K. Rajagopal, V. S. Reddy and M. Hariharan, *CrystEngComm*, 2016, **18**, 5089-5094; (c) P. Deria, J. Yu, T. Smith and R. P. Balaraman, *J. Am. Chem. Soc.*, 2017, **139**, 5973-5983; (d) J. Yu, J. Park, A. Van Wyk, G. Rumbles and P. Deria, *J. Am. Chem. Soc.*, 2018, **140**, 10488-10496.
 185. (a) K. C. Stylianou, J. Rabone, S. Y. Chong, R. Heck, J. Armstrong, P. V. Wiper, K. E. Jelfs, S. Zlatogorsky, J. Bacsá, A. G. McLennan, C. P. Ireland, Y. Z. Khimyak, K. M. Thomas, D. Bradshaw and M. J. Rosseinsky, *J. Am. Chem. Soc.*, 2012, **134**, 20466-20478; (b) J. E. Mondloch, W. Bury, D. Fairen-Jimenez, S. Kwon, E. J. DeMarco, M. H. Weston, A. A. Sarjeant, S. T. Nguyen, P. C. Stair, R. Q. Snurr, O. K. Farha and J. T. Hupp, *J. Am. Chem. Soc.*, 2013, **135**, 10294-10297; (c) C.-W. Kung, T. C. Wang, J. E. Mondloch, D. Fairen-Jimenez, D. M. Gardner, W. Bury, J. M. Klingsporn, J. C. Barnes, R. Van Duyne, J. F. Stoddart, M. R. Wasielewski, O. K. Farha and J. T. Hupp, *Chem. Mater.*, 2013, **25**, 5012-5017; (d) R.-J. Li, M. Li, X.-P. Zhou, D. Li and M. O'Keeffe, *Chem. Commun.*, 2014, **50**, 4047-4049; (e) R.-J. Li, M. Li, X.-P. Zhou, S. W. Ng, M. O'Keeffe and D. Li, *CrystEngComm*, 2014, **16**, 6291-6295; (f) P. Li, N. A. Vermeulen, X. Gong, C. D. Malliakas, J. F. Stoddart, J. T. Hupp and O. K. Farha, *Angew. Chem., Int. Ed.*, 2016, **55**, 10358-10362; (g) V. A. Milichko, S. V. Makarov, A. V. Yulin, A. V. Vinogradov, A. A. Rasilin, E. Ushakova, V. P. Dzyuba, E. Hey-Hawkins, E. A. Pidko and P. A. Belov, *Adv. Mater.*, 2017, **29**, 1606034; (h) A. Gładysiak, T. N. Nguyen, M. Spodaryk, J.-H. Lee, J. B. Neaton, A. Züttel and K. C. Stylianou, *Chem. Eur. J.*, 2019, **25**, 501-506.
 186. (a) O. M. Yaghi, M. O'Keeffe, N. W. Ockwig, H. K. Chae, M. Eddaoudi and J. Kim, *Nature*, 2003, **423**, 705-714; (b) C. Zhou, L. Longley, A. Krajnc, G. J. Smales, A. Qiao, I. Erucar, C. M. Doherty, A. W.

- Thornton, A. J. Hill, C. W. Ashling, O. T. Qazvini, S. J. Lee, P. A. Chater, N. J. Terrill, A. J. Smith, Y. Yue, G. Mali, D. A. Keen, S. G. Telfer and T. D. Bennett, *Nat. Commun.*, 2018, **9**, 5042.
187. M. Li, D. Li, M. O'Keeffe and O. M. Yaghi, *Chem. Rev.*, 2014, **114**, 1343-1370.
188. Y. He, F. Chen, B. Li, G. Qian, W. Zhou and B. Chen, *Coord. Chem. Rev.*, 2018, **373**, 167-198.
189. L. Wang, D. W. Agnew, X. Yu, J. S. Figueroa and S. M. Cohen, *Angew. Chem., Int. Ed.*, 2018, **57**, 511-515.
190. Y. Zhang, S. Yuan, G. Day, X. Wang, X. Yang and H.-C. Zhou, *Coord. Chem. Rev.*, 2018, **354**, 28-45.
191. M. Andrzejewski and A. Katrusiak, *J. Phys. Chem. Lett.*, 2017, **8**, 929-935.
192. (a) B. V. Harbuzaru, A. Corma, F. Rey, P. Atienzar, J. L. Jordá, H. García, D. Ananias, L. D. Carlos and J. Rocha, *Angew. Chem.*, 2008, **120**, 1096-1099; (b) Z. Hu, B. J. Deibert and J. Li, *Chem. Soc. Rev.*, 2014, **43**, 5815-5840; (c) N. B. Shustova, A. F. Cozzolino, S. Reineke, M. Baldo and M. Dincă, *J. Am. Chem. Soc.*, 2013, **135**, 13326-13329; (d) E. A. Dolgoplova, A. M. Rice, C. R. Martin and N. B. Shustova, *Chem. Soc. Rev.*, 2018, **47**, 4710-4728; (e) F. M. Ebrahim, T. N. Nguyen, S. Shyshkanov, A. Gładysiak, P. Favre, A. Zacharia, G. Itskos, P. J. Dyson and K. C. Stylianou, *J. Am. Chem. Soc.*, 2019, **141**, 3052-3058.
193. P. Müller, F. M. Wisser, P. Freund, V. Bon, I. Senkovska and S. Kaskel, *Inorg. Chem.*, 2017, **56**, 14164-14169.
194. L. Wang, Y. Ye, Z. Li, Q. Lin, J. Ouyang, L. Liu, Z. Zhang and S. Xiang, *Cryst. Growth Des.*, 2017, **17**, 2081-2089.
195. M. Andrzejewski, N. Casati and A. Katrusiak, *Dalton Trans.*, 2017, **46**, 14795-14803.
196. Y. Cui, Y. Yue, G. Qian and B. Chen, *Chem. Rev.*, 2012, **112**, 1126-1162.
197. (a) M. Gutiérrez, F. Sánchez and A. Douhal, *Chem. Eur. J.*, 2016, **22**, 13072-13082; (b) W.-M. Liao, J.-H. Zhang, S.-Y. Yin, H. Lin, X. Zhang, J. Wang, H.-P. Wang, K. Wu, Z. Wang, Y.-N. Fan, M. Pan and C.-Y. Su, *Nat. Commun.*, 2018, **9**, 2401.
198. S. S. Park, C. H. Hendon, A. J. Fielding, A. Walsh, M. O'Keeffe and M. Dincă, *J. Am. Chem. Soc.*, 2017, **139**, 3619-3622.
199. (a) E. H. H. Chow, F. C. Strobridge and T. Friščić, *Chem. Commun.*, 2010, **46**, 6368-6370; (b) M. Kang, T. Liu, X. Wang, D. Luo, R. Li and Z. Lin, *Inorg. Chem. Commun.*, 2014, **44**, 155-158.
200. (a) F. Gándara, E. Gutiérrez-Puebla, M. Iglesias, N. Snejko and M. Á. Monge, *Cryst. Growth Des.*, 2010, **10**, 128-134; (b) L. Lü, B. Mu, C.-X. Li and R.-D. Huang, *J. Solid State Chem.*, 2016, **234**, 93-102.
201. B. Cui, H. Sun, Y. Xu, L. Duan and Y.-M. Li, *Tetrahedron*, 2017, **73**, 6754-6762.
202. A. Balena, A. Perulli, M. Fernandez, M. L. De Giorgi, G. Nedelcu, M. V. Kovalenko and M. Anni, *J. Phys. Chem. C*, 2018, **122**, 5813-5819.
203. H. Port, P. Fischer and R. Seyfang, *J. Lumin.*, 1990, **45**, 260-262.
204. (a) Q. Zhang, J. Su, D. Feng, Z. Wei, X. Zou and H.-C. Zhou, *J. Am. Chem. Soc.*, 2015, **137**, 10064-10067; (b) C.-X. Chen, Z.-W. Wei, Y.-N. Fan, P.-Y. Su, Y.-Y. Ai, Q.-F. Qiu, K. Wu, S.-Y. Yin, M. Pan and C.-Y. Su, *Chem*, 2018, **4**, 2658-2669.
205. S. Khatua, S. Goswami, S. Biswas, K. Tomar, H. S. Jena and S. Konar, *Chem. Mater.*, 2015, **27**, 5349-5360.
206. X. Du, R. Fan, J. Fan, L. Qiang, Y. Song, Y. Dong, K. Xing, P. Wang and Y. Yang, *Inorg. Chem. Front.*, 2016, **3**, 1480-1490.
207. S. Alvarez, *Dalton Trans.*, 2013, **42**, 8617-8636.
208. G. J. Halder, C. J. Kepert, B. Moubaraki, K. S. Murray and J. D. Cashion, *Science*, 2002, **298**, 1762.
209. W. Cai, A. Gładysiak, M. Anioła, V. J. Smith, L. J. Barbour and A. Katrusiak, *J. Am. Chem. Soc.*, 2015, **137**, 9296-9301.
210. J. S. O. Evans, *J. Chem. Soc. Dalton Trans.*, 1999, 3317-3326.
211. (a) J. Chen, L. Hu, J. Deng and X. Xing, *Chem. Soc. Rev.*, 2015, **44**, 3522-3567; (b) Z. Liu, Q. Gao, J. Chen, J. Deng, K. Lin and X. Xing, *Chem. Commun.*, 2018, **54**, 5164-5176.
212. K. Takenaka, *Sci. Technol. Adv. Mat.*, 2012, **13**, 013001.
213. J. R. Salvador, F. Guo, T. Hogan and M. G. Kanatzidis, *Nature*, 2003, **425**, 702-705.
214. (a) T. A. Mary, J. S. O. Evans, T. Vogt and A. W. Sleight, *Science*, 1996, **272**, 90-92; (b) J. N. Hancock, C. Turpen, Z. Schlesinger, G. R. Kowach and A. P. Ramirez, *Phys. Rev. Lett.*, 2004, **93**, 225501.
215. B. K. Greve, K. L. Martin, P. L. Lee, P. J. Chupas, K. W. Chapman and A. P. Wilkinson, *J. Am. Chem. Soc.*, 2010, **132**, 15496-15498.
216. W. Yao, X. Jiang, R. Huang, W. Li, C. Huang, Z. Lin, L. Li and C. Chen, *Chem. Commun.*, 2014, **50**, 13499-13501.
217. L. Hu, J. Chen, L. Fan, Y. Ren, Y. Rong, Z. Pan, J. Deng, R. Yu and X. Xing, *J. Am. Chem. Soc.*, 2014, **136**, 13566-13569.
218. A. L. Goodwin and C. J. Kepert, *Phys. Rev. B*, 2005, **71**, 140301.
219. K. Takenaka and H. Takagi, *Appl. Phys. Lett.*, 2005, **87**, 261902.
220. Y. Wu, A. Kobayashi, G. J. Halder, V. K. Peterson, K. W. Chapman, N. Lock, P. D. Southon and C. J. Kepert, *Angew. Chem., Int. Ed.*, 2008, **47**, 8929-8932.
221. Y. Wu, V. K. Peterson, E. Luks, T. A. Darwish and C. J. Kepert, *Angew. Chem.*, 2014, **53**, 5175-5178.
222. N. Lock, Y. Wu, M. Christensen, L. J. Cameron, V. K. Peterson, A. J. Bridgeman, C. J. Kepert and B. B. Iversen, *J. Phys. Chem. C*, 2010, **114**, 16181-16186.
223. Z. Liu, Q. Li, H. Zhu, K. Lin, J. Deng, J. Chen and X. Xing, *Chem. Commun.*, 2018, **54**, 5712-5715.

224. (a) A. C. Bailey and B. Yates, *J. Appl. Phys.*, 1970, **41**, 5088-5091; (b) S. J. Hibble, A. M. Chippindale, A. H. Pohl and A. C. Hannon, *Angew. Chem., Int. Ed.*, 2007, **46**, 7116-7118.
225. H. Takahashi and R. Tamura, *CrystEngComm*, 2015, **17**, 8888-8896.
226. (a) G. Shirane, S. Hoshino and K. Suzuki, *Phys. Rev.*, 1950, **80**, 1105-1106; (b) G. A. Rossetti, J. P. Cline and A. Navrotsky, *J. Mater. Res.*, 1998, **13**, 3197-3206.
227. X. G. Zheng, H. Kubozono, H. Yamada, K. Kato, Y. Ishiwata and C. N. Xu, *Nat. Nanotechnol.*, 2008, **3**, 724.
228. S. Khmelevskiy, I. Turek and P. Mohn, *Phys. Rev. Lett.*, 2003, **91**, 037201.
229. (a) K. S. Knight, *J. Miner. Petrol. Sci.*, 2014, **109**, 118-124; (b) W. G. Marshall, R. H. Jones and K. S. Knight, *CrystEngComm*, 2018, **20**, 3246-3250.
230. A. L. Goodwin, M. Calleja, M. J. Conterio, M. T. Dove, J. S. O. Evans, D. A. Keen, L. Peters and M. G. Tucker, *Science*, 2008, **319**, 794-797.
231. A. D. Fortes, E. Suard and K. S. Knight, *Science*, 2011, **331**, 742-746.
232. (a) L. D. DeVries, P. M. Barron, E. P. Hurley, C. Hu and W. Choe, *J. Am. Chem. Soc.*, 2011, **133**, 14848-14851; (b) I. E. Collings, M. G. Tucker, D. A. Keen and A. L. Goodwin, *CrystEngComm*, 2014, **16**, 3498-3506; (c) J. Pang, C. Liu, Y. Huang, M. Wu, F. Jiang, D. Yuan, F. Hu, K. Su, G. Liu and M. Hong, *Angew. Chem., Int. Ed.*, 2016, **55**, 7478-7482; (d) Z. Liu, C. Liu, Q. Li, J. Chen and X. Xing, *Phys. Chem. Chem. Phys.*, 2017, **19**, 24436-24439.
233. W. Cai and A. Katrusiak, *Nat. Commun.*, 2014, **5**, 4337.
234. (a) A. L. Goodwin, K. W. Chapman and C. J. Kepert, *J. Am. Chem. Soc.*, 2005, **127**, 17980-17981; (b) I. Grobler, V. J. Smith, P. M. Bhatt, S. A. Herbert and L. J. Barbour, *J. Am. Chem. Soc.*, 2013, **135**, 6411-6414; (c) D. Ma, B. Li, X. Zhou, Q. Zhou, K. Liu, G. Zeng, G. Li, Z. Shi and S. Feng, *Chem. Commun.*, 2013, **49**, 8964-8966; (d) H. L. Zhou, Y. B. Zhang, J. P. Zhang and X. M. Chen, *Nat Commun*, 2015, **6**, 6917.
235. A. E. Phillips, A. L. Goodwin, G. J. Halder, P. D. Southon and C. J. Kepert, *Angew. Chem., Int. Ed.*, 2008, **120**, 1396-1399.
236. Q. Gao, J. Chen, Q. Sun, D. Chang, Q. Huang, H. Wu, A. Sanson, R. Milazzo, H. Zhu, Q. Li, Z. Liu, J. Deng and X. Xing, *Angew. Chem., Int. Ed.*, 2017, **56**, 9023-9028.
237. I. de Pedro, A. García-Saiz, J. Dupont, P. Migowski, O. Vallcorba, J. Junquera, J. Rius and J. Rodríguez Fernández, *Cryst. Growth Des.*, 2015, **15**, 5207-5212.
238. B. R. Hester, A. M. dos Santos, J. J. Molaison, J. C. Hancock and A. P. Wilkinson, *J. Am. Chem. Soc.*, 2017, **139**, 13284-13287.
239. J. Chen, Q. Gao, A. Sanson, X. Jiang, Q. Huang, A. Carnera, C. G. Rodriguez, L. Olivi, L. Wang, L. Hu, K. Lin, Y. Ren, Z. Lin, C. Wang, L. Gu, J. Deng, J. P. Attfield and X. Xing, *Nat. Commun.*, 2017, **8**, 14441.
240. S. R. G. Balestra, R. Bueno-Perez, S. Hamad, D. Dubbeldam, A. R. Ruiz-Salvador and S. Calero, *Chem. Mater.*, 2016, **28**, 8296-8304.
241. (a) L. Sarkisov, R. L. Martin, M. Haranczyk and B. Smit, *J. Am. Chem. Soc.*, 2014, **136**, 2228-2231; (b) A. U. Ortiz, A. Boutin, A. H. Fuchs and F. X. Coudert, *Phys. Rev. Lett.*, 2012, **109**, 195502; (c) S. M. Moosavi, P. G. Boyd, L. Sarkisov and B. Smit, *ACS Cent. Sci.*, 2018, **4**, 832-839.
242. J.-C. G. Bünzli, *J. Coord. Chem.*, 2014, **67**, 3706-3733.
243. (a) T.-M. Zhao, S. Chen, R. Shang, B.-W. Wang, Z.-M. Wang and S. Gao, *Inorg. Chem.*, 2016, **55**, 10075-10082; (b) Z. Zhang, X. Jiang, G. Feng, Z. Lin, B. Hu and W. Li, *J. Solid State Chem.*, 2016, **233**, 289-293.
244. S. L. Anderson, A. Gładysiak, P. G. Boyd, C. P. Ireland, P. Miéville, D. Tiana, B. Vlaisavljevich, P. Schouwink, W. van Beek, K. J. Gagnon, B. Smit and K. C. Stylianou, *CrystEngComm*, 2017, **19**, 3407-3413.
245. CrysAlisPro, Rigaku Oxford Diffraction, 1.171.38.43 edn., 2015.
246. M. J. Cliffe and A. L. Goodwin, *J. Appl. Crystallogr.*, 2012, **45**, 1321-1329.
247. J. F. Nye, *Physical properties of crystals. Their representation by tensors and matrices*, Oxford University Press, Oxford, 1957.
248. P. Lama, R. K. Das, V. J. Smith and L. J. Barbour, *Chem. Commun.*, 2014, **50**, 6464-6467.

CV

Andrzej Gładysiak
– chemist, crystallographer

Doctoral Assistant
Laboratory of Molecular Simulation
EPFL Valais
Rue de l'Industrie 17
CH-1951 Sion
andrzej.gladysiak@epfl.ch

Scientific experience

(education background and research projects with key contribution)

- 10.2015–present **PhD in Chemistry and Chemical Engineering**
École polytechnique fédérale de Lausanne, Sion, Switzerland
supervisors: Dr. Kyriakos C. Stylianou and Prof. Berend Smit
- [15] A. Gładysiak, S. M. Moosavi, L. Sarkisov, B. Smit, and K. C. Stylianou, Guest-dependent negative thermal expansion in a lanthanide-based metal–organic framework, *CrystEngComm*, **21**, 5292–5298, (2019).
- [14] A. Gładysiak, T. N. Nguyen, R. Bounds, A. Zacharia, G. Itskos, J. A. Reimer, and K. C. Stylianou, Temperature-dependent interchromophoric interaction in a fluorescent pyrene-based metal–organic framework, *Chem. Sci.*, **10**, 6140–6148, (2019).
- [13] A. Gładysiak, T. N. Nguyen, M. Spodaryk, J.-H. Lee, J. B. Neaton, A. Züttel, and K. C. Stylianou, Incarceration of Iodine in a Pyrene-Based Metal–Organic Framework, *Chem. Eur. J.*, **25**, 501–506, (2019).
- [12] A. Gładysiak, K. S. Deeg, I. Dovgaliuk, A. Chidambaram, K. Ordiz, P. G. Boyd, S. M. Moosavi, D. Ongari, J. A. R. Navarro, B. Smit, and K. C. Stylianou, Biporous Metal–Organic Framework with Tunable CO₂/CH₄ Separation Performance Facilitated by Intrinsic Flexibility, *ACS Appl. Mater. Interfaces*, **10**, 36144–36156, (2018).
- [11] A. Gładysiak, T. N. Nguyen, S. L. Anderson, P. G. Boyd, R. G. Palgrave, J. Bacsá, B. Smit, M. J. Rosseinsky, and K. C. Stylianou, Shedding Light on the Protonation States and Location of Protonated N Atoms of Adenine in Metal–Organic Frameworks, *Inorg. Chem.*, **57**, 1888–1900, (2018).
- [10] A. Gładysiak, T. N. Nguyen, J. A. R. Navarro, M. J. Rosseinsky, and K. C. Stylianou, A Recyclable Metal–Organic Framework as a Dual Detector and Adsorbent for Ammonia, *Chem. Eur. J.*, **23**, 13602–13606, (2017).
- [9] S. L. Anderson, A. Gładysiak, P. G. Boyd, C. Ireland, P. Miéville, D. Tiana, B. Vlaisavljevich, P. Schouwink, W. van Beek, K. J. Gagnon, B. Smit, and K. C. Stylianou, Formation pathways of metal–organic frameworks proceeding through partial dissolution of the metastable phase, *CrystEngComm*, **19**, 3407–3413, (2017).
- 10.2010–06.2015 **BSc and MSc in Chemistry, *maxima cum laude***
Adam Mickiewicz University in Poznań, Poland
supervisor: Prof. Andrzej Katrusiak
- [8] W. Cai, A. Gładysiak, M. Aniola, V. J. Smith, L. J. Barbour, and A. Katrusiak, Giant Negative Area Compressibility Tunable in a Soft Porous Framework Material, *J. Am. Chem. Soc.*, **137**, 9296–9301, (2015).

Other publications

- [7] P. G. Boyd, A. Chidambaram, E. García-Díez, C. P. Ireland, T. D. Daff, R. Bounds, A. Gładysiak, P. Schouwink, S. M. Moosavi, M. M. Maroto-Valer, J. A. Reimer, J. A. R. Navarro, T. K. Woo, S. Garcia, K. C. Stylianou, and B. Smit, *Nature* (2019) *Accepted*.
- [6] S. L. Anderson, P. G. Boyd, A. Gładysiak, T. N. Nguyen, R. G. Palgrave, D. Kubicki, L. Emsley, D. Bradshaw, M. J. Rosseinsky, B. Smit, and K. C. Stylianou, *Nat. Commun.*, **10**, 1612, (2019).
- [5] F. P. Kinik, T. N. Nguyen, E. Oveisi, B. Valizadeh, F. Ebrahim, A. Gładysiak, M. Mensi, and K. C. Stylianou, *J. Mater. Chem. A*, **7**, 23830–23837, (2019).
- [4] F. M. Ebrahim, T. N. Nguyen, S. Shyshkanov, A. Gładysiak, P. Favre, A. Zacharia, G. Itskos, P. J. Dyson, and K. C. Stylianou, *J. Am. Chem. Soc.*, **141**, 3052–3058 (2019).
- [3] T. N. Nguyen, G. Capano, A. Gładysiak, F. M. Ebrahim, S. V. Eliseeva, A. Chidambaram, B. Valizadeh, S. Petoud, B. Smit, and K. C. Stylianou, *Chem. Commun.*, **54**, 6816–6819, (2018).
- [2] M. Witman, S. Ling, A. Gładysiak, K. C. Stylianou, B. Smit, B. Slater, and M. Haranczyk, *J. Phys. Chem. C*, **121**, 1171–1181, (2017).
- [1] P. A. Guńka, K. F. Dziubek, A. Gładysiak, M. Dranka, J. Piechota, M. Hanfland, A. Katrusiak, and J. Zachara, *Cryst. Growth Des.*, **15**, 3740–3745, (2015).

External courses

- | | |
|---------|---|
| 08.2018 | Crystallography Online: structural tools of the Bilbao Crystallographic Server
31st European Crystallographic Meeting satellite, Oviedo, Spain |
| 10.2017 | 33rd Ad Hoc Workshop on Jana2006: Modulated structures for chemists
Institute of Physics, Czech Academy of Sciences, Prague, Czech Republic |
| 06.2017 | Zurich School of Crystallography
University of Zurich, Switzerland
<i>awarded with the 1st prize for the best young crystallographer</i> |
| 09.2016 | Synchrotron Radiation School
Diamond Light Source, Didcot, UK |
| 07.2014 | Summer Workshop on Solid State Physics and Chemistry
Institute of Low Temperature and Structural Research in Wrocław, Poland |

Conferences

- | | |
|---------|--|
| 09.2019 | Annual Meeting of the Swiss Crystallographic Society (oral presentation [14]) |
| 07.2019 | 4th UK Porous Materials Conference (poster presentation [14]) |
| 09.2018 | Annual Meeting of the Swiss Crystallographic Society (poster presentation [15]) |
| 08.2018 | 31st European Crystallographic Meeting (poster presentation [12]) |
| 04.2015 | 8th Frolic Goats Workshop on High-Pressure X-Ray Diffraction (oral presentation [8]) |

Teaching experience

co-supervision of the MSc thesis of Mr. Sylvain Sudan (2018/2019)

supervision of laboratory works for BSc students in Chemistry and Chemical Engineering (4 semesters in total)

Skills

experimental, advanced: Inorganic and Organic Synthesis, Crystallisation, Single-Crystal X-ray Diffraction Analysis, Powder X-ray Diffraction Analysis, Solid-state Characterisation techniques, High-pressure techniques

experimental, basic: Scanning Electron Microscopy, Nuclear Magnetic Resonance, Extended X-Ray Absorption Fine Structure Spectroscopy

software, crystallography related: CrysAlisPRO, APEX3, XPREP, XP, SHELX, Jana2006, Olex2, Platon, ConQuest, Mercury, Diamond, Eva, FOX, FullProf, ToposPro

software, other: MS Office, OriginPro, ChemDraw, Athena

Experience at synchrotron facilities

European Synchrotron Radiation Facility, Grenoble, France

- BM01, single-crystal and powder X-ray diffraction: 02–03.05.2016; 13–14.07.2016; 30.07–01.08.2016; 29–30.08.2016; 31.10–01.11.2016; 12–14.03.2017; 11–14.04.2017; 03–09.05.2017; 01–06.12.2017; 28–31.01.2018; 09–15.04.2018
- BM31, powder X-ray diffraction: 06–08.11.2016

Diamond Light Source, Didcot, UK

- B18, X-ray absorption spectroscopy: 21–23.04.2017
- I12, high-energy powder X-ray diffraction: 17–19.09.2017

Awards

05.2019	Travel grant of the Swiss Crystallographic Society
04.2018	Chemistry Travel Award by the 'Platform Chemistry' of the Swiss Academy of Sciences (SCNAT) and the Swiss Chemical Society (SCS)
10.2015	Medal of the Adam Mickiewicz University in Poznań for the outstanding achievements in science and distinctive participation in life of the University
06.2014	2nd place in the National Crystallographic Olympiad, organized by the Committee of Crystallography of the Polish Academy of Sciences

Membership in scientific societies

Swiss Crystallographic Society

European Crystallographic Association

Languages

English (fluent)

French (fluent)

Russian

Polish (native)

